TRACE GAS AND AEROSOL TRANSPORTS INTO AND OUT OF THE AMAZON BASIN

NASA Cooperative Agreement NCC1-106

Progress Report
for the period

1 January 1990-31 August 1991

Submitted by

Michael Garstang
Principal Investigator

and

Steven Greco

Department of Environmental Sciences
University of Virginia
Charlottesville, VA 22903

September 1991

TRACE GAS AND AEROSOL TRANSPORTS INTO AND OUT OF THE AMAZON BASIN

NASA Cooperative Agreement NCC1-106

Progress Report
for the period

1 January 1990-31 August 1991

Submitted by

Michael Garstang
Principal Investigator

and

Steven Greco

Department of Environmental Sciences
University of Virginia
Charlottesville, VA 22903

September 1991

TABLE OF CONTENTS

Summary

Research under Agreement NCC1-106 during the period 1 October 1990 to 31 August 1991 has continued to use the data collected during all three ABLE missions ABLE I (1984), ABLE IIA (1985) and ABLE IIB (1987).

Overviews of the wet season ABLE IIB are presented by Garstang et al. (1990) and Harriss et al. (1990). The overview papers give the context of the wet season experiment and some of the results. Copies of all reprints and manuscripts published or accepted for publication are attached. A complete list of all papers published in the reviewed literature, papers presented as well as published as part of conference proceedings and articles published in the news media are listed as Appendix I.

Two scales of interaction of the rain forest have been pursued in this work:

1) global interactions

2) local and regional interactions.

Under the first scale, the role of the rain forest in the global system has been the central thrust of the work.

Under the second scale, the role of the rain forest on the basin and smaller scales has been focussed upon.

The contributions on each of these scales are summarized below.

1. Global Interactions

Garstang (1991) establishes the basis for the postulate that the tropical rain forests, and, in particular, that of Amazonia, are

a) linked to the global system
b) undergoing substantial change.

Harriss et al. (1990) gives the rationale for the ABLE and links the global atmosphere to the rain forests of Amazonia through the trace gas emissions eminating from that ecosystem.

Connors and Garstang (1991) and Connors (1991) show that there are identifiable weather regimes which persist over the Amazon Basin for time periods of days to 10's of days. These regimes are identified objectively by pattern recognition of satellite visible images. Synoptic scale systems characterize each regime on a sub-regime scale. Some 14 regimes account for 75% of the annual basin scale rainfall. Two regimes dominate the wet and dry seasons, each contributing most of the respective season's rainfall. The wet season regime accounts for 20% of the heat required to supply the high latitude global deficit of net radiation. Connors (1991) also finds that the major difference between the wet and dry season regimes is not the occurrence of penetrative (hot tower) convection but the increase in low and middle cloudiness in the wet season. She postulates that such an increase in low and middle tropospheric cloudiness permits mean (Hadley and smaller) circulations to transport heat. Thus, the importance of the hot tower is reduced. This finding had been suggested on a much smaller cloud (Scala et al., 1990) and mesoscale (Massie and Garstang, 1991).

Swap et al. (1991) provides evidence of synoptic scale forcing in the Amazon Basin which injects some 13 M tons of Saharan dust into the Basin. Wet deposition of this dust is demonstrated and up to 1 kg ha^{-1} of critical nutrients such as phosphate are postulated to reach the soils of the eastern and central Amazon Basin every year. The authors of this paper suggest that not only are the nutrient poor forests of Amazonia maintained by this airborne supply, but that the fluctuation in the size of the Amazon rain forest is directly linked to the fluctuation in the size of the Sahara. Turnover rate calculations based upon the calculated range of nutrient supply, such as phosphate, give the time to regenerate the Amazon rain forest as lying between about 500 and 2000 years.

2. Local and Regional Interactions

a. Aerosols

Talbot et al. (1990) show that wet season aerosol chemistry varies in association with 3 to 5 day rainfall events. Evidence is presented in this paper which provides the foundation for the Saharan dust hypothesis described above.

b. Trace Gases

Scala et al. (1990) and Scala (1990) show that convective clouds differ

markedly in their transport depending upon such controls as atmospheric stablility. "Dry" environment clouds are of the hot tower type in which > 90% of the cloud air at 12 km originates in the boundary layer below 2 km. Wet environment clouds grow in a more stable atmosphere and detrain considerable amounts of cloud air in the mid-troposphere. The "wet" cloud transports less than 15% from the boundary layer to 12 km. More than 60% of the cloud air at 12 km originates above 6 km.

Pickering et al. (1991) examined convective transport of trace gases and ozone production. Transient effects in the cloud were found to reduce the O_3 production by 50 to 60%. However, integrated O_3 production changed from net destruction to net production in the 5 to 13 km layer due to convective transports.

c. Energy

Massie and Garstang (1991) and Massie (1991) found that the ensemble transport of convection on the scale of 1000 km^2 was partitioned nearly equally between "convective" and "stratiform" transport over the lifetime of the system. They found that a mature convective system could contribute 20% of the heat required to balance the deficit due to longwave losses at higher latitudes. This result, on a much smaller space and time scale, is identical to that of Connors. The lifetime transport (growing, maturity, decaying) of a synoptic scale system was found to account for 33% of the required heat to balance the heat budget.

Greco et al. (1991) found nocturnal wind accelerations at altitudes of a few hundred meters above the forest canopy of 10 m s^{-1} from a daytime value of about 5 m s^{-1} to a nighttime value of 15 m s^{-1}. Horizontal pressure gradients between the terra firma forest canopy and the large rivers together with the formation of a strong low level inversion and the resulting frictional decoupling lead to the observed accelerations. These strong low level nocturnal winds on clear or nearly clear nights must serve to disperse boundary layer constituents which have been elevated during the growth of the BL in the daytime. Such dispersal is likely to be a very important mechanism in dispersing the products of forest and biomass fires.

d. Water

Greco et al. (1990) showed that most (80%) of the wet season rainfall occurs in bursts of a few days under the influence of what they called Coastal

Occurring Systems (COS) or Basin Occurring Systems (BOS). The remaining 20% was due to Local Occurring Systems (LOS). The well organized synoptic scale COS and BOS produce up to 5 cm of rain per day (2 inches) and cover a larger fraction of the Basin. Water supply (vapor) to these systems must be largely (perhaps as much as 90%) oceanic. They conclude that wet season rainfall is not critically dependent upon the rain forest. Dry season rainfall as suggested by Connors (1991), however, may be a critically controlling factor in maintaining the rain forest.

Appendix II provides a summary of future work. Appendix III provides a listing of degrees awarded during this report period.

APPENDIX I

List of Papers Published in Reviewed Literature

1990

Garstang, M., S. Ulanski, S. Greco, J. Scala, R. Swap, D. Fitzjarrald, D. Martin, E. Browell, M. Shipham, V. Connors, R. Harriss and R. Talbot: The Amazon Boundary Layer Experiment (ABLE 2B): A meteorological perspective. Bull. Amer. Meteor. Soc., 71, 19-32.

Greco, S., R. Swap, M. Garstang, S. Ulanski, M. Shipham, R.C. Harriss, R. Talbot, M.O. Andreae and P. Artaxo: Rainfall and surface kinematic conditions over Central Amazonia during ABLE 2B. J. Geophys. Res., 95, 17001-17014.

Harriss, R.C., M. Garstang, S. Wofsy, S. Beck, R. Bendura, J.R.B. Coelho, J.W. Drewry, J.M. Hoell, Jr., P. Matson, R.J. McNeal, L.C.B. Molion, R. Navarro, V. Rabine and R.L. Snell: The Amazon Boundary Layer Experiment (ABLE 2B): Wet season 1987. J. Geophys. Res., 95, 16721-16736.

Scala, J., M. Garstang, W.-K. Tao, K. Pickering, A. Thompson, J. Simpson, V.W.J.H. Kirchhoff, E. Browell, G. Sachse, A. Torres, G. Gregory, R. Rasmussen and M.A.K. Khalil: Cloud draft structure and trace gas transport. J. Geophys. Res., 95, 17015-17030.

Talbot, R., M. Andreae, H. Berresheim, P. Artaxo, M. Garstang, R. Harriss, K. Beecher and S.M. Li: Aerosol chemistry during the wet season in Central Amazonia: The influence of long-range transport. J. Geophys. Res., 95, 16955-16969.

1991

Garstang, M.: Destruction of the rain forest and climate change. Accepted for publication in the New Zealand Geographer, Special Volume.

Garstang, M. and C. Martin: PAM stations weather Amazon rainforest. The ATD Observer, NCAR/UCAR Publication, Winter 1991, pgs. 1-3.

Greco, S., S. Ulanski, M. Garstang and S. Houston: Low-level nocturnal wind accelerations over the Central Amazon Basin. Accepted for publication in Bound.-Layer Meteor.

Pickering, K.E., A.M. Thompson, J.R. Scala, W.-K. Tao, J. Simpson and M. Garstang: Photochemical ozone production in tropical squall line convection during NASA/GTE/ABLE 2A. J. Geophys. Res., 96, 3099-3114.

Swap, R., M. Garstang, S. Greco, R. Talbot and P. Kållberg: Saharan dust in the Amazon Basin. Accepted for publication in Tellus.

Papers Under Preparation

1991

Harriss, R.C., M. Garstang and S. Wofsy: Role of the tropical rain forests in the global system. To be submitted to Scientific American.

Massie, H.L., M. Garstang, J. Halverson and S. Greco: Amazon coastal squall lines: Part I: Structure and kinematics. To be submitted to Mon. Wea. Rev.

Massie, H.L., M. Garstang, J. Halverson and S. Greco: Amazon coastal squall lines: Part II: Heat and moisture transports. To be submitted to Mon. Wea. Rev.

Conference Proceedings/Presentations

1990

Connors, V., D.R. Cahoon, H. Reichle, M. Garstang, W. Seiler and H.E. Scheel: Savanna burning and convective mixing in southern Africa: Implications for CO emissions and transport. Paper presented at Chapman Conference on Global Biomass Burning, Williamsburg, VA.

Harriss, R.C., S. Wofsy and M. Garstang: Air chemistry over the Amazon Basin. Proc. AMS Symp. on Global Change Systems, Special Session on Climate Variation and Hydrology, Anaheim, CA.

Scala, J., M. Garstang, W.-K. Tao and K. Pickering: The complexity of convective transport. Pape presented at Chapman Conference on Global Biomass Burning, Williamsburg, VA.

1991

Connors, V., M. Garstang and S. Nolf: Atmospheric weather regimes over tropical south America. Proc. AMS 19th Conf. on Hurr. and Trop. Meteor., Miami, FL, pp. 64-67.

Garstang, M: The role of the Amazon rain forst in the global climate. AAAS Paul McInerney Memorial Lecture, Millersville University, Millersville, PA. Seminar also presented at the University of Canterbury, Christchurch, N.Z., Ortago University, Dundedin, N.Z., University of Auckland, Auckland, N.Z., Massey University, Palmerston North, N.Z., Meteorological Office, Auckland, N.Z.

Garstang, M.: Saharan dust transport. Seminar presented at the Max-Planck Institute, Biochemistry Department, Mainz, Germany.

Greco, S., M. Garstang, S. Ulanski and S. Houston: Nocturnal boundary layer accelerations in the Central Amazon Basin. Proc. AMS 19th Conf. on Hurr. and Trop. Meteor., Miami, FL, pp. 140-143.

Massie, H. and M. Garstang: Heat and moisture budgets in an Amazon traveling disturbance line. Proc. AMS 19th Conf. on Hurr. and Trop. Meteor., Miami, FL, pp. 162-167.

Scala, J., W.-K. Tao, K. Pickering, A. Thompson, J. Simpson and M. Garstang: The effect of tropical squall-type convection on the vertical transport and redistribution of trace gases. Proc. AMS Seventh Joint Conf. on Appl. Air Poll. Meteor. with AWMA, New Orleans, LA, 228-231.

Swap, R., M. Garstang, S. Greco and P. Kållberg: Long-range transport of Saharan dust into the Central Amazon Basin over 10-14 days. Proc. AMS Seventh Joint Conf. on Appl. Air Poll. Meteor. with AWMA, New Orleans, LA, 20-23.

Swap, R., S. Greco, M. Garstang, P. Kållberg, R. Talbot and P. Ataxo: Saharan dust transport into the Central Amazon Basin. Proc. AMS 19th Conf. on Hurr. and Trop. Meteor., Miami, FL, pp. 77-80.

Media Coverage of Work

1991

"The Saharan-Amazonian Connection", The World and I, February 1991.

"Amazon depends on Sahara's winds", Richmond Times-Dispatch, February 1991.

"UVa scientists find Sahara dust saving Amazon forest", The Daily Progress, February 1991.

"Amazon basin may be eating Sahara's dust: Theory sees wind ferrying nutrients", The Washington Post, February 1991.

"Desert dust keeps rain forest alive, researchers find", Inside UVa, March 1991.

"African dust 'feeds' Amazon rain forest", International Wildlife, May/June 1991.

"Dust busters: Amazon 'vacuum cleaners' draw nutrients from the Sahara", UVa Alumni News, May/June 1991.

"Desert dust nurtures faraway rain forest", Geotimes, June 1991.

"Is Africa's windblown loss the Amazon's gain?", National Geographic, September 1991.

APPENDIX II

Future Work

Future work will focus upon the following research areas:

1) Structure and kinematics of Amazon squall lines
2) Heat budgets/transports of Amazon squall lines: (a) Observations and (b) Comparison between observations and model results.

2) Saharan dust in the CAB: Part II: History of ecosystem linkage.

3) Moisture or water budgets over the CAB: Mesoscale and synoptic scale.

4) Basin occurring systems (BOS) over the CAB: structure and energetics.

5) Mesoscale circulations and rainfall gradients near Manaus and the Amazon river system.

6) CAB wet season boundary layer structure and comparison with dry season results.

7) Hydrocarbon and water vapor effects on emissivity and nocturnal temperatures in the CAB.

8) Intra-seasonal variability over the CAB.

APPENDIX III

Degrees Awarded

1990/1991

Connors, V.: "Equatorial atmospheric weather regimes: Their structure and role. PhD dissertation, University of Virginia, August 1991.

Massie, H.L.: "The structure and energetics of Amazon squall lines." PhD dissertation, University of Virginia, May 1991, 194 pp.

Scala, J.R.: "Convective draft structure and transport over the Amazonian rain forest." PhD dissertation, University of Virginia, May 1990, 248 pp.

Swap, R.: "The nature and origin of Central Amazonian wet season rainfall." M.S. thesis, University of Virginia, August 1990, 116 pp.

Accepted - Tellus

SAHARAN DUST IN THE AMAZON BASIN

R. Swap, M. Garstang, S. Greco,

University of Virginia

Department of Environmental Sciences

Charlottesville, VA 22903, U.S.A.

R. Talbot

Institute for the Study of Earth, Oceans and Space

University of New Hampshire,

Durham, NH 03824, U.S.A.

and

P. Kållberg

Swedish Meteorological and Hydrological Institute,

Norrköping, Sweden

Abstract

Saharan dust is shown to enter the Central Amazon Basin (CAB) in bursts which accompany major wet season rain systems. Low level horizontal convergence feeding these rain systems draws dust from plumes which have crossed the tropical Atlantic under the large-scale circulation fields. Mass exchange of air between the surface and 4 km over the eastern Amazon basin is calculated using rawinsonde data collected during storm events. Mean concentrations of dust observed by aircraft over the western tropical Atlantic are used to calculate the amount of dust injected into the Basin. Individual storm events inject some 480,000 tons of dust into the northeastern Amazon Basin. Storm and dust climatology suggest that the annual importation of dust is in the order of 13 Mtons. In the northeastern basin, this may amount to as much as 190 kg ha^{-1} yr^{-1}. Deposition of trace species, such as phosphate, associated with this dust ranges from 1-4 kg/ha/yr. Uncertainties in these estimates are not believed to be greater than ± 50% and may be as low as ± 20%. The deposition fluxes from Saharan dust are essentially identical to the CAB wet deposition fluxes from precipitation in the wet season; a result that implies that the major ionic composition of rain water in the CAB wet season may be strongly influenced by inputs of material originating on the African continent nearly 5000 km away.

The total amount of Saharan dust calculated to enter the Amazon basin is one half to one third of that estimated to cross 60°W longitude between 10° and 25°N latitude. We conclude that part of the productivity of the Amazon rain forest is dependent upon critical trace elements contained in the soil dust originating in the Sahara/Sahel. This dependence should be reflected by expansions and contractions of the Amazon rain forest in direct relationship to expansions and contractions of the Sahara/Sahel. Turnover rates for nutrient species deposited with Saharan dust in the Amazon Basin suggest a time scale of 500 to 20,000 years. We believe the dependence of one large ecosystem upon another separated by an ocean and coupled by the atmosphere to be fundamentally important to any view of how the global system functions. Any strategy designed to preserve the Amazonian rain forest or any part thereof should equally concern itself with the interrelationship between the rain forest, global climate and arid zones well removed from Amazonia.

1. Introduction

The tropical rain forests of the world are generally regarded as large ecosystems in relatively delicate nutrient balance. Balance is achieved by efficient cycling in a nutrient-limited environment (Jordan, 1985; Vitousek and Sanford, 1986). In the northeastern and parts of central Amazonia, where nutrient poor oxisols and ultisols are present and nutrient supply by rivers is limited, deposition of airborne soil dust particles is needed to achieve a nutrient balance (Jordan, 1985; Salati and Vose, 1984; Vitousek and Sanford, 1986). The amounts of aeolian influx have been estimated to be relatively high (in the order of millions to tens of millions of tons per year). In the case of some of the critical trace elements, this influx may be crucial to the health of the forest. Jordan (1985) and Vitousek and Sanford (1986), for example, have suggested that phosphorus may be a critical airborne element which could limit annual net primary production of the rain forest.

A substantial body of literature identifies the Sahara and sub-Saharan Sahel as the probable source region of dust found over a large fraction of the earth's surface. Saharan dust transported over distances of greater than 5000 km has been shown to reach areas in northern Europe (DeAngelis and Gaudichet, 1991; Reiff et al., 1986) and the middle east (Levin et al., 1980). In addition, there is considerable evidence mainly provided by Prospero and colleagues that Saharan dust reaches the eastern

Caribbean (Prospero and Carlson, 1972; Talbot et al., 1990), southern North America (Savoie and Prospero, 1977) and the northeastern coast of South America (Parkin et al., 1972; Prospero et al., 1981; Prospero et al., 1987; Talbot et al., 1990).

There is also general agreement that transport of dust to the far western tropical Atlantic and the Caribbean occurs in the northeasterly trades at relatively low altitudes, mostly below 6-7 km (Prospero and Carlson, 1972; Jaenicke and Schütz, 1978; D'Almeida, 1986; Westphal et al., 1988; Bergametti et al., 1989). This layer of air, called the Saharan Air Layer (SAL), is situated most frequently between 850 and 700 mb (1.5 and 3 km) (Prospero and Carlson, 1972; Reiff et al., 1986; Bergametti et al., 1989).

Our results suggest that a considerable amount of the dust found in the Central Amazon Basin (CAB) is of Saharan origin. This Saharan dust is transported across the Atlantic under steady state (undisturbed) conditions in the 850 to 700 mb layer (Prospero and Carlson, 1972). However, we suggest that such steady state transport is not sufficient to bring the dust into the CAB. Synoptic scale weather systems, with associated organized low level convergence, are required to gather the dust into the Basin. Thus, dust events in the CAB are a function of synoptic scale systems coinciding with the existence of a dust plume in the far western tropical Atlantic. The role played by synoptic scale systems in producing pulses of Saharan dust in the

CAB may also explain why Prospero et al. (1981) observed the maximum in dust concentrations in Cayenne, French Guiana to occur during the height of the wet season. Similarly, synoptic scale systems provide a mechanism in the far western Atlantic to inject dust across an active Intertropical Convergence Zone (ITCZ). Penetration of Saharan dust across an active ITCZ into the southern hemisphere has been deemed unlikely (Junge, 1979) because of wet removal of the dust.

Prospero and Carlson (1972) and Prospero et al. (1981) have made estimates of the annual amount of dust reaching a particular location. D'Almeida (1986) has also given estimates of the annual amount of particulate matter exported northward, westward and southward from the Sahara/Sahel. Uncertainties, however, remain in the estimates of the total amount of dust reaching such locations. An associated uncertainty also exists in the number and amount of trace elements delivered to a given location.

In the discussion which follows, aircraft sampling of aerosols, mass divergences calculated from rawinsonde stations and rain and dust storm climatology are used to calculate the storm and annual amount of dust brought into the Amazon Basin. A breakdown of the trace species concentrations present in the dust is also attempted. The resulting annual amounts of dust are compatible with those obtained by Prospero and Carlson (1972) across 60°W between 10 and 25°N latitude. The results obtained support the belief that the dust observed during the wet season in the central Amazon basin is of Saharan origin. The storm

convergence mechanism called upon to inject dust into the CAB provides a means to calculate the event, seasonal and annual amounts of dust imported.

If Saharan dust provides a major source of nutrients for the Amazonian rain forests, then a series of most important consequences follow. Reichholf (1986) has suggested that major fluctuations in rainfall over northern Africa during and following the pleistocene should be reflected by parallel expansions and contractions of the Amazon rain forest. Petit et al. (1981) have indeed reported evidence of increased continental aerosol concentrations during the pleistocene, attributed to increased size and activity of sand deserts located between 30°N and 30°S. Short term variations in the amount of particulate matter coming off West Africa have been related to the recent Sahelian droughts (Prospero and Nees, 1977, 1986). The possible response of the Amazon rain forest to variations in the airborne nutrient supply depends upon whether, how, what kind and how much dust is imported into the Amazon basin. The findings we present below to answer some of these questions are based upon a series of National Aeronautics and Space Administration (NASA) experiments carried out under the Division of Atmospheric Chemistry's Global Tropospheric Experiment (GTE).

2. GTE Atlantic and Amazon Boundary Layer Experiment (ABLE)

The NASA GTE is attempting to document the chemical composition of the global troposphere by selecting and examining

the atmosphere over important ecosystems. The Atlantic Boundary Layer Experiment (ABLE 1) (Gregory et al., 1986; Talbot et al., 1986) examined the troposphere over the open western tropical ocean in June 1984. The two Amazon experiments ABLE 2a and 2b, examined conditions over the relatively undisturbed tropical rain forest of the CAB in the dry, July-August 1985, and wet, April-May 1987, seasons (Harriss et al., 1988; 1990).

Field measurements made in the ABLE 1, 2a and 2b provide information on a range of interacting scales (e.g., space scales from 50 km to 5000 km) which appear essential to the understanding of both the chemistry and the dynamics of this fluid system (Figs. 1(a) and (b)). The field experiments, associated observations and results are summarized in two special issues of the JGR devoted to ABLE 2a and 2b (JGR, 1988; 1990). A number of these results are used to present a mechanism to introduce Saharan dust into the CAB and to calculate the total importation of dust and associated trace species.

Sampling of atmospheric aerosols was conducted from the ground (Artaxo et al., 1990) and at various altitudes (0.2 to 6.0 km) from the NASA Electra research aircraft (Talbot et al., 1990). The ground-based sampling network was located on three of the towers shown in Fig. 1(b) at 45 m, 28 m and 2 m. Sampling duration ranged from 24 to 48 h. Samples were collected continuously from April 8 to May 14, 1987. The concentration of particulates and elements contained in soil dust (e.g., Si, Al, Fe) was determined on a daily basis.

Elemental concentrations were determined using particle induced x-ray emission (PIXE) analysis. Coarse (> 2 microns) and fine (< 2 microns) mode particle contributions were determined. Artaxo et al. (1990) found the following 22 elements in the ABLE 2b ground-based aerosol samples: Na, Mg, Al, Si, P, S, Cl, K, Ca, Ti, V, Cr, Mn, Fe, Ni, Cu, Zn, Br, Rb, Sr, Zr, and Pb. Rain water analysis was performed on samples collected at 3 of the tower locations shown in Fig. 1(b) (Andreae et al., 1990). Rain water samples were collected on an event basis at each station.

Airborne (NASA Electra) sampling of aerosols consisted of collection on teflon filters and subsequent analysis of the water-soluble trace species using ion chromatography (Talbot et al., 1990). The constituents observed included Na, NH_4, K, Cl, NO_3, SO_4, C_2O_4, CH_3SO_3, HCOO, and CH_4COO (Talbot et al., 1990).

The European Centre for Medium Range Weather Forecasting (ECMWF) global wind analyses are used for the computation of 10 day backward and forward isobaric trajectories. An overview of the ECMWF data assimilation system may be found in Hollingsworth (1987). The ECMWF analyses are available every 6th h with a horizontal resolution corresponding to 125 km at 19 vertical hybrid levels.

The 2-D trajectory method is a straightforward Lagrangian following of air parcels in the analyzed wind field with wind components interpolated linearly in time every 6 h. The wind components are further interpolated, both horizontally and vertically (pressure), to the actual position of the parcel. The

interpolated wind components are then used to track the parcel forward or backward over 6 h in 15 min increments.

Horizontal wind fields were compiled using ECMWF global data together with commercial aircraft and satellite wind observations (T. Krishnamurti, personal communication). The data at 850, 500, and 200 mb are used to determine the streamline fields over the tropical Atlantic, Africa, and South America during the ABLE 2b experiment.

Satellite imagery from the European Meteosat are used to provide coverage of the tropical Atlantic from northern Africa to the coast of South America including the arid region of northeast Brazil.

Ground-based rawinsonde measurements, obtained 4 times daily, were made in a basin scale network (1000-1500 km apart) shown in Fig. 1(a). Local meteorological measurements used in this study include rawinsondes from the three corner stations of the mesoscale network in Fig. 1(b) (approximately 50 km spacing) together with rainfall measurements made on the towers at 5 m above the canopy.

Aerosol optical thickness values deduced from the Advanced Very High Resolution Radiation (AVHRR) satellite measurements (Rao et al., 1988) were not available during any of the ABLE missions. We refer to post field experiment aerosol optical thickness data to confirm the frequency and geographic extent of Sahara dust outbreaks.

3. Analysis and Results

Ground-based measurements of aerosol concentration and composition during ABLE 2b indicate the occurrence of several large pulses containing both terrestrial and marine aerosols (Fig. 2a). Three maxima were centered around April 12-14 (experimental days 12-14), April 29-May 1 (experimental days 29-31) and May 5-8 (experimental days 36-40).

Aerosols associated with these pulses had relatively high concentrations of alkali and alkaline earth elements in the atmospheric mixed layer of the CAB (Talbot et al., 1990). Amazonian soils, however, are highly weathered and exhibit deficits of these elements. This finding suggested a non-local source region for the dust, which Talbot et al. (1990) believe to be the Sahara. Pulses of Saharan dust were also observed at Barbados during ABLE-2b (Talbot et al., 1990). These pulses, with concentrations at the surface reaching 180 $\mu g\ m^{-3}$, appeared at Barbados 1 to 2 days before Saharan dust was seen in the CAB.

The temporal variation of major mineral aerosol constituents (e.g., Fe, Al, Si) shown in Fig. 2, are compared with the mean regional mesoscale (4 station) rainfall in Fig. 2. Both aerosols and rainfall occur in distinct pulses. The two major pulses in Si coincided with the two major rain events. The third, weaker aerosol pulse preceded a weaker rainfall event by about 48 h. Other rain events show little or no association with increases in dust. On days with little or no rain, however, very low

concentrations of dust are observed.

Analysis of the rainfall during ABLE 2b (Greco et al., 1990; Garstang et al., 1990; Swap, 1990) showed that more than 80% of the rain was due to large (linear scales of 1000 km or larger) organized synoptic scale systems.

Wet season rainwater chemistry associated with large systems compared to small or local rain systems is different. The highest concentrations of SO_4^{2-} and Cl^- as well as higher pH values occur in large organized rain systems compared to local rain showers (Andreae et al., 1990). The presence of marine constituents (e.g., Na^+ and Cl^-) in these large rain systems suggest that they are ingesting low level air from over the western tropical Atlantic. Higher pH values in rain water, however, have also been found to be associated with Sahara dust (Löye-Pilot et al., 1986). Therefore, marine chemical constituents and continental components from African regions south of the Sahara may contribute to the rainwater composition of large rain systems in the CAB.

High concentrations of mineral aerosols occurring in close association with large rain events requires an explanation because wet removal would suggest the opposite result. We propose below that low level convergence covering a large area and preceding such large rain systems by 24 to 72 h is responsible for increasing the dust concentrations in near coincidence with the production of rain from these weather systems. This explanation requires the presence of a Saharan

dust plume in the far western tropical Atlantic at the time that the synoptic scale weather system is organizing on the northeastern South American coast. First, we show from trajectory analysis that Saharan dust can reach the eastern and central Amazon basin. Secondly, we calculate mass convergence in the low troposphere preceding the weather system and will show that this convergence can concentrate the dust from the pre-existing plume residing over the western tropical Atlantic. Finally, we show that measured values of concentrations in the oceanic dust plume allow the calculation of both the total mass of dust and the mass of the associated chemical constituents transported into the Amazon Basin.

3.1 Streamline and Trajectory Analysis

The large subtropical anticyclones are indicators of the nature of the lower tropospheric fields of motion linking western Africa and eastern South America. The position of the West African Subtropical High (WASH) with ridging over the central tropical Atlantic has been shown to influence low level flow across the Atlantic into the Amazon Basin (Talbot et al., 1990). Figure 3 shows that, with the WASH centered in a prescribed area of West Africa, flow at 500 mb extends across the Atlantic and into the Amazon Basin. Each of the three concentrated pulses of soil dust into the CAB shown in Fig. 2 followed a 4-7 day period of the WASH so established over West Africa (Talbot et al., 1990). Meteosat visible images (not shown) confirm that, during such periods of dominance by the WASH, fair weather extends

across the low latitude north Atlantic. Under a slowly changing large scale anticyclonic streamline field, the streamlines approach trajectories. The absence of deep convection or other forms of strong vertical motion along the path provide conditions which are near optimal for the calculation of trajectories.

Two-dimensional horizontal isobaric trajectories were calculated at 975, 950, 925, 900, 850, 800, 700, and 600 mb based upon the 6 h ECMWF global wind analysis. The 2-D trajectory calculations at multiple levels over 10 days were used to produce an envelope to bound the possible path taken and as an indication of the approximate origin or end point of the air parcels. Visible satellite imagery and the large scale wind fields in the 5-7 day period prior to a soil dust event in the CAB suggest near steady state conditions with little or no deep convection in the region of dust transport (Talbot et al., 1990). In the absence of deep convective clouds, vertical motions in the lower troposphere are confined to large scale subsidence in the order of 400 m day^{-1} (Riehl, 1954; Riehl et al., 1951). Forward trajectories were calculated from two locations:

15°N latitude 10°E longitude in the Sahel, and

20°S latitude 15°E longitude in the Namib.

Backward trajectories were calculated from

0 latitude 60°W longitude in the CAB.

Three ten-day periods were chosen, two to coincide with the two major dust events seen in the CAB and one to coincide with a period of very low dust concentrations in the CAB (Fig. 2). The

results of these calculations are discussed below.

Dust event of 12 April-14 April: Backward trajectories starting on 12 April 1987 (Figs. 4a and 4b) and 14 April 1987 (Figs. 4c and 4d) and forward trajectories starting on 4 April 1987 (Figs. 5a and 5b) suggest that air parcels between 800 and 700 mb (Figs. 4b, 4d and 5b) originate from a region near Lake Chad. Air below 800 mb is traced back to the eastern Atlantic and the West African coast (Figs. 4a and 4c). Air below 800 mb originating (Fig. 5a) near Lake Chad does not leave the west coast of Africa after 10 days of travel time. Air above 700 mb is either not traced back to Africa (Fig. 4b) or does not reach the Sahel in the backward trajectory calculation. In the 10-day forward calculation (Fig. 5b), air at 600 mb heads towards, but does not reach the mouth of the Amazon.

Backward and forward trajectories were also calculated for the dust event of 29 April-1 May 1987 and for a low dust concentration day, 26 April 1987. We discuss our findings from these trajectory calculations without showing the graphical results. The backward trajectories starting on 29 April 1987 and 1 May 1987 and forward trajectories starting on 21 April 1987 show results similar to the April 12-14 event. Backward trajectories at 800 to 700 mb once again end up near Lake Chad. Above 800 mb and below 700 mb, however, parcels show a diverse set of pathways. Forward trajectories with the calculation beginning on 21 April 1987 just west and north of Lake Chad do not show any connection to the Amazon Basin. Backward trajectory

results suggest that the point of origin chosen for the calculation is too far north and east.

Ten-day forward trajectories were also calculated for three separate dates: 4th, 16th and 21st April 1987 to determine whether dust could be coming from the southern hemisphere deserts of the Namib and Kalahari. No such connection was found.

While the trajectory calculations carried out as part of this paper do not rule out any other source of soil dust, we believe that the results show support for the contention that the Sahara/Sahel is the primary source. We find no evidence in the trajectory calculations that would support a South American location as a source region in the April/May time of year. None of the backward trajectories calculated from the CAB point (0° latitude, 60°W longitude) approach the dry zone of northeastern Brazil. Transport from the Namib/Kalahari, as well as from NE Brazil, into the Amazon basin may well, however, occur during astral spring and summer.

3.2 Horizontal Mass Divergence Calculations

The large triangle in Fig. 1(a) shows the relative location of three of the six basin scale rawinsonde network stations operated during ABLE 2b and designed to describe large-scale meteorological conditions over the entire Amazon Basin. The line from Boa Vista to Belém is nearly parallel to the northeast coast of South America. This line is also approximately normal to low level inflow into the Amazon Basin under conditions which favor both the transport of dust across the Atlantic (Fig. 4 and the

development of synoptic scale weather systems in the Amazon Basin. The Belém, Boa Vista and Embrapa triangle over the northeastern Amazon Basin is thus positioned to capture any enhanced mass inflow into the Basin drawing lower tropospheric air from over the western tropical Atlantic.

Rawinsonde data from the basin-scale stations were used to calculate horizontal divergence for the Belém, Boa Vista and Embrapa triangle by employing a line integral method utilizing the wind components normal to each leg of the triangle (Brummer, 1978). The horizontal divergence calculated for the triangle serves to determine the amount of air and, with measured aerosol concentrations, the amount of dust imported into the triangle volume as a function of the circulation of the synoptic scale storm system.

Figures 6(a) and 6(b) show the experiment time series of horizontal divergence at 850 mb and 700 mb. The rawinsonde network was not fully functional until 15 April 1987. The dust event of 29 April-1 May 1987 is captured by this time series and is used below to calculate total mass inflow into the volume above the triangle. The divergence signal in Fig. 6 shows a major perturbation about the 29 April-1 May event. Increasing low level convergence precedes the event, followed by divergence which is coincident with the major rain pulses.

Divergence calculations for the triangle were repeated based solely upon ECMWF data. The results of this calculation are also shown in Fig. 6. While the ECMWF data captures much of the

temporal variation in the signal, divergence is an order of magnitude lower than that obtained from the calculations based on the soundings.

Divergence calculated for the smaller mesoscale triangle shown in Fig. 1(b) (Scala et al., 1990) yield divergence values an order of magnitude higher (10^{-4} s^{-1}) than those obtained from the large scale triangle network soundings. Such a hierarchal increase in divergence (10^{-6}, 10^{-5}, 10^{-4} s^{-1}) proceeding from the large scale flow fields, as represented by the ECMWF, to the synoptic fields large scale triangle (Fig. 1(a)) to the mesoscale (mesoscale triangle soundings, Fig.1(b)) is consistent with other work in the tropical atmosphere (see for example the GARP Atlantic Tropical Experiment results such as Frank, 1978). We, therefore, use a 48 h mean convergence of 2.0×10^{-5} s^{-1} as representative of the mass inflow into the volume bounded by the surface to 4 km and the sides Boa Vista to Belem to Manaus.

3.3 Calculation of Mass Transports of Saharan Dust into the Amazon Basin

The area of the large triangle in Fig. 1(a) is approximately 4.0×10^{11} m^2. The volume of air from the surface to 4 km over the triangle is 1.6×10^{15} m^3. If the mean divergence over 48 h preceding the dust event is -2.0×10^{-5} s^{-1}, then the amount of air exchanged during this time is $(-2.0 \times 10^{-5}\ s^{-1})(1.728 \times 10^{5}\ s)$ = 3.5 times the original volume. In contrast, with large scale flow in the absence of an organized synoptic scale weather system (divergence = 10^{-6} s^{-1}), the exchange rate would be an order of

magnitude less, or only one third of the low level volume would be exchanged in 48 h. Under synoptic scale forcing, the volume of air contained below 4 km over the triangle is exchanged 3.5 times in 48 h equalling $(3.5)(1.6 \times 10^{15}\ m^3) = 5.6 \times 10^{15}\ m^3$ of air.

Under northeasterly inflow into the Amazon basin, we may assume that all of this exchange occurs across the side of the triangle parallel to the coast. Figure 7 shows the dust plume lying off the NE coast of South America. Figure 8 shows a Saharan dust plume immediately east of Barbados (60°W, 13°N) as observed by downward looking airborne lidar (Browell, personal communication). The plume lies between 1.5 and 4.2 km. In the presence of such a dust plume, the air being brought into the basin-scale triangle by the storm system will contain large amounts of dust. Talbot et al. (1986) showed that these dust plumes contained up to 400 $\mu g\ m^{-3}$, with a mean value of 51 $\mu g\ m^{-3}$ for the surface to 3.7 km layer. A weighted mean for the layer between 1.5 and 4 km from Prospero and Carlson (1972) gives a value of 45 $\mu g\ m^{-3}$. We take a mean value of 50 $\mu g\ m^{-3}$ for the dust concentration in such a plume between the surface and 4 km over a continuous period of 48 h. Using this mean concentration, we calculate the mass of dust entering the volume in 48 h to be:

(the volume of air exchanged in 48 h)(mean concentration)

$(5.6 \times 10^{15}\ m^3)(5.0 \times 10^{-5}\ g\ m^{-3})$

$= 2.8 \times 10^{11}$ g or

280,000 tons per storm system.

A given storm may have a convergence field which acts on the dust plume for longer than 48 h. However, this may be counteracted by the fact that a mean concentration of 50 $\mu g\ m^{-3}$ may be high for the entire duration of the inflow. Thus, we feel that 48 h and 50 $\mu g\ m^{-3}$ are representative of the average dust event.

The calculation above assumes the dust enters across the side of the triangle (Fig. 1(a)) parallel to the coast. In fact, the dust will enter across the entire NE coast of South America. Aerosol optical depth data from the Advanced Very High Resolution Radiometer (AVHRR) presented in (Fig. 7) shows that the length of coastline across which the dust is transported extends from Sao Luis, Brazil (44°30'W longitude, 2°30'S latitude) to the Gulf of Paria (63°0'W longitude, 10°30'N latitude), a total distance of 2500 km. The linear distance of the triangle side to the coastline is 1:1.7. We thus increase our above estimate by 1.7:

$$(2.8 \times 10^5)(1.7) = 4.8 \times 10^5 \text{ tons/storm system.}$$

Greco et al. (1990) have shown that 80% of the CAB rainfall during the wet season is produced by organized synoptic scale weather systems. The average amount of rainfall in the CAB during the 6 months (December-May) of the CAB wet season coincident with Saharan dust outbreaks is about 1600 mm (Villa Nova et al., 1976; Marques-Filho et al., 1981). Swap (1990) shows that the average amount of rain per synoptic scale system

is 20 mm. Thus, approximately 60 synoptic scale weather systems occur in the 6 month wet season or approximately 10 systems a month. Other evidence (Madden and Julian, 1972) show a 5-day periodicity in the equatorial tropics or 6 systems a month.

The wet season for the eastern Amazon basin (EAB) is approximately 2 months longer than the CAB wet season. The EAB wet season lasts from December to July (Villa Nova et al., 1976), and with approximately 2000 mm of rain falling during this period. If 80% of the EAB rain is also delivered by organized synoptic scale systems, approximately 80 storms occur in the 8 month wet season (10 systems a month). These numbers are supported by Cohen (1989) who reported an average annual value of 67.5 synoptic scale instability lines in the EAB during these months between 1979 and 1986. Cohen's numbers are confined to "instability lines" and do not include all synoptic scale systems.

Aerosol optical thickness measurements made from the AVHRR equipped satellite over a 32 month period from June 4, 1987 to March 1, 1990 are used to obtain a measure of the number of weeks in which Saharan dust outbreaks are present off the NE coast of South America. Table 1 shows that 34.1% of the weeks during the 32 months have aerosol optical thickness values of at least .3 within the area bounded by 10°N-0°, 60°W-40°W. Values of .3 or greater are representative of heavy aerosol outbreaks (Carlson, 1979). Table 1 also shows that heavy dust outbreaks are seen from December to July. This corresponds to the height of the wet

season for eastern and northeastern Amazon basin (Villa Nova et al., 1976) and to the period of increased coastal squall line activity (Cohen, 1989).

Based on the results of rainfall per system and the aerosol optical depth analysis, 34.1% of the 80 or 27.3 synoptic scale systems have the potential to carry dust into the eastern Amazon basin during the extended wet season of December-July. If we round off the number of dust bearing storms to 27 per wet season then the annual amount of Saharan dust introduced into the Amazon Basin is

$(4.8 \times 10^5$ tons per storm) X (27 storms/wet season).

If all of the Saharan dust introduced into the Amazon basin in a year is accomplished in the wet season, then the amount of dust per year is 13.0 Mtons/year.

Prospero and Carlson (1972) have estimated the annual transport of Saharan dust through a wall extending from 10°N latitude to 25°N latitude along 60°W longitude to range between 25 and 37 Mtons per year. D'Almeida (1986) has estimated annual westward transport immediately off West Africa to lie between 45 and 53 Mtons per year. Estimates of the total annual West African source strength for westward transport vary from 80 Mtons per year (Prospero and Carlson, 1972) to 260 Mtons/year (Jaenicke and Schütz, 1978) with 190 Mtons per year having been reported by D'Almeida (1986).

Our results suggest that the amount of dust that enters the Amazon basin is between one half and one third of the amount of dust found by Prospero et al. (1981) to cross the 60th meridian between 10 and 25°N. The major uncertainties in our calculations are the mean concentration (50 $\mu g\ m^{-3}$) and the number of synoptic scale systems (27) which bring dust into the Amazon Basin. Mean concentrations of dust in the outbreaks coinciding with synoptic scale systems in the Amazon Basin are unlikely to drop below 25 $\mu g\ m^{-3}$ or to rise above 75 $\mu g\ m^{-3}$. Extreme variations in mean wet season rainfall in the CAB reach $\pm$ 20% (Kousky and Kagano, 1981). The presence or absence of a single synoptic scale system in each of the 8 wet season months can account for such a variation in rainfall. Thus, a maximum or minimum possible variation in dust supply due to a variation in storm systems is $\pm$ 8 systems. These extremes, if coincident, give a range of 4.4 Mtons/year to 24.4 Mtons/year. We believe that such an extreme range is unrealistic. For example, all storms added or subtracted will not coincide with dust events; nor are concentrations of dust likely to go down in dry years or up in wet years. Both effects reduce the extremes. A more realistic range is half the extreme range or 8.5 to 18.5 Mtons/year.

3.4 Transport of Trace Species with Saharan Dust

The mass concentrations of selected water-soluble species associated with Saharan dust over the western tropical Atlantic and the CAB are given in Table 2. Many of the nutrient species associated with Saharan dust (e.g., K, NH_4, NO_3, PO_4) are believed

critical to the physiology of tropical rain forests (Vitousek and Sanford, 1986). The mass percentage contributions of the various species range from tenths of a percent to several percent.

Mass concentrations of Na and Cl are enhanced over the CAB compared to their levels in the Sahara air layer over the western tropical Atlantic (Table 2). This apparent enrichment is presumably due to entrainment of sea salt into dust-containing air masses that are advected inland from the South American coast. The sea salt concentration over the CAB is on the order of 0.5 $\mu g\ m^{-3}$ during periods influenced by the injection of marine air (Talbot et al., 1990). Besides Na and Cl, NH_4 and SO_4 appear to be enriched two-fold and NO_3 three-fold over the CAB compared to the Sahara air layer over the western tropical Atlantic. We attribute these differences to inputs of nitrogen-rich biomass burning emissions along coastal Africa (Delmas, 1982). The levels of NH_4, NO_3, and SO_4 associated with Saharan dust over the tropical Atlantic appear to be strongly influenced by African biomass burning products during the winter-to-spring time of the year (Savoie et al., 1989). Our ABLE 1 measurements over the western tropical Atlantic were conducted during summertime and exhibit minimal influence from African biomass combustion products; a dramatic seasonal signal in this source appears in the annual record of aerosol composition at Barbados (Savoie et al., 1989). Thus, Saharan air intrusions into the CAB during the wet season appear to reflect combined chemical inputs from mineral aerosol, sea salt, and possibly biomass burning products.

The annual rates of supply of trace species were estimated assuming that all the dust entering the Boa Vista/Manaus/Belem triangle is deposited within that area. In assessing this assumption, it should be noted that Manaus lies more than 1300 km inland from the NE coast of South America. If all the Saharan dust introduced into the triangle (Fig. 1(b)) in a year was effectively deposited in that area, its deposition flux would be:

$$\frac{13 \times 10^{9} \text{ kg yr}^{-1}}{(1.7)(4.0 \times 10^{7} \text{ ha})} = 190 \text{ kg ha}^{-1} \text{ yr}^{-1}$$

This value, 190 kg ha^{-1} yr^{-1}, is on the high end of other reported Saharan dust depositional rates; 13 kg ha^{-1} yr^{-1} at Miami, Florida (Prospero et al., 1987) and 77 kg ha^{-1} yr^{-1} in the French Alps (DeAngelis and Gaudichet, 1991).

Using the mass concentrations of selected trace species associated with Saharan dust over the CAB (Table 2) and our above estimate of dust deposition to the Amazonian ecosystem, we find that most species are deposited at a rate of 1-4 kg ha^{-1} yr^{-1} (Table 3). These deposition fluxes are essentially identical to the average wet deposition fluxes measured at two stations within the triangle area during the ABLE 2B experiment (Table 3). This result suggests that precipitation scavenging is the principal removal mechanism of Saharan dust associated material from the atmosphere during the CAB wet season. During the CAB wet season, the average residence time of aerosols in boundary layer air

relative to precipitation washout is 0.25-1 day (Andreae et al., 1990). Our analysis suggests that the major ionic composition of precipitation (e.g., NH_4, NO_3, SO_4) in the CAB wet season may be strongly influenced by inputs of material originating on the African continent nearly 5000 km away. This transcontinental biogeochemical link appears to be severed during the dry season when the large-scale meteorological regime which favors transport of Saharan air masses into the CAB migrates to the north. The aerosol and precipitation chemistries in the CAB dry season support such a scenario (Talbot et al., 1988; Andreae et al., 1988). Long-range transport of aerosol-associated species to the CAB appears to explain the higher wet season precipitation fluxes of Na, Cl, and K compared to the dry season. It also seems to be responsible for the similar seasonal precipitation fluxes of NH_4, NO_3, and SO_4 despite a five-fold contrast in rainfall amounts. Our estimate of long-range chemical inputs to the CAB are significantly lower than Reichholf's (1986), who suggests at least 2 orders of magnitude higher dust transport to the western tropical Atlantic atmosphere than any reported estimate.

Table 4 compares our deposition fluxes to reported annual internal fluxes (the amount of nutrients internally recycled) and standing stock values (the total ecosystem amount of a nutrient) for the Amazon Basin. Inputs of K and P associated with Saharan dust aerosols represent from a few tenths to 6 percent of the annual nutrient turnover due to litterfall, and from a few thousandths to a few tenths of a percent of the total

ecosystem standing stock. The nutrient influx of these and other trace elements into the EAB and CAB does not appear important on short time scales (10^1-10^2 years). However, with respect to the long-term geochemical mass balance of the Basin, Saharan dust and associated aerosols are important as an outside source of elements that help replenish those lost from the system. This importance is amplified in a tightly constrained nutrient system such as the EAB and CAB.

The time required for the imported K and P to be equal to the amount of their respective Amazonian standing stocks is estimated using our deposition fluxes to evaluate the potential biogeochemical importance of Saharan dust inputs to the Amazon rainforest. Dividing the standing stock of K in the Amazon oxisol rainforest, ~ 380 kg ha^{-1} (Jordan, 1985), by our maximum and minimum values of K influx (Table 3), we arrive at values ranging from 440 to 1700 years. The same calculation for P, using a standing stock value of 220 kg ha^{-1} for the CAB (Golley et al., 1975) results in values ranging from 4700 years to 20,000 years. These calculations do not account for losses from the system, such as the Amazon River outflow (Gibbs, 1972). Hydrologic loss values (Franken and Leopoldo, 1984) of P from the CAB vary from an order of magnitude less than our deposition values to the same order of magnitude.

These results suggest that if Saharan dust aerosol is a principal source of these trace species to the EAB and CAB, then the effect on the biogeochemical cycling would be on the long

term (10^2-10^3 years). Other possible mechanisms may play additional roles in this seemingly storm event driven system. The accumulation of nutrients in rain water stored in epihytes may be one such mechanism. Increased tree falls in tropical rain forests are noted during the wet season (Oldeman, 1972; Brokaw, 1985). Large trees heavily loaded with epiphytes may therefore be prime candidates to fall during the CAB wet season. Tree fall is most likely to occur in the synoptic scale storms called upon to gather the dust into the Basin. Downdrafts from deep convective clouds in these storm systems reach speeds of 20 to 25 m s^{-1} (45-55 mph). The creation of gaps in the rain forest at the time of maximum soil dust influx may be an important component in the utilization of small amounts of trace elements.

4. Summary and Conclusions

We conclude that Saharan dust penetrates the eastern Amazon Basin and is detected in the Central Basin. The dust is delivered in intermittent pulses which occur in association with major pulses in rainfall. Since these large rain events are due to organized storm systems with horizontal scales of up to a few thousand kilometers and time scales of days, we conclude that part of the mechanism driving the storm system is responsible for the accumulation of dust.

Low level (up to 4 km) horizontal negative divergence associated with the storm system is shown to be sufficient to draw dust into the Amazon Basin. Previous work together with results provided here show that Saharan dust easily reaches the

western tropical north Atlantic. Mean flow into the Basin can neither concentrate the dust nor deliver it in the aperiodic fashion observed. Storm systems are shown to be sufficiently frequent to draw upon existing dust plumes. The presence of Saharan dust off the northeast coast of South America is also shown to coincide with the high frequency of storms. Not all rain events in the CAB are accompanied by dust, but all of the dust events we observed occurred in association with rain events.

Observations of the horizontal extent, vertical depth and concentrations of dust permit an estimate of the amount of dust introduced into the Amazon Basin in a given storm event. Storm climatology yields an estimate of 13 Mtons/year of dust introduced into the Amazon Basin. In the northeastern basin, this may amount to as much as 190 kg ha^{-1} yr^{-1} of dust. The amount of trace species supplied with this dust ranges from a few kg ha^{-1} yr^{-1} to less than 1 kg ha^{-1} yr^{-1}.

The total amount of Saharan dust calculated to enter the Amazon Basin is one half to one third of that estimated by others to cross 60°W longitude between 10° and 25°N latitude (Prospero and Carlson, 1972). It is two orders of magnitude less than is implied by Reichholf (1986) who has estimated quantities of trace species needed by the rain forest on nutrient poor soils. This large discrepancy may be due to an underestimate in the total amount of soil dust supplied to the Amazon Basin if, as we have, one confines the calculation to the Sahara as the only source. The discrepancy may also be due to an overestimation of the

necessary nutrient influxes and a simultaneous underestimation of the efficiency in recycling nutrients in this ecosystem.

Whatever the resolution of the above paradox is we conclude that part of the Amazon rain forest is dependent upon soil dust which originates in the Sahara/Sahel region of western Africa. We concur with conclusions drawn by others that such a dependence must be reflected by expansions and contractions of the Amazon rain forest in direct relationship to expansions and contractions of the Sahara/Sahel. We hypothesize that such fluctuations in the size of the rain forest are on time scales which lie between about 500 and 20,000 years. Evidence for such a coupled response must be present in the records of the pleistocene pluvial periods. Such a dependence of one large ecosystem upon another separated by an ocean is of fundamental importance to our view of the role of these ecosystems in the global atmosphere. A view of the role of Amazonian rain forest in the global system must take this coupled process into account. Any strategy designed to preserve the Amazonian rain forest or any part thereof should equally concern itself with the interrelationship between the rain forest, global climate and arid zones well removed from Amazonia.

Acknowledgements

We wish to acknowledge the support provided by the Tropospheric Chemistry Program of NASA which has included the three ABLE missions and continued support of analytical work at the University of Virginia. The contributions of many individuals through the field experiments can regretfully only be acknowledged collectively. Similarly, we wish to acknowledge the help of the graduate students and faculty of the Department of Environmental Sciences. Data and computer support for the trajectory analysis by the ECMWF is recognized with appreciation. This paper draws upon Mr. Swap's thesis submitted in partial fulfillment of the Master of Science degree at the University of Virginia.

This paper is dedicated to Robert Harriss in recognition of his wisdom and enthusiasm in creating and carrying out the Atlantic and Amazon Boundary Layer Experiments.

References

Andreae, M.O., Browell, E.V., Garstang, M., Gregory, G.L., Harriss, R.C., Hill, G.F., Jacob, D.J., Pereira, M.C. Sachse, G.W., Setzer, A.W., Silva Dias, P.L., Talbot, R. W., Torres, A.L. and Wofsy, S.C., 1988. Biomass-burning emissions and associated haze layers over Amazonia. J. Geophys. Res., 93, 1509-1529.

Andreae, M.O., Talbot, R.W., Berresheim, H. and Beecher, K.M., 1990. Precipitation chemistry in Central Amazonia. J. Geophys. Res., 95, 16987-16999.

Artaxo, P., Maenhaut, W., Storms, H. and Van Grieken, R., 1990. Aerosol characteristics and sources for the Amazon Basin during the wet season. J. Geophys. Res., 95, 16971-16985.

Bergametti, G., Gomes, L., Coude-Gaussen, G., Rognon, P. and Le Coustumer, M.N., 1989. African dust observed over Canary Islands: Source-regions identification and transport pattern for some summer situations. J. Geophys. Res., 94, 14855-14864.

Brokaw, N.V.L., 1985. Treefalls regrowth and community structure in tropical forests. In The Ecology of Natural Disturbance and Patch Dynamics, S.T.A. Pickett and P.S. White (eds.), Academic Press, Inc., Orlando, pp. 53-69.

Brummer, B., 1978. Mass and energy budgets of a 1 km high atmospheric box over the GATE C-scale triangle during undisturbed and disturbed weather conditions. J. Atmos.

Sci., 35, 997-1011.

Carlson, T.N., 1979. Atmospheric turbidity in Saharan dust outbreaks as determined by analyses of satellite brightness data. Mon. Wea. Rev., 107, 322-335.

Cohen, J.C.P., 1989. Um estudo observacional de linhas de instabilidade na Amazônia. INPE-4865-TDL/376, San Jose dos Campos, Brazil.

D'Almeida, G.A., 1986. A model for Saharan dust transport. J. Clim. and Appl. Meteor., 25, 903-916.

DeAngelis, M. and Gaudichet, A., 1991. Saharan dust deposition over Mount Blanc (French Alps) during the last 30 years. Tellus, 43B, 61-75.

Delmas, R., 1982. On the emission of carbon, nitrogen and sulfur in the atmosphere during brushfires in the inter-tropical savannah zones. Geophys. Res. Lett., 9, 761-764.

Frank, W.M., 1978: The life cycles of GATE convective systems. J. Atmos. Sci., 35, 1256-1264.

Franken, W. and Leopoldo, P.R., 1984. Hydrology of catchment areas of Central-Amazonian forest streams. In The Amazon: Limnology and Landscape Ecology of a Mighty Tropical River and Its Basin, H. Sioli (ed.), Junk Pub., Dordecht, 501-519.

Garstang, M., Ulanski, S., Greco, S., Scala, J., Swap, R., Fitzjarrald, D., Martin, D., Browell, E., Shipham, M., Connors, V., Harriss, R. and Talbot, R., 1990. The Amazon Boundary Layer Experiment (ABLE 2B): A meteorological

perspective. Bull. Amer. Meteor. Soc., 71, 19-32.

Gibbs, R.J., 1972. Water chemistry of the Amazon River. Geochim. Cosmochim. Acta, 36, 1061-1066.

Golley, F.B., McGinnis, J.T., Clements, R.G., Child, G.I. and Duever, M.J., 1975. Mineral Cycling in a Tropical Moist Forest Ecosystem. University of Georgia Press, Athens, GA.

Greco, S., Swap, R., Garstang, M., Ulanski, S., Shipham, M., Harriss, R.C., Talbot, R., Andreae, M.O. and Artaxo, P., 1990. Rainfall and surface kinematic conditions over Central Amazonia during ABLE 2B. J. Geophys. Res., 95, 17001-17014.

Gregory, G.L., Harriss, R.C., Talbot, R.W., Rasmussen, R.A., Garstang, M., Andreae, M.O., Hinton, R.R., Browell, E.V., Beck, S.M., Sebacher, D.I., Khalil, M.A.K., Ferek, R.J. and Harriss, S.V., 1986. Air chemistry over the tropical forest of Guyana. J. Geophys. Res., 91, 8603-8612.

Harriss, R.C., Wofsy, S.C., Garstang, M., Browell, E.V., Molion, L.C.B., McNeal, R.J., Hoell, J.M., Jr., Bendura, R.J., Beck, S.M., Navarro, R.L., Riley, J.T. and Snell, R.L., 1988. The Amazon Boundary Layer Experiment (ABLE 2A): Dry season 1985. J. Geophys. Res., 93, 1351-1360.

Harriss, R.C., Garstang, M., Wofsy, S.C., Beck, S.M., Bendura, R.J., Coelho, J.R.B., Drewry, J.W., Hoell, J.M., Jr., Matson, P.A., McNeal, R.J., Molion, L.C.B., Navarro, R.L., Rabine, V. and Snell, R.L., 1990. The Amazon Boundary Layer

Experiment: Wet season 1987. J. Geophys. Res., 95, 16721-16736.

Hollingsworth, A., 1987. Objective analysis for numerical weather prediction. Short- and Medium-Range Numerical Weather Prediction, Collection of Papers Presented at the WMO/IUGG NWP Symp., Tokyo, Japan, August 4-8, 1986.

Jaenicke, R. and Schutz, L., 1978. Comprehensive study of physical and chemical properties of the surface aerosols in the Cape Verde Islands region. J. Geophys. Res., 83, 3585-3589.

Jordan, C.F., 1985. Nutrient cycling in tropical forest ecosystems: Principles and their application in management and conservation. John Wiley and Sons, New York, 190 pp.

Junge, C., 1979. The importance of mineral dust as an atmospheric constitutent. In Saharan Dust, Mobilization, Transport, Deposition, C. Morales (ed.), John Wiley and Sons, New York, pp. 49-60.

Klinge, H., 1976. Bilanzierung von Haupt nahrstoffen im Okosystem tropischer regenwald (Manaus) - vovlaufige daten. Biogeographica, 7, 59-76.

Kousky, V. and Kagano, K., 1981. A climatological study of the tropospheric circulation over the Amazon region. Acta Amazonica, 11, 743-758.

Levin, Z., Joseph, J.H. and Mekler, Y., 1980. Properties of Saharan (Khamsin) dust - comparison of optical and direct sampling data. J. Atmos. Sci., 37, 882-891.

Löye-Pilot, M.D., Martin, J.M. and Morelli, J., 1986. Influence of Saharan dust on the rain acidity and atmospheric input to the Mediterranean. Nature, 321, 427-428.

Madden, R.A. and Julian, P.R., 1972. Description of global-scale circulation cells in the tropics with a 40-50 day period. J. Atmos. Sci., 29, 1109-1123.

Marques-Filho, Ade O., Ribeiro, M.N.G., dos Santos, H.M. and dos Santos, J.M., 1981. Estudos climatológicos da Reserva Florestal Ducke - Manaus - AM, IV. Precipitacao. Acta Amazonica, 11, 759-768.

Oldeman, R.A.A., 1972. L'architecture de la végétation ripicole forestiére des flueves et criques guyanais. Adansonia, N.S., 12, 253-265.

Parkin, D.W., Phillips, D.R., Sullivan, R.A.L. and Johnson, L. R., 1972. Airborne dust collections down the Atlantic. Quart. J. Roy. Meteor. Soc., 98, 798-808.

Petit, J.R., Briat, M. and Royer, A., 1981. Ice age aerosol content from East Antartic ice-core samples and past wind strength. Nature, 293, 391-394.

Proctor, J., 1984. Tropical forest litterfall. II. The data set. In Tropical Rainforest: The Leeds Symposium, S.L. Sutton and A.C. Chadwick (eds.), Leeds: Leeds Philos. Nat. Hist. Soc., pp. 83-113.

Prospero, J.M. and Carlson, T.N., 1972. Vertical and areal distribution of Saharan dust over the Western Equatorial North Atlantic Ocean. J. Geophys. Res., 77, 5255-5265.

Prospero, J.M. and Nees, R.T., 1977. Dust concentration in the atmosphere of the Equatorial North Atlantic: Possible relationship to the Sahelian drought. Science, 196, 1196-1198.

Prospero, J.M. and Nees, R.T., 1986. Impact of the North African drought and El Niño on mineral dust in the Barbados trade winds. Nature, 320, 735-738.

Prospero, J.M., Glaccum, R.A. and Nees, R.T., 1981. Atmospheric transport of soil dust from Africa to South America. Nature, 289, 570-572.

Prospero, J.M., Nees, R.T. and Uematsu, M., 1987. Deposition rate of particulate and dissolved aluminum derived from Saharan dust in precipitation at Miami, Florida. J. Geophys. Res., 92, 14723-14731.

Rao, C.R.N., Stowe, L.L., McClain, E.P. and Sapper, J., 1988. Development and application of aerosol remote sensing with AVHRR data from the NOAA satellites. In Aerosols and Climate, P.V. Hobbs and M.P. McCormick (eds.), A Deepak Publishing, Hampton, VA, 69-79.

Reichholf, J.H., 1986. Is Saharan dust a major source of nutrients for the Amazonian rain forest? Studies on Neotropical Fauna and Environment, 21, 251-255.

Reiff, J., Forbes, G.S., Spieksma, F.TH.M. and Reynders, J.J., 1986. African dust reaching northwestern Europe: A case study to verify trajectory calculations. J. Clim. and Appl. Meteor., 25, 1543-1567.

Riehl, H., 1954: Tropical Meteorology. McGraw-Hill Book Company, New York, 392 pp.

Riehl, H., Yeh, T.C., Malkus, J.S. and LaSeur, N.E., 1951. The north-east trade of the Pacific Ocean. Quart. J. Roy. Meteor. Soc., 77, 598-626.

Salati, E. and Vose, P.B., 1984. Amazon Basin: A system in equilibrium. Science, 225, 129-138.

Savoie, D.L. and Prospero, J.M., 1977. Aerosol concentration statistics for the northern tropical Atlantic. J. Geophys. Res., 82, 5954-5964.

Savoie, D.L., Prospero, J.M. and Saltzman, E.S., 1989. Non-sea-salt sulfate and nitrate in trade wind aerosols at Barbados: Evidence for long-range transport. J. Geophys. Res., 94, 5069-5080.

Scala, J.R., Garstang, M., Tao, W.-K., Pickering, K.E., Thompson, A.M., Simpson, J., Kirchhoff, V.W.J.H., Browell, E.V., Sachse, G.W., Torres, A.L., Gregory, G.L., Rasmussen, R.A. and Khalil, M.A.K., 1990. Cloud draft structure and trace gas transport. J. Geophys. Res., 95, 17015-17030.

Swap, R.J., 1990. The nature and origin of central Amazonian wet season rainfall. M.S. Thesis, University of Virginia, 116 pp. (Available University Microfilm, Ann Arbor, MI.)

Talbot, R.W., Harriss, R.C., Browell, E.V., Gregory, G.L., Sebacher, D.I. and Beck, S.M., 1986. Distribution and geochemistry of aerosols in the tropical north Atlantic

troposphere: Relationship to Saharan dust. J. Geophys. Res., 91, 5173-5182.

Talbot R.W., Andreae, M.O., Andreae, T.W. and Harriss, R.C., 1988. Regional aerosol chemistry of the Amazon Basin during the dry season. J. Geophys. Res., 93, 1499-1508.

Talbot, R.W., Andreae, M.O., Berresheim, H., Artaxo, P., Garstang, M., Harriss, R.C., Beecher, K.M. and Li, S.M., 1990. Aerosol chemistry during the wet season in Central Amazonia: The influence of long range transport. J. Geophys. Res., 95, 16955-16969.

Villa Nova, N.A., Salati, E. and Matsui, E., 1976. Estimativa do evapotranspiraçao na Bacia Amazônica. Acta Amazonica, 6, 215-228.

Vitousek, P.M. and Sanford, R.L., Jr., 1986. Nutrient cycling in moist tropical forest. Ann. Rev. Ecol. Syst., 17, 137-167.

Westphal, D.L., Toon, O.B. and Carlson, T.N., 1988. A case study of mobilization and transport of Saharan dust. J. Atmos. Sci., 45, 2145-2175.

Figure Captions

Fig. 1. Basin-scale rawinsonde network (a) and local mesoscale network (b) employed in the Amazon basin during ABLE 2B. Location of the mesoscale network is indicated by the darkened triangle in (a).

Fig. 2. Time series of ground-based concentrations of terrestrial elements (Fe, Al, Si) measured at Ducke tower with mesoscale network rainfall.

Fig. 3. 500 mb streamlines on April 17, 1987 illustrating the West African Subtropical High and associated with flow across the Atlantic Ocean and into the Amazon basin.

Fig. 4. 10-day backward isobaric trajectories beginning on 12 April 1987 (a) and (b) and 14 April 1987 (c) and (d).

Fig. 5. 10-day forward trajectories beginning on 4 April 1987.

Fig. 6 Time series of horizontal divergence at 850 mb (a) and 700 mb (b) calculated for the Belém-Boa Vista-Embrapa triangle using rawinsonde (solid) and ECMWF (dashed) data.

Fig. 7. Aerosol optical depth (x100) on 7 April 1988 showing a dust plume between western Africa and the northeastern coast of Brazil.

Fig. 8. Lidar-measured aerosol attenuation coefficient near Barbados on 21 July 1984 (courtesy of E. Browell, personal communication). The dust plume is seen between 1.5 km and 4.2 km.

Table 1

Percent of weeks with aerosol optical thickness values of (a) < .2, (b) < .3 and (c) ≥ .3 for the area bounded by 10°N and 0° and 60°W-40°W from June 4, 1987 to March 1, 1990.

	a	b	c
January	27.2	18.2	54.6
February	0	16.7	83.3
March	9.1	9.1	81.8
April	0	14.3	85.7
May	12.5	37.5	50.0
June	0	53.8	46.2
July	7.7	61.5	30.8
August	66.7	33.3	0
September	83.3	16.7	0
October	83.3	16.7	0
November	64.3	35.7	0
December	58.3	25.0	16.7
OVERALL	36.2	29.7	34.1

Table 2.

Mass concentrations (%) of selected trace species associated with Saharan dust over the Western Tropical Atlantic and the Central Amazon Basin.

Species	Average (%)	Range (%)
a) Western Tropical Atlantic[1]		
Na	0.37	0.24-0.85
K	0.17	0.10-0.33
NH_4	0.18	0.01-0.27
Cl	0.32	0.19-0.50
NO_3	0.51	0.21-1.5
SO_4	1.29	0.35-3.0
PO_4	0.037	0.017-0.071
b) Central Amazon Basin[2]		
Na	1.1	0.42-1.8
K	0.29	0.12-0.46
NH_4	0.44	0.08-0.91
Cl	1.9	1.3-2.6
NO_3	1.6	0.20-2.6
SO_4	2.4	0.22-3.7
PO_4	N/A	N/A

[1]From Talbot et al., 1986.

[2]From Talbot et al., 1990.

Table 3.

Comparison of deposition fluxes (kg ha^{-1} yr^{-1}) of selected trace species associated with intrusions of Saharan dust and precipitation in the Amazonian wet season (December-May).

	Dust Intrusions[1]		Precipitation[2]	
Species	Average	Range	Average	Range[3]
Na	2.1	0.80-3.4	1.7	0.73-2.9
K	0.55	0.23-0.87	1.3	0.41-2.3
NH_4	0.84	0.15-1.7	0.71	0.38-1.4
Cl	3.6	2.5-4.9	2.9	1.4-5.1
NO_3	3.0	0.38-4.9	1.4	0.90-3.7
SO_4	4.6	0.42-7.0	1.8	1.2-3.1
PO_4	0.07[4]	0.032-0.14[4]	0.04[5]	0.01-0.12[5]

[1]Calculated using mass concentrations reported in Table 2.

[2]Based on measurements reported in Table 1 from Andreae et al. (1990).

[3]Based on upper and lower quartile concentrations observed at two sites within the triangle area (Andreae et al., 1990).

[4]Estimated using average mass concentration (see Table 2) reported by Talbot et al. (1986).

[5]Based on unpublished data from ABLE 2b (R. Talbot and M. Andreae, personal communication, 1987).

Table 4.

Range of values for depositional influx of P and K due to Saharan dust and associated aerosols compared to and expressed as percentages of annual internal flux from litterfall and total ecosystem nutrient amount.

	Depositional Input kg ha^{-1} yr^{-1}	Internal Flux from Litterfall kg ha^{-1} yr^{-1}	Input as % of Litterfall (min-max)	Standing Stock kg ha^{-1}	Input as % of Standing Stock
P	.011-.047	1.4-4.1[1]	.27-3.4	220[2]	.005-.021
K	.23-.87	13-21[1]	1.1-6.7	378[3]	.061-.23

[1] Proctor (1984).

[2] Klinge (1976).

[3] Golley et al. (1975).

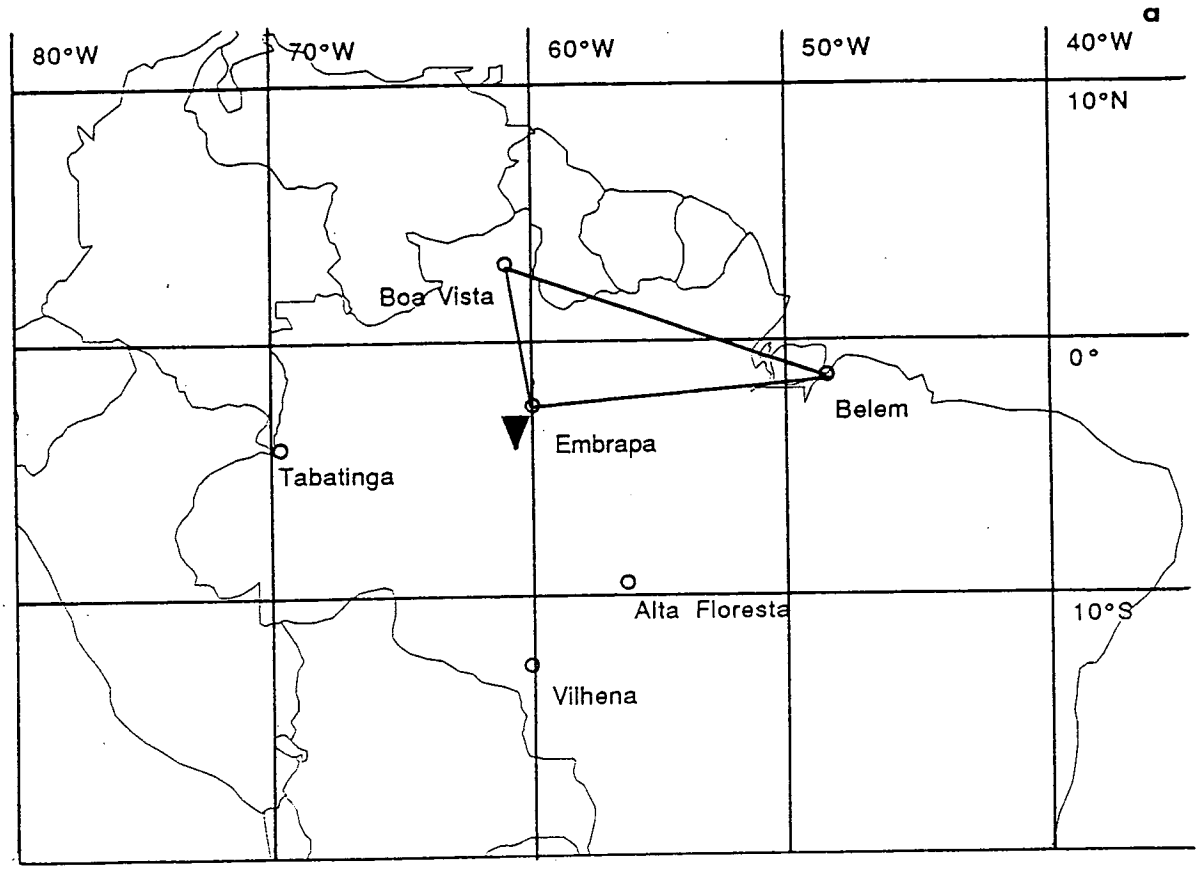
a
80°W
70°W
60°W
50°W
40°W
10°N
0°
10°S
Boa Vista
Embrapa
Belem
Tabatinga
Alta Floresta
Vilhena

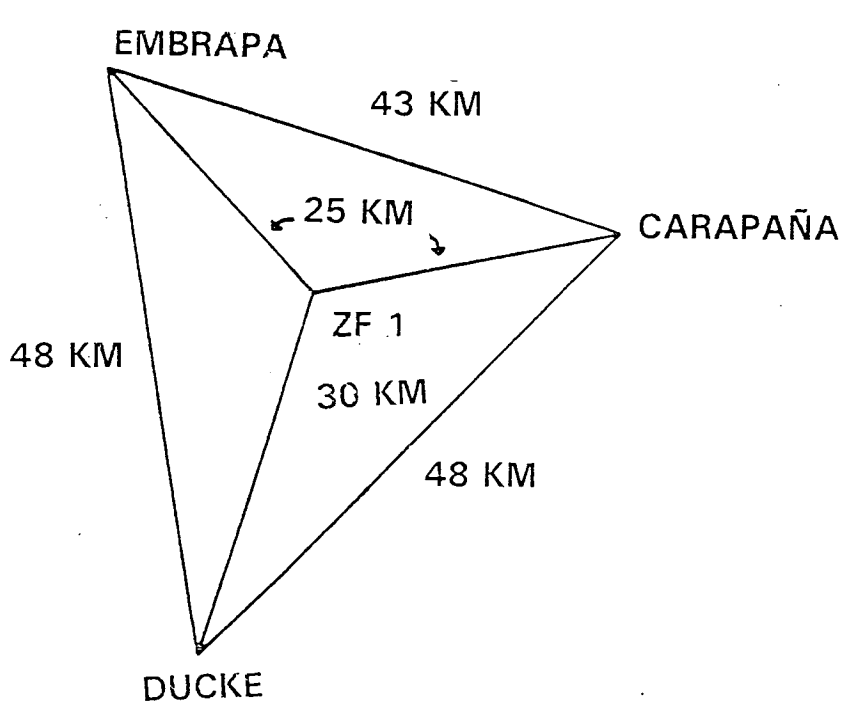
b
EMBRAPA
43 KM
25 KM
CARAPAÑA
ZF 1
48 KM
30 KM
48 KM
DUCKE

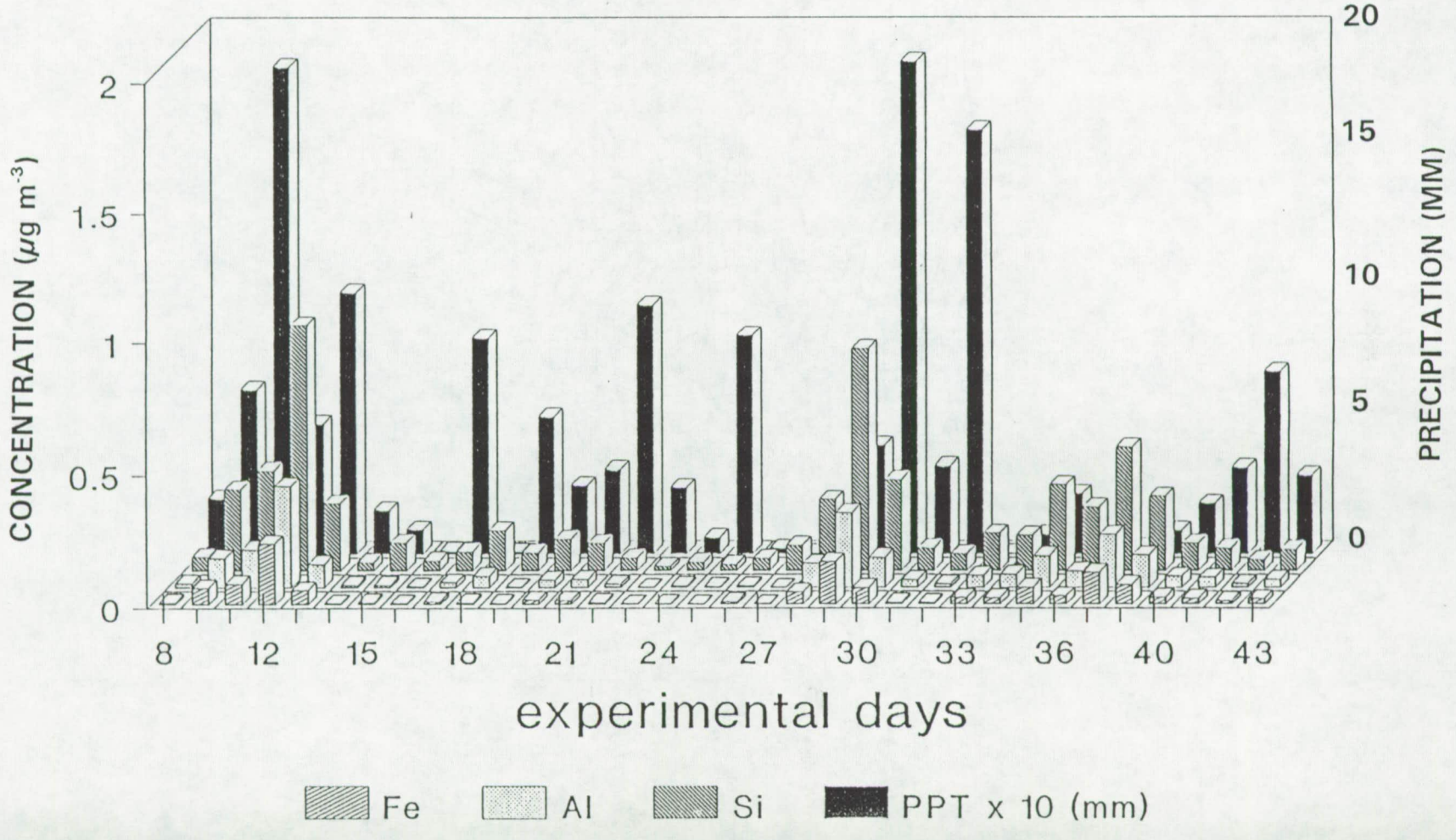
CONCENTRATION (μg m-3)
2
1.5
1
0.5
0
20
15
10
5
0
PRECIPITATION (MM)
8
12
15
18
21
24
27
30
33
36
40
43
experimental days
Fe
Al
Si
PPT x 10 (mm)

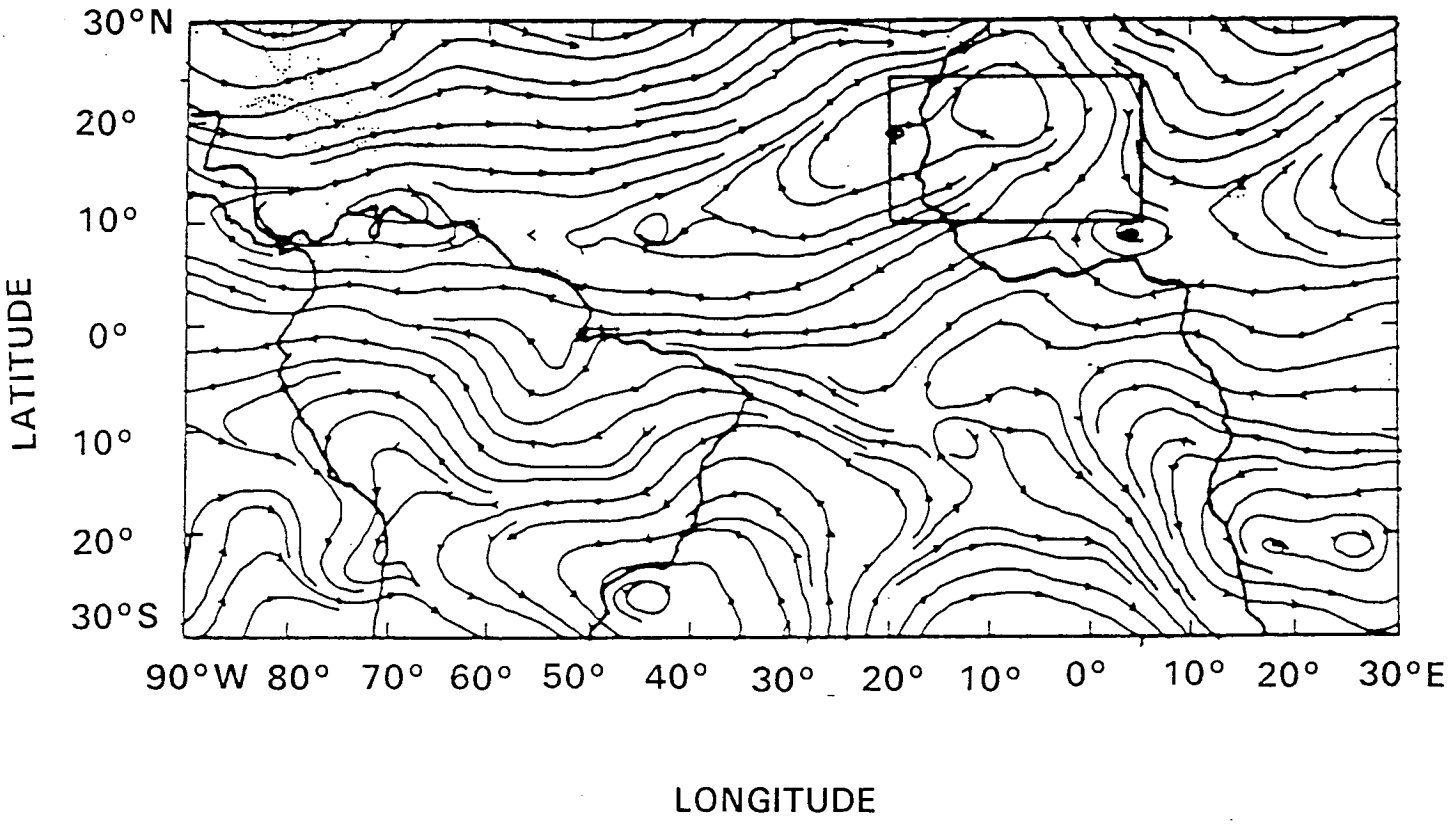
30°N
20°
10°
0°
10°
20°
30°S
LATITUDE
90°W 80° 70° 60° 50° 40° 30° 20° 10° 0° 10° 20° 30°E
LONGITUDE

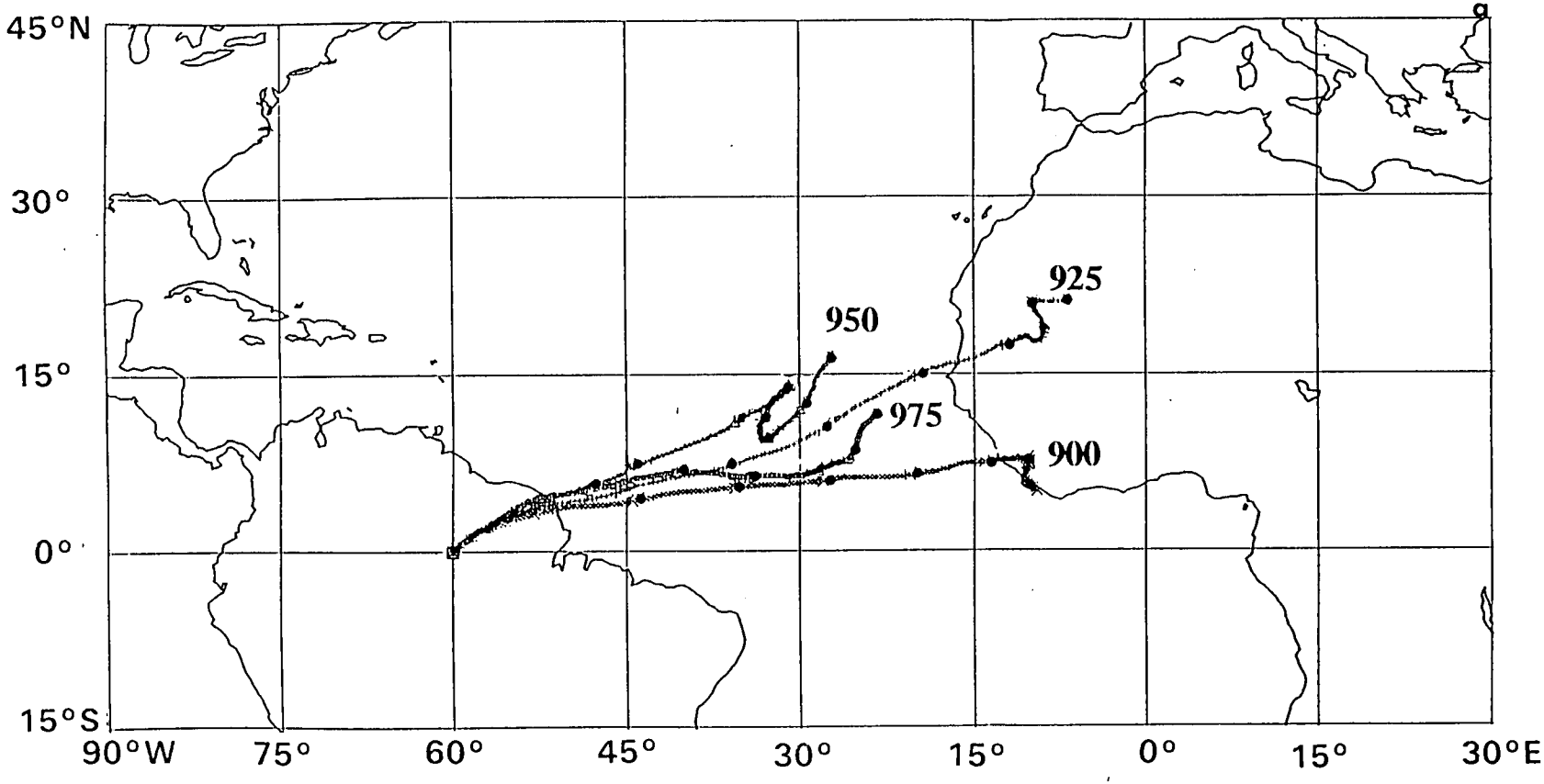
45°N
30°
15°
0°
15°S
90°W
75°
60°
45°
30°
15°
0°
15°
30°E
950
925
975
900

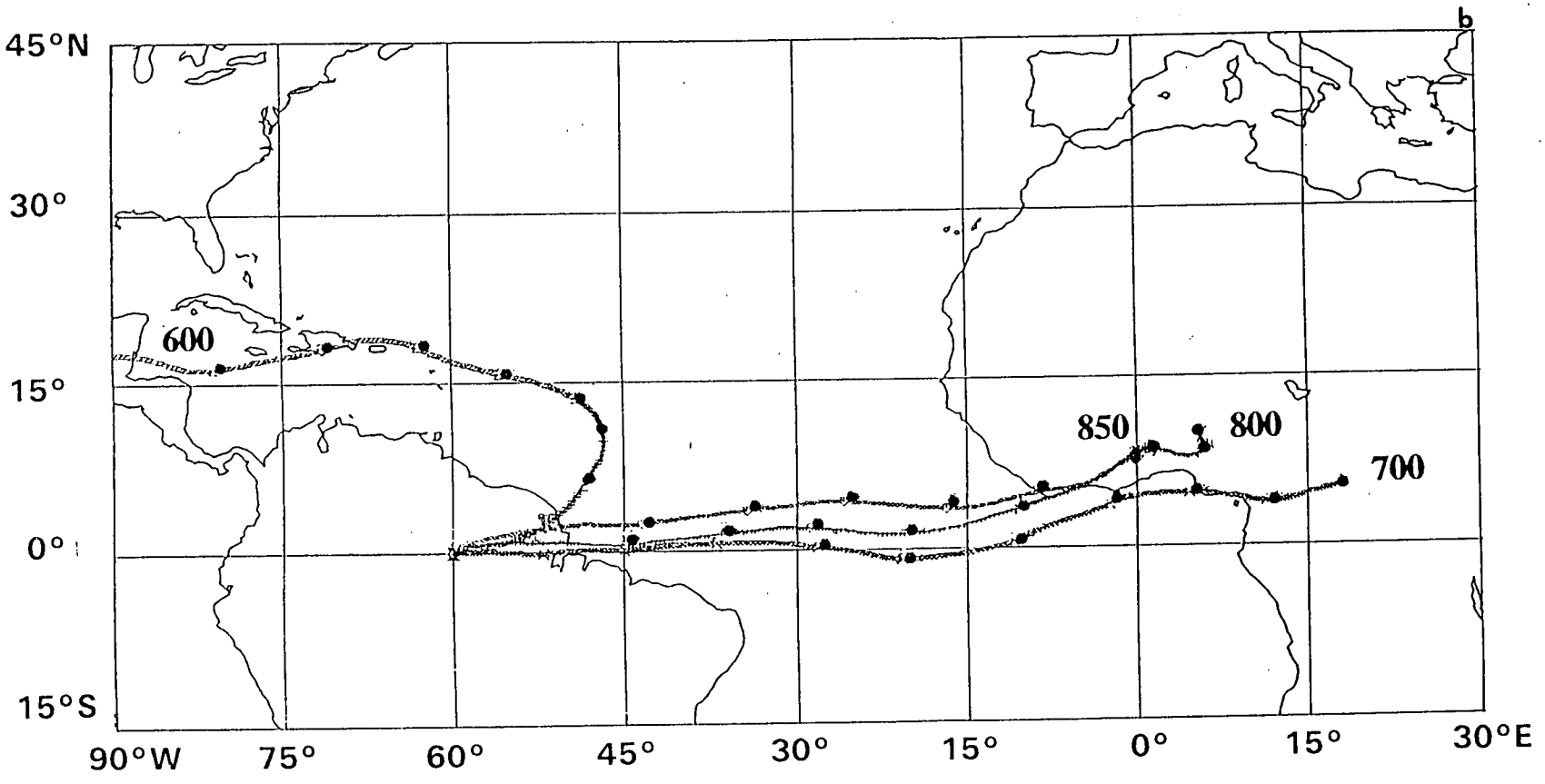
b
45°N
30°
15°
0°
15°S
90°W
75°
60°
45°
30°
15°
0°
15°
30°E
600
850
800
700

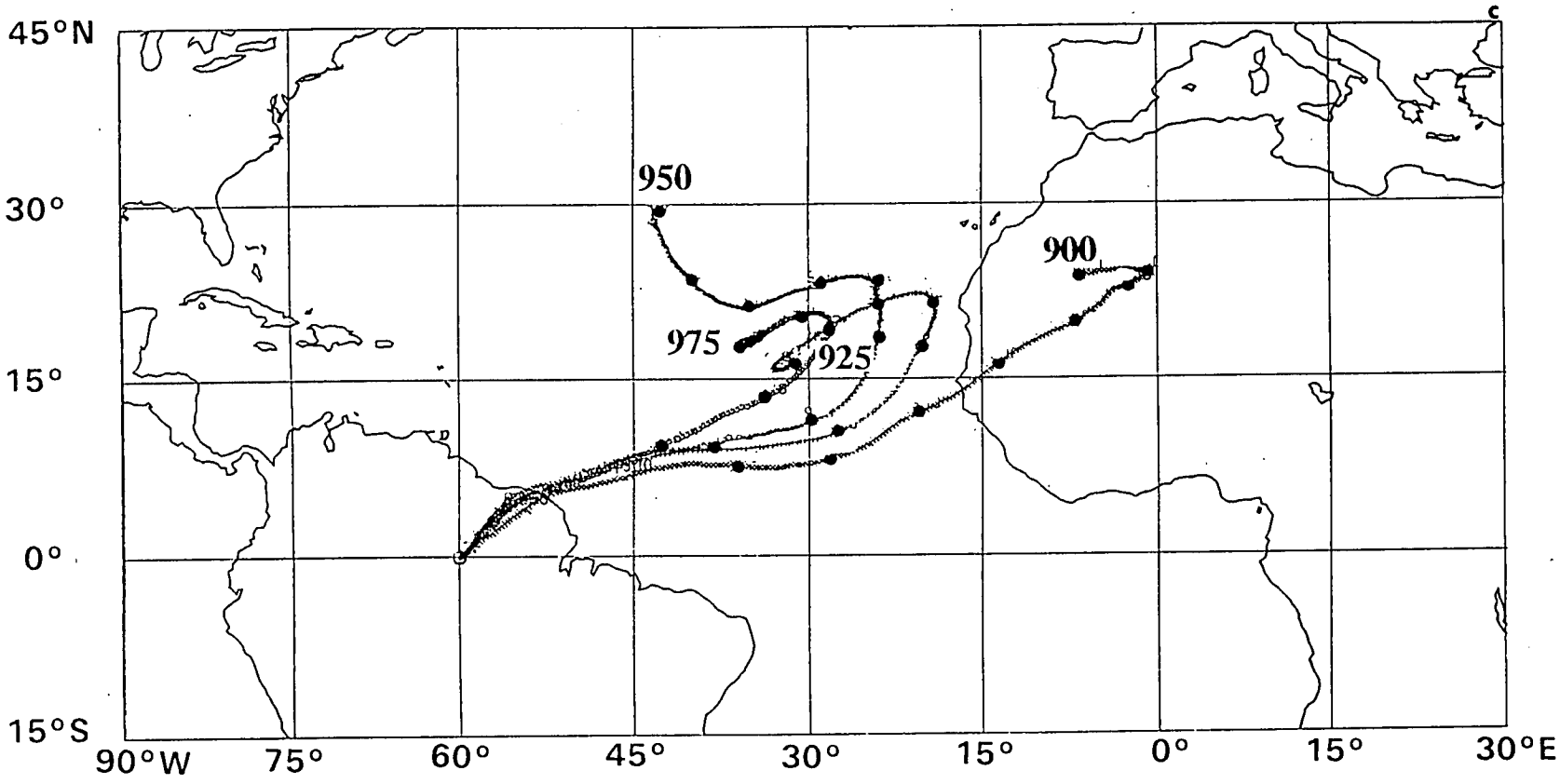
45°N
30°
15°
0°
15°S
90°W
75°
60°
45°
30°
15°
0°
15°
30°E
950
900
975
925

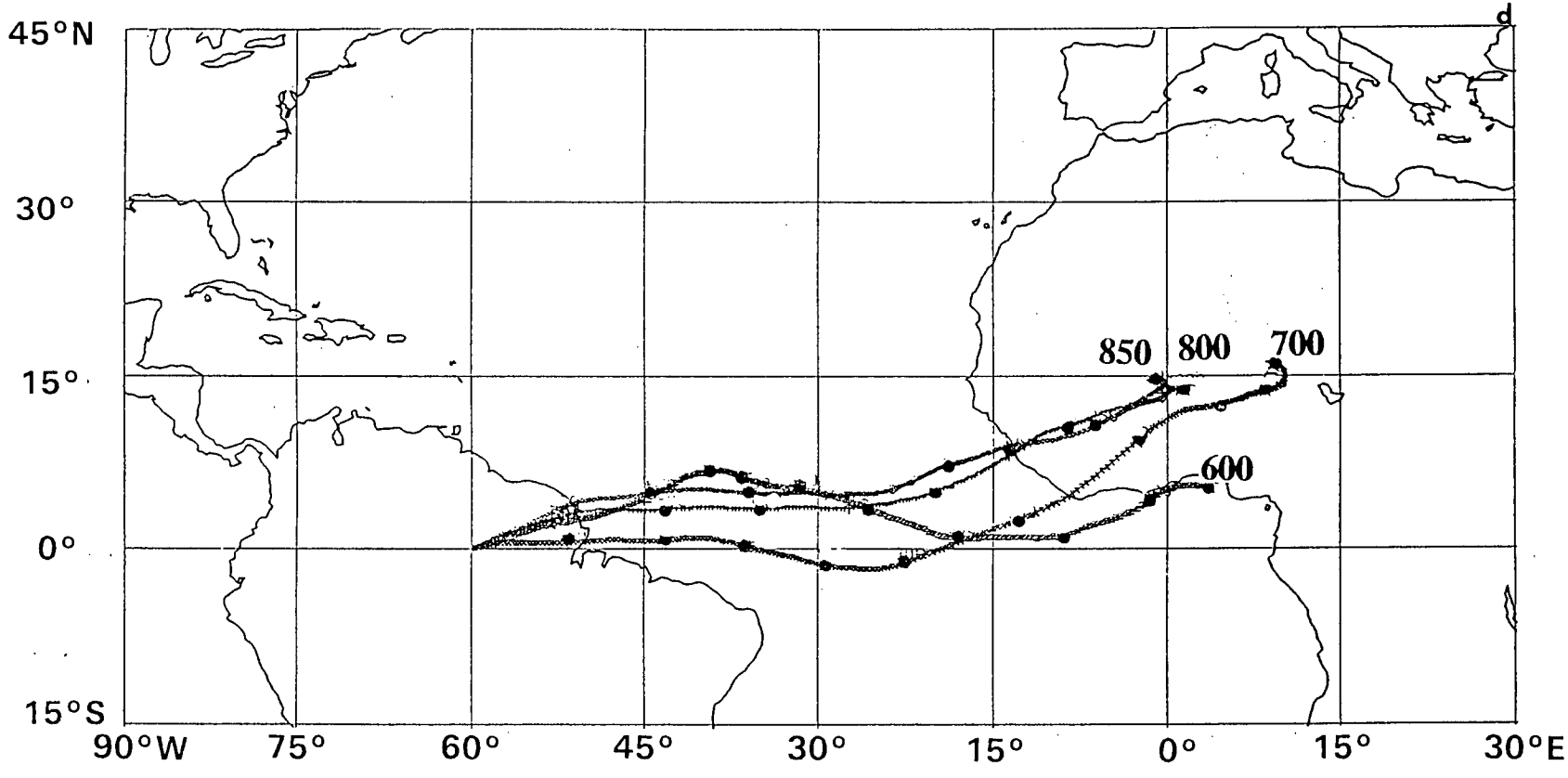
d
45°N
30°
15°
0°
15°S
90°W
75°
60°
45°
30°
15°
0°
15°
30°E
850
800
700
600

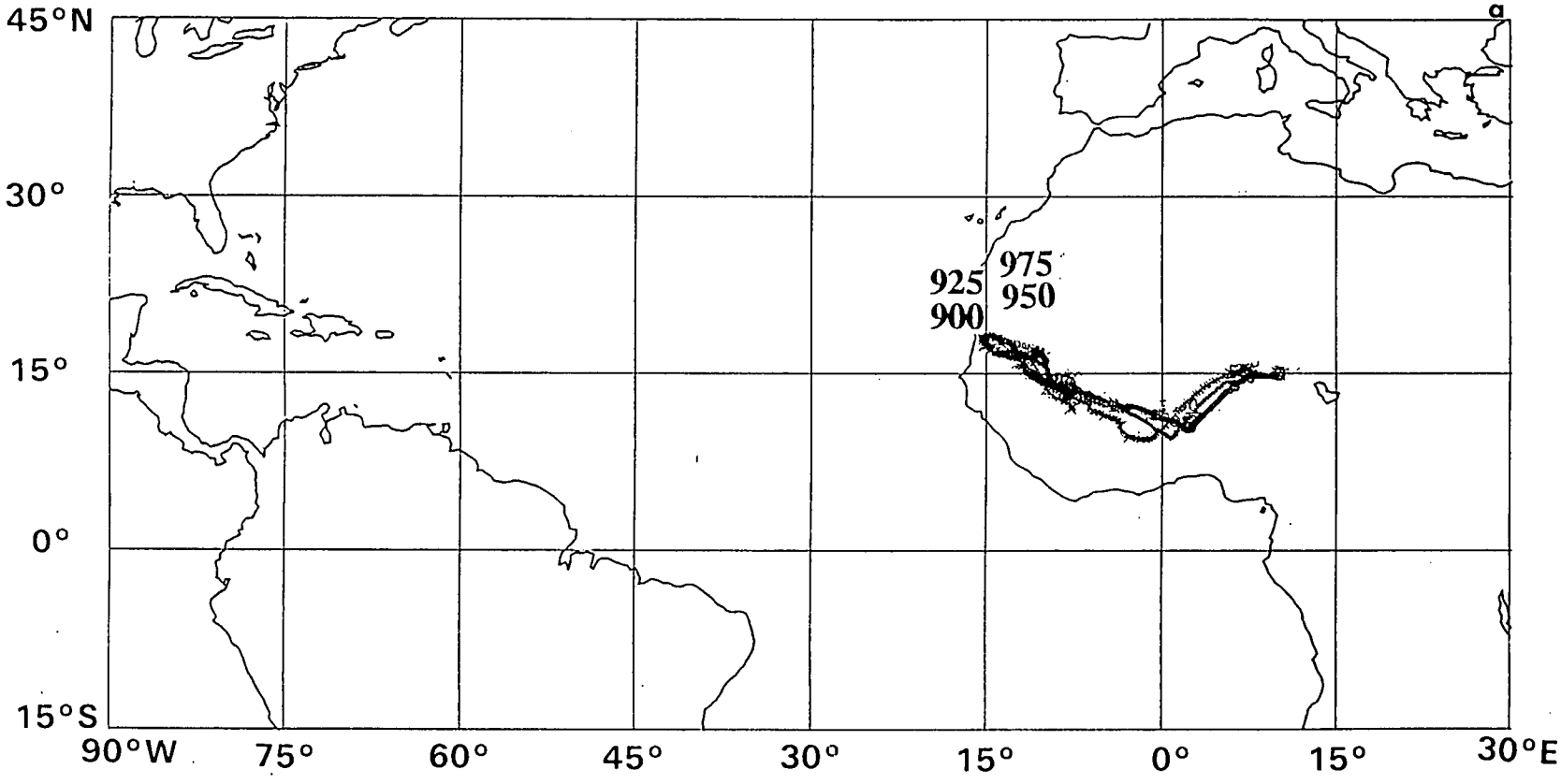
45°N
30°
15°
0°
15°S
90°W
75°
60°
45°
30°
15°
0°
15°
30°E
975
950
925
900

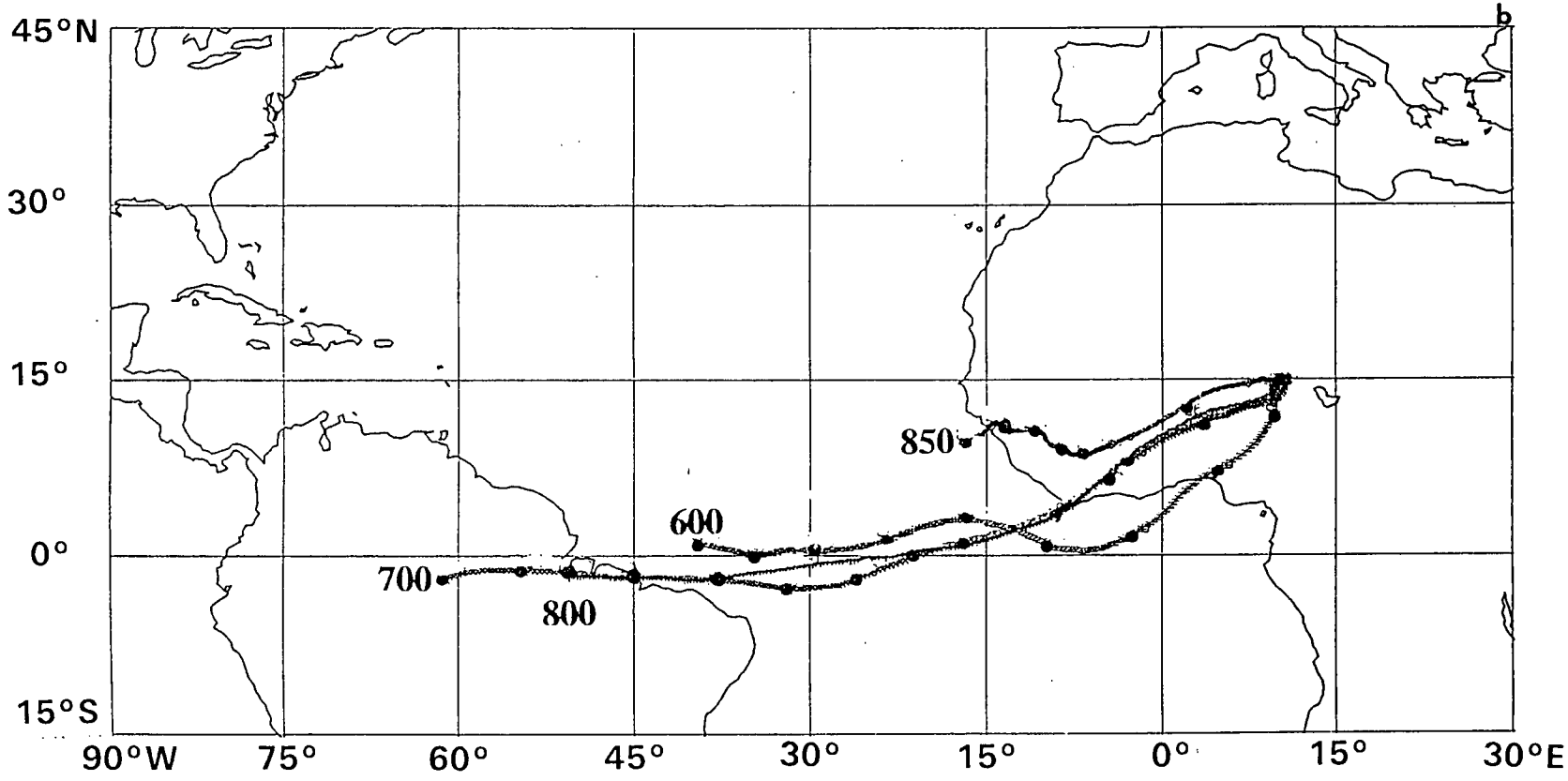
b
45°N
30°
15°
0°
15°S
90°W
75°
60°
45°
30°
15°
0°
15°
30°E
850
600
700
800

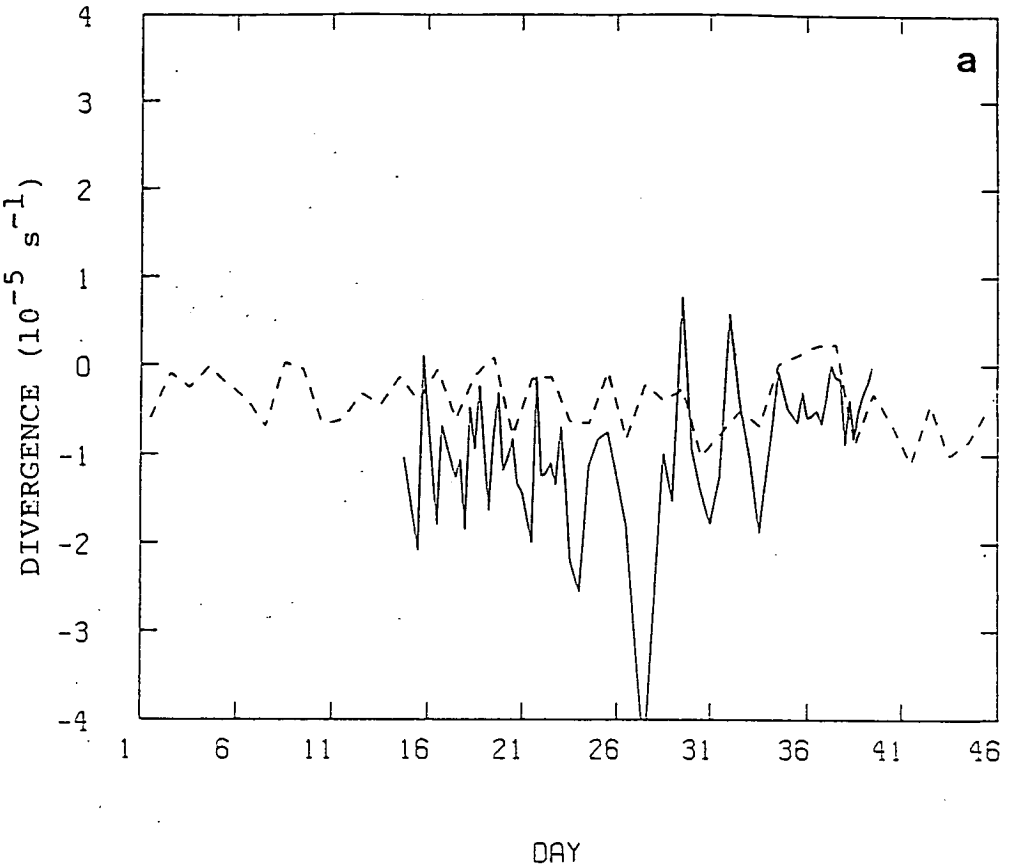
a
DIVERGENCE (10^{-5} s^{-1})
4
3
2
1
0
-1
-2
-3
-4
1
6
11
16
21
26
31
36
41
46
DAY

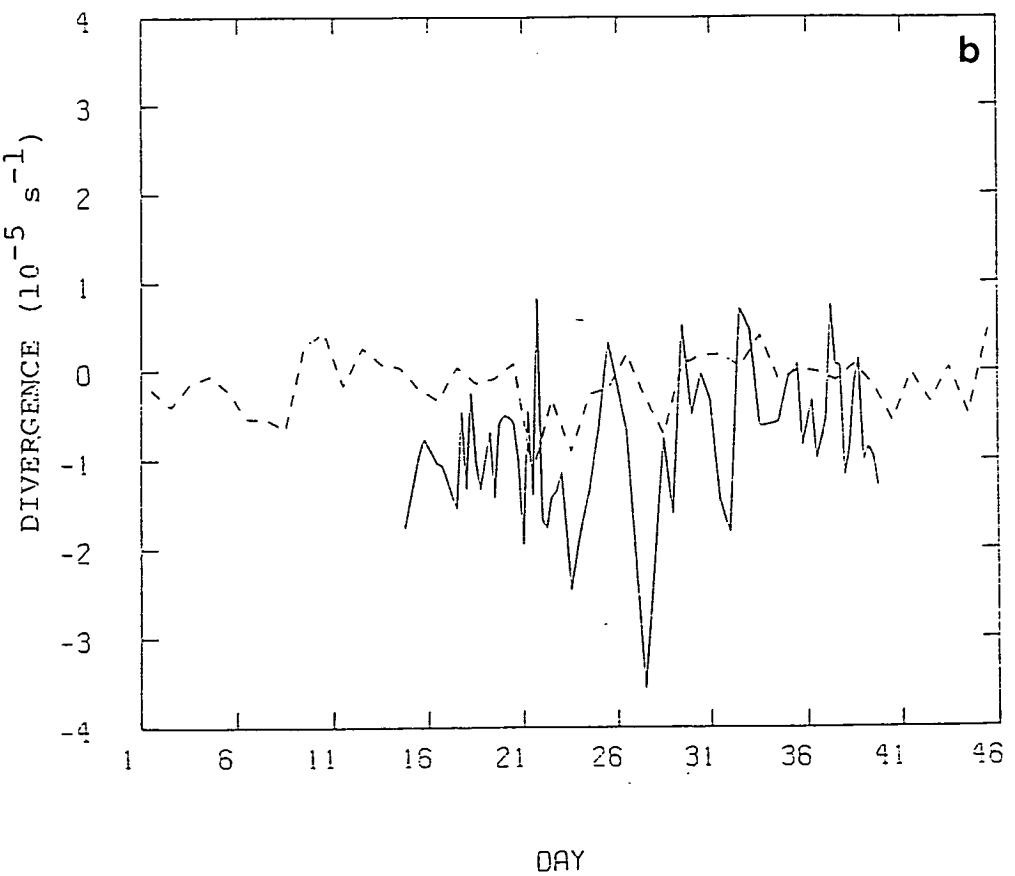
b
DIVERGENCE (10^{-5} s^{-1})
4
3
2
1
0
-1
-2
-3
-4
1
6
11
16
21
26
31
36
41
46
DAY

NASA
L-85-6805

Fig. 8

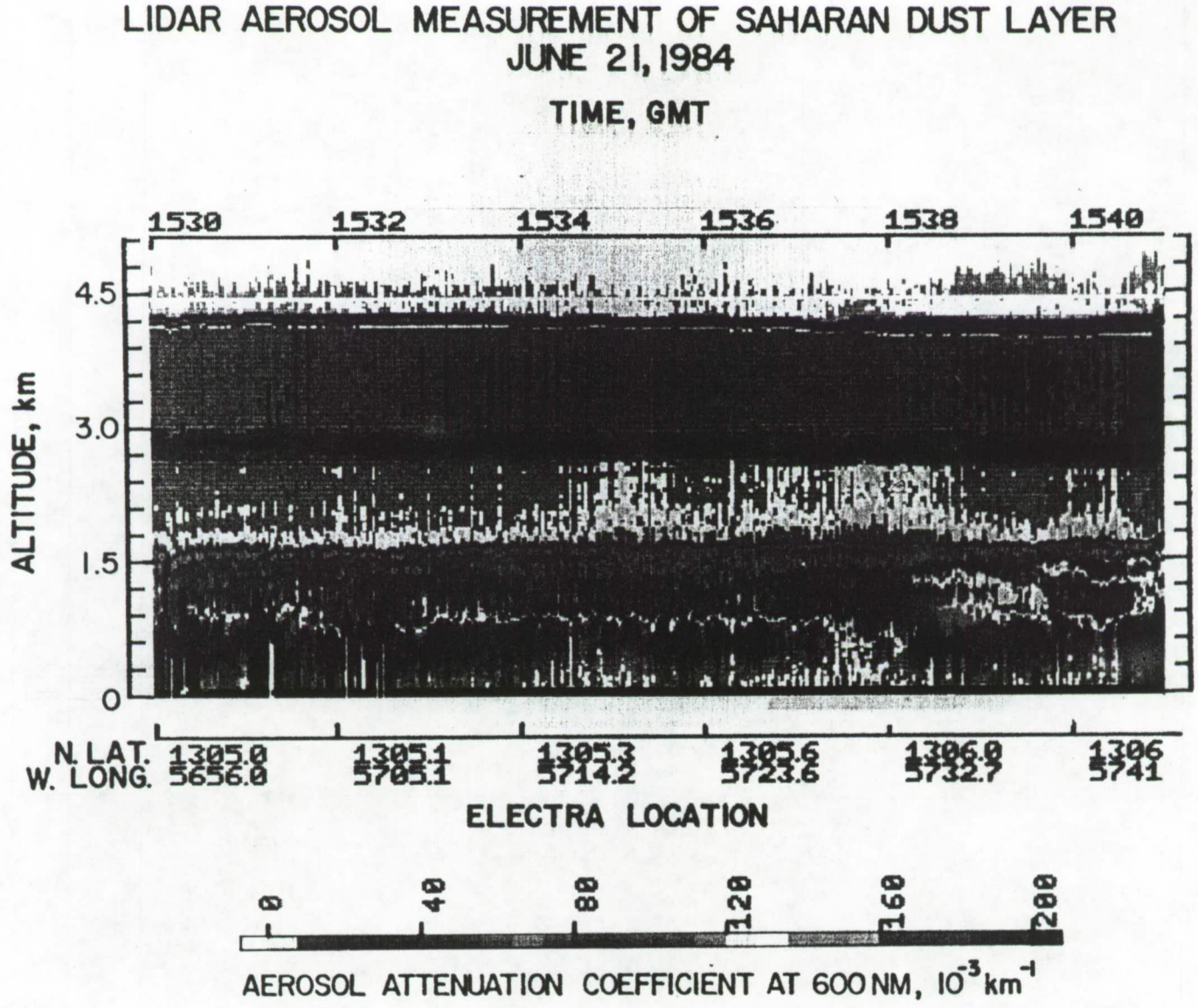

DESTRUCTION OF THE RAIN FOREST AND CLIMATE CHANGE

Michael Garstang

University of Virginia
Department of Environmental Sciences
Charlottesville, VA 22903 U.S.A.

INTRODUCTION

No a priori consequences can be inferred from the possible destruction of the rain forest and the impact of that act upon the global climate. The reason why we cannot project such a response is that we have little or no understanding of how the undisturbed forest influences the global system. If we do not know how the present system works, how can we predict the effect of a changed state of one component on the whole?

Instead the possible effect of the destruction of the rain forest should be posed as a series of questions. Our ability to answer these questions will be a measure of how well we may be able to assess the possible global effect of deforestation.

Three questions will be addressed in this paper. First, are there grounds for assuming that the tropical rain forests play a role in the global atmospheric system? Second, are the tropical rain forests being destroyed and at what rate? Third, depending upon the answers to the first two questions, how do the current rain forests function in the global system? A follow on to this last question is then, how well can we predict a response of global climate to a change in the rain forest?

SOME BASIC FACTS ABOUT THE TROPICAL RAIN FORESTS

While rain forests occur in both temperate and tropical latitudes, the tropical rain forests are by far the most extensive. Tropical rain forests occupy about 7% of the land surface of the Earth. Nearly half of the world's tropical rain forests are in Brazil's Amazon Basin covering some 336 Mha.

One's view of the potential effect of an ecosystem occupying only 7% of the earth's surface is greatly changed when it is recognized that that ecosystem contains 60% of the total global biomass. The primary productivity of the tropical rain forest is some 5 Btons of dry material per year, fixing 6.58 tons of carbon per year (Salati, 1987).

The rain forests are the most diverse of all ecosystems on the planet and are thought to contain as many as 30 million species of which only 3 million are known. The rain forests contain 2500 tall tree species compared to a few dozen tall tree species in temperate zone forests. The abundance of life in the tropical rain forest means that this ecosystem produces 15-20% of trace gases found in the earth's atmosphere (Harriss et al., 1988). Carbon dioxide, carbon monoxide, hydroxyls, heavy and light hydrocarbons, methane and nitrogen species are all produced and are all directly or indirectly involved in capture and emission of terrestrial radiation. Primary and secondary aerosols, mostly organic in composition, influence the transmission (scattering) of solar radiation and the formation of clouds which in turn influence the albedo. Water in these environments is in abundance (precipitation exceeding evaporation). High water vapor content in the equatorial atmosphere implies high latent heat content. High precipitation (in the order of 2 to 3000 mm/year) means that large amounts of latent heat are being converted to sensible and ultimately geopotential energy. Fresh water runoff is high, the Amazon river alone accounting for 25% of the world's river discharge.

THE PHYSICAL SYSTEM

The equatorial regions which contain the bulk of the tropical rain forests are the firebox of the global atmosphere (Riehl and Malkus, 1958). Vertical injection and subsequent poleward transport of heat to achieve global thermal balance does not occur uniformly around the girdle of the planet. "Hot spots" coincident with the large tropical rain forests are found over the Amazon, the Congo (Zaire) and over the warm ocean continent of Indonesia-New Guinea. Hadley and Walker cells represent mean circulations which are fueled by the intermittent action of deep convection coupled to the forest-atmosphere interface at the top of the canopy some 40 m above the ground. The rain forest canopy has an albedo near 10% allowing 90% of incident solar radiation to be absorbed. Solar radiant energy at the surface is used in photosynthesis. Up to 65% of heat may be returned to the atmosphere via evapotranspiration; the remainder returned by evaporation and sensible heat transfer. Some 20% of the rain falling upon the forest is captured, much in unique species such as bromiliads which amount to 10% of the biomass of the Amazon rain forest. It is estimated, but not known accurately, that 50% of the rain falling in the Amazon basin is recycled through the vegetation and surface waters.

The sum total of the physical processes outlined above leads to the conclusion that the tropical rain forest is coupled in an intimate way with the overlying atmosphere. The overlying atmosphere in turn is connected through the larger scale Hadley-

Walker circulations to the global atmosphere.

POLITICAL AND ECONOMIC FORCES

The rain forests are subject to large political and economic forces. Forces acting on the Amazon rain forest illustrate the situation. Much, if not all, of the stress imposed upon the rain forest stems from the increase in human population. The population of Brazil in 1990 is near 150 million. By the year 2050 that population is expected to double. In 1975 it was estimated that 0.56 ha of arable land was required to support each person in the Brazilian population. Increases in population and the need to improve nutrition (upping the amount of arable land to 0.6 ha/person) means that by the year 2050 an additional 180 Mha of arable land will be needed. If such a demand is met by clearing the Amazon rain forest it would mean consuming more than half the current area of rain forest.

Brazil is under serious energy pressure. Energy needs are expected to double in the next decade. Brazil has no reserves of fossil fuel. Hydroelectric power and wood (charcoal) are the most immediate sources of energy in Brazil. The Amazon basin is estimated to contain 1000 GW of hydroelectricity. It is expected that 22 GW will be tapped by 2000. Dams needed to supply these 22 GW of hydroelectricity would inundate 100 Mha of forest.

Projected use of charcoal, primarily to fuel iron ore smelters in the Amazon basin, is estimated to require some 90 Mha of forest over the next 10 years. Unless the efforts to successfully employ tree species that can sustain such a demand,

this use will rapidly encroach upon the existing forest.

Global biomass burning is currently estimated to produce 4 Bton C/year. This compares to 5 Btons C yr^{-1} produced by burning fossil fuel. While not all of the biomass burning is due to consuming the tropical rain forests, a large fraction comes from this source. In Brazil it is estimated that only 5% of the rain forest timber is extracted and effectively used. Ninety-five percent is burnt or left to decompose.

Estimates of the rate of deforestation range from 0.5 to 3.0% per year with some estimates as high as 6% per year. Most studies (Logan et al., 1981; Setzer and Pereira, 1986; Salati, 1987; Watson et al., 1990) suggest that deforestation is increasing at an exponential rate. Evidence from satellite imaging suggests that in the Brazilian state of Rondonia this may have been the case from 1982 to 1987. There is now some possibility that the rate of destruction has slowed.

The above suggests that the first two questions posed are both answered in the affirmative. There is substantial basis to argue that the tropical rain forests are coupled to the global atmospheric system and that the tropical rain forests themselves are undergoing rapid change.

The remainder of the paper will address the third question: how do the tropical rain forests function in the global system?

CHEMICAL AND BIOLOGICAL STATES

Trace gases like carbon dioxide (CO_2), carbon monoxide (CO), methane (CH_4), isoprene ($C_5 H_8$) and nitrous oxide (N_2O) are injected into the atmospheric boundary layer immediately above the forest canopy under undisturbed and disturbed (burning) conditions.

In the undisturbed state, trace gases generated in the rain forest are well mixed vertically by active moist convection. Figure 1 shows the vertical distribution of a trace gas (CO) with its source at the surface (forest) under undisturbed conditions and in the wake of widespread biomass burning. When burning is taking place, the background concentrations of CO are seen to treble and marked layers of trace gas are formed in the lower troposphere.

Horizontal distributions of the trace gases under undisturbed and disturbed conditions have been shown to be large (JGR, 1990). Measurements in the dry season (burning season) show that products of biomass burning extend over the entire Amazon basin over linear distances of up to 2500 km.

The presence of soil dust was also noted in the Central Amazon Basin (CAB) (Talbot et al., 1990). Figure 2 shows pulses of soil dust elements (Fe, Al, Si) occurring at or nearly at the same time that major rain events are detected in the CAB.

PHYSICAL PROCESSES

The chemical measurements show that gases and particles originating in the forest canopy are injected into the atmosphere. The sections below will examine aspects of the vertical transport through three atmospheric layers:

* the canopy-atmosphere interface (100 m deep);
* the atmospheric boundary layer (2 km deep); and
* the cloud layer (15 km deep).

CANOPY-ATMOSPHERE INTERFACE

Figure 3 shows the diurnal flux across the canopy of sensible heat ($\overline{w'T'}$), latent heat ($\overline{w'q'}$), solar radiation (R_s) and the net radiation ($R_n = R_s$ - outgoing longwave radiation). Air temperature (T) and specific humidity (q) are also shown.

Strong diurnal forcing is noted with latent heat flux reaching 400 W m^{-2} and sensible heat flux 100 W m^{-2} soon after midday. Latent heat fluxes decrease to very small values at night while sensible heat flux reverses direction with heat being lost by the atmosphere to the forest.

The maximum latent heat flux over the forest is twice the amount exchanged by the tropical ocean to the atmosphere. The corresponding sensible heat flux of the forest is six times that occurring over the open tropical ocean. The combined latent and sensible heat input equals the net radiation and approaches the total solar input.

The flux of latent heat during the day is such that water vapor divergence occurs at the top of the canopy with specific humidities dropping 2 to 3 g/kg. This "draw-down" of the canopy

water vapor must be compensated for by nighttime and early morning recharge.

Other measurements suggest that the greater fraction of the latent energy input is by evapotranspiration (65%) as compared to evaporation from water surfaces (35%). The large energy injection via water vapor during the central hours of the day is clearly an important characteristic of the rain forest. It is likely to trigger a significant buoyant response in the lower atmosphere leading to convective cloud development and further and deeper vertical transport of quantities out of the canopy.

ATMOSPHERIC BOUNDARY LAYER

Figure 4 shows the growth of the mixed layer over the rain forest. For a 5-hour period beginning 1 hour after sunrise, the mixed layer grows at a rate of 8-10 cm s^{-1}. Entrainment across the top of the mixed layer approaches 600 W m^{-2} which is a contributing factor to the drying observed in the surface layer above the canopy in Figure 3 above.

Mixed layer growth ceases at about 1600 LST decaying rapidly to a shallow (< 300 m) nighttime mixed layer. A fossil mixed layer (well mixed but no longer actively mixing) remains. In the absence of cloud convection (particularly precipitating), the fossil mixed layer builds concentrations of species on a day-to-day basis. Moist convection acts as a siphon drawing down these concentrations.

The vertical transport of quantities out of the forest canopy depends not only upon the fluxes across the top of the

canopy but upon the depth and rate of growth of the mixed layer.

Mixed layer growth rates as predicted by models (Tennekes, 1973; Betts, 1973; Lilly, 1968; Fitzjarrald, 1982) show a good agreement in the early hours of growth after which model produced mixed layer heights are too large. Adjustment to the excessive model heights can be achieved by calling upon convective cloud induced subsidence in the order of 2 to 3 cm s^{-1}. Thus, cloud transports which take over from the mixed layer transports are both upward and downward.

CLOUD LAYER

Cloud transports are calculated using observations of clouds captured within an observational triangle (Figure 5). Rawinsonde measurements were made at the corners of a triangle 50 km on a side. Convergence into the triangle was calculated and vertical motions in the cloud cells deduced from the fraction of active cloud (10% of total area) present. It was assumed that the calculated upward motion in the triangle in the presence of clouds occurred within the cloud cores. Vertical motions of up to 5 m s^{-1} were obtained in the clouds.

The observations of cloud transports were then used to help verify cloud model calculations of transports. A two-dimensional moist cloud model was used (Garstang et al., 1988; Scala et al., 1990). Figure 6 shows the cloud model results. Figure 6(a) shows a single cell cloud which was found to develop in the very moist environment of the wet season. Figure 6(b) shows a multicell cloud which occurred in the dry season and

intermittently in the wet season. Significantly different vertical transport is achieved by the single and multiple cell clouds. Backward trajectories from 12 km elevation in the single cell cloud (Figure 7(a)) show that 73% of the air reaching 12 km originates above 6 km. Only 15% of the air reaching 12 km originates in the mixed layer. The single cell wet clouds do not effectively couple the deeper atmosphere to the surface and mixed layers. These clouds, however, are very effective mixers of the middle and upper troposphere.

The multicell cloud occurring in drier conditions (Figure 7(b)) however, forms a very different link between the surface and deeper atmosphere. Ninety-two percent of the air reaching 12 km originates below 4 km, 60% below 2 km in the multicell cloud.

Dogma which has persisted for 30 years since the first formulation of the "hot tower" concept (Riehl and Malkus, 1958) has held that all deep vertical transport in the equatorial trough region is performed by the multicell clouds. We believe from our findings that the single cell clouds which predominate in wet season conditions create a condition that permits mean circulations such as the Hadley and Walker, to perform deep vertical transport.

Thus, over the rain forest at least two mechanisms exist for deep vertical transport:

* multicell clouds occurring in drier unstable atmospheres, and

* single cell clouds occurring in wetter more stable atmospheres.

When the latter exists, mean circulations can transport surface species through the depth of the troposphere.

HORIZONTAL TRANSPORTS

The physical processes described above have concentrated on vertical transports in the atmosphere over the rain forest. Our results suggest that at least one long range horizontal transport phenomena is of importance. Figure 2 showed pulses of soil dust coinciding with the major rain events in the Amazon basin. The occurrence of high dust concentrations under the rainiest conditions would appear to be a paradox in the sense that rain cleanses the atmosphere of aerosols. We explain this paradox by showing that the large rain systems of the Amazon basin draw dust into the basin from dust plumes that have originated in the Sahara-Sahel and spread across the Atlantic (Swap et al., 1991). Synoptic scale (~ 1000 km) convergence between the surface and 4 km is needed to draw the dust into the basin. Calculations show that some 460,000 tons of Saharan dust are injected into the basin by a single synoptic scale storm system. Storm and dust climatology suggest that more than 12 Mtons of Saharan dust are introduced to the basin each year. In the northeastern basin this may amount to as much as 180 kg/ha/yr. The amount of trace elements, such as phosphate, supplied in this dust range from a few kg/ha/yr to less than a kg/ha/yr. The delicate energy balance existing in the rain forests which have developed on nutrient poor soils suggests that the critical trace elements supplied by Sahara dust may be a limiting factor in the survival

of the rain forest. Dependence of one ecosystem upon an ecosystem on another continent separated by an ocean and linked by the atmosphere is a real possibility.

CONCLUSIONS

The rain forests inject significant amounts of trace gases into the atmosphere. These gases are detected through much of the troposphere and over the region of the rain forest. Major regional enhancements of certain gases are noted as a product of biomass burning.

Local, regional and large scale circulations suggest that the rain forests are coupled to the global atmosphere. The only clear linkage that has been documented by our research is an effect that has originated outside of the rain forest and impinged upon the forest. We are yet to document effects of the rain forest upon the global atmosphere. We believe that we are in a better position now than before undertaking field measurements to speculate upon the potential effect of changes in the rain forest upon the global atmosphere. Further research is necessary before we can move from speculation to well-founded conclusions about the links and consequences between the rain forest and global system.

ACKNOWLEDGEMENTS

The research reported on in this paper has been conducted with the support of the Tropospheric Chemistry Program of the National Aeronautics and Space Administration and is based upon the Amazon Boundary Layer Experiments (ABLE) conducted by NASA and the Brazilian Space Agency (INPE). Results of the ABLE II(a) and II(b) have been reported on in special issues of the J. Geophys. Res. Many scientists and technicians are involved in such research. Their contributions are recognized and acknowledged.

REFERENCES

Betts, A.K., 1973: Non-precipitating cumulus convection and its parameterization. Quart. J. Roy. Meteor. Soc., 99, 178-196.

Fitzjarrald, D., 1982: New applications of a simple mixed layer model. Bound.-Layer Meteor., 22, 431-453.

Garstang, M., J. Scala, S. Greco, R. Harriss, S. Beck, E. Browell, G. Sachse, G. Gregory, G. Hill, J. Simpson, W.-K. Tao and A. Torres, 1988: Trace gas exchanges and convective transports over the Amazonian rain forest. J. Geophys. Res., 93, 1528-1550.

Harriss, R.C., S.C. Wofsy, M. Garstang, E.V. Browell, L.C.B. Molion, R.J. McNeal, J.M. Hoell, Jr., R.J. Bendura, S.M. Beck, R.L. Navarro, J.T. Riley and R.L. Snell, 1988: The Amazon Boundary Layer Experiment (ABLE 2A): Dry season 1985. J. Geophys. Res., 93, 1351-1360.

Journal of Geophysical Research, ABLE 2B: Amazon Boundary Layer Experiment 2B, 95, No. D10, 16721-17050.

Lilly, D.K., 1968: Models of cloud-topped mixed layers under a strong inversion. Quart. J. Roy. Meteor. Soc., 94, 292-309.

Logan, J.A., M.J. Prather, S.C. Wofsy and M.B. McElroy, 1981: Tropospheric chemistry: a global perspective. J. Geophys. Res., 86, 7210-7254.

Riehl, H. and J.S. Malkus, 1958: On the heat balance in the equatorial trough. Geophysica, 6, 503-538.

Salati, E., 1987: 'The forest and the hydrological cycle', In The Geophysiology of Amazonia: Vegetation and Climate

Interactions, R. Dickerson (ed.), pp. 273-296, John Wiley and Sons, New York.

Scala, J., M. Garstang, W.-K. Tao, K. Pickering, A. Thompson, J. Simpson, V.W.J.H. Kirchhoff, E. Browell, G. Sachse, A. Torres, G. Gregory, R.A. Rasmussen and M.A.K. Khalil, 1990: Cloud draft structure and trace gas transport. J. Geophys. Res., 95, 17015-17030.

Setzer, A.W. and M.C. Pereira, 1986: Detection of large biomass burning in the Amazon with satellite images. EOS Trans., AGU, 67, 247.

Swap, R., M. Garstang, S. Greco and P. Kållberg, 1991: Long-range transport of Saharan dust into the Central Amazon Basin over 10-14 days. Proc. AMS 71st Annual Meeting, 7th Joint Conf. on Appl. of Air Poll. Meteor., January, New Orleans, LA, 20-23.

Talbot, R.W., M.O. Andreae, H. Beresheim, P. Artaxo, M. Garstang, R.C. Harriss, K.M. Beecher and S.M. Li, 1990: Aerosol chemistry during the wet season in Central Amazonia: The influence of long-range transport. J. Geophys. Res., 95, 16955-16969.

Tennekes, H., 1973: A model for the dynamics of the inversion above a convective boundary layer. J. Atmos. Sci., 30, 558-567.

Watson, C.E., J. Fishman and H.G. Reichle, Jr., 1990: Significance of biomass burning as a source of CO and ozone in the southern hemisphere tropics: Satellite analysis. J. Geophys. Res., 95, 16443-16450.

List of Figures

Figure 1: Vertical distribution of carbon monoxide in the central Amazon basin under wet (July 12, 1985) and dry (August 12, 1985) conditions. Biomass burning is responsible for the enhanced concentrations observed on August 12.

Figure 2: Time-series over approximately 6 weeks in the central Amazon basin of ground-based concentrations of terrestrial elements (Fe, Al, Si) together with rainfall.

Figure 3: Time series under fair weather conditions in the central Amazon basin at 5 m above the forest canopy of heat flux $\overline{w'T'}$, temperature (T), moisture flux $\overline{w'q'}$, specific humidity (q), incoming solar radiation flux R_s, net radiational flux R_n, and rainfall. SR and SS are approximate sunrise and sunset.

Figure 4: A composite of 7 fair days in the CAB showing the mean mixed layer height (solid line) and individual daytime mixed layer heights (crosses and squares). The nocturnal mixed layer heights are marked with an asterisk. Contours are virtual potential temperature θ_v in °K.

Figure 5: Observational triangle 50 km on a side in the central Amazon basin with vertical soundings of wind, temperature and humidity on the corners and radar coverage. Radar echoes are shown with

the cores of the echoes shaded.

Figure 6a: Model generated single cell cloud showing the boundary of the cloud in terms of zero specific humidity (g/kg). Areas of upward and downward motion are shown by light and dark stippling respectively. Model grid units (abscissa) equal .05 km.

Figure 6b: As for Fig. 6a except for a multicell cloud with potential temperature (°K) instead of specific humidity.

Figure 7: Model generated backward trajectories from 12 km for (a) the single cell cloud and (b) the multicell cloud.

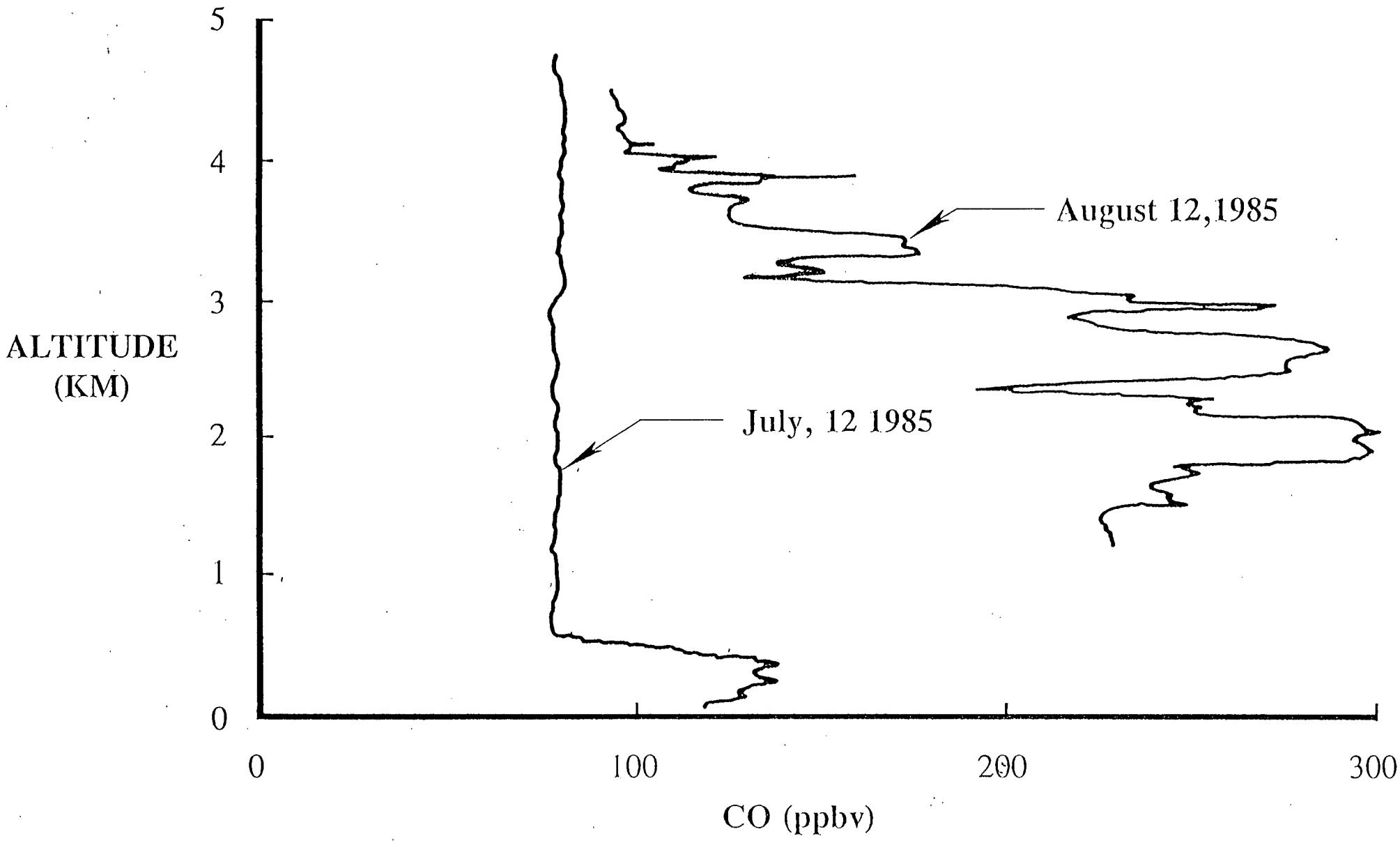
ALTITUDE
(KM)
5
4
3
2
1
0
August 12,1985
July, 12 1985
0
100
200
300
CO (ppbv)

Fig 2

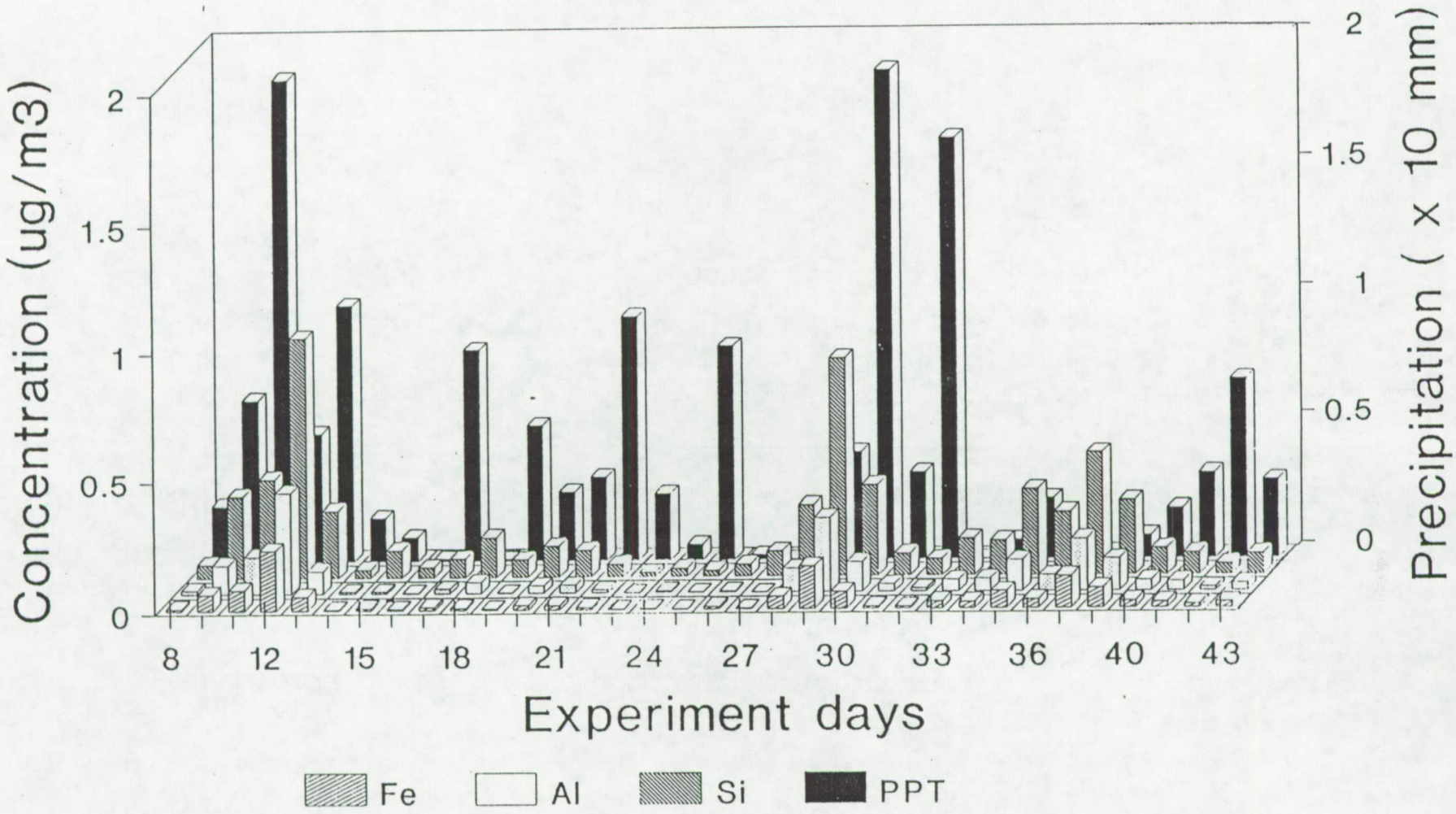
Concentration (ug/m3)
2
1.5
1
0.5
0
Precipitation (x 10 mm)
2
1.5
1
0.5
0
8
12
15
18
21
24
27
30
33
36
40
43
Experiment days
Fe
Al
Si
PPT

Fig 3

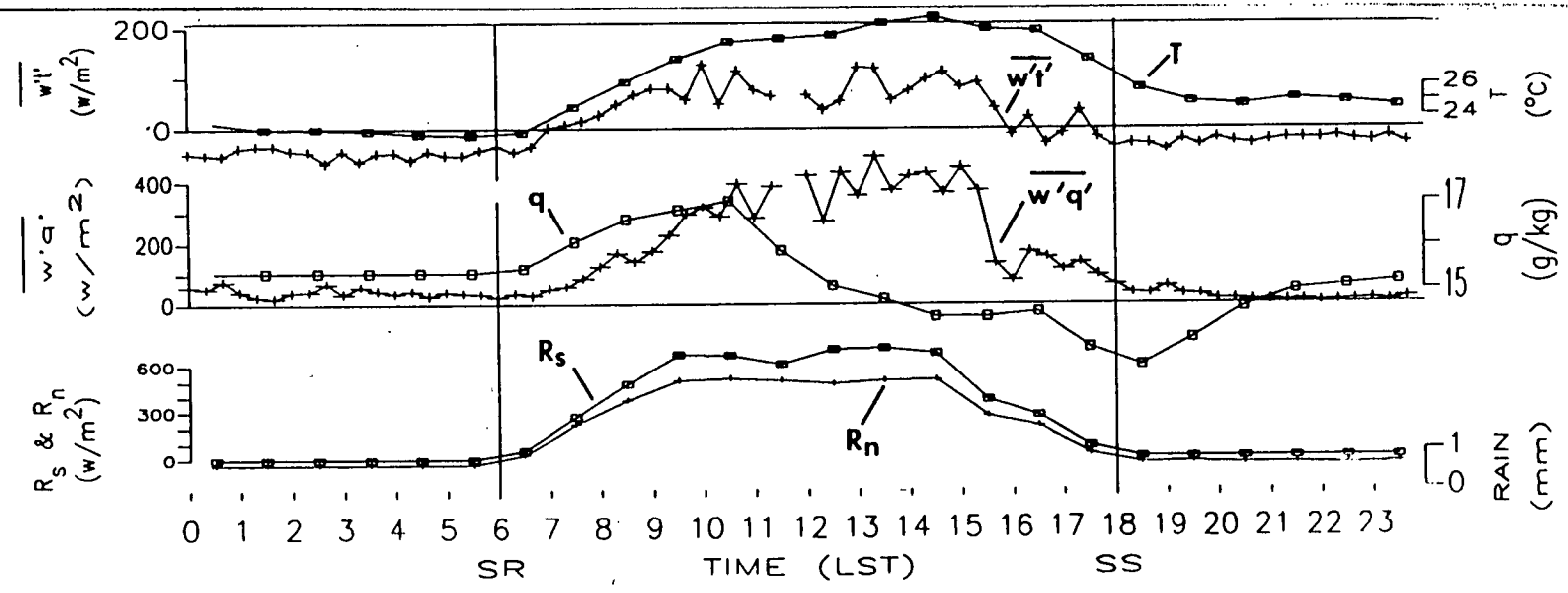
200
0
$\overline{w't'}$ (w/m²)
$\overline{w't'}$
T
26
24
T (°C)
400
200
0
$\overline{w'q'}$ (w/m²)
q
$\overline{w'q'}$
17
15
q (g/kg)
600
300
0
R_s & R_n (w/m²)
R_s
R_n
1
0
RAIN (mm)
0 1 2 3 4 5 6 7 8 9 10 11 12 13 14 15 16 17 18 19 20 21 22 23
SR
TIME (LST)
SS

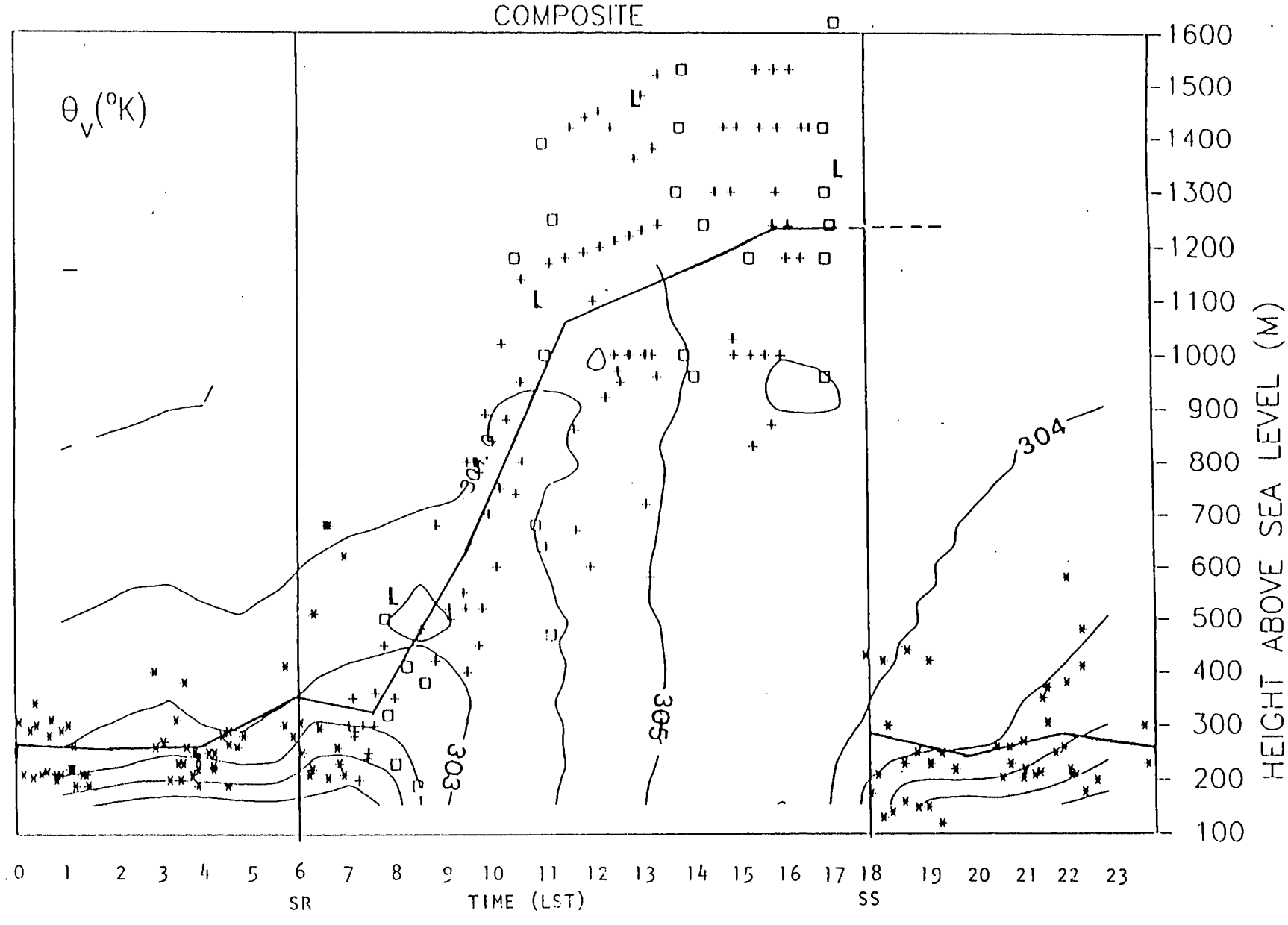
COMPOSITE
θ_v(°K)
L
L
L
L
303
304
305
1600
1500
1400
1300
1200
1100
1000
900
800
700
600
500
400
300
200
100
HEIGHT ABOVE SEA LEVEL (M)
0 1 2 3 4 5 6 7 8 9 10 11 12 13 14 15 16 17 18 19 20 21 22 23
SR
TIME (LST)
SS

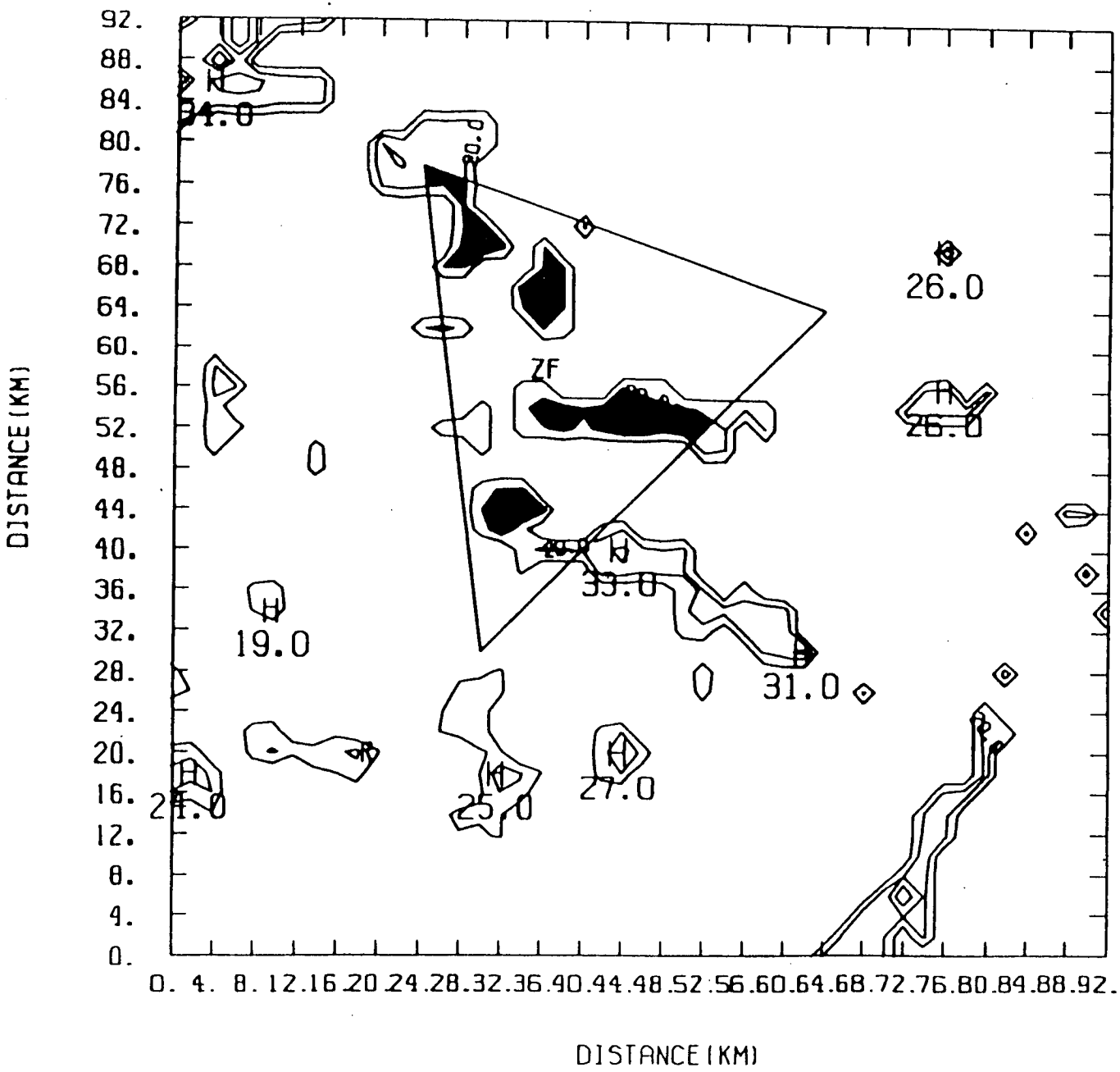
92.
88.
84.
80.
76.
72.
68.
64.
60.
56.
52.
48.
44.
40.
36.
32.
28.
24.
20.
16.
12.
8.
4.
0.
DISTANCE(KM)
0. 4. 8. 12. 16. 20. 24. 28. 32. 36. 40. 44. 48. 52. 56. 60. 64. 68. 72. 76. 80. 84. 88. 92.
DISTANCE(KM)
ZF
26.0
26.0
33.0
19.0
31.0
24.0
25.0
27.0

Fig. 6a

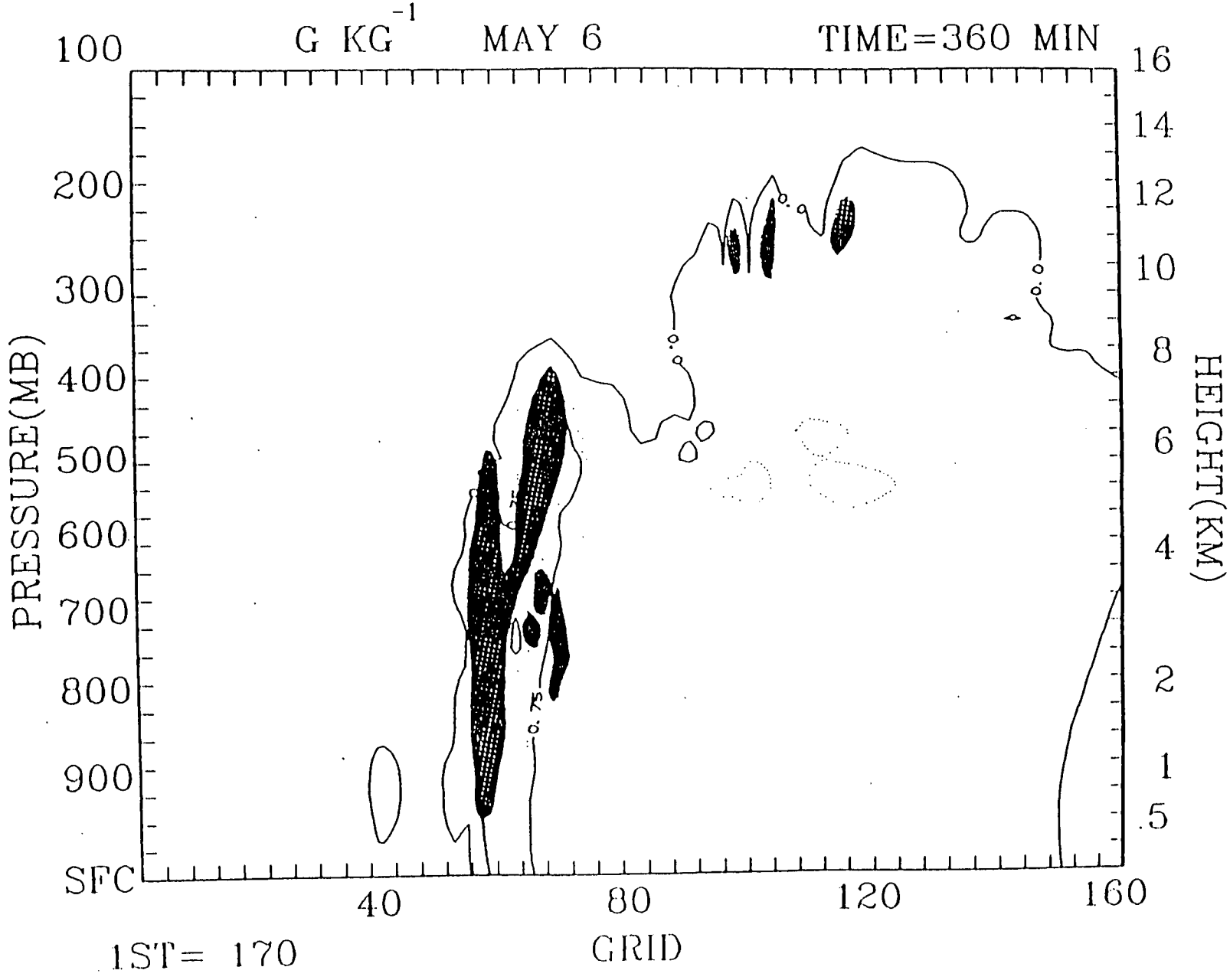
G KG^{-1}
MAY 6
TIME=360 MIN
100
200
300
400
500
600
700
800
900
SFC
PRESSURE(MB)
16
14
12
10
8
6
4
2
1
.5
HEIGHT(KM)
40
80
120
160
GRID
1ST= 170

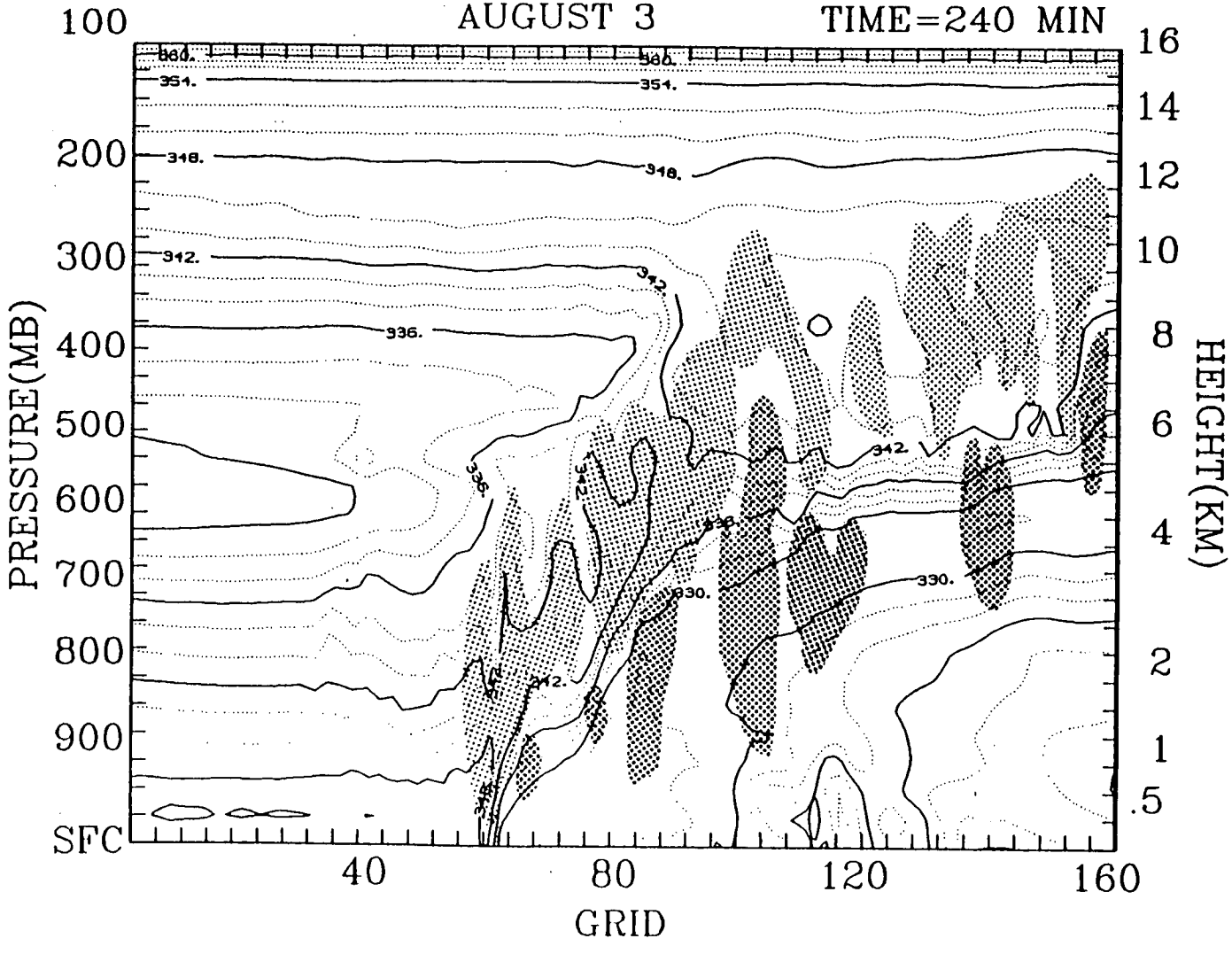
AUGUST 3
TIME=240 MIN
PRESSURE(MB)
HEIGHT(KM)
GRID
100
200
300
400
500
600
700
800
900
SFC
16
14
12
10
8
6
4
2
1
.5
40
80
120
160
360.
354.
348.
342.
336.
330.

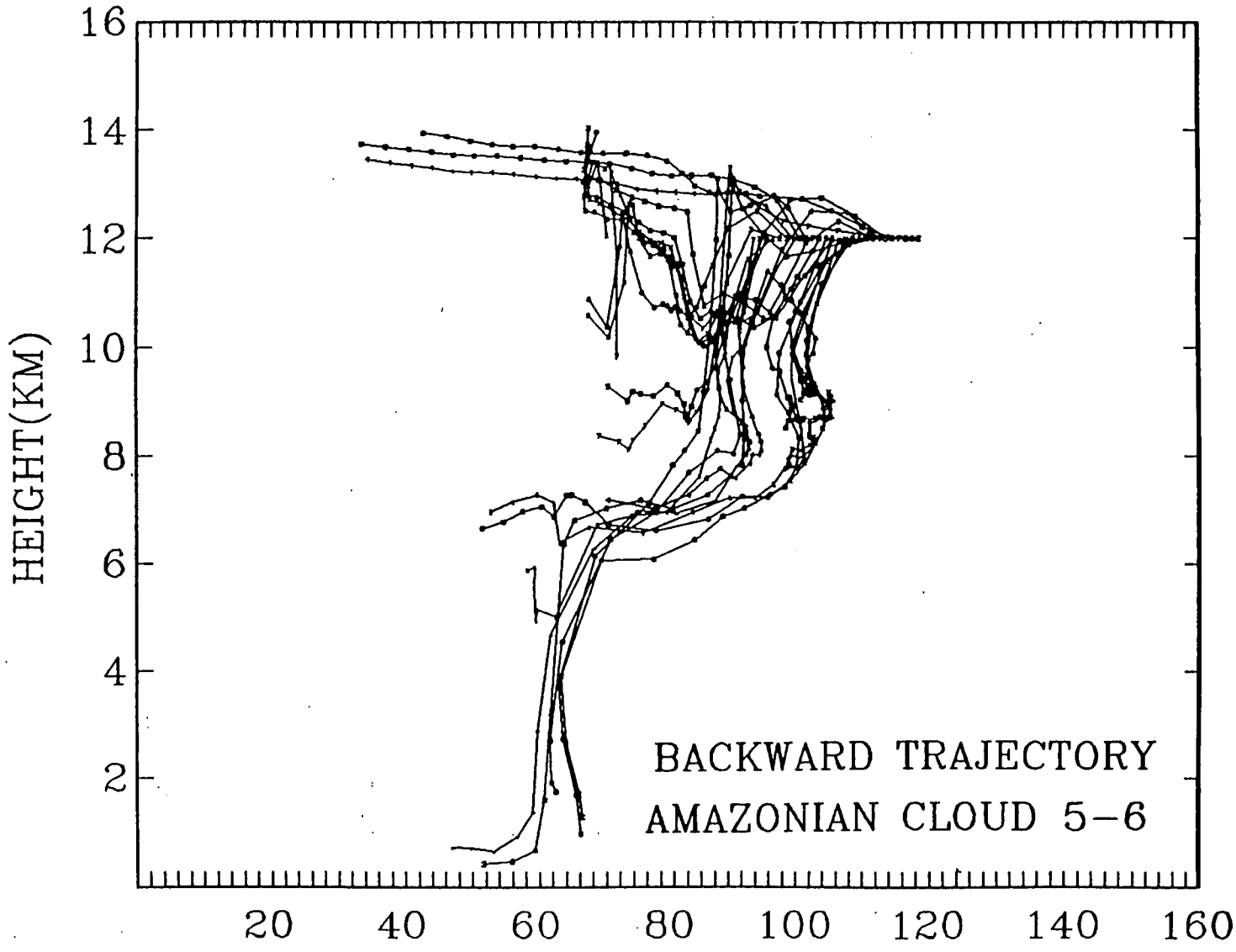
16
14
12
10
8
6
4
2
HEIGHT(KM)
20
40
60
80
100
120
140
160
BACKWARD TRAJECTORY
AMAZONIAN CLOUD 5-6

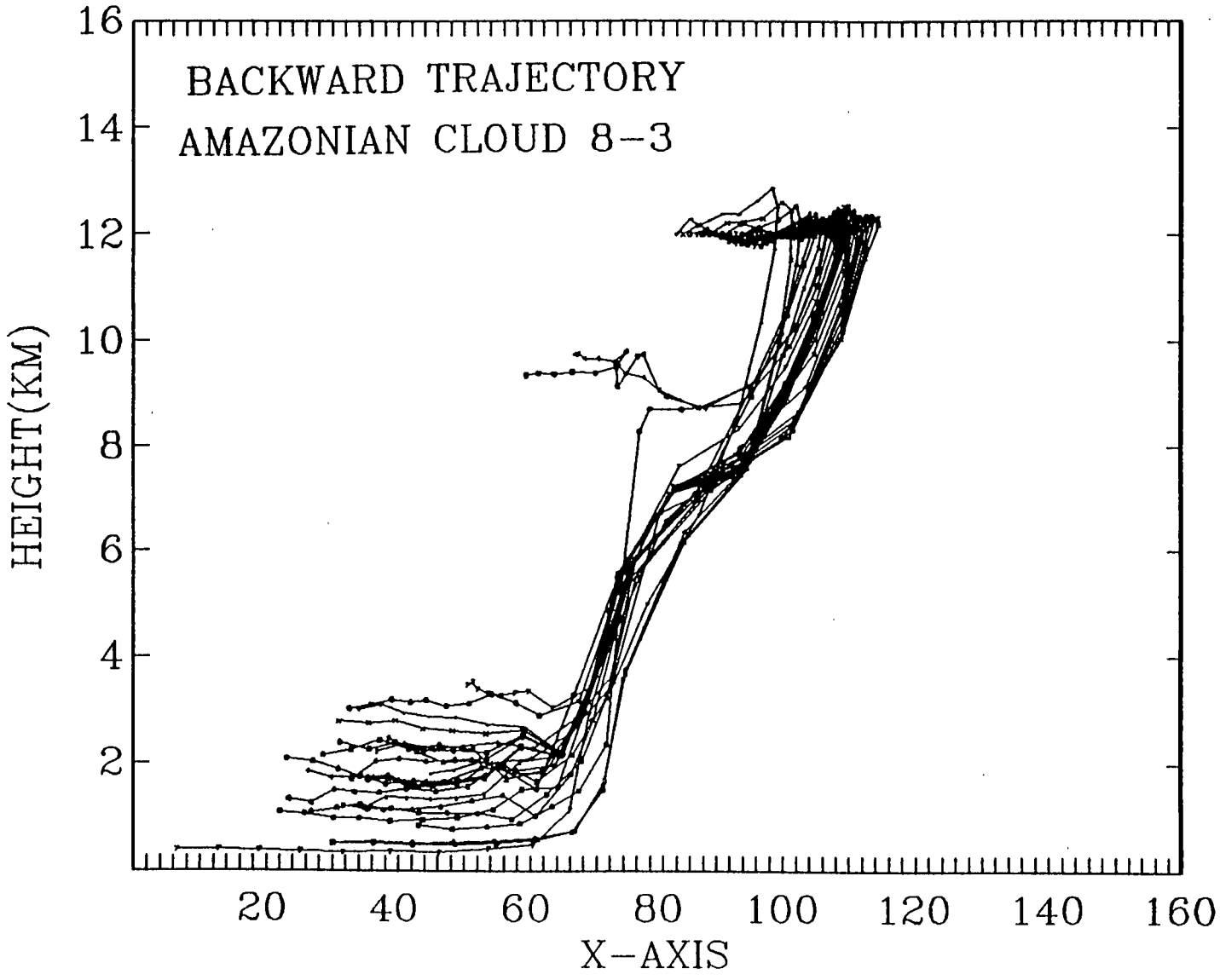
BACKWARD TRAJECTORY
AMAZONIAN CLOUD 8-3
HEIGHT(KM)
16
14
12
10
8
6
4
2
20
40
60
80
100
120
140
160
X-AXIS

The
ATD Observer

Covering Research and Development in Observational Atmospheric and Oceanic Science

Published by the Atmospheric Technology Division of the National Center for Atmospheric Research Winter 1991

PAM Stations Weather Amazon Rainforest

By Michael Garstang and Charles Martin

Four of NCAR's Portable Automated Mesonet (PAM) systems were used in the middle of the Amazon Basin as part of NASA's Amazon Boundary Layer Experiment (ABLE 2B) in April and May 1987.

The experiment, directed at documenting and understanding the biosphere-atmosphere interactions of the world's largest rainforest, dealt with a wide range of atmospheric scales of motion. The PAMs were deployed in the form of a triangle, with three systems on the corners and one in the center. They provided a continuous time series of measurements for the duration of the experiment over an area of rainforest covering approximately 1000 km^2. These continuous measurements have proved to be invaluable in support of a large portion of the analyses carried out on the ABLE 2B data.

As shown at right, a high tower had to be erected in the jungle to get the PAM sensors, communications antenna, and solar panel in their proper position 5 m above a 40 m forest canopy. The location of the PAM network at approximately 3°S, 60°W was some 4,000 miles from NCAR in Boulder, the terminal point for the telemetered data. No previous PAM application had faced either the challenge offered by the forest or the remoteness of this experiment.

The tower system had to be designed so that it could be backpacked into the jungle and then erected in the forest with minimal disturbance to the natural vegetation. The towers consisted of 3 m sections guyed at 10 m intervals. The guy wires had to be installed through a dense understory of brush and trees. This was done by firing a crossbow bolt attached to a light fishing line and spinning reel. A heavier line, retrieved by the fishing line, was used to pull up the steel guy wire. Once all the equipment was assembled at a site, it took four technicians about four days to get the PAM system operational.

The measurements obtained included horizontal wind speed and direction, temperature, humidity, and rainfall at a height of 5 m above the forest canopy, and atmospheric pressure at the base of the tower. In addition, aerosol samplers were located at three heights on two of the four PAM towers. Most of the variables were sampled at a rate of 1 Hz and formed into one-minute averages. The maximum wind speed within each minute was also retained in the data set.

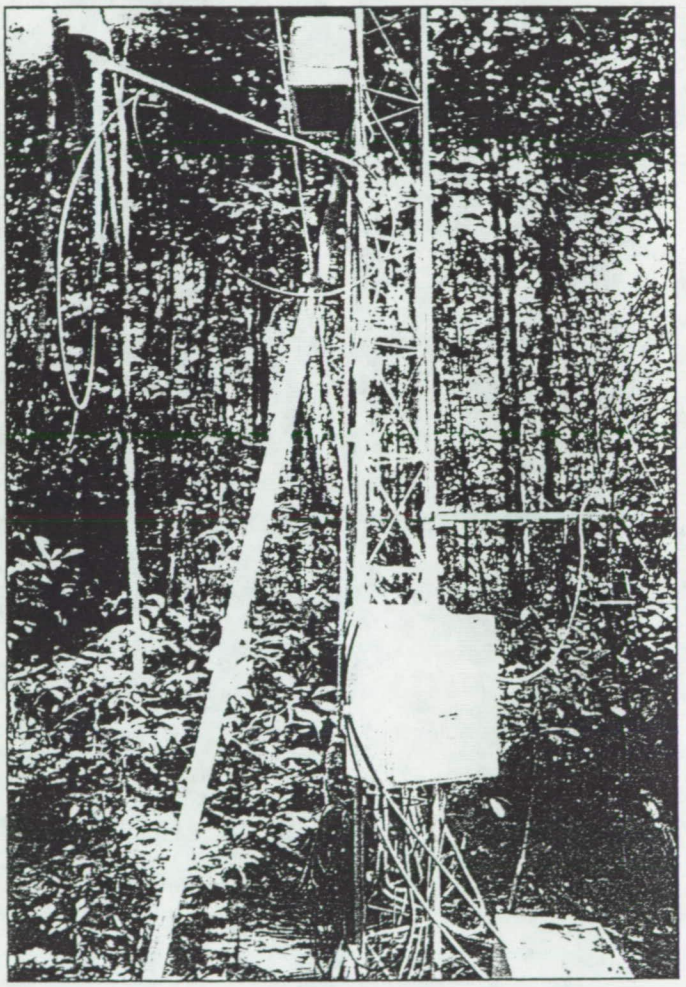

Base of the 45-m PAM tower in the Amazon jungle (photo by Michael Garstang).

The data stream was sent via satellite to Boulder, where quality control checks, basic calculations, and data plots were made. These processed data were transmitted back to the field

See PAM on page 2

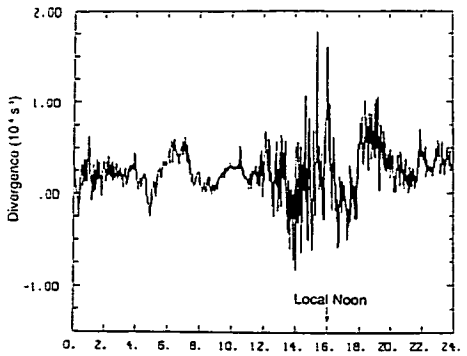

Fig. 1. The 24-hr surface network divergence for 6 May 1987, calculated from 1-min PAM wind averages. The onset of diurnal heating, indicated by larger fluctuations in the wind field, is evident after 1000 UT.

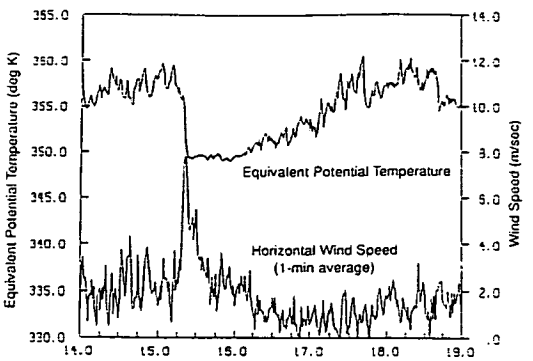

Fig. 2. Gust front passage at 1520 UT on 6 May 1987, as recorded by the Embrapa PAM instruments.

PAM continued from page 1

with a time lapse of only about five minutes. In the field, the PAM results were used to guide the operations on the ground and plan the use of the NASA Electra research aircraft.

Surface mass divergence over the 1000 km^2 triangle was calculated on a continuous basis. Figure 1 shows the transition from the nighttime stratified state above the canopy to daytime heating. This is followed by rapid fluctuations in convergence and divergence associated with an organized deep convective system that traversed the PAM triangle. The PAM records also captured the gust front and downdrafts of the synoptic scale weather system as elements of the storm crossed individual PAM stations (see Figure 2).

Integration of the PAM data with aircraft observations in the volume over the PAM triangle allowed horizontal velocity fields, divergence, and vertical velocities to be calculated and compared with cloud model calculations. These data, along with flux calculations made from a separate micrometeorological tower, show that convective clouds act to remove from the rainforest canopy constituents normally trapped there by persistent static stability. Upward transport by convective clouds can take two substantially different routes. Under "dry" but unstable conditions, more than 85% of the air at anvil levels originates below 3 km. In "wet" well-mixed conditions, less than 15% of the air at anvil levels originates below 3 km. In the latter conditions most of the cloud air is detrained in the mid-troposphere.

Our analyses have indicated that during a substantial part of the wet season, deep mixing will allow the mean motions of the Hadley and Walker circulations to export constituents from the Amazon Basin to the global atmosphere. Energy budget calculations show that the upward transport of energy by the continental equatorial clouds is large — some four times that calculated over the eastern tropical Atlantic from the results of the GATE program. This makes continental tropical regions like the Amazon Basin important contributors to the global circulation.

The PAM measurements of rainfall at 5 m above the forest canopy were also a "first." Figure 3 compares the occurrence with time of measured rainfall amounts and terrestrial dust concentrations. As indicated, both rainfall and dust tend to occur together in periodic pulses. The rain events seen in the time series of rainfall are evidence that most of the rain that occurs in the Amazon Basin is due to large, organized synoptic-scale systems. These systems were responsible for more than 80% of the rain that fell during the experiment. The remaining rainfall came from the "local" systems. Since our analyses show that the large-scale synoptic systems draw most, if not all, of their water vapor from the Atlantic Ocean, this finding has bearing upon the potential effect of deforestation.

The near coincidence of large terrestrial dust events with the high rainfall events has produced a separate and intriguing result. While trajectory analysis (see Figure 4) shows that this dust is almost certainly of Sahara origin, the coincidence with the rain event must have a separate explanation. The explanation lies in the widespread low-level convergence generated by the storm. Thus, the storm acts as a large vacuum cleaner, sucking dust into the Amazon Basin from the western Atlantic and eastern Caribbean. Calculations based

See PAM on page 3

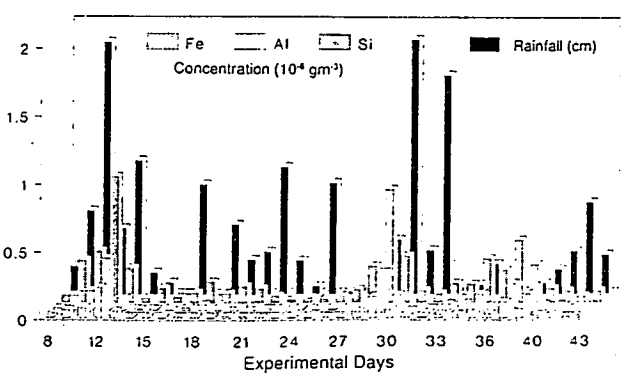

Fig. 3. Time series of terrestrial constituent concentrations and rainfall amounts for 8 April-13 May 1987.

Director's Corner

By Richard Carbone

On 17 December Larry Radke assumed the leadership of NCAR's Research Aviation Facility. A twenty-year veteran of research aircraft management within Peter Hobbs' Cloud and Aerosol Group at the University of Washington (UW), Larry's qualifications are unsurpassed. He has led more than 1000 missions as lead or principal scientist on numerous aircraft including the entire NCAR fleet, the NSF Polar Programs C-130, the NOAA P-3s, DC-6 and King Air, and the US Navy P-3s. Larry's career has centered on the application of technology, systematically organized on an airborne platform, to solve problems of interest in the atmospheric sciences. He has developed instruments to measure cloud condensation nuclei and ice particle concentrations. As a consultant to Boeing, Larry has worked with the Laser Technology and Physics groups on a range of topics.

A native and lifetime resident of Seattle, Larry received the B.S. (Physics), M.S. and Ph.D. degrees from UW in 1964, 1966, and 1968, respectively. His research interests are cloud and precipitation physics, atmospheric chemistry, and air pollution. He has authored over 90 papers published in scientific journals and over 90 informal works. Recent contributions emphasize the distribution, composition, and role of aerosols from volcanoes, biomass burning, and other anthropogenic sources in the arctic, mid-latitudes, and tropics. Analyses of the effects of aerosols on cloud microphysics and cloud radiative properties are also among his recent works.

Among numerous appointments, Larry has served as Associate Editor of the Journal of Atmospheric and Oceanic Technology, as Chairman of the AMS Cloud Physics Committee, and as a member of the Army Basic Research Committee of the National Research Council, the AMS Committee on Measurements, NASA's GLOBE Working Group, and the FIRE Science Team.

Speaking personally, I am delighted that Larry decided to join ATD after a very distinguished career at UW. I am particularly enthusiastic about his fresh approach and the leadership skills he brings to RAF. Larry is highly creative, innovative, and purely science-driven. I am confident that his efforts at RAF will benefit the atmospheric sciences more broadly than ever before and, in so doing, make a very good RAF even better.

Welcome Larry!

Larry Radke, ATD's new Research Aviation Facility Manager.

Richard (Rit) Carbone is Director of the Atmospheric Technology Division at NCAR ❖

PAM continued from page 2

on the mass convergence in the storm and observations of the dust concentrations suggest that 100,000 tons of dust can enter the basin in such a storm event. Not all storms bring in dust, but all major observed dust events were accompanied by storms. Using storm climatology as a guide, it is possible that 10M tons of Sahara dust are imported into the Amazon Basin in a given wet season. The Saharan dust may contain trace elements critical to the health of the delicately balanced rainforest. Thus, it is clearly possible that the health of this ecosystem is inversely related to that of the Saharan-Sahelian ecosystem.

Another product from the PAM, the one minute wind gust maximum, may have implications in the Amazonian rainforest. Wind gusts are related to tree falls. In tropical rainforests, the greatest opportunity for new growth lies with the creation of canopy gaps by tree falls. In addition, maximum nutrient supply from trees, epiphytic growths, and atmospheric deposition to the forest floor are believed to occur in tree fall canopy gaps. Analyses are now underway using the PAM gust data to examine the relationship between tree falls and wind gusts.

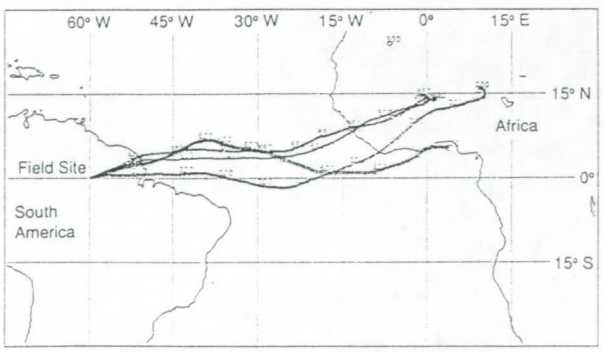

Fig. 4. Ten-day backwards isobaric (850, 800, 700, 600 mb) trajectories of air parcels arriving at the field site at 00 UT, 14 April 1987.

The reliability, continuity, and real-time capability of the PAM system make it an extremely valuable field experimental tool. The PAM provides three components of a four-dimensional field. While knowledge of the deeper atmosphere is often essential to understanding, the benefit-to-cost ratio of the PAM is very high.

(Editor's Note: A large fraction of the research results from the Amazon Boundary Layer Experiments, ABLE 2A and 2B, can be found in two special issues of the Journal of Geophysical Research: Vol. 93, No. D2, February 20, 1988, and Vol. 95, No. D10, September 20, 1990.)

Michael Garstang is a Professor in the Department of Environmental Sciences at the University of Virginia. Charles Martin is a Software Engineer III and heads the Data Management Group of ATD's Surface and Sounding Systems Facility. ❖

Accepted Bound.-Layer Met.

LOW-LEVEL NOCTURNAL WIND ACCELERATIONS OVER THE CENTRAL AMAZON BASIN

Steven Greco, Stanley Ulanski[1], Michael Garstang, and Samuel Houston[2]

University of Virginia
Department of Environmental Sciences
Charlottesville, VA 22903

[1]Department of Geology and Geography, James Madison University, Harrisonburg, VA 22807.

[2]Hurricane Research Division, AOML/NOAA, Key Biscayne, FL 33149.

Abstract

A low-level nocturnal wind acceleration is shown to exist over extensive and nearly undisturbed rainforest near the central Amazon city of Manaus. Analysis of meteorological data collected during the 1985 and 1987 Amazon Boundary Layer Experiments (ABLE 2A and 2B) indicate the presence of this nocturnal wind acceleration during both the wet and dry seasons of the Central Amazon Basin (CAB). Daytime wind speeds which are characteristically 3-7 m s^{-1} between 300 m and 1000 m accelerate to 10-15 m s^{-1} shortly after sunset. The wind speed maximum is reached in the early evening, with wind speeds remaining high several hours after sunrise. The nocturnal wind acceleration is closely linked to a strong low-level inversion formed by radiational cooling of the rainforest canopy. The nighttime inversion extends up to 300 m with strong vertical shear of the horizontal wind below the inversion top and uniformly strong horizontal winds above the inversion top. Frictional decoupling of the air above the inversion from the rough forest below, however, is responsible for only part of the observed acceleration. Surface and low-level pressure gradients between the undisturbed forest and the large Amazon river system and the city of Manaus are shown to be responsible for much of the nocturnal wind acceleration. The pressure gradients are interpreted as a function of the thermal differences between undisturbed forest and the

river/city. The importance of both the frictional decoupling and the horizontal pressure gradient suggest that the nocturnal wind acceleration is not uniformly occurring over all Amazonia. We suspect that stronger low-level winds are pervasive under clear skies and strong surface cooling and that, in many places (i.e., near rivers), local pressure gradients enhance the low-level nocturnal winds.

1. INTRODUCTION

The lower atmosphere of the global tropics is generally embedded within the equatorial trough and is mainly thought of as a region of low wind speed. The term "doldrums" has been used as a descriptor for the surface velocity fields about the meteorological equator. It came, therefore, as a considerable surprise to these investigators to find low level, nocturnal wind speeds in the near-equatorial central Amazonian rainforests to be in excess of 15 m s^{-1} during both the wet and dry seasons.

Equatorial continental regions of the earth's surface beyond the immediate environs of a few cities and settlements remain relatively inaccessible. The rainforest, with its attendant size (canopies at 40 to 50 m) and biological and physical conditions, presents a hostile environment, particularly in the wet season, for scientific measurements. Despite these obstacles, considerable work has been done in equatorial rainforests. Most has focussed upon the biological aspects of this large and diverse ecosystem. The work that has dealt with the atmosphere has been mainly directed at the larger scale dynamics. In the Amazon Basin, for example, several researchers (Kousky, 1979; Kousky and Ferreira, 1981; Kousky and Kagano, 1981; Paegle, 1987; Salati and Vose, 1984; Silva Dias et al., 1987; Nobre et al., 1987) have all been responsible for

pioneering work. The British-Brazilian experiments of the early 1980's (Shuttleworth et al., 1984, 1985) were the first in Amazonia to address the detail of the hydrologic cycle and the micrometeorology of the rainforest.

In 1985 and 1987, the U.S. National Aeronautics and Space Administration (NASA), as part of its Global Tropospheric Experiment (GTE), joined with the Brazilian Instituto de Pesquisas Espaciais (INPE) and the Instituto Nacional de Pesquisas da Amazonia (INPA) to mount two major experiments in central Amazonia. These experiments, called the Amazon Boundary Layer Experiments (ABLE), were conducted in the dry (July-August 1985) and wet (April-May 1987) seasons and were directed at establishing the base atmospheric chemistry state over the forest and wet lands of the Amazon basin (Harriss et al., 1988, 1990; Garstang et al., 1990). We will draw upon these experiments to document the structure and nature of the nocturnal velocity field in the boundary layer over the rainforest of central Amazonia.

The occurrence of a pronounced nocturnal wind acceleration over the central Amazon basin (CAB) was first noted by Greco et al. (1989). Garstang et al. (1990) and Oliveira (1990) have also discussed this feature. In this paper, we will describe the nocturnal evolution of the boundary layer winds together with the associated

temperature and pressure fields. We will then present a mechanism which accounts for the nighttime acceleration of winds in the first kilometer above the forest.

Nocturnal low-level jets and wind accelerations have been documented in many locations around the globe (Bonner, 1968; Wipperman, 1973). The low-level jet of the Great Plains region of the United States has been extensively studied by among others, Hoecker (1963, 1965); Blackadar (1957); Wexler (1961) and Bonner (1968). Other mid-to-higher latitude low-level nocturnal wind accelerations have been detected in southeastern Australia (Clark et al., 1971), southern England (Thorpe and Guymer, 1977), northwestern Germany (Kraus et al., 1985), the United States Gulf coast (Hsu, 1979), and the coastal regions of northeastern United States and the Canadian Maritimes (Dickerson and Neumann, 1982). In the tropical and subtropical regions of the world, however, only a few documented cases of low-level nocturnal jets or wind accelerations are in existence. DeSouza et al. (1971) showed remarkable accelerations below 500 m over the island of Barbados (near 13°N, 60°W). These accelerations were not, however, strictly nocturnal. In the Daly Waters region of Australia (16°16'S, 133°23'E), Clark and Brooke (1979), Brooke (1985), and Garrat (1982, 1985) all have documented a nocturnal jet based upon measurements from the 1974 Korrin

expedition. Virji (1981) found a nocturnal jet in the western Amazon basin near the foothills of the Andes.

Although these strong nocturnal winds form in numerous and varied locations, they have a number of features in common. The nocturnal wind accelerations all form shortly before or after sunset, within the nocturnal planetary boundary layer (often at heights between 300-700 m above ground level), and can reach speeds which are 2-3 times larger than daytime values. Each low-level jet or wind acceleration, however, may owe its origin to a different mechanism or set of mechanisms.

One of the mechanisms most often responsible for the nocturnal accelerations is the inertial oscillation induced when frictional constraint imposed by daytime turbulence is released by the formation of an inversion near sunset (Blackadar, 1957). This allows the wind above the inversion to reach supergeostrophic levels. Other prime mechanisms include: winds associated with surface radiational cooling over sloping terrain (Lettau, 1967, 1983; Zeman, 1979); advective accelerations (Paegle and Rasch, 1973); variations in the synoptic scale geostrophic wind (Mahrt, 1981); and the generation of mesoscale pressure gradients in response to the heating and cooling over sloping or non-uniform terrain (McNider and Pielke, 1981).

The ABLE, located in the CAB essentially on the equator, precludes inertial oscillation (period too long), Coriolis force (approaches zero for horizontal motion) or terrain (large scale slope ≤ 1:2000 km) as forces driving the acceleration of the low-level wind. However, horizontal surface temperature gradients produced by the confluence of the large Negro and Solimoes rivers to form the Amazon may play a role in generating the nocturnal wind acceleration of the CAB. In addition, the effective removal of surface frictional drag by the formation of a low-level nocturnal radiation inversion may also play a significant role in producing the nocturnal wind accelerations.

The low-level nocturnal wind acceleration mechanisms will be discussed in Section 4, with Sections 2 and 3 discussing, respectively, the experimental design and data collection, and the observed structure and evolution of the nocturnal boundary layer.

2. EXPERIMENTAL DESIGN AND DATA COLLECTION

A manned tethersonde and radiosonde station was operated in ABLE 2A from July 15 to August 7, 1985 at Ducke Forest Reserve, approximately 20 km northeast of Manaus, Brazil (Figure 1). Vertical profiles of temperature, horizontal wind speed and direction, pressure, and humidity up to 1000 m were taken by a sonde-equipped tethered

balloon. The ascent rate of the balloon was 1 m s^{-1} and measurements of horizontal velocity were made every 2 m and those of temperature, humidity and pressure every 4 m. Each sounding lasted between 15 and 20 minutes and both up and down profiles were taken. Three to four vertical soundings were made during most hours. In addition to the tethersondes, rawinsondes using a high-resolution Atmospheric Instrumentation Research (AIR) sonde and a digital recording and processing system were launched every three h. These rawinsondes ascended to 500-400 mb and provided measurements of wind speed and direction, temperature, and specific humidity. Hours of operation were mainly confined to the daytime hours, except for six days when measurements were taken throughout the 24 h. The data from these six days will be a main focus in this paper.

In the ABLE 2B wet season experiment, held from April 1 to May 14, 1987, Ducke Reserve was one of three sonde-equipped stations forming a mesoscale triangle of approximately 1000 km^2 (Figure 2). The mesoscale network consisted of 3 stations (Ducke, Embrapa, and Carapaña) located at the triangle corners and one station (ZF-1) located in the center. The tethered balloons ascended up to 500 m at Carapaña and Embrapa and up to 1000 m at Ducke. No balloons were launched from ZF-1. Vertical profiles of the boundary layer during ABLE 2B were not done as often as

during the earlier dry season experiment. At most, 2-3 vertical profiles were taken during each hour of observation and there were many periods of up to 2 hours without a vertical tethersonde profile. Reasons for this included logistics, different experimental objectives, and preventive maintenance on strained equipment. Rawinsonde launches occurred 4 times a day at Ducke and Carapaña (0800, 1100, 1400, and 1700 LST) and 6 times a day at Embrapa (2000, 0200, 0800, 1100, 1400, and 1700 LST).

The four stations shown in Figure 2 were also equipped with a Portable Automated Mesonet (PAM) system mounted on 45 m towers, placing them 5 m above the forest canopy. Measurements of horizontal wind speed and direction, temperature, humidity, and pressure were taken at a frequency of 1 Hz and compiled into 1 min averages.

Similar to ABLE 2A, most of the ABLE 2B experiment was conducted during the daytime. However, a four day period of continuous 24-h operation was carried out near the end of the experiment to examine the structure and evolution of the transition (dusk, dawn) and nighttime boundary layer during the wet season.

3. OBSERVED BOUNDARY LAYER STRUCTURE

3.1 ABLE 2A

Meteorological conditions during the 1985 ABLE 2A

experiment were typical of the CAB dry season when undisturbed conditions with suppressed convection tend to dominate.

Nighttime observations in the dry season period were taken on 6 occasions: July 25-26, July 26-27, July 30-31, July 31-August 1, August 1-2, and August 2-3. With the exception of the initial nighttime observation period (July 25-26), the tethersonde data coverage was fairly continuous throughout the night.

Composite soundings for the ABLE 2A experiment were created from the 3-hourly rawinsonde launches made at Ducke Reserve. Figure 3 displays the composite wind speed profiles below 700 mb for soundings taken at 2000, 0200, 0800 and 1400 LST*. Between the midafternoon (1400 LST) and the early evening (2000 LST), there is a noticeable increase in wind speed throughout the lower troposphere. The strongest increase is found below 1000 m/900 mb where winds increase from 4-5 m s^{-1} to 7-8 m s^{-1} with a nose-like feature found between 950-900 mb at 2000 LST. After this initial acceleration,

---

*Footnote: Since sunrise and sunset in the ABLE mesoscale triangle region (2-3°S latitude) is near 6 a.m. and 6 p.m. during the entire year, and the subject of this paper is closely tied to the diurnal cycle, we will use Local Standard Time (60th meridian) throughout.

the winds below 1000 m remain relatively constant through most of the night before decelerating after sunrise. Above this level, the horizontal wind speeds increase 1 m s^{-1} between 2000 and 0200 LST and then decrease 1 m s^{-1} after sunrise.

The composite wind profiles from the rawinsonde shown in Figure 3 do offer some evidence of a boundary layer nocturnal low-level jet or wind acceleration (WA hereafter). However, the rawinsonde speeds are averaged over a depth of 200-300 m and give a smoothed profile of the boundary layer winds which perhaps does not capture the full extent of the nocturnal wind speeds. Table I shows a comparison between rawinsonde and tethersonde measured wind speeds at similar heights and near-coincident times. During the afternoon (1400 LST), there is little difference between the values of wind speed measured by tethersondes and by rawinsondes. This is mainly an indication of the well-mixed afternoon boundary layer. At night, however, the rawinsondes, unlike the finer resolution tethersonde, are unable to capture the strong nocturnal winds and the vertical shear of the horizontal wind which are present. This is illustrated by the 2-5 m s^{-1} difference between the tethersonde and rawinsonde wind measurements shown in Table I. The absence of detailed measurements with high vertical resolution in the lower atmosphere of the CAB before the ABLE may be a

reason why a nocturnal WA has not been previously detected. To document the existence of this WA, we will concentrate on measurements taken by the tethered balloons.

As seen in Tables IIa-b, the six nights of the tethersonde profiles show a relatively strong WA on 3 nights and a weak WA on 2 nights. The last night was disrupted by a synoptic scale weather system as seen by satellite and ground observations. Figure 4 shows the 0200 LST composite rawinsonde profiles for all 6 nights and the 3 nights with a strong nocturnal WA. The rawinsondes, despite their poor vertical resolution, are still able to capture the nocturnal WA on nights when the tethersonde data indicated the existence of a strong acceleration. However, on nights when the WA is more modest, the rawinsonde smooths the vertical profile to the point where any evidence of a nocturnal WA is lost.

A more detailed description of the nocturnal WA can be seen from analysis of the tethersonde data. Tables IIa-b summarize the salient features of the diurnal evolution of the boundary layer wind and temperature tethersonde profiles for the 5 cases (omitting the August 2-3 synoptic event) of day-to-night operations. The nocturnal WA and surface-based temperature inversion is seen to exist on all 5 nights, although with varying intensities. In addition, in all 5 cases, there is a common wind direction shift from SE/ESE to NE/ENE between day and night. The wind shift is especially

strong during the 3 nights with substantial accelerations of wind speed from day to night.

The nighttime feature illustrated in Table II and Figures 3-4 is examined in greater depth by contrasting cases of strong and weak WA. Figures 5a-b show that, after the decay of the previous nights stable conditions and strong horizontal winds (7-11 m s^{-1}), turbulent mixing and surface heating dominate during the afternoon of July 26. By 1300 LST adiabatic to super-adiabatic lapse rates exist and nearly uniform wind speeds are found in the lower 1000 m. Horizontal wind speeds in the surface-1000 m layer are only 3 to 7 m s^{-1} between 1300 LST and sunset.

Broken cumulus cloud cover was present near sunset on July 26, and it was not until 0200 LST on July 27 that skies totally cleared over Ducke Forest Reserve. Despite the cloud cover, the radiative cooling near sunset is still intense enough to lead to thermally stable conditions (Figure 6a) which last through the night. As skies cleared, a weak inversion forms early on July 27 (0200 LST). Coincident with the inversion after 0200 LST, the wind accelerated to 6-9 m s^{-1} between 200 and 1000 m (Figure 6b). Figures 7a-b show that thermally stable conditions and strong horizontal winds persist through the late morning hours of July 27 before being erased by turbulent mixing and surface heating.

After a one day suspension of operations, observations resumed at 1800 LST on July 30. The formation of a strong surface-based temperature inversion (2.5°C/150 m) shortly after sunset can be seen in Figure 8a. This inversion lasts throughout the night, weakening slightly by 0600 LST. The top of the inversion is situated near 380 m above mean sea level (MSL) or 300 m above ground level (AGL) (Ducke is 78 m above MSL). This inversion is much stronger than the one noted on the night of July 26-27 due to the more intense radiative cooling produced by the clear skies as noted by weather observations.

A strong acceleration in horizontal wind speed at and above the inversion top accompanies the stable conditions in the lower 300 m. As illustrated by Figure 8b, winds above the inversion top increase from 6-12 m s^{-1} near 1800 LST to 12-15 m s^{-1} through the night. The winds above the inversion top are uniformly strong up to at least 1000 m. Below the inversion top, there is a layer of strong vertical shear of the horizontal wind with winds increasing from near calm at the surface to 11-13 m s^{-1} at 300 m AGL. The inversion, low level WA and separation of layers noted on July 30-31 are all stronger than during the night of July 26-27 when broken cloudiness lasted throughout 0200 LST.

However, similar to the July 26-27 case, the strong horizontal winds continue through 0900-1000 LST of the next

morning (July 31) until the inversion breaks down and adiabatic lapse rates resume (Figures 9a-b). After 1000 LST, turbulent mixing and surface heating once again produce well mixed horizontal wind speeds of < 7 m s^{-1}. Shortly before sunset, the surface-based inversion has once again formed. With the inversion formation, a significant acceleration in the horizontal wind speed is seen before 1800 LST with winds reaching 9 m s^{-1} between 250 and 400 m AGL.

The night of July 31-August 1 was almost identical to the previous night (Figures 10a-b). Clear skies and radiation cooling enhance the surface-based temperature inversion which extends up to 300-320 m AGL and lasts the entire night. This inversion exhibits a lapse rate of +1-2°/100 m and also weakens slightly by morning. Strong nocturnal winds develop above the inversion top with speeds of 10-14 m s^{-1} between 300 and 1000 m. Once again, a strong stratification is seen with the inversion separating the lower atmosphere into two layers. Strong shear of the horizontal wind exists betwen these two layers.

3.2 ABLE 2B

The rainfall of the April-May 1987 wet season was organized on scales ranging from the convective to the synoptic, with most of the rain (80%) produced by meso- to synoptic-scale systems originating in the eastern Amazon

basin and the northern Atlantic coast of Brazil (Greco et al., 1990). However, Greco et al. (1990) also show that 40% of the days were dominated by fairly undisturbed conditions with only scattered airmass-type convection. These days are similar to the ABLE 2A dry season period. With this in mind, a goal of this work was to see if the WA seen during ABLE 2A also existed during the wet season. In addition, with the expansion of the data gathering network to 3 manned stations during ABLE 2B, the spatial extent of this phenomenon could be examined.

The 24 hours of continuous observations began at 0600 LST, May 5 and ended at 1500 LST, May 9. Tethersonde and rawinsonde measurements were taken at all three corner stations of the mesoscale network (Figure 2). As an example, we will present a series of tethersonde profiles for May 5-6, a day and night characterized by generally undisturbed conditions similar to the dry season.

Figures 11a-b and 12a-b show tethersonde profiles of temperature and wind speed at Ducke during the afternoon of May 5 and the night of May 5-6. In the late afternoon (1706 LST), the wind speeds through the entire surface-1000 m layer are 3-7 m s^{-1}. No inversion is present and the surface temperature is 28°C. By 2219 LST (Figure 12a), a strong surface-based inversion (1-2°C/100 m) is in place which extends up to 250 m AGL and there is a strong WA (Figure 12b) with wind speeds above the inversion top of 8-12 m s^{-1}.

Although slightly weaker than during ABLE 2A, the nighttime wind speeds of the wet season are as high as twice the daytime values. Below the inversion top, strong shear of the horizontal wind is also present. The inversion and strong low-level winds continue through the night (0432 LST) before diminishing after sunrise (0712, 0807 LST). These characteristics are very similar to those observed during the dry season and are substantiated by further wet season cases not shown. Generalization can, however, be made from the wet season cases.

Examination of the tethersoundings at the other stations in Figure 2 show that the low-level nocturnal acceleration develops over the entire area. Figures 13a-b illustrate the evolution of the surface-based inversion and significant day-to-night wind acceleration which occurred at Carapaña during the evening of May 5. Above the inversion top, wind speeds accelerate to near 11 m s^{-1}. Due to equipment failure, no tethersonde data exist after 0100 LST on May 6. Nocturnal wind accelerations similarly evolve over Embrapa but with evidence that the nocturnal accelerations at both Carapaña and Embrapa are not as large as at Ducke.

The greatest difference seen between the wet and dry season development of the nocturnal WA is related to the increase of disturbed weather during the wet season. More

frequent and larger amounts of cloudiness reduce nocturnal cooling and the intensity of the inversion and thus the associated accelerations in the wet season.

Another factor influencing the magnitude of the nocturnal WA is the prevailing wind direction. Figures 14a-c present a 24-hour time series contour of rawinsonde measured wind direction on, respectively, May 5-6, 6-7, and 7-8 at Ducke. The nights of May 5-6 and 6-7 were characterized by a strong low-level nocturnal WA. On May 5-6, there was a shift from a southerly component before 1700 LST to a more northerly component during the night and early morning. The shift in the boundary layer winds from ESE to ENE also occurs on May 6-7, as does a significant nocturnal WA. In contrast, Figure 14c shows that on a night with a relatively weak WA (May 7-8), the predominant wind direction in the boundary layer after sunset was 85-120°. Wind directions measured at Carapaña and Embrapa reveal the same wind shifts as found at Ducke. The relationship between wind direction shifts and the strength of the nocturnal WA will be discussed in the following section.

4. NOCTURNAL WIND ACCELERATION MECHANISM

A necessary condition shown in Section 3 for a strong nocturnal WA is the establishment of a surface-based inversion near or after sunset. This inversion, which

extends up to 300 m, is produced by significant radiative cooling at the surface during nights with clear or mostly clear skies.

With the formation of the inversion, a two-layered fluid is established during the nighttime hours. Below the inversion top is a layer of strong wind shear and mechanical turbulence as winds increase from near calm at the surface to 10-12 m s^{-1} at the inversion top. The layer above the inversion top is effectively decoupled from turbulence and surface frictional affects within the inversion layer. Such a decoupling will lead to a relative acceleration of the winds above the inversion. The WA associated with the frictional decoupling is not, as will be shown below, sufficient to account for the observed nocturnal WA.

The strength of the nocturnal acceleration of the wind is also controlled by a thermally-driven pressure gradient and associated wind generated between the forest sites and the nearby Negro-Solimoes-Amazon river system in the presence of the frictional decoupling. The river-land circulation mechanism was also proposed by Oliviera (1990). Figure 2 shows that Ducke is approximately 20 km north of the river system while Carapaña is more than 50 km away from the Amazon river. The rivers reach widths of > 15 km near their confluence and are potentially large enough to generate an observed mesoscale circulation.

With only indirect measurements (aircraft) made over the rivers, Ducke-Carapaña is used as a measure of the river to forest gradient. Ducke, which lies 20 km north and east of the rivers and north of the City of Manaus, will be under the influence of both the rivers and the city. Carapaña, however, lying 65 km upwind of the city and 45 km north of the Amazon is regarded as a representative rainforest site.

Airborne radiometric temperatures taken during the ABLE 2A and 2B experiments show the rivers to be 2-3°C cooler than the forest canopy during the day and 6-8°C warmer at night. Figure 15 shows a 24 hour time series of the ABLE 2B composite horizontal Δt and Δp at the surface as measured by PAM towers located at Ducke and Carapaña. During the night (1800 LST-0600 LST), it is warmer at Ducke than at Carapaña. After 0800 LST, the gradient starts decreasing but it is not until 1000-1100 LST when it is warmer over the Carapaña forest site (C) than at the Ducke river/city site (D). The forest station reaches its maximum at 1400 LST and is warmer than Ducke until 1700 LST. The similarity in the trends and slight lag (~1 h) between Δt and Δp indicates that the pressure gradient is controlled by the thermal differences between the land/forest and river/city at night.

The pressure gradient (D-C) becomes negative and reaches a maximum (-.25 mb/50 km) during the late afternoon and early evening (1900 LST). The time of maximum surface

horizontal pressure gradient coincides with the maximum nocturnal WA. The negative pressure gradient between Ducke and Carapaña implies that the wind generated by the pressure gradient force should blow from Carapaña (higher pressure) to Ducke (lower pressure). This is indeed the case. As illustrated in Figure 14, the two nights with the strongest WA observe a wind shift from the ESE to ENE during the period of the intensifying pressure gradient. A wind direction from the ENE will see winds blowing from Carapaña to Ducke. For the remainder of the night and early-to-late morning, the pressure gradient, like the temperature gradient, is fairly constant. During this period, the nocturnal winds shown in Section 3 remain strong but with no large accelerations. Late morning to early afternoon sees both a reversal in the temperature and pressure gradients along with a diminishing of the boundary layer winds.

The horizontal acceleration of the wind can be expressed in the usual fashion:

$$\frac{d\underset{\sim}{v}}{dt} = \frac{-1}{\rho} \nabla P - f\underset{\sim}{K} \times \underset{\sim}{V} + \underset{\sim}{F} \qquad (1)$$

For the purpose of this paper, we will represent the frictional drag within the tropical PBL in the simplified form

$$\underset{\sim}{F} = -a \underset{\sim}{V} \qquad (2)$$

where "a" is a frictional coefficient with some dependence upon wind speed, surface roughness and static stability.

Neglecting the Coriolis effect as very small near the equator, the equation of motion reduces to:

$$\frac{dv}{dt} = \frac{-1}{\rho} \nabla P - a\underset{\sim}{V} \qquad (3)$$

After a large initial acceleration near sunset, the wind speed throughout the PBL was shown above to remain relatively constant during the night. With the acceleration near zero at night, Eq. (3) reduces to

$$\frac{-1}{\rho} \nabla P = -a \underset{\sim}{V} \qquad (4)$$

Figures 16a-d illustrate the PAM-derived pressure gradient (ΔP) between D and C on the days of May 5-8. It is seen that the Δp during the times of the nocturnal WA on each night vary between .15 and .60 mb. These values are significantly higher than seen in the composite (Figure 15). After the early evening WA, Δp values remain fairly constant through to the next morning for all 3 cases with mean values of .15, .25 and .20 mb on, respectively, May 5-6, May 6-7 and May 7-8.

The frictional coefficient "a" can thus be calculated for these cases using Eq. (4) and the mean nocturnal values of p and observed wind speeds. These results are summarized in Table III for Ducke. With the mean value of the frictional coefficient "a" from the three nights, a predicted day-to-night acceleration can be calculated using Eq. (3) and the observed $\overline{\Delta p}$ and wind speed during

the nocturnal acceleration period. These values are also summarized in Table III.

Predicted values of dv/dt during the period of acceleration on all 3 nights are within 1.5 m s^{-1} of the observed wind accelerations (see Table III). The results suggest that the initial forcing of the WA is due to the acceleration produced by a combination of the thermal/pressure gradients between Carapaña (forest) and Ducke (river/city), and the decrease in the frictional forcing. Through most of the night, little wind acceleration is observed as the pressure gradient and frictional forces are in near-equilibrium.

After sunrise, deceleration in the horizontal wind speeds responds to the imbalance between the frictional and pressure gradient terms. Figures 15 and 16 show that the pressure remains higher at Carapaña than at Ducke through midday, well after the observed deceleration of the wind. This deceleration in wind speed between the surface and 1000 m is caused by the increase in friction resulting from the destruction of the surface-based inversion by strong surface heating and recoupling through turbulence to the rough forest. This deceleration can be explained by Eq. (3) in terms of a higher daytime value of the frictional coefficient "a" than used during the night.

As an example, an observed deceleration of 2.5 m s^{-1} was

noted at the inversion top by Ducke tethersondes between 0627 and 1027 LST on May 7-8. Using a value of $a = 1 \times 10^{-4}$ (slightly higher than the night values) and $\overline{v} = 5.2$ m s^{-1} and $\overline{\Delta p} = .20$ mb during the deceleration period, the acceleration by the pressure gradient force is 6 m s^{-2} and the frictional deceleration is 7.6 m s^{-2}. The calculated total deceleration of 1.6 m s^{-2} per 4 hours is only 1 m s^{-2} below the observed deceleration (Table III).

5. SUMMARY AND CONCLUSIONS

A nocturnal wind acceleration in the atmosphere below 1000 m is observed over the extensive and nearly undisturbed rainforest north and east of the central Amazon city of Manaus. Wind speeds which are characteristically less than 5 m s^{-1} at 3-500 m above the canopy during the day, accelerate to 10-15 m s^{-1} after sunset. A maximum is reached during the early evening after which wind speeds remain high until after dawn.

The nocturnal wind speeds occur during both the dry and the wet seasons of central Amazonia but are closely linked to the formation of a strong low-level inversion. The inversion is due to radiational cooling of the rainforest canopy and is strongly controlled by cloudiness. Thus, nocturnal inversions and associated wind accelerations are more frequent in the dry than in the wet season. The

intensity of the nocturnal wind acceleration is influenced by the prevailing wind direction. Wind shifts observed during the times of wind accelerations suggest that the forcing is related to surface pressure gradients.

Surface pressure gradients are observed and interpreted as a function of surface thermal gradients between forest and the large river system and the City of Manaus. The surface pressure gradients are shown to be responsible for part of the observed accelerations. Frictional decoupling of the air above the inversion from the rough forest below must be called upon to explain the total acceleration.

The dual nature of the nocturnal wind acceleration depending upon both the existence of a horizontal pressure gradient and frictional decoupling would suggest that the phenomenon is not uniformly occurring over the vast reaches of Amazonia. We suspect, however, that in many places local pressure gradients are enhancing the low level nocturnal winds and that, in general, stronger winds in the lower atmosphere are pervasive when strong surface nocturnal cooling exists. Thus, the phenomena has seasonal characteristics which relate to cloudiness. We suspect that in the dry season, in particular, strong low-level nocturnal winds over wide regions of Amazonia are important in terms of advection of air above the surface-based inversion. The finding that biomass burning products were, for example,

very widely dispersed over the Amazon basin early in the dry season of ABLE 2A may be largely due to this process.

Acknowledgements

We wish to acknowledge the broad support of NASA in the GTE-ABLE program. We would also like to give special thanks to Ms. Mary Morris for doing an excellent job in proofreading, typing and formatting this manuscript.

References

Blackadar, A.K.: 1957, 'Boundary layer wind maxima and their significance for the growth of nocturnal inversions', *Bull. Amer. Meteor. Soc.*, 38, 283-290.

Bonner, W.D.: 1968, 'Climatology of the low level jet', *Mon. Wea. Rev.*, 96, 83-95.

Brooke, R.R.: 1985, 'The Koorin nocturnal low level jet', *Bound.-Layer Meteor.*, 32, 133-154.

Clark, R.H. and Brooke, R.R.: 1979, 'The Koorin experiment', Australian Government Publishing Service, Bureau of Meteorology, Canberra, Australia, 359 pp.

Clark, R.H., Dyer, A.J., Brooke, R.R., Reid, D.G., and Troup, A.J.: 1971, 'The Wangara experiment: Boundary layer data', Tech. Paper No. 19, Division of Meteorological Physics, CSIRO, Australia.

DeSouza, R.L., C.I. Aspliden, M. Garstang, N.E. LaSeur and Y. Hsueh, 1971: A low-level jet in the tropics. *Mon. Wea. Rev.*, 99, 559-563.

Dickerson, R.B. and Neumann, H.H.: 1982, 'The occurrence of nocturnal low-level jets in New England and the Canadian maritimes', *Atmos.-Ocean*, 20, 287-300.

Garrat, J.R.: 1982, 'Observations in the nocturnal boundary layer', *Bound.-Layer Meteor.*, 22, 21-48.

Garrat, J.R.: 1985, 'The inland boundary layer at low latitudes', *Bound.-Layer Meteor.*, 32, 307-327.

Garstang, M., Ulanski, S., Greco, S., Scala, J., Swap, R., Fitzjarald, D., Martin, D., Browell, E., Shipman, M., Connors, V., Harriss, R., and Talbot, R.: 1990, 'The Amazon Boundary Layer Experiment (ABLE 2B): A meteorological perspective', *Bull. Amer. Meteor. Soc.*, 71, 19-31.

Greco, S., Garstang, M., Ulanski, S., Houston, S., and Swap, R.: 1989, 'Local circulations over the central Amazon basin', *Proc. Third International Conf. on Southern Hemisphere Meteorology and Oceanography,* 213-215.

Greco, S., Swap, R., Garstang, M., Ulanski, S., Shipham, M., Harriss, R.C., Talbot, R., Andreae, M., and Artaxo, P.: 1990, 'Rainfall and surface kinematic conditions over central Amazonia during ABLE 2B', *J. Geophys. Res.*, 95, 17001-17014.

Harriss, R., Wofsy, S., Garstang, M., Browell, E., Molion, L., McNeal, R., Hoell, J., Bendura, R., Beck, S., Navarro, R., Riley, J., and Snell, R.: 1988, 'The Amazon Boundary Layer Experiment (ABLE 2A): Dry season', *J. Geophys. Res.*, 93, 1351-1360.

Harriss, R., Garstang, M., Wofsy, S., Beck, S., Bendura, R., Coelho, J., Drewry, J., Hoell, J., Matson, P., McNeal, R., Molion, L., Navarro, R., Rabine, V., and Snell, R.: 1990, 'The Amazon Boundary Layer Experiment: Wet season 1987', *J. Geophys. Res.*, 95, 16721-16736.

Hoecker, W.H.: 1963, 'Three southerly low-level jet systems

delineated by the Weather Bureau special pibal network', *Mon. Wea. Rev.*, 91, 573-582.

Hoecker, W.H.: 1965, 'Comparative physical behavior of southerly boundary-layer wind jets', *Mon. Wea. Rev.*, 93, 133-144.

Hsu, S.A.: 1979, 'Mesoscale nocturnal jet-like winds within the planetary boundary layer over a flat, open coast', *Bound.-Layer Meteor.*, 17, 485-494.

Kousky, V.E.: 1979, 'Frontal influence on northeast Brazil', *Mon. Wea. Rev.*, 107, 1140-1153.

Kousky, V.E., and Ferreira, N.J.: 1981, 'Interdiurnal surface pressure variation in Brazil: Their spatial distributions, origins and effects', *Mon. Wea. Rev.*, 109, 1999-2008.

Kousky, V.E., and Kagano, M.: 1981, 'A climatological study of the tropospheric circulation over the Amazon region', *Acta Amazonica*, 11, 743-758.

Kraus, H., Malcher, J., and Schaller, E.: 1985, 'A nocturnal low-level wind during PUKK', *Bound.-Layer Meteor.*, 31, 187-195.

Lettau, H.H.: 1967, 'Small to large-scale features of boundary layer structure over mountain slopes', *Proc. Symp. Mount. Meteor.*, Atmos. Sci. Paper No. 122, Colorado State University.

Lettau, H.H.: 1983, 'Thoughts on priorities in boundary-layer research', *Bound.-Layer Meteor.*, 25, 429-432.

Mahrt, L.: 1981, 'The early evening boundary layer transition',

Quart. J. Roy. Meteor. Soc., 107, 329-343.

McNider, R., and Pielke, R.: 1981, 'Diurnal boundary-layer development over sloping terrain', *J. Atmos. Sci.*, 38, 2198-2210.

Nobre, C.A., Silva Dias, P., dos Santos, M.A.R., Cohen, J., da Rocha, J.P., Guedes, R., Ferreira, R., and dos Santos, J.A.: 1987, 'Mean large scale meteorological aspects of ABLE 2B', Paper presented at Spring AGU Meeting, Baltimore, MD.

Oliveira, A.P.: 1990, 'Planetary boundary layer dynamics over the Amazon rain forest', PhD dissertation, College of Sciences and Mathematics, Department of Atmospheric Sciences, State University of New York at Albany, 295 pp.

Paegle, J.: 1987, 'Interactions between convective and large-scale motions over Amazonia', In *The Geophysiology of Amazonia: Vegetation and Climate Interactions,* R. Dickerson (ed.), Wiley Intersciences, New York, 347-390.

Paegle, J., and Rasch, G.E.: 1973, 'Three-dimensional characteristics of diurnally varying boundary-layer flows', *Mon. Wea. Rev.*, 101, 746-755.

Salati, E., and Vose, P.B.: 1984, 'Amazon basin: A system in equilibrium', *Science,* 225, 129-138.

Shuttleworth, W.J., Gash, J., Lloyd, J., Moore, C.J., Robert, C.J., Filho, A., Fisch, G., Filho, V., Ribeiro, M., Molion, L., Sa de Abreu, L., Nobre, C., Cabral, O.M.R., Pitel, S.R.,

and Moraes, J.C.: 1984, 'Eddy correlation measurements of energy partition for Amazonia forest', *Quart. J. Roy. Meteor. Soc.*, 110, 1143-1160.

Shuttleworth, W.J., et al.: 1985, 'Daily variations of temperature and humidity within and above Amazonian forest', *Weather*, 40, 102-108.

Silva Dias, P., Benatti, J.P., and Kousky, V.: 1987, 'Diurnally forced tropical tropospheric circulation over South America', *Mon. Wea. Rev.*, 115, 1465-1478.

Thorpe, A.J., and Guymer, T.H.: 1977, 'The nocturnal jet', *Quart. J. Roy. Meteor. Soc.*, 103, 633-653.

Virji, H.: 1981, 'A preliminary study of summertime tropospheric circulation patterns over South America estimated from cloud winds', *Mon. Wea. Rev.*, 109, 599-610.

Wexler, H.: 1961, 'A boundary layer interpretation of the low-level jet', *Tellus*, 13, 368-378.

Wippermann, F.: 1973, 'Numerical study on the effects controlling the low-level jet', *Beitr. Phys. Atmos.*, 46, 137-154.

Zeman, O.: 1979, 'Parameterization of the dynamics of stable boundary layer and nocturnal jets', *J. Atmos. Sci.*, 36, 792-804.

List of Figures

wind speed measured by tethersonde at Ducke during May 5, 1987. Height is in meters above ground level.

Figure 12: Same as Figure 11, but for May 5-6, 1987.

Figure 13: Vertical profiles of (a) temperature and (b) wind speed measured by tethersonde at Carapaña during May 5-6, 1987. Height is in meters above ground level.

Figure 14: Time-height contours of rawinsonde measured wind direction at Ducke during (a) May 5-6, 1987, (b) May 6-7, 1987, and (c) May 7-8, 1987.

Figure 15: ABLE 2B daily time-series composite of the temperature (solid) and pressure (dashed) differences between Ducke and Carapaña (D-C) as measured by the PAM towers. Pressure and temperature values were recorded every minute.

Figure 16: Daily time-series of the pressure difference between Ducke and Carapaña (D-C) as measured by the PAM towers on (a) May 5, 1987, (b) May 6, 1987, (c) May 7, 1987, and (d) May 8, 1987.

Table I

Average wind speed values in the 1000-900 mb layer as measured by near-coincident tethersondes and rawinsondes at Ducke during ABLE 2A. Several times are given and a mean difference is calculated.

	#	Rawinsonde ($\bar{R}$ in m s^{-1})	Tethersonde ($\bar{T}$ in m s^{-1})	$\overline{T-R}$
1400 LST				
975 mb	12	2.9	3.9	1.0
950 mb	13	4.9	4.4	-0.5
925 mb	13	4.7	4.7	0.1
900 mb	11	5.6	6.4	0.8
2000 LST				
975 mb	4	3.5	8.0	4.6
950 mb	6	7.0	8.6	1.5
925 mb	6	7.8	9.1	1.2
900 mb	3	3.7	8.8	5.6
0200 LST				
975 mb	5	2.4	8.2	5.8
950 mb	6	7.3	9.5	2.2
925 mb	6	8.0	10.5	2.5
900 mb	2	6.6	8.5	1.9
0800 LST				
975 mb	8	1.8	5.6	3.9
950 mb	11	4.1	6.6	2.6
925 mb	10	5.4	7.9	2.6
900 mb	9	5.0	9.1	3.6

Table II

Tethersonde-measured boundary layer temperature (°C) and wind conditions (m s^{-1} and degrees) at Ducke during 5 nights of ABLE 2A operation. Conditions are noted for the surface, inversion top (300 m) and 700 m.

a) **Temperature**

	7/25-7/26	7/26-7/27	7/30-7/31	7/31-8/1	8/1-8/2
1600 LST					
sfc temp	28.7	27.5	25.4	29.8	---
300 m temp	27.0	26.4	27.3	28.5	---
700 m temp	23.4	22.8	24.5	24.7	---
0000 LST					
sfc temp	22.1	22.7	23.9	22.7	22.2
300 m temp	23.2	23.3	26.4	26.7	26.0
700 m temp	23.1	21.7	23.7	23.9	24.2
0800 LST					
sfc temp	23.6	22.5	23.7	22.2	21.3
300 m temp	23.8	24.0	26.0	26.2	25.0
700 m temp	21.9	22.3	23.1	23.3	23.8
1200 LST					
sfc temp	26.4	28.3	29.4	---	30.6
300 m temp	24.6	26.7	27.7	---	28.8
700 m temp	21.8	23.1	23.9	---	24.7

b) **Wind**

	7/25-7/26	7/26-7/27	7/30-7/31	7/31-8/1	8/1-8/2
1600 LST					
sfc wind	2.4/84	1.1/106	1.1/95	4.2/94	---
300 m wind	3.8/106	3.1/70	7.3/98	6.3/114	---
700 m wind	4.7/111	2.6/25	12.0/87	7.0/95	---
0000 LST					
sfc wind	0.4/80	1.2/50	2.0/55	0.5/44	1.2/10
300 m wind	4.5/-	4.7/66	11.7/59	10.1/90	7.9/11
700 m wind	9.5/94	5.8/103	10.7/92	10.8/85	11.7/10
0800 LST					
sfc wind	2.3/45	2.1/52	3.4/50	0.6/80	0.6/344
300 m wind	6.3/50	8.4/44	11.9/74	10.6/90	7.4/345
700 m wind	8.5/93	8.7/63	12.0/80	8.8/96	9.5/0
1200 LST					
sfc wind	4.1/26	2.6/130	5.3/120	---	4.5/150
300 m wind	5.1/30	3.8/148	3.8/48	---	7.5/136
700 m wind	7.5/33	4.1/90	4.1/90	---	7.9/135

Table III

Observed pressure gradients and wind accelerations along with predicted values of total wind acceleration, acceleration by the pressure gradient force, and deceleration by friction. Computed using the simplified model proposed in Section 4.

	May 5-6	May 6-7	May 7-8
Ave. nocturnal ΔP	.15 mb	.25 mb	.20 mb
Ave. nocturnal wind	11 m s^{-1}	11 m s^{-1}	6 m s^{-1}
a	2.8×10^{-5} s^{-1}	4.7×10^{-5} s^{-1}	6.9×10^{-5} s^{-1}
Observed Day/Nite dv/dt	5 m s^{-1} in 4 h	5 m s^{-1} in 4 h	3 m s^{-1} in 4 h
Ave. ΔP during wind acceleration (WA)	.30 mb	.30 mb	.20 mb
$\overline{V}$ during WA	7 m s^{-1}	7.5 m s^{-1}	5 m s^{-1}
Accel. by PGF (in 4 h)	9 m s^{-2}	9 m s^{-2}	6 m s^{-2}
Damping by Fric. (in 4 h)	4.7 m s^{-2}	5.1 m s^{-2}	3.4 m s^{-2}
Calculated dv/dt (in 4 h)	4.3 m s^{-2}	3.9 m s^{-2}	2.6 m s^{-2}

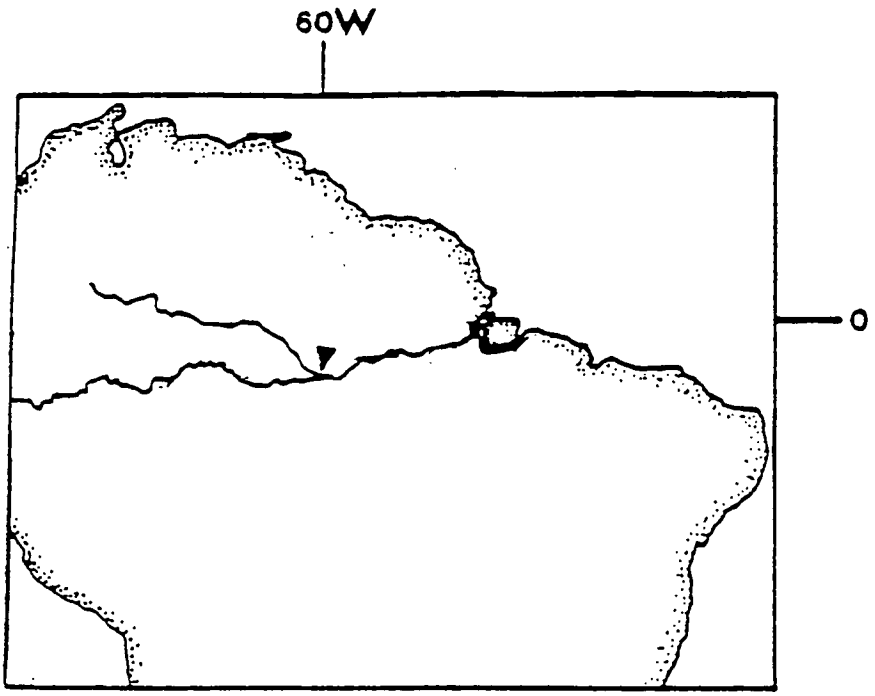
60W
0

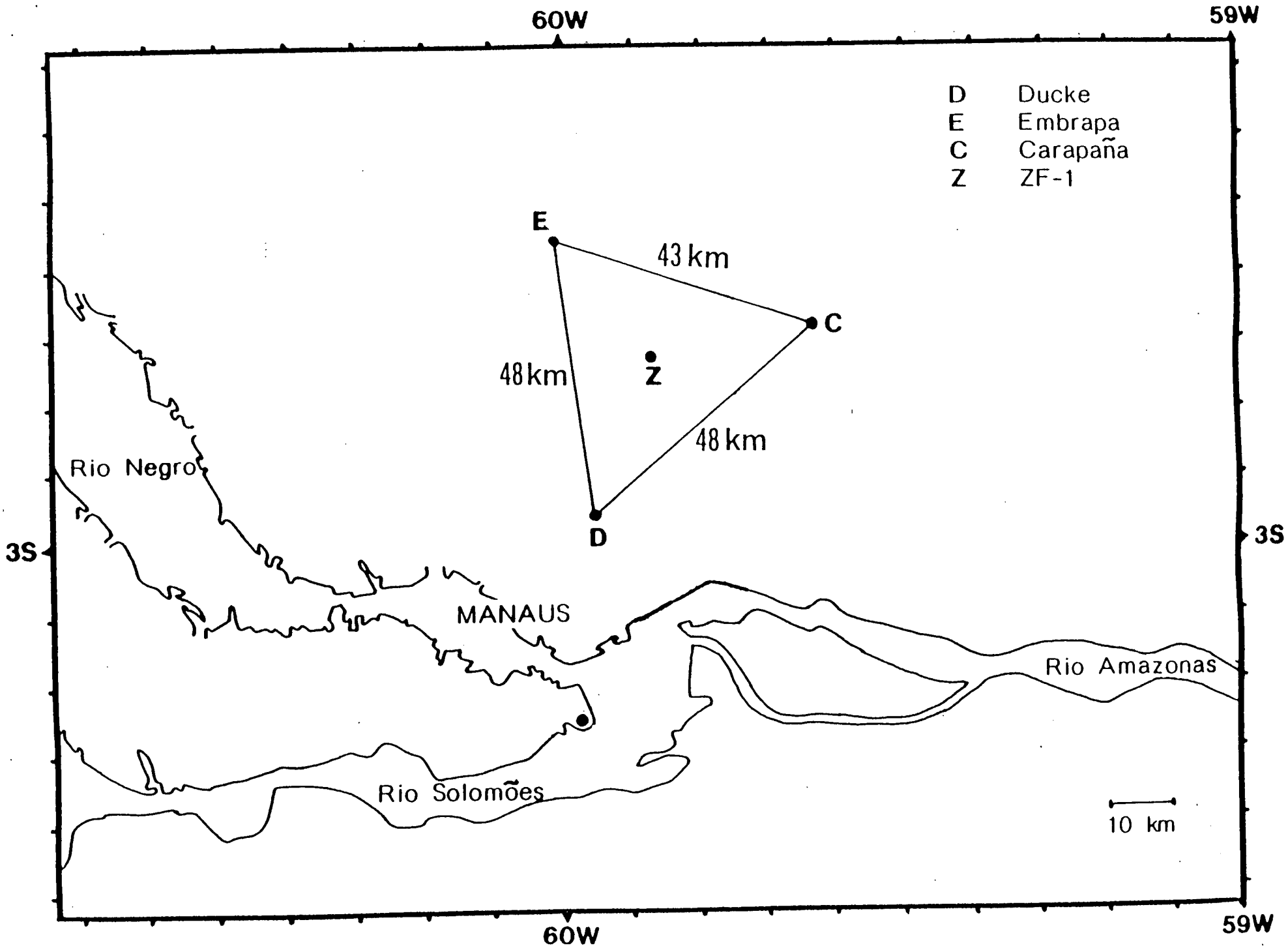
60W
59W
D Ducke
E Embrapa
C Carapaña
Z ZF-1
E
43 km
C
48 km
Z
48 km
D
Rio Negro
3S
MANAUS
Rio Amazonas
Rio Solomões
10 km
60W
59W

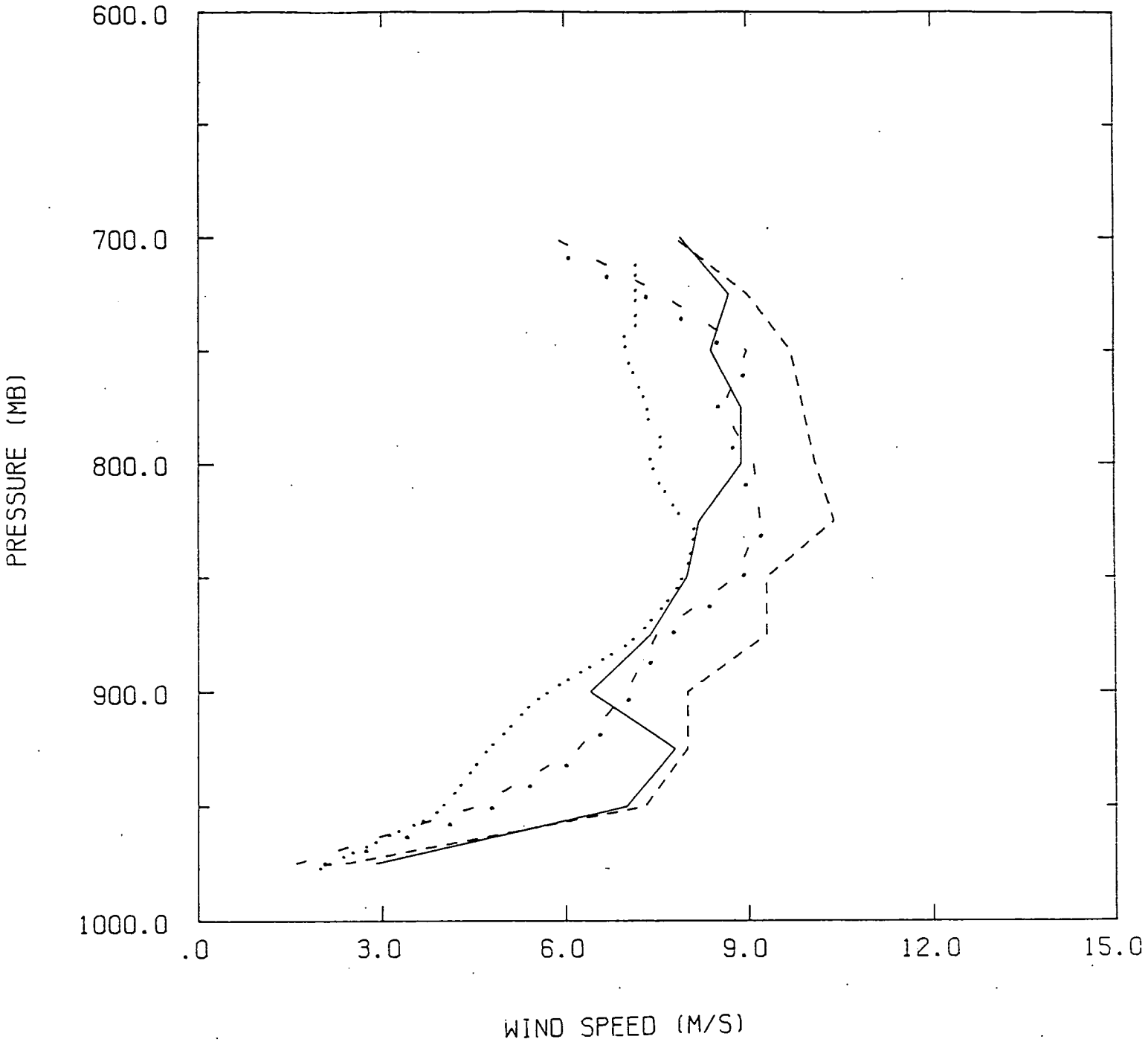
600.0
700.0
800.0
900.0
1000.0
PRESSURE (MB)
.0
3.0
6.0
9.0
12.0
15.0
WIND SPEED (M/S)

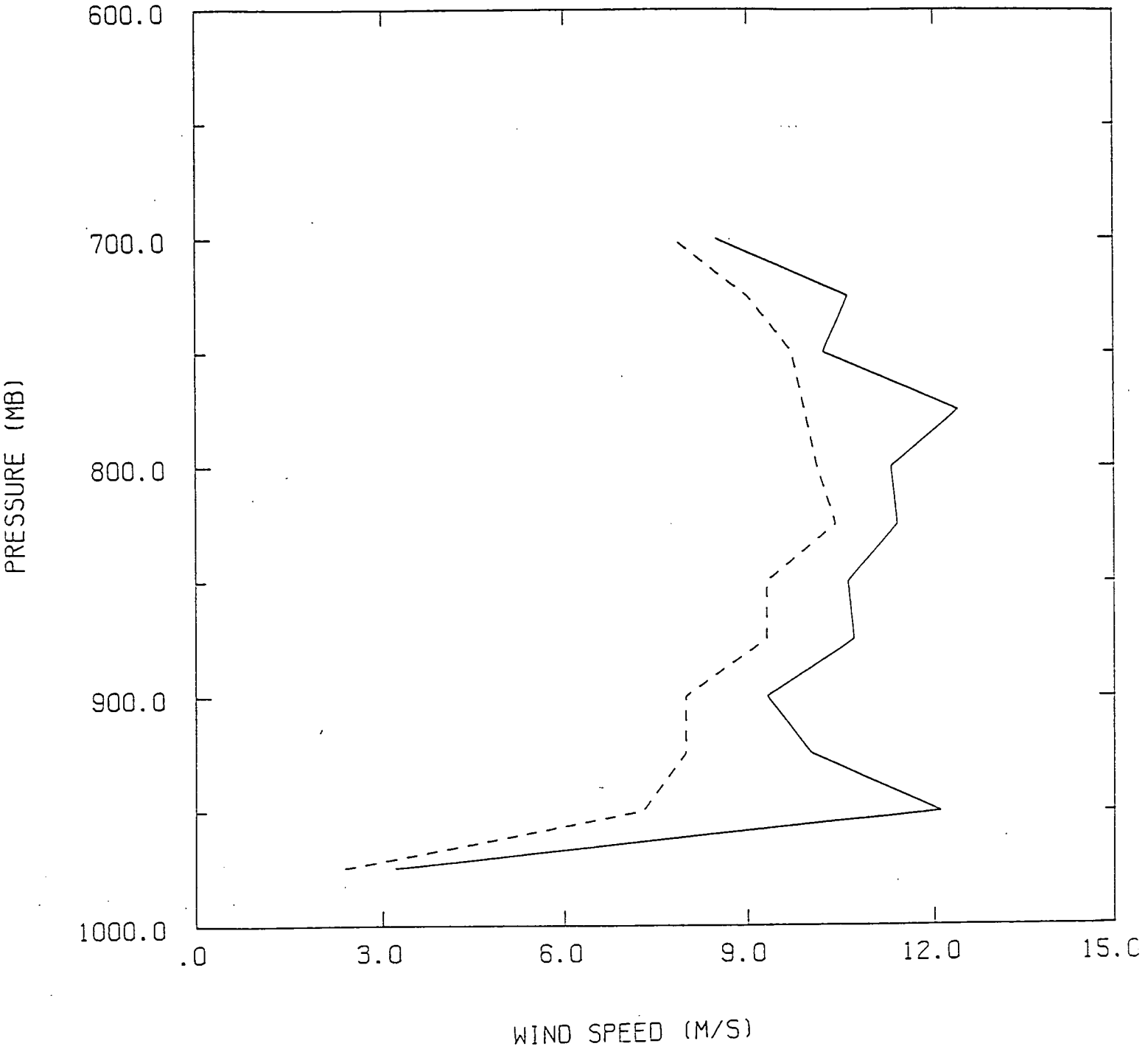
600.0
700.0
800.0
900.0
1000.0
PRESSURE (MB)
.0
3.0
6.0
9.0
12.0
15.0
WIND SPEED (M/S)

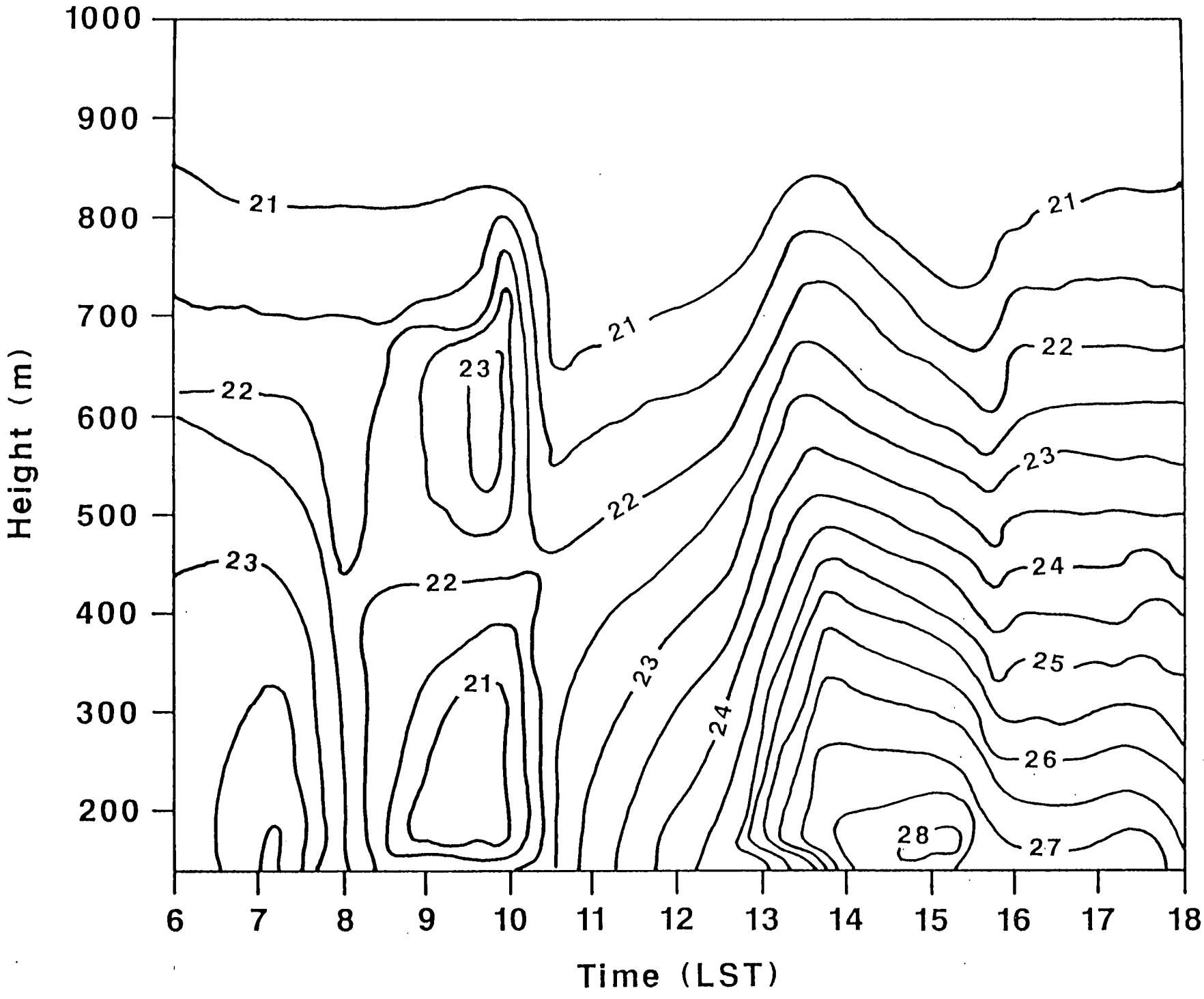
1000
900
800
700
600
500
400
300
200
Height (m)
6
7
8
9
10
11
12
13
14
15
16
17
18
Time (LST)
21
22
23
24
25
26
27
28

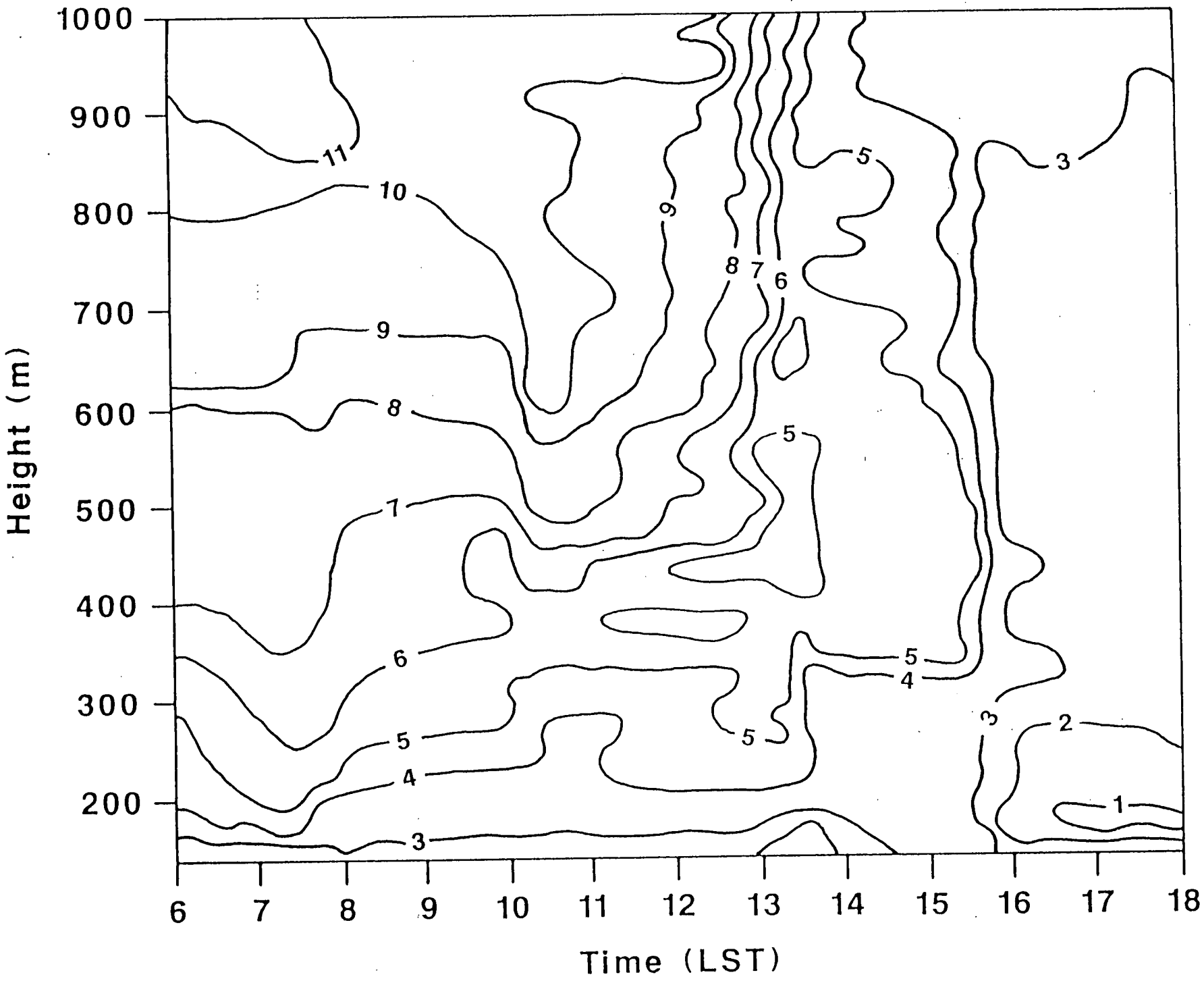
1000
900
800
700
600
500
400
300
200
Height (m)
6
7
8
9
10
11
12
13
14
15
16
17
18
Time (LST)
11
10
9
8
7
6
5
3
9
8
5
7
6
5
4
5
4
3
5
3
2
1

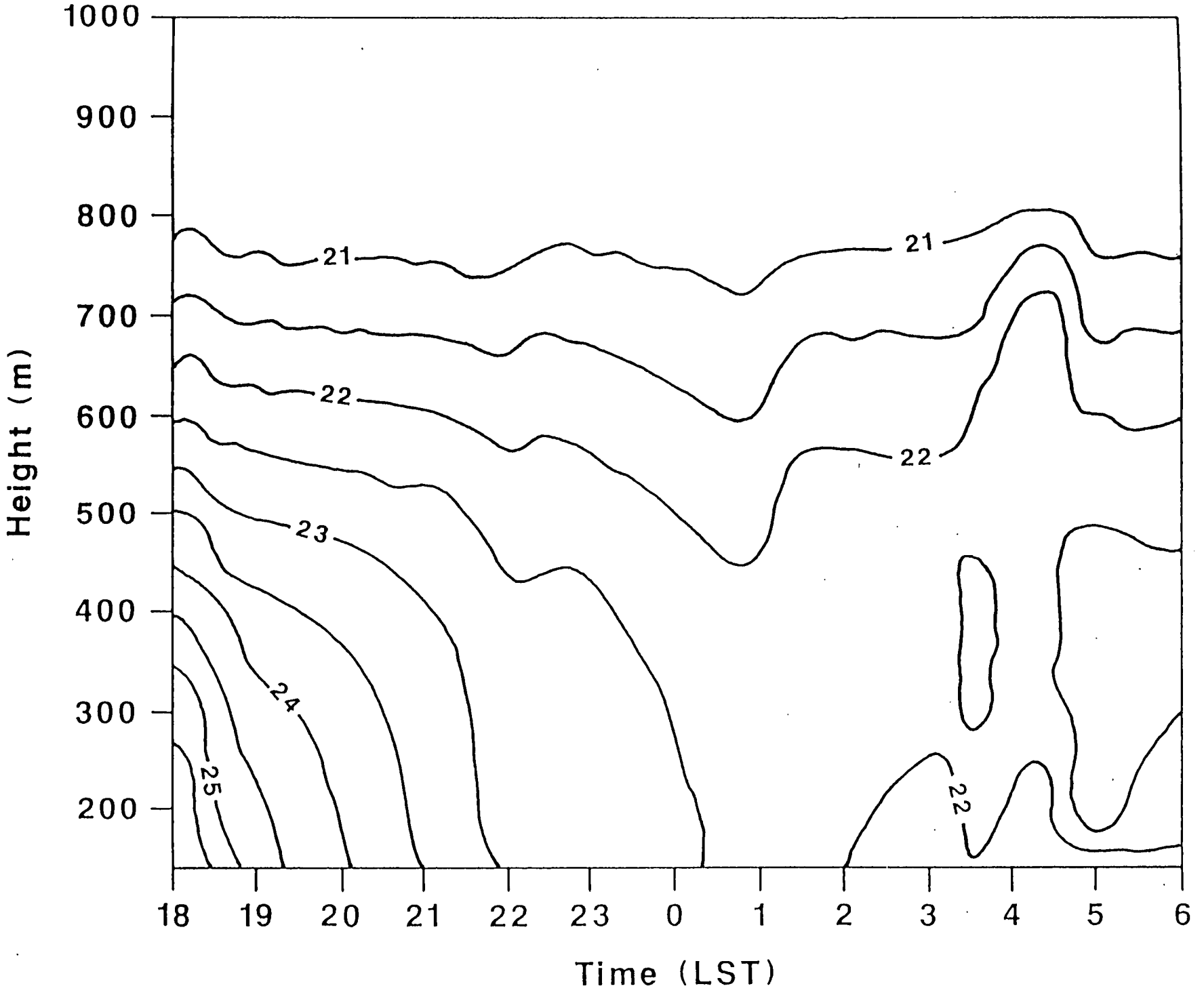
1000
900
800
700
600
500
400
300
200
Height (m)
21
21
22
22
23
24
25
22
18
19
20
21
22
23
0
1
2
3
4
5
6
Time (LST)

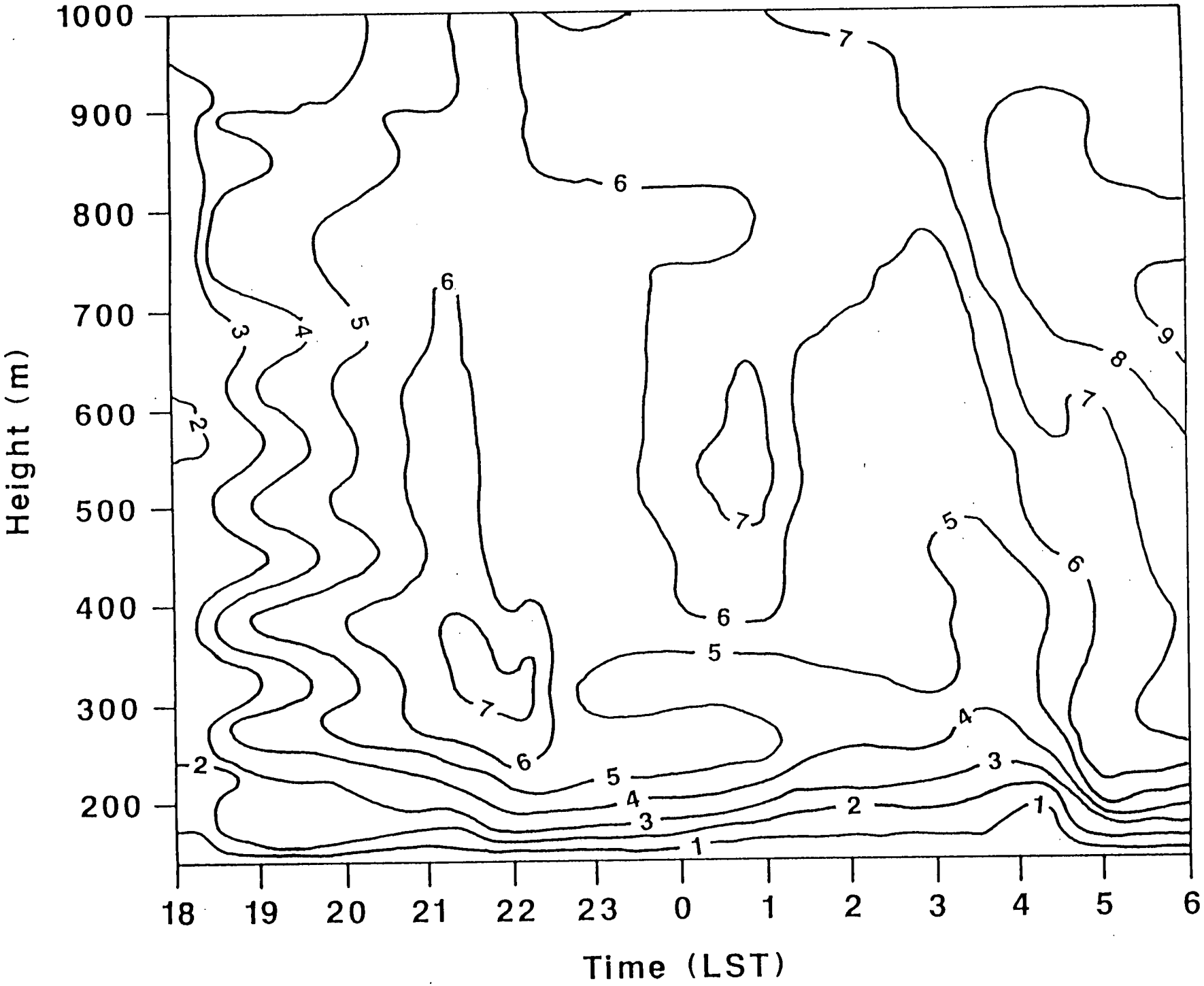
1000
900
800
700
600
500
400
300
200
Height (m)
18
19
20
21
22
23
0
1
2
3
4
5
6
Time (LST)

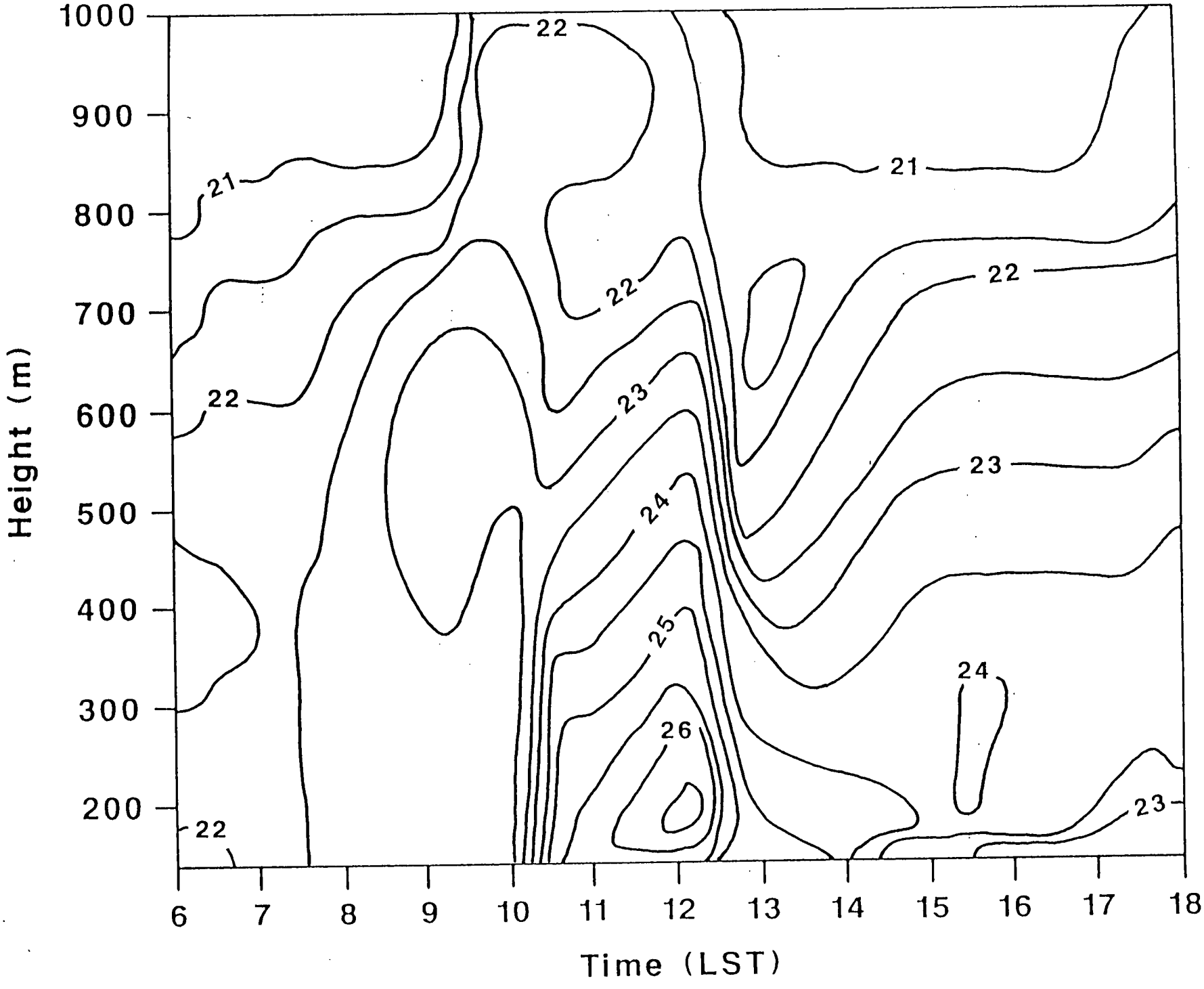
1000
900
800
700
600
500
400
300
200
Height (m)
6
7
8
9
10
11
12
13
14
15
16
17
18
Time (LST)
21
22
23
24
25
26

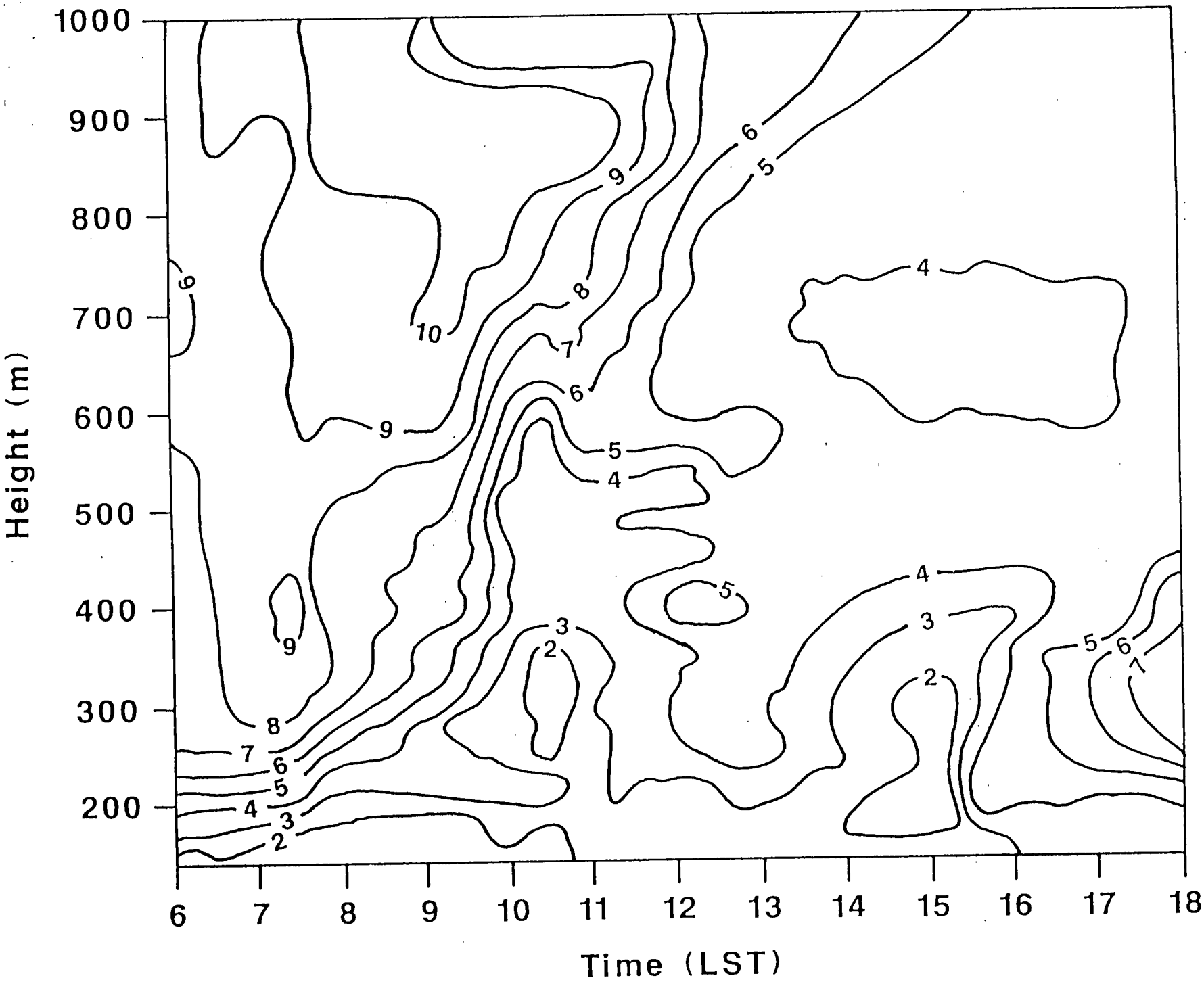
1000
900
800
700
600
500
400
300
200
Height (m)
6
7
8
9
10
11
12
13
14
15
16
17
18
Time (LST)

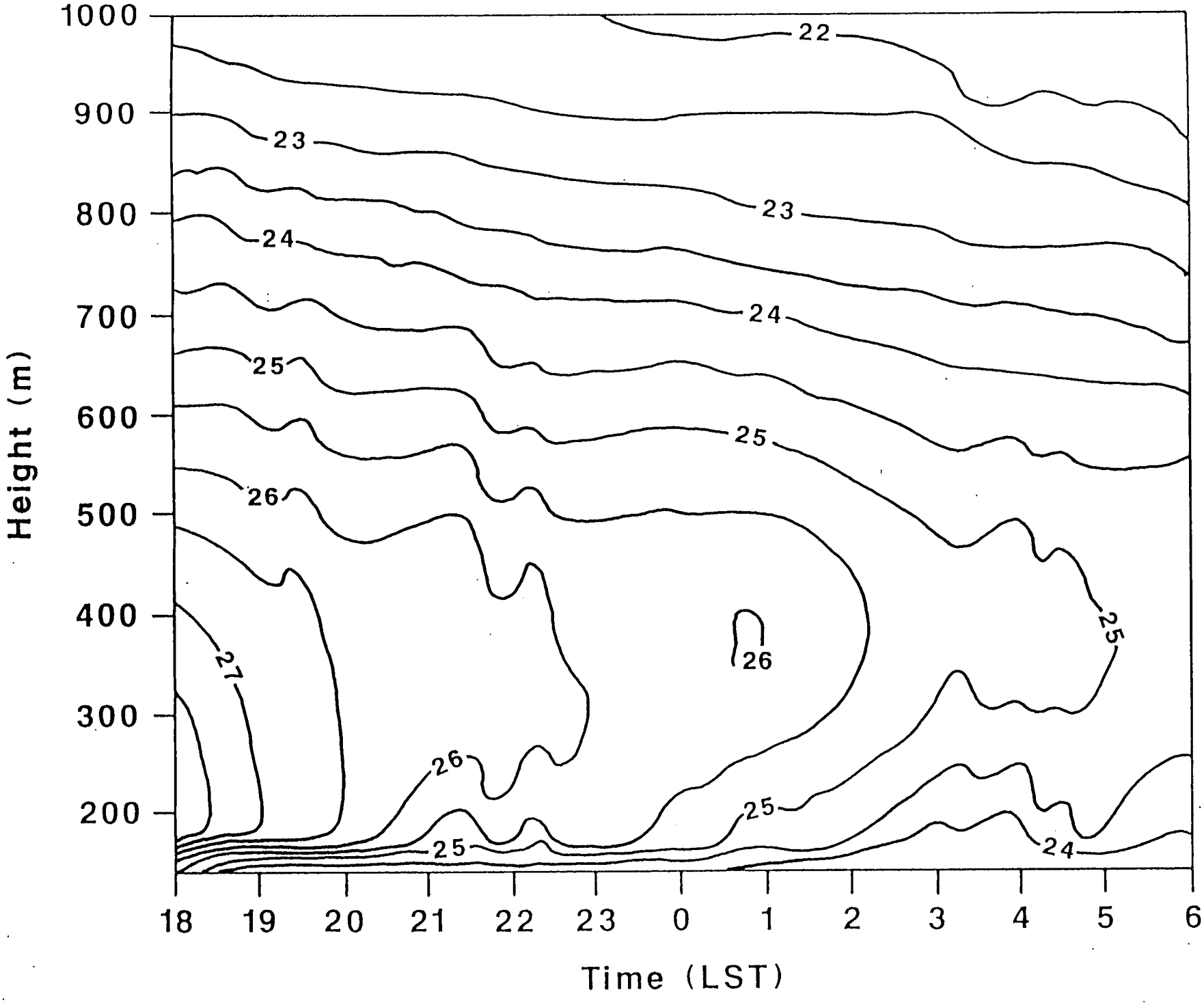
1000
900
800
700
600
500
400
300
200
Height (m)
22
23
23
24
24
25
25
26
26
27
26
25
25
24
25
18
19
20
21
22
23
0
1
2
3
4
5
6
Time (LST)

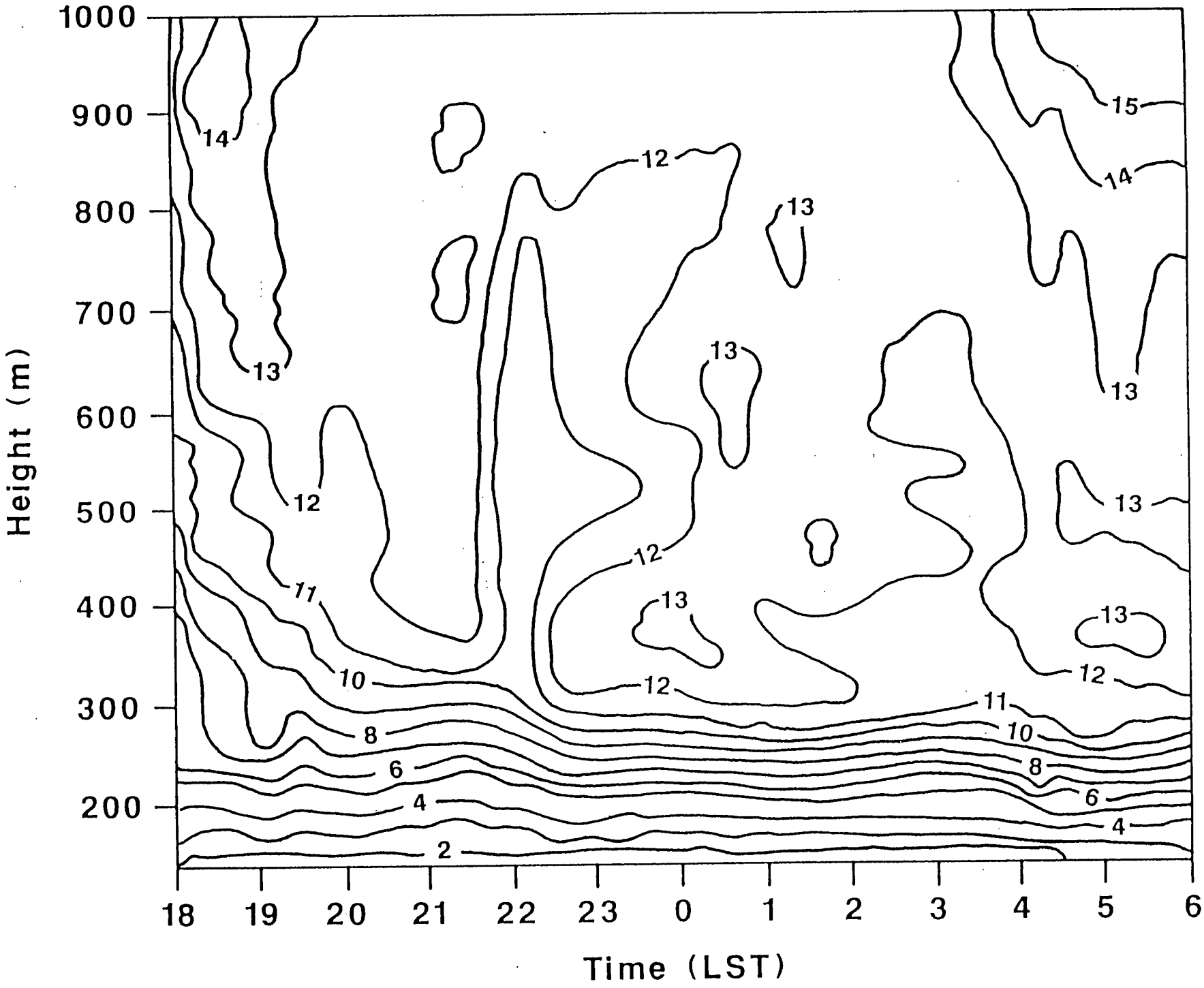
1000
900
800
700
600
500
400
300
200
Height (m)
18
19
20
21
22
23
0
1
2
3
4
5
6
Time (LST)
14
13
12
13
13
15
14
13
12
13
12
11
13
13
12
10
12
11
10
8
8
6
6
4
4
2

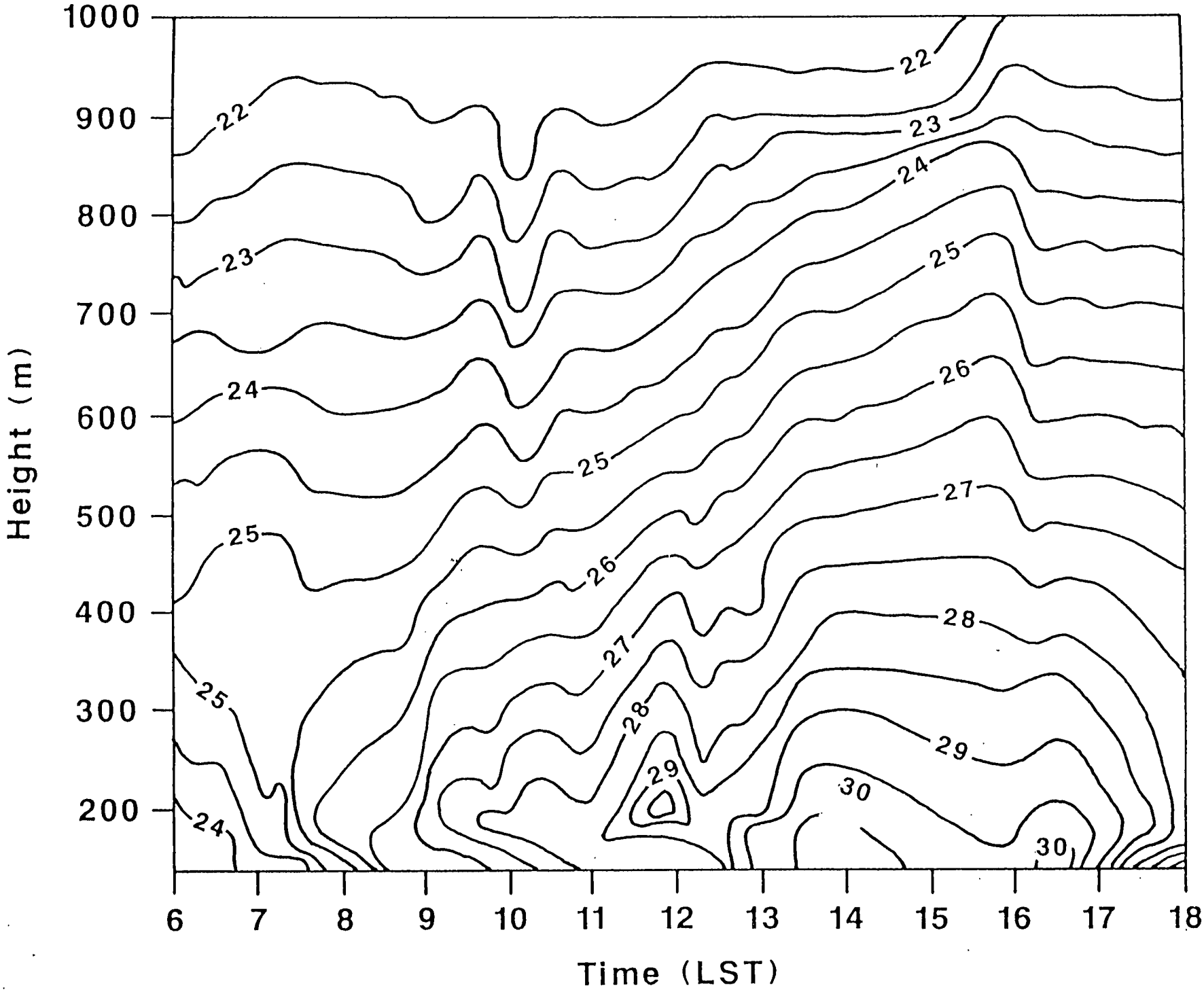
1000
900
800
700
600
500
400
300
200
Height (m)
6
7
8
9
10
11
12
13
14
15
16
17
18
Time (LST)
22
23
24
25
26
27
28
29
30

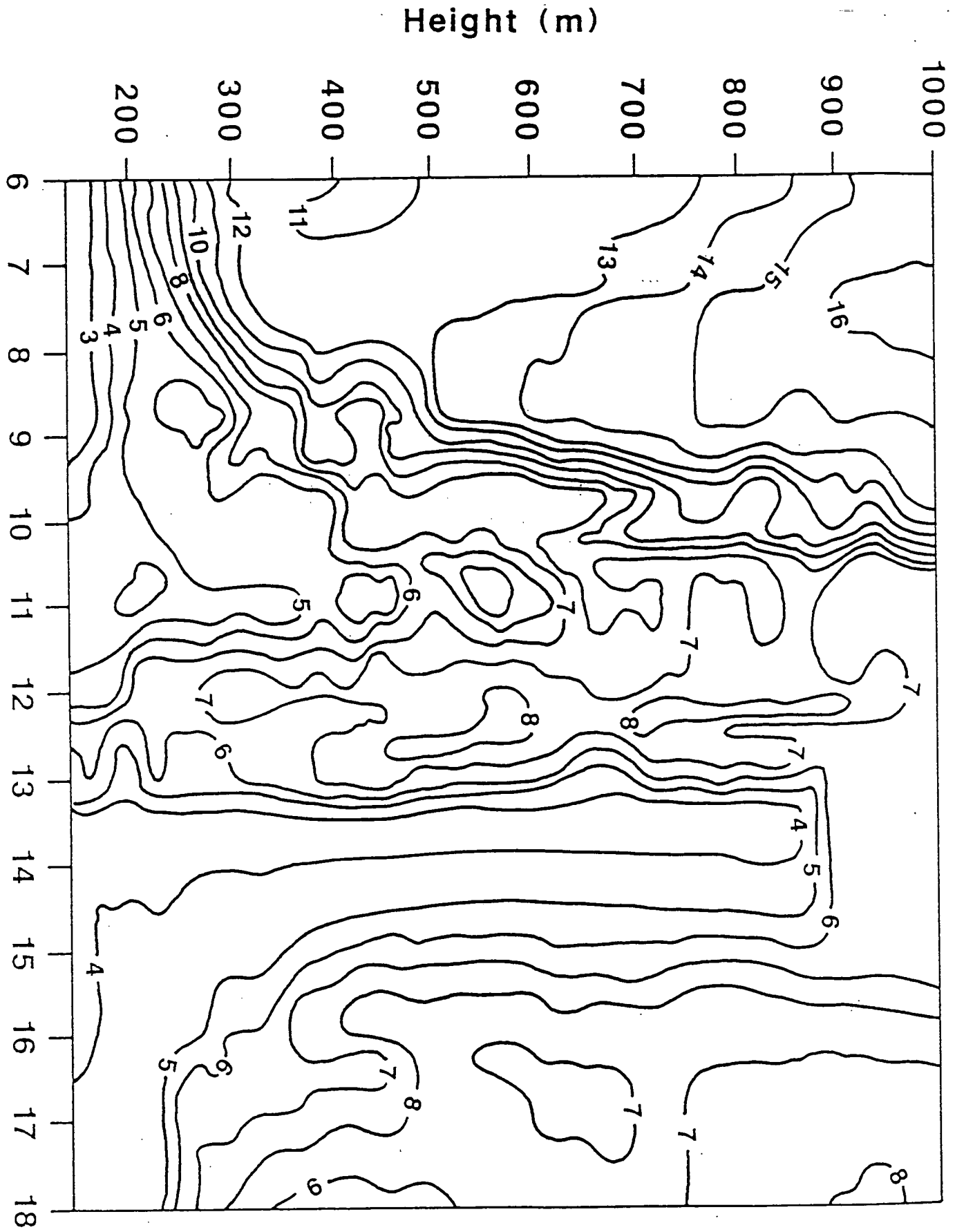
Height (m)
1000
900
800
700
600
500
400
300
200
6
7
8
9
10
11
12
13
14
15
16
17
18
Time (LST)

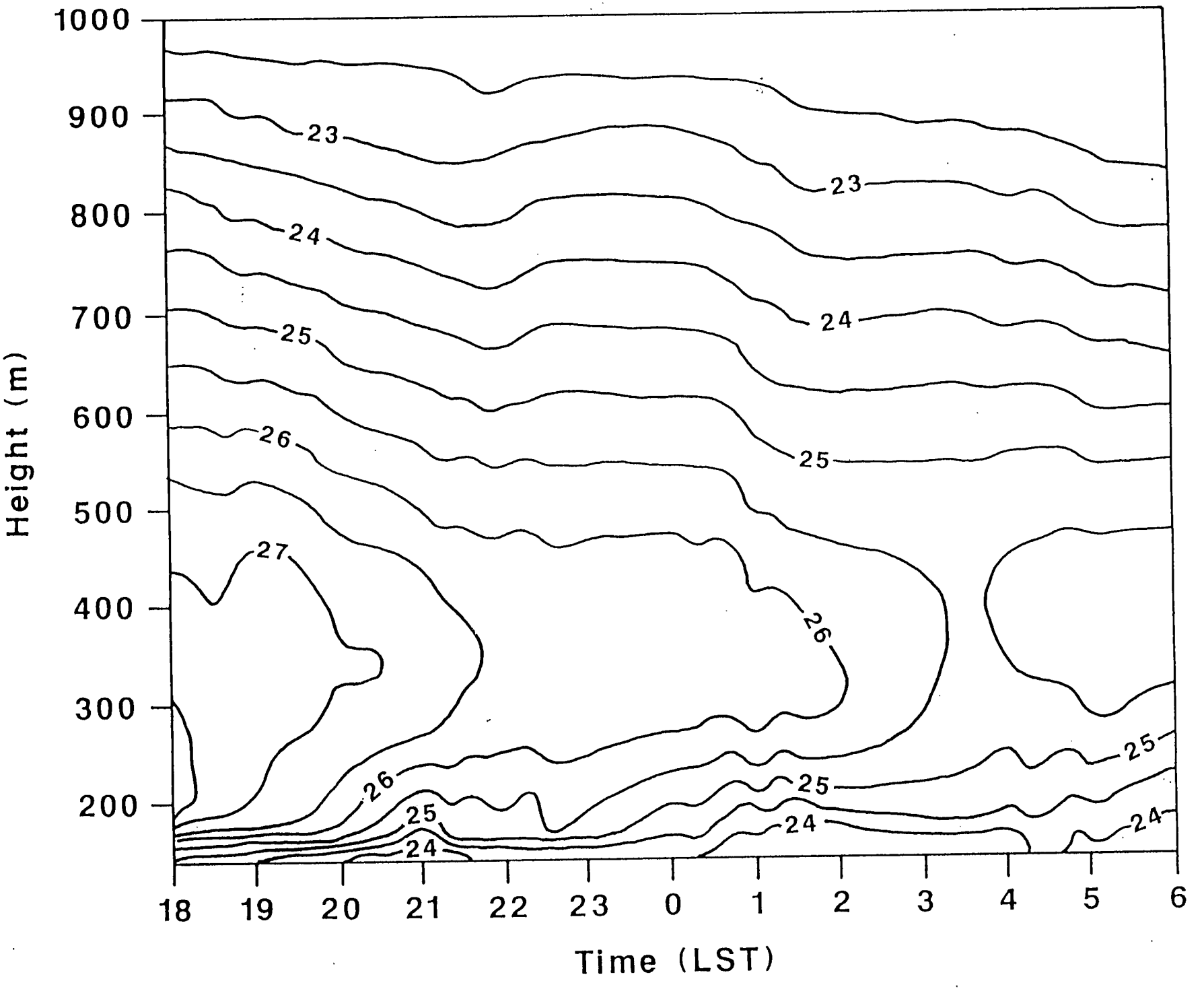
1000
900
800
700
600
500
400
300
200
Height (m)
23
23
24
24
25
25
26
26
27
25
26
25
25
24
24
18
19
20
21
22
23
0
1
2
3
4
5
6
Time (LST)

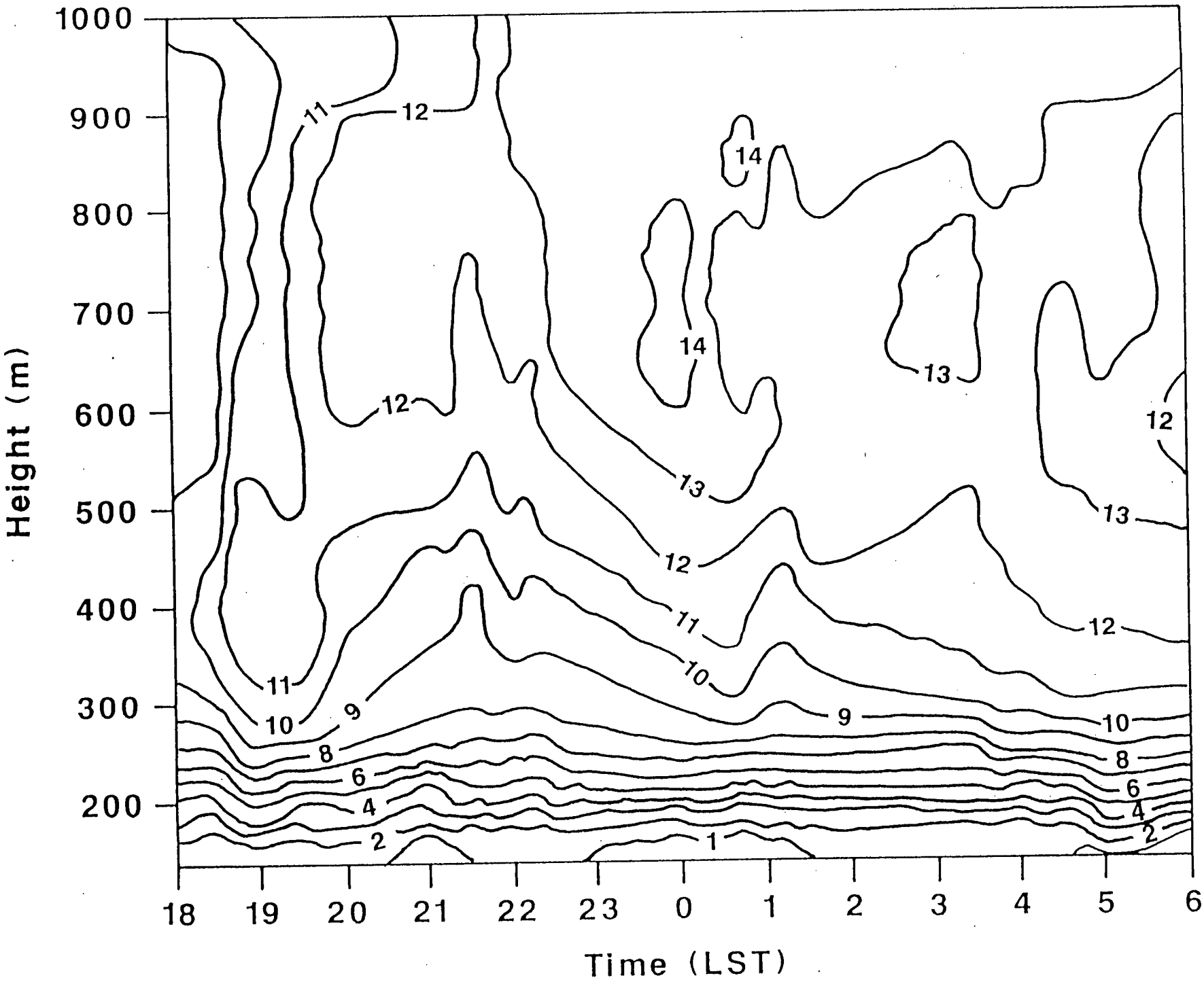
1000
900
800
700
600
500
400
300
200
Height (m)
18
19
20
21
22
23
0
1
2
3
4
5
6
Time (LST)
11
12
14
13
10
9
8
6
4
2
1

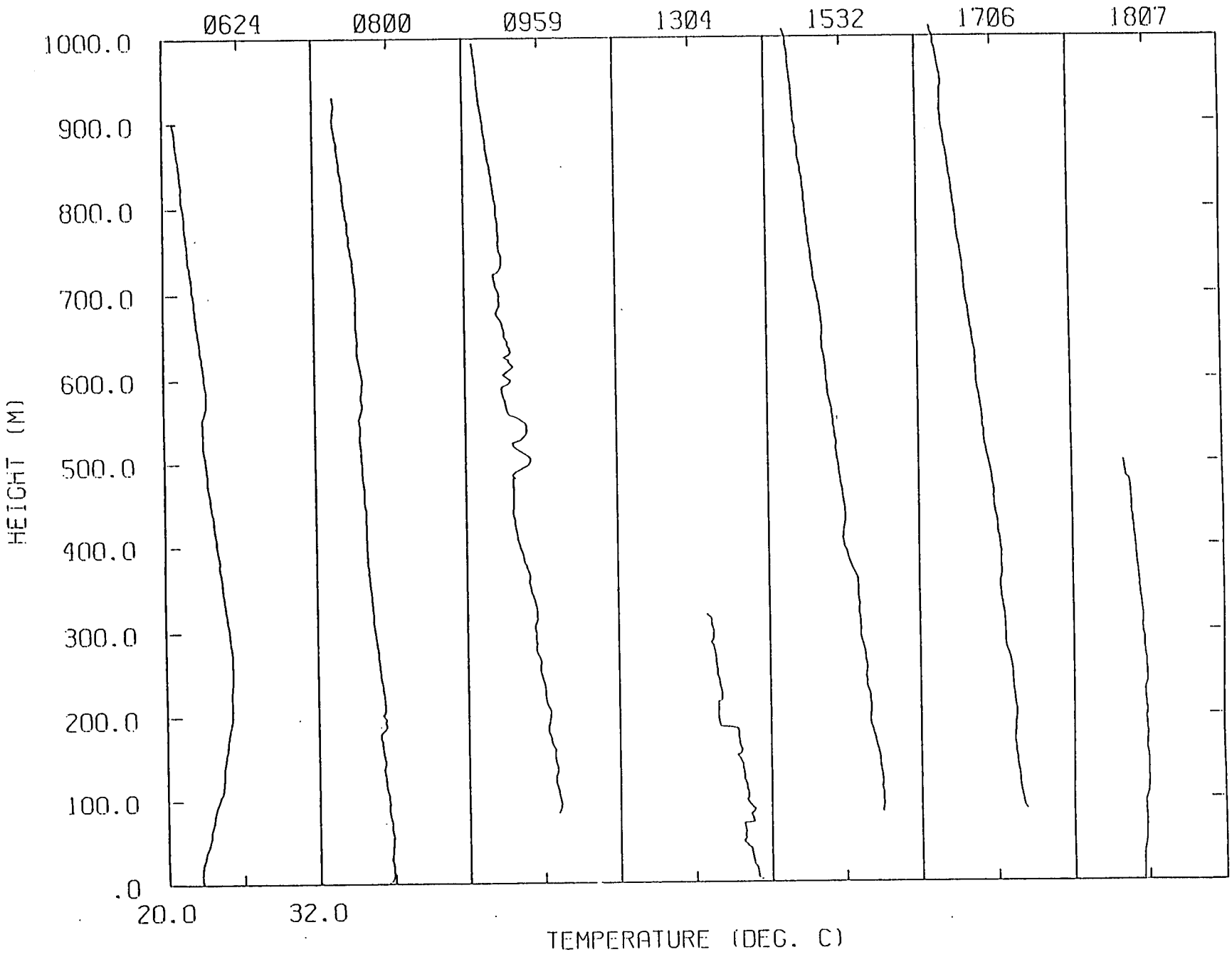
0624
0800
0959
1304
1532
1706
1807
1000.0
900.0
800.0
700.0
600.0
500.0
400.0
300.0
200.0
100.0
.0
HEIGHT (M)
20.0
32.0
TEMPERATURE (DEG. C)

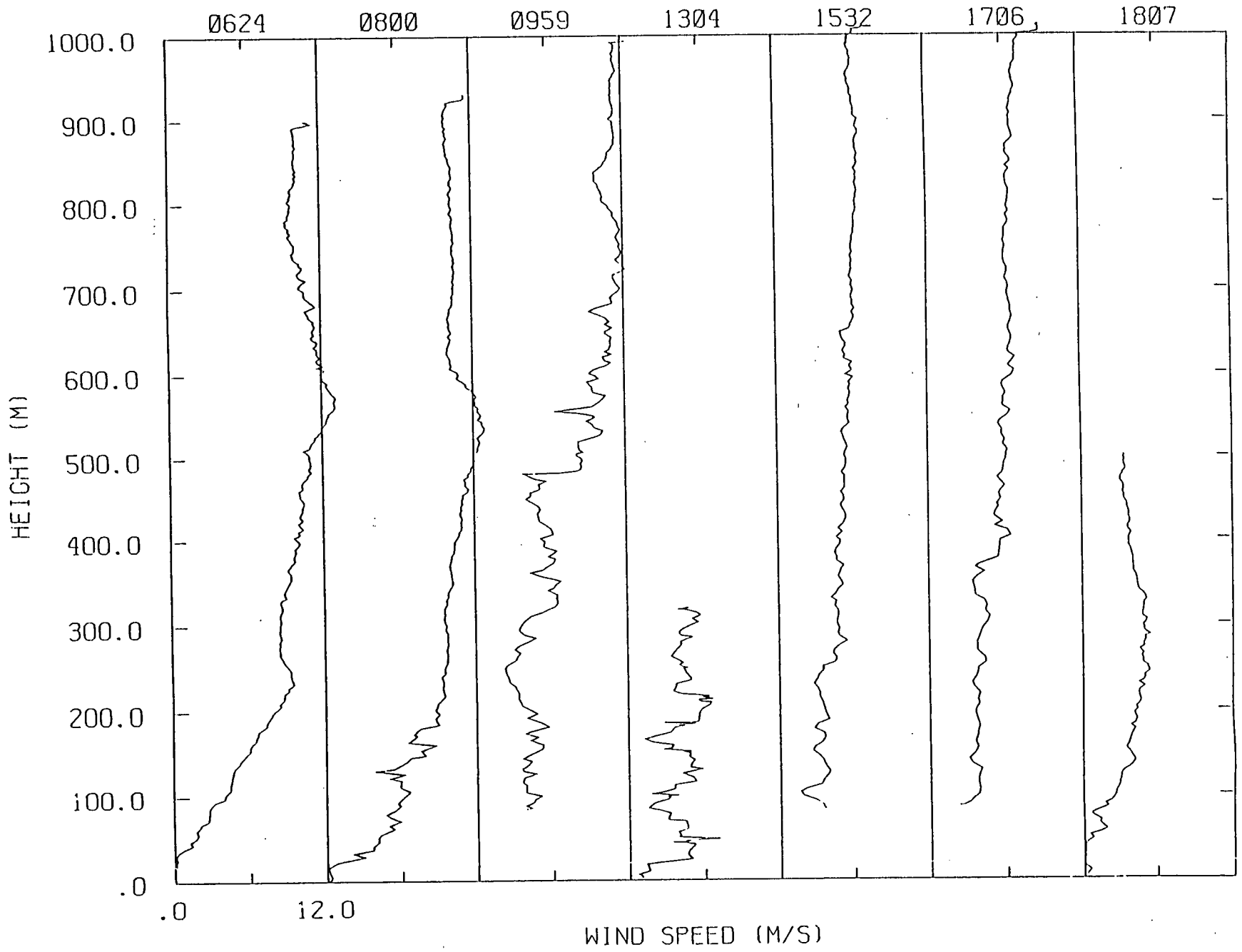
0624
0800
0959
1304
1532
1706
1807
1000.0
900.0
800.0
700.0
600.0
500.0
400.0
300.0
200.0
100.0
.0
HEIGHT (M)
.0
12.0
WIND SPEED (M/S)

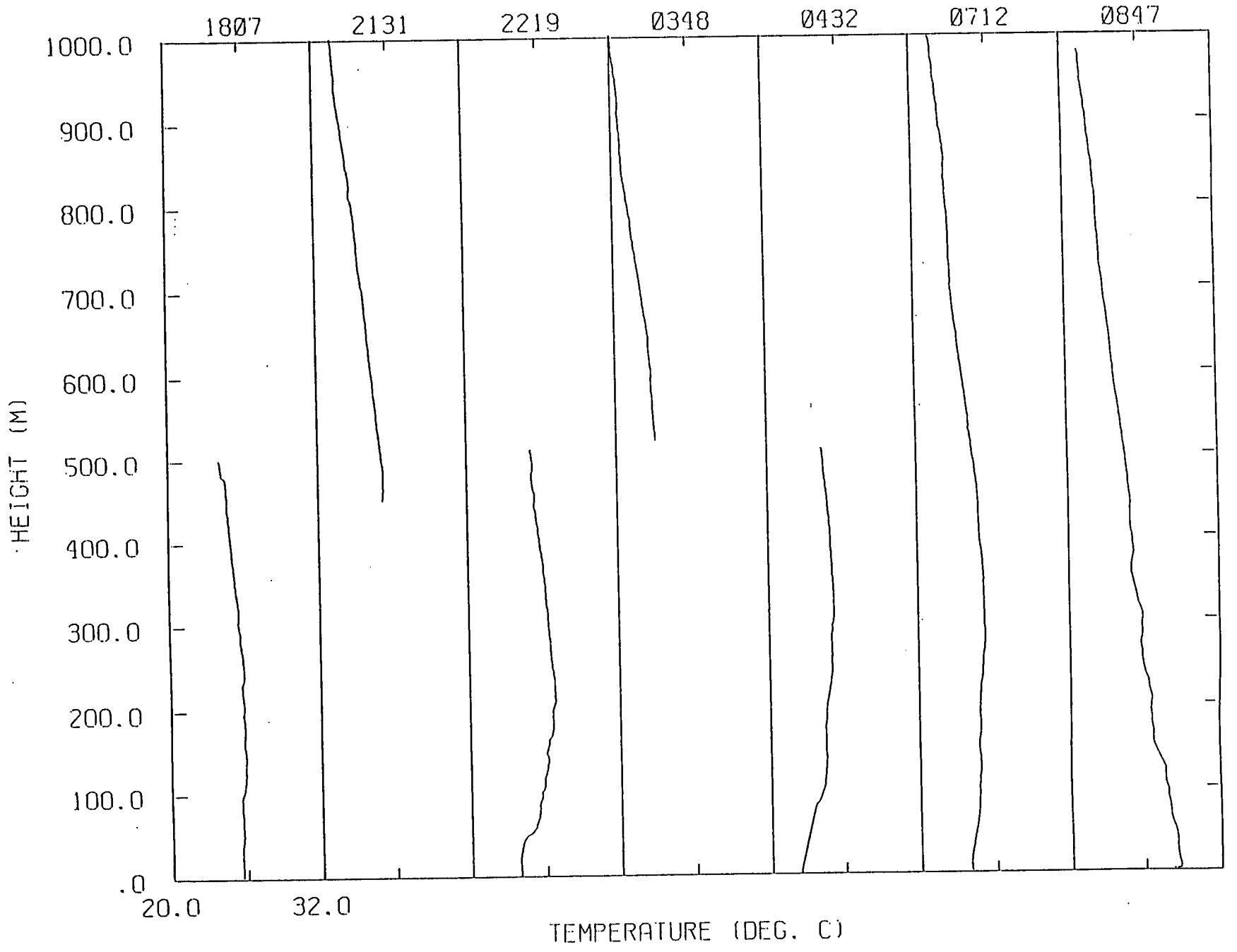
1807
2131
2219
0348
0432
0712
0847
1000.0
900.0
800.0
700.0
600.0
500.0
400.0
300.0
200.0
100.0
.0
HEIGHT (M)
20.0
32.0
TEMPERATURE (DEG. C)

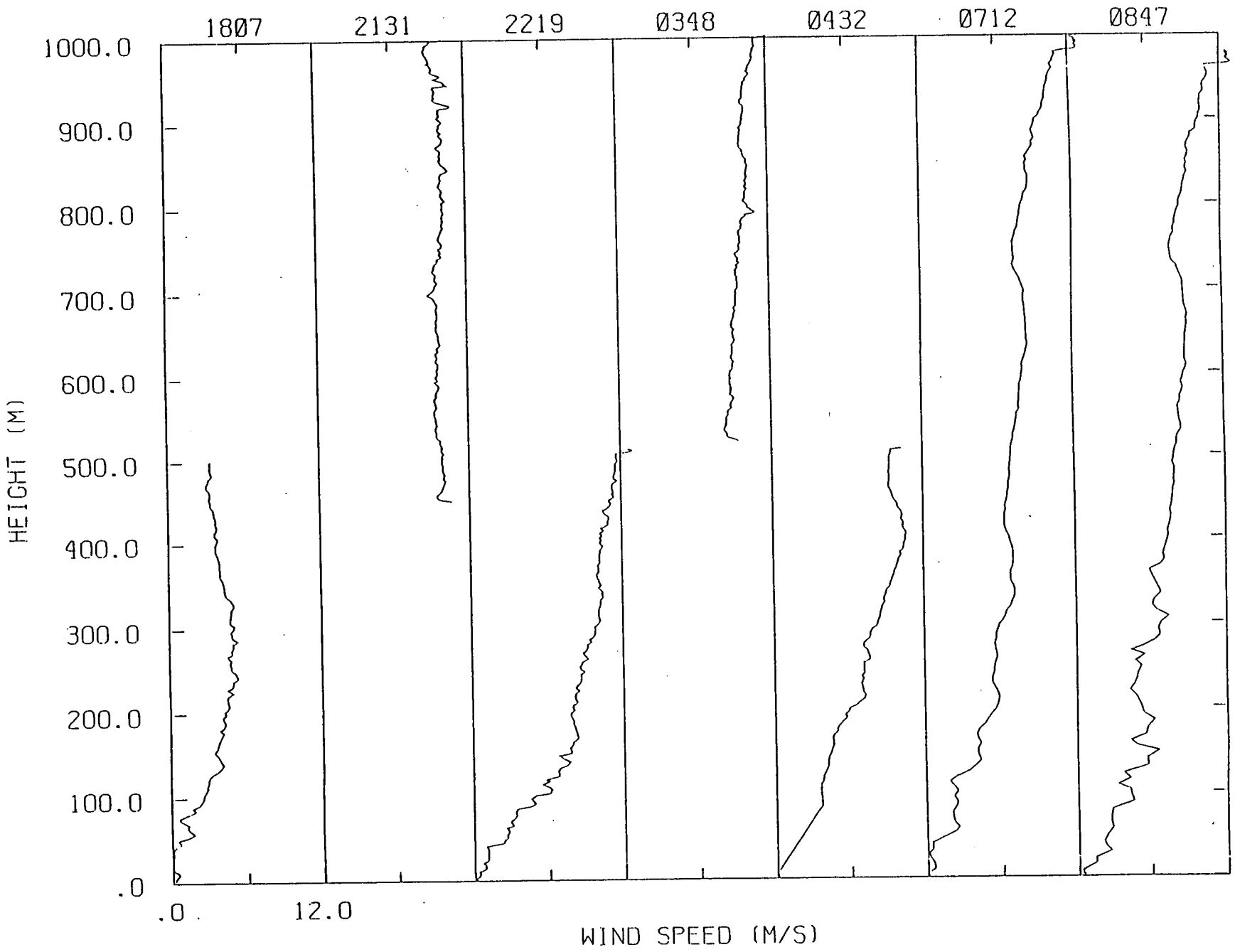
1807
2131
2219
0348
0432
0712
0847
1000.0
900.0
800.0
700.0
600.0
500.0
400.0
300.0
200.0
100.0
.0
HEIGHT (M)
.0
12.0
WIND SPEED (M/S)

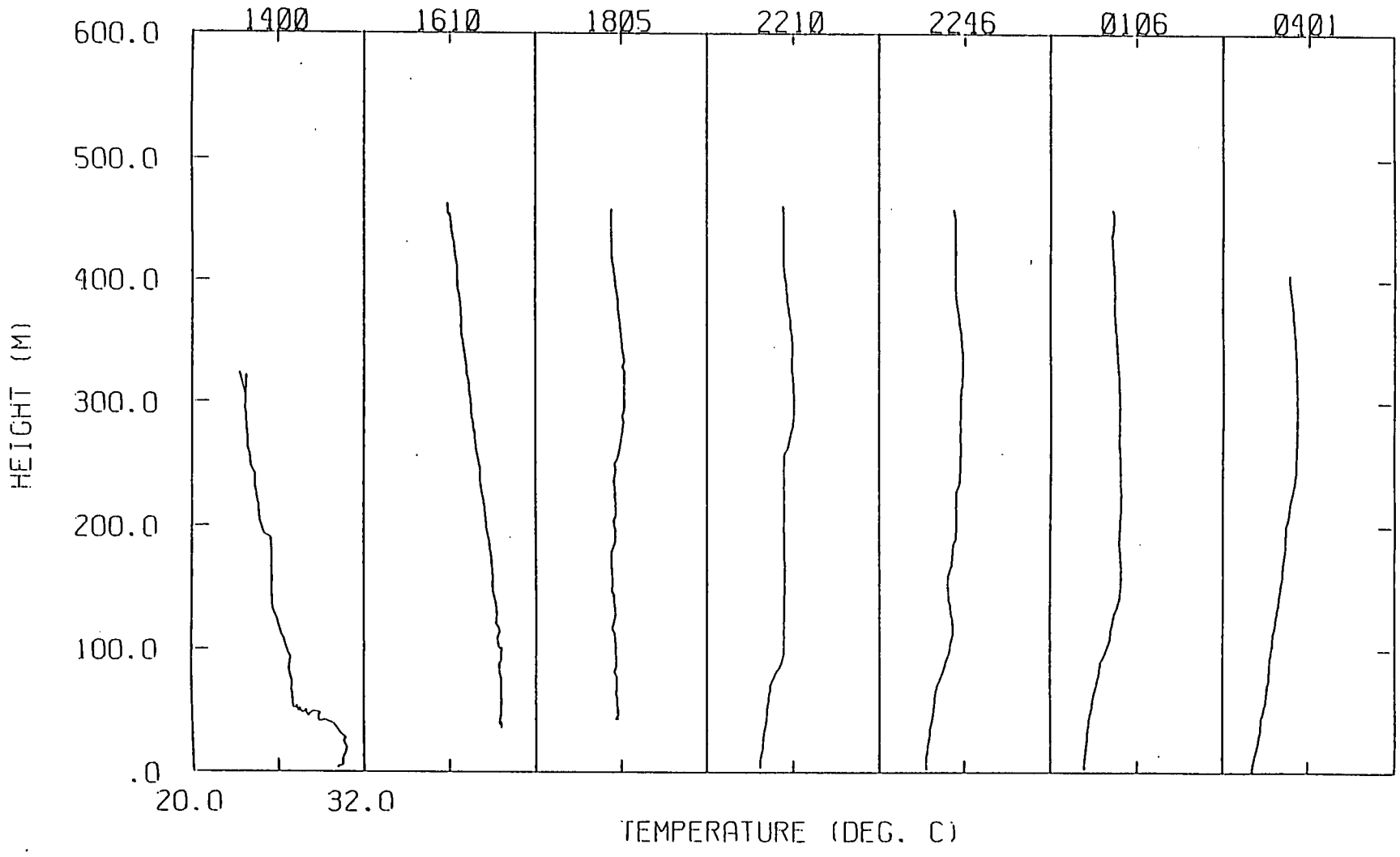
1400
1610
1805
2210
2246
0106
0401
600.0
500.0
400.0
300.0
200.0
100.0
.0
HEIGHT (M)
20.0
32.0
TEMPERATURE (DEG. C)

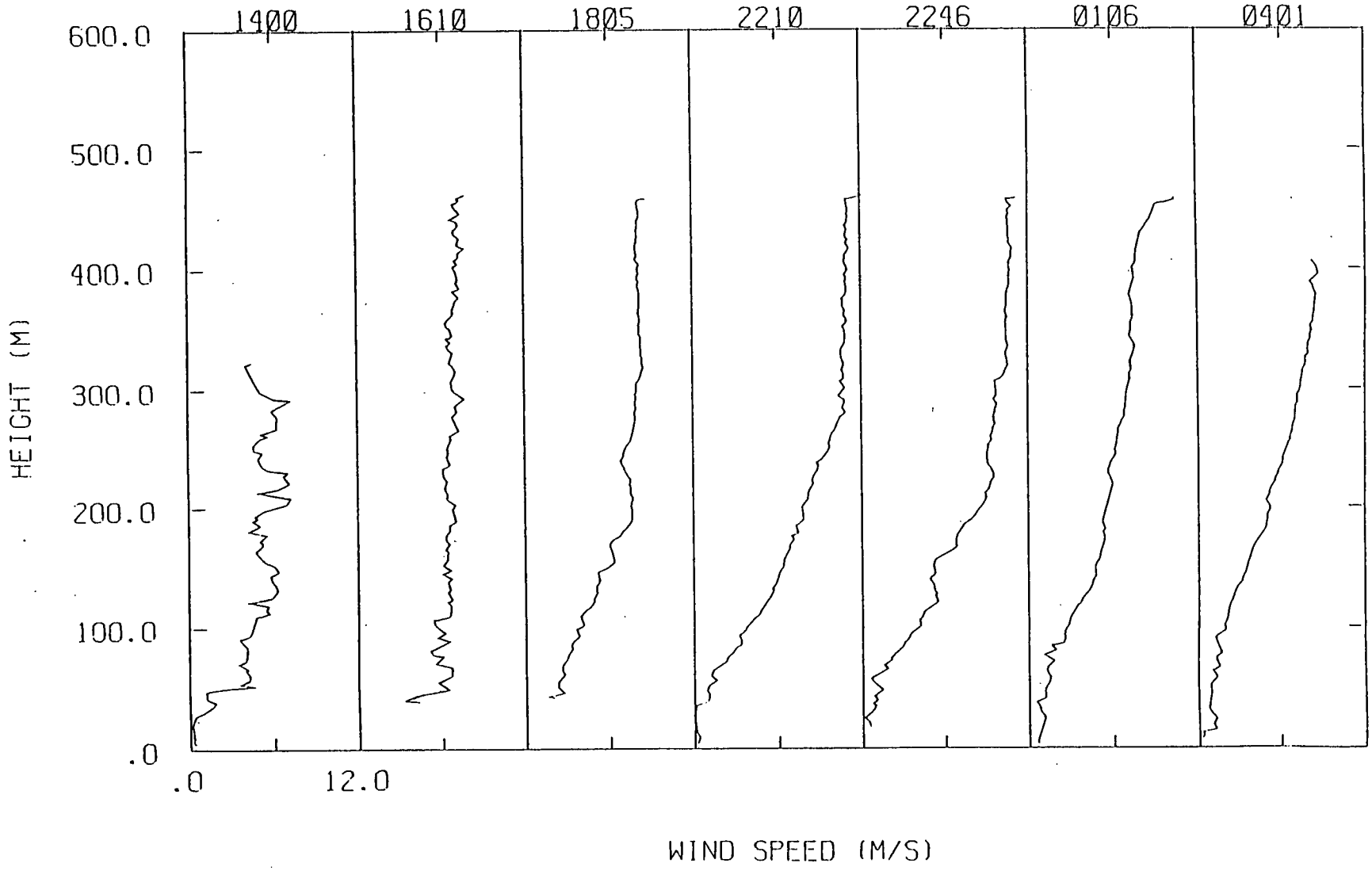
1400
1610
1805
2210
2246
0106
0401
600.0
500.0
400.0
300.0
200.0
100.0
.0
.0
12.0
HEIGHT (M)
WIND SPEED (M/S)

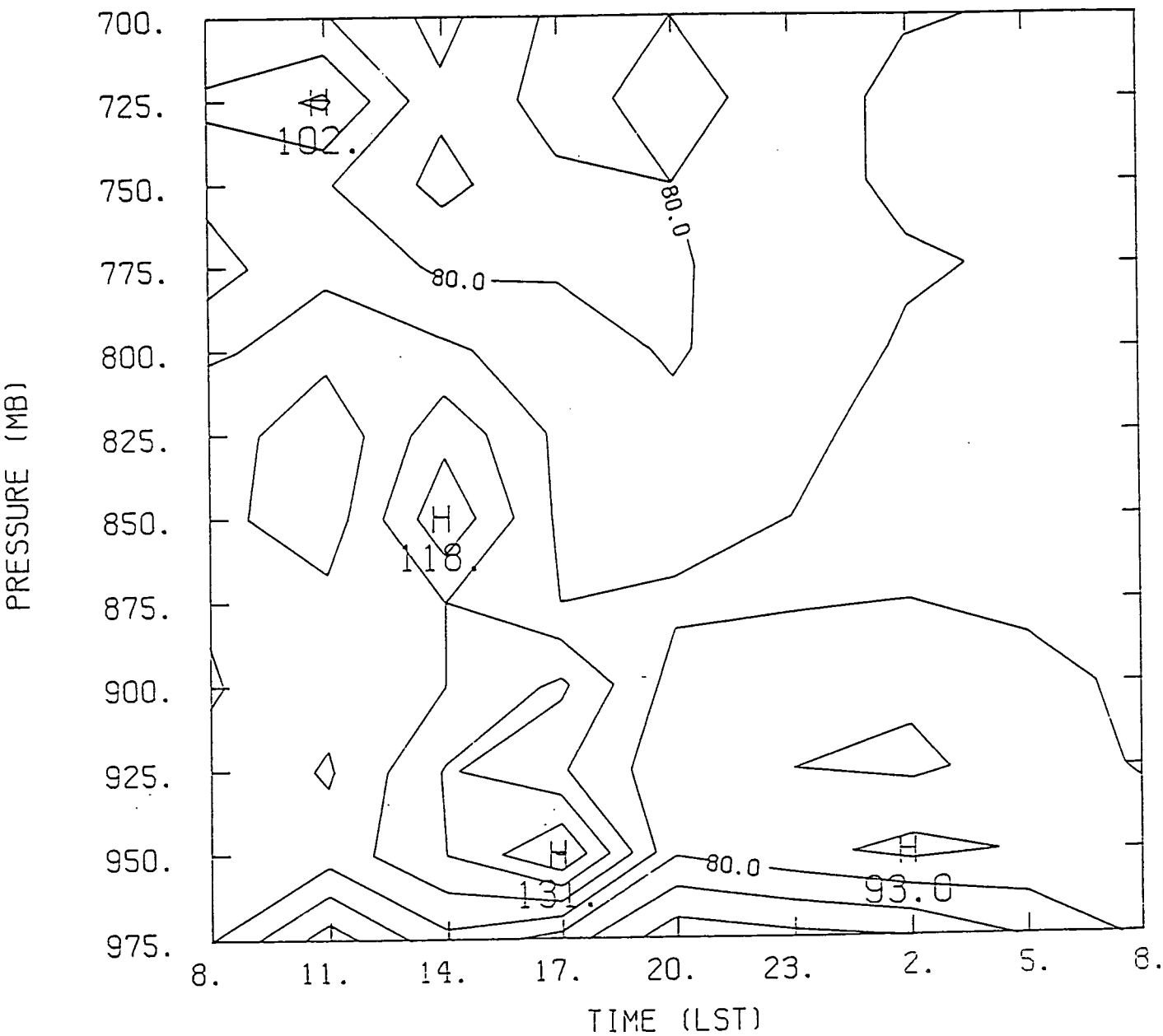
700.
725.
750.
775.
800.
825.
850.
875.
900.
925.
950.
975.
PRESSURE (MB)
H
102.
80.0
80.0
H
118.
H
131.
80.0
H
93.0
8.
11.
14.
17.
20.
23.
2.
5.
8.
TIME (LST)

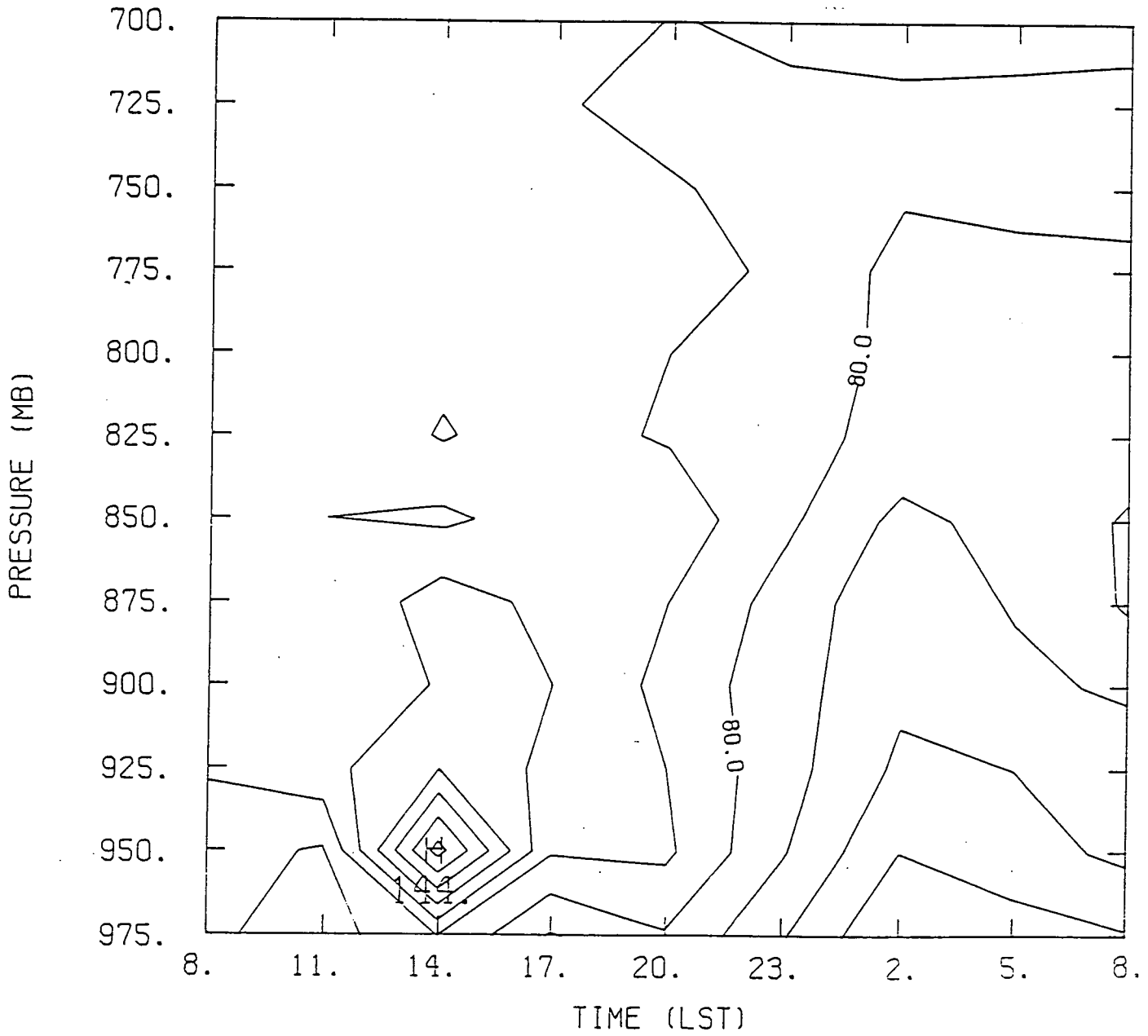
700.
725.
750.
775.
800.
825.
850.
875.
900.
925.
950.
975.
PRESSURE (MB)
8.
11.
14.
17.
20.
23.
2.
5.
8.
TIME (LST)
80.0
80.0
144

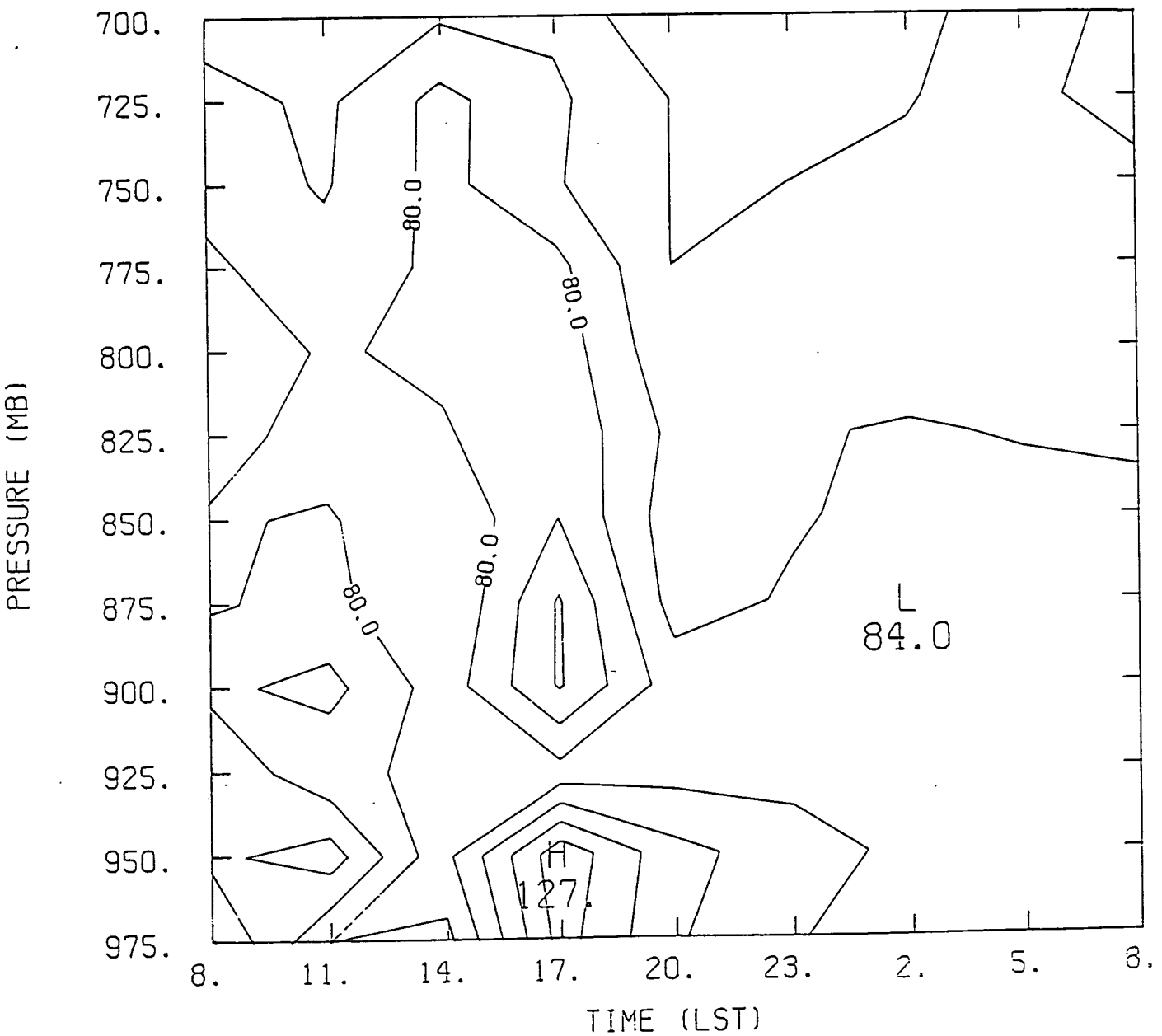
700.
725.
750.
775.
800.
825.
850.
875.
900.
925.
950.
975.
PRESSURE (MB)
80.0
80.0
80.0
80.0
L
84.0
H
127.
8.
11.
14.
17.
20.
23.
2.
5.
8.
TIME (LST)

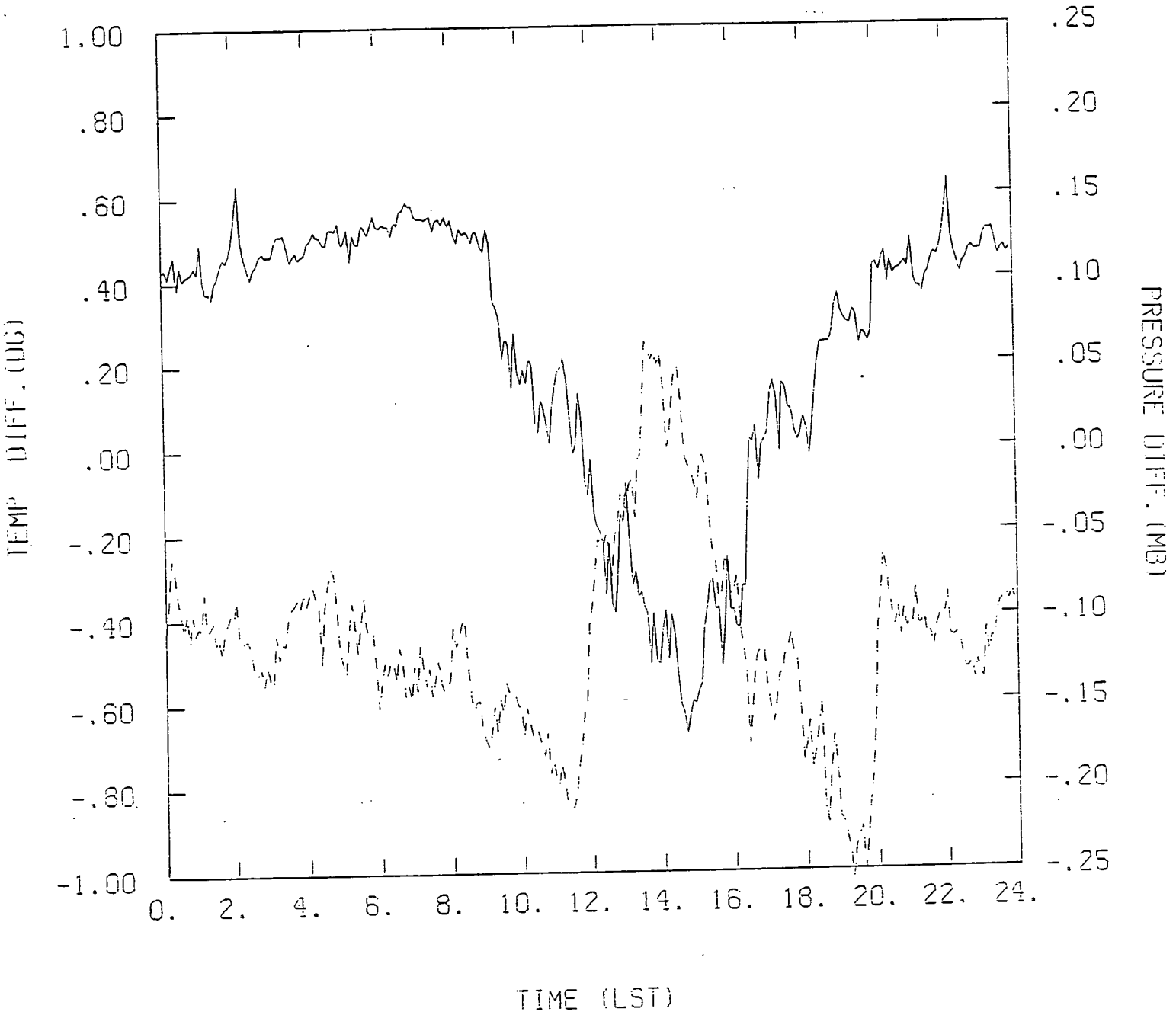
1.00
.80
.60
.40
.20
.00
-.20
-.40
-.60
-.80
-1.00
TEMP DIFF. (DG)
.25
.20
.15
.10
.05
.00
-.05
-.10
-.15
-.20
-.25
PRESSURE DIFF. (MB)
0. 2. 4. 6. 8. 10. 12. 14. 16. 18. 20. 22. 24.
TIME (LST)

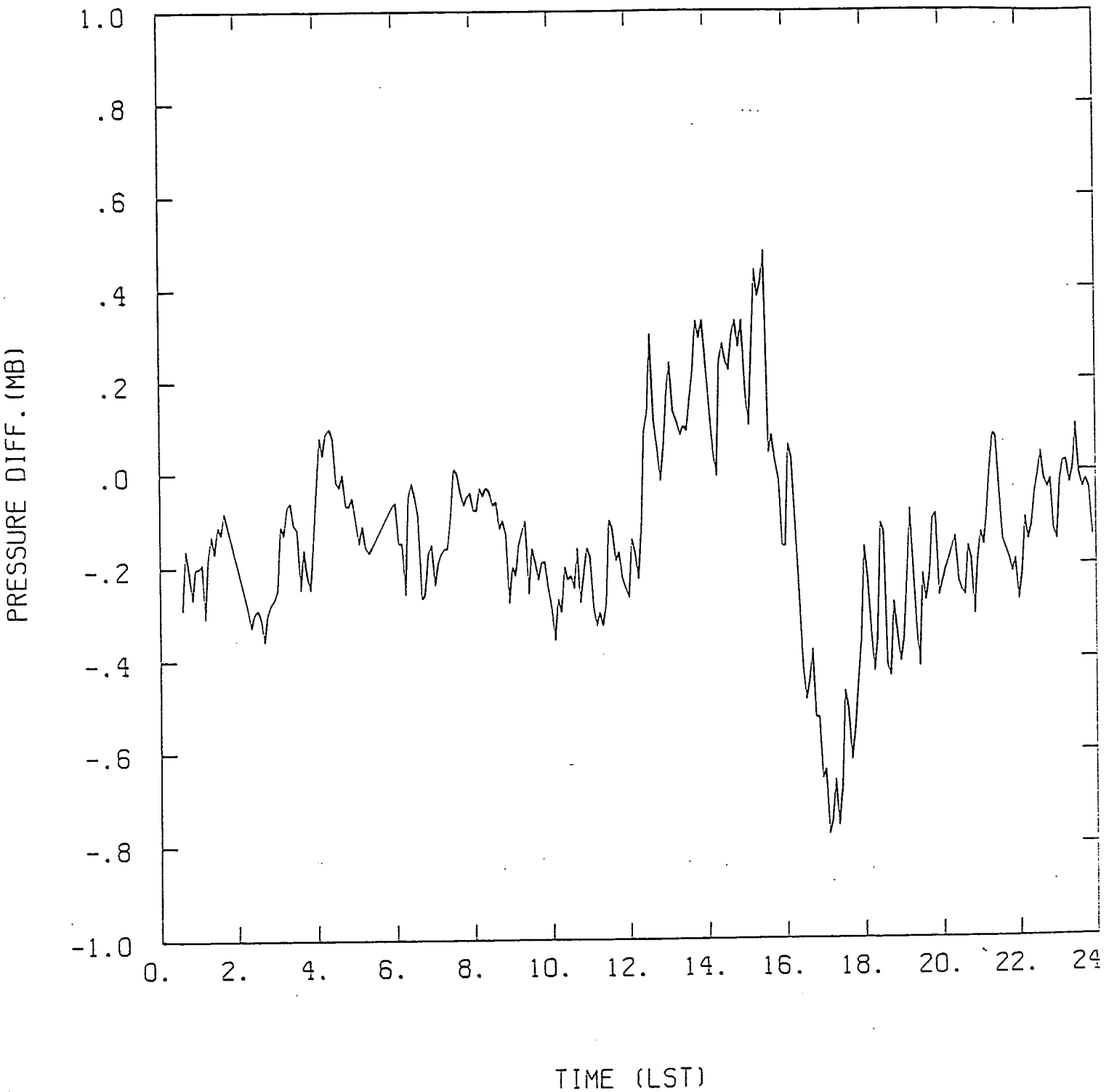
1.0
.8
.6
.4
.2
.0
-.2
-.4
-.6
-.8
-1.0
PRESSURE DIFF. (MB)
0.
2.
4.
6.
8.
10.
12.
14.
16.
18.
20.
22.
24
TIME (LST)

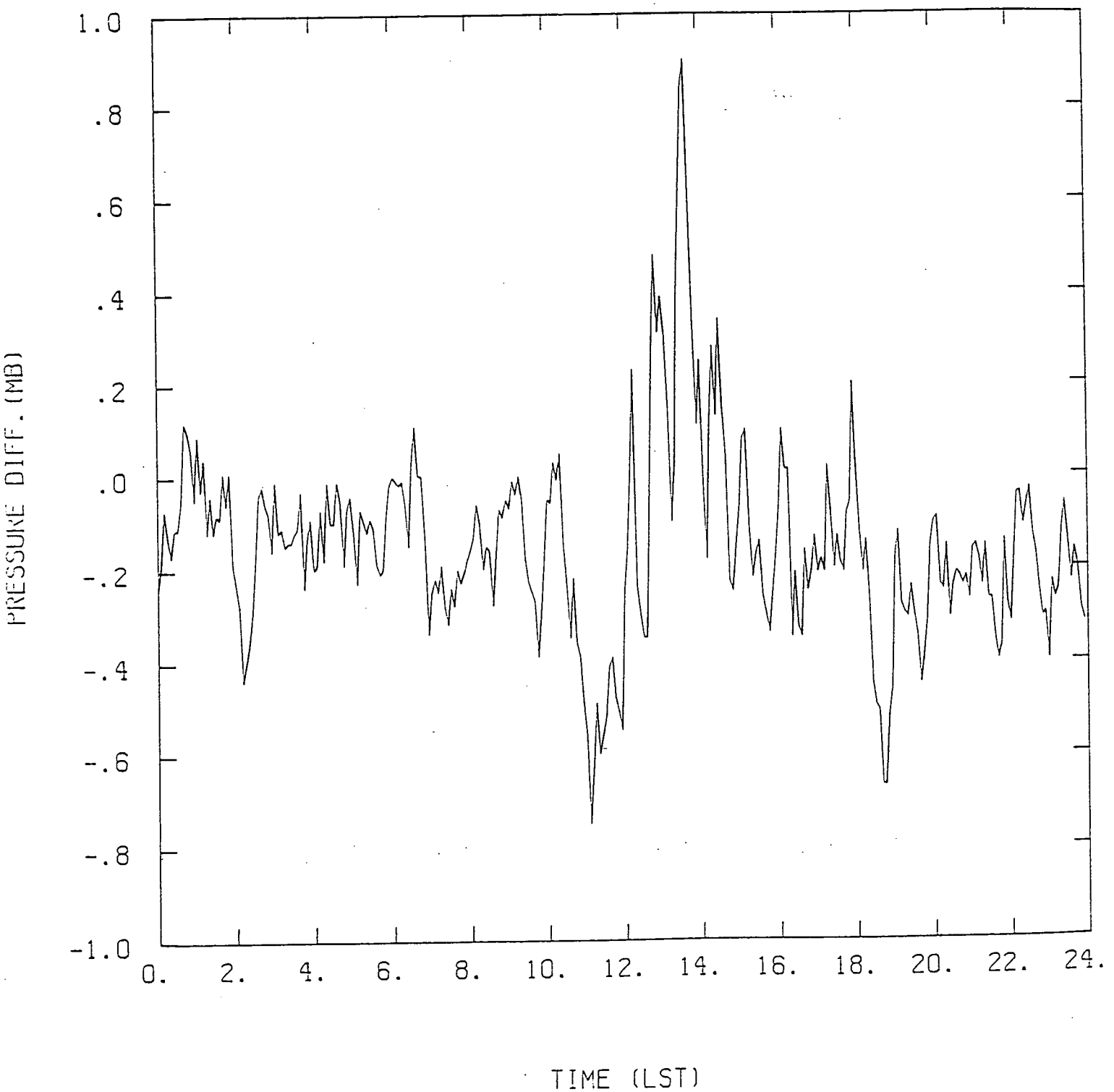
1.0
.8
.6
.4
.2
.0
-.2
-.4
-.6
-.8
-1.0
0.
2.
4.
6.
8.
10.
12.
14.
16.
18.
20.
22.
24.
PRESSURE DIFF. (MB)
TIME (LST)

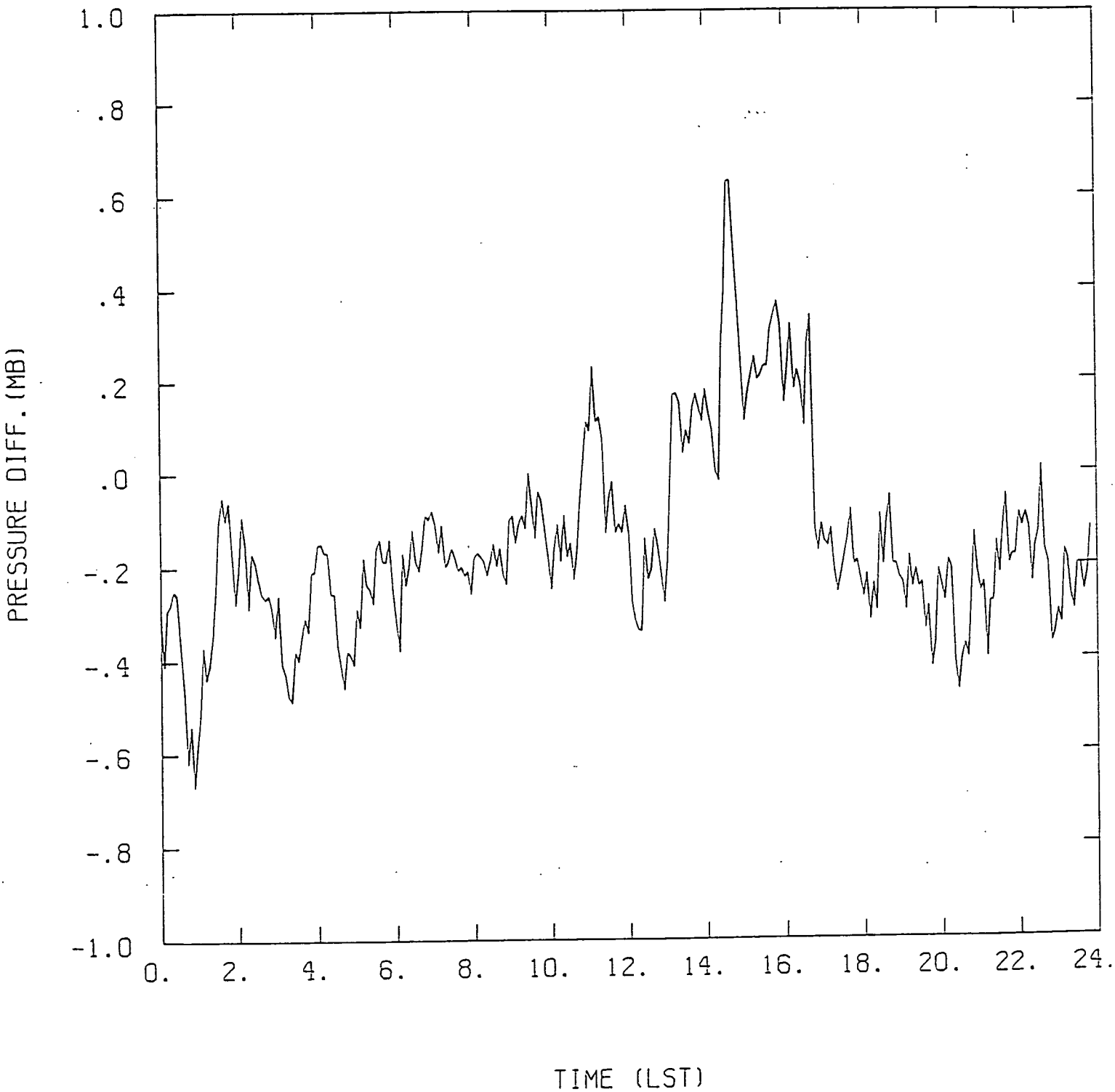
1.0
.8
.6
.4
.2
.0
-.2
-.4
-.6
-.8
-1.0
PRESSURE DIFF. (MB)
0.
2.
4.
6.
8.
10.
12.
14.
16.
18.
20.
22.
24.
TIME (LST)

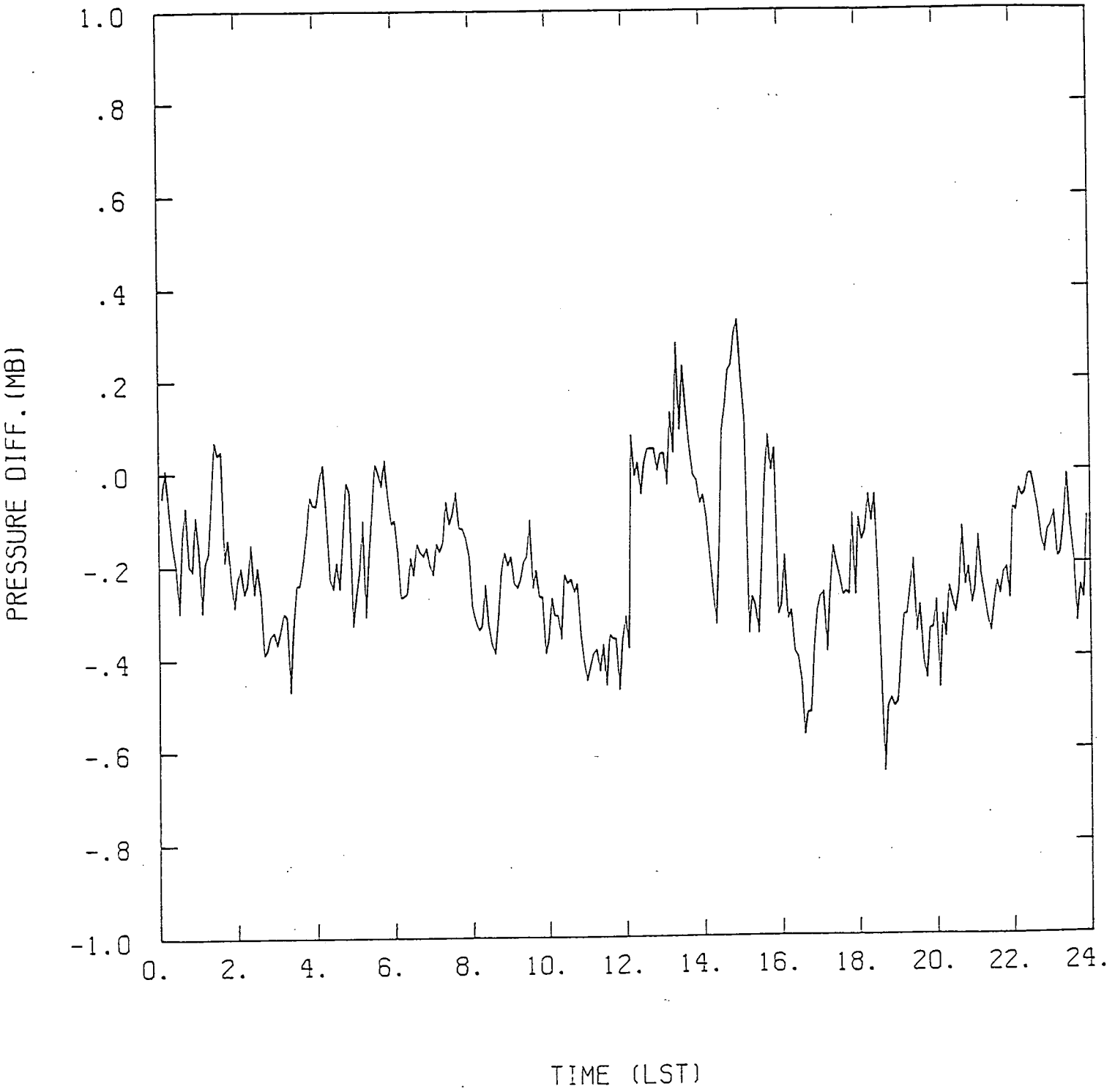
1.0
.8
.6
.4
.2
.0
-.2
-.4
-.6
-.8
-1.0
PRESSURE DIFF. (MB)
0.
2.
4.
6.
8.
10.
12.
14.
16.
18.
20.
22.
24.
TIME (LST)

JOURNAL OF GEOPHYSICAL RESEARCH, VOL. 96, NO. D2, PAGES 3099–3114, FEBRUARY 20, 1991

Photochemical Ozone Production in Tropical Squall Line Convection During NASA Global Tropospheric Experiment/ Amazon Boundary Layer Experiment 2A

KENNETH E. PICKERING,[1] ANNE M. THOMPSON,[2] JOHN R. SCALA,[3,4] WEI-KUO TAO,[2] JOANNE SIMPSON,[2] AND MICHAEL GARSTANG[3]

We have examined the role of convection in trace gas transport and ozone production in a tropical dry season squall line sampled on August 3, 1985, during NASA Global Tropospheric Experiment/ Amazon Boundary Layer Experiment 2A (NASA GTE/ABLE 2A) in Amazonia, Brazil. Two types of analyses were performed. (1) Transient effects within the cloud are examined with a combination of two-dimensional cloud and one-dimensional photochemical modeling. Tracer analyses using the cloud model wind fields yield a series of cross sections of NO_x, CO, and O_3 distribution during the lifetime of the cloud; these fields are used in the photochemical model to compute the net rate of O_3 production. At noon, when the cloud was mature, the instantaneous ozone production potential in the cloud is between 50 and 60% less than in no-cloud conditions due to reduced photolysis and cloud scavenging of radicals. (2) Analysis of cloud inflows and outflows is used to differentiate between air that is undisturbed and air that has been modified by the storm. These profiles are used in the photochemical model to examine the aftereffects of convective redistribution in the 24-hour period following the storm. Total tropospheric column O_3 production changed little due to convection because so little NO_x was available in the lower troposphere. However, the integrated O_3 production potential in the 5- to 13-km layer changed from net destruction to net production as a result of the convection. The conditions of the August 3, 1985, event may be typical of the early part of the dry season in Amazonia, when only minimal amounts of pollution from biomass burning have been transported into the region.

INTRODUCTION

Both observations and theory point to an important role for convective clouds in redistributing trace gases in the atmosphere. *Gidel* [1983] and *Chatfield and Crutzen* [1984] were the first to model convective transport of trace chemical species. More recently, *Chatfield and Delany* [1990] have developed a traveling one-dimensional model that simulates vertical and divergent motions of the tropical atmosphere. This model was used to examine ozone production in two types of convective scenarios.

Observations of trace gas venting from the boundary layer to the free troposphere by fair weather cumulus and nonprecipitating cumulus congestus clouds were reported by *Ching and Alkezweeny* [1986] and *Ching et al.* [1988]. *Dickerson et al.* [1987] were the first to observe marked trace gas redistribution by a deep convective storm, although when frontal convective clouds are cut off from the boundary layer source of pollutant gases, they may not be capable of large trace gas redistribution [*Pickering et al.*, 1988]. Long-range transport of pollutant trace gases in the free troposphere after vertical transport in upstream convection was noted by *Pickering et al.* [1989]. We previously examined the effects of convective redistribution on potential ozone production using observations for both fair weather cumulus and deep convective events in the mid-latitudes [*Pickering et al.*, 1990]. In that study we found enhancement of ozone production over the 24 hours following convection by up to a factor of 4 in the upper troposphere and enhancement in the entire tropospheric column to be about 50%.

In contrast, we found virtually no enhancement of ozone production in tropical wet season convection when transport dominated the distribution of ozone and all NO levels were <20 pptv (parts per trillion volume) [*Scala et al.*, 1990]. Meteorological and trace gas data were used with a two-dimensional convective cloud model and a one-dimensional photochemical model to investigate transport of CO and O_3 and to estimate ozone production in an active cell sampled during the NASA Global Tropospheric Experiment/Amazon Boundary Layer Experiment 2B (NASA GTE/ABLE 2B) mission in Brazil in April and May 1987. A survey of other ABLE 2B flights shows similar patterns (that is, transport dominating photochemistry during an extended period of cumulus convection and low photochemical activity).

The present study employs a diagnostic modeling approach similar to that used by *Scala et al.* [1990] to estimate ozone production within and following an active tropical cloud sampled during GTE/ABLE 2A (conducted in July and August 1985), the dry season counterpart to ABLE 2B. Compared to ABLE 2B, profiles of ozone, NO, and CO during ABLE 2A show higher levels of photochemical reactivity due to enhanced UV (more clear sky conditions) and to some pollutant injection from biomass burning [*Kirchhoff et al.*, 1988]. This is similar to the situation described by Crutzen and coworkers during the dry season Brazilian rain forest and savanna burning in 1979 and 1980 [*Crutzen et al.*, 1985; *Delany et al.*, 1985; *Chatfield and Delany*, 1990].

The data for the present study were taken from the NASA GTE/ABLE 2A data archive resident at NASA Langley Research Center. The ABLE 2A experiment was described by *Harriss et al.* [1988], and initial aircraft and ground-based

[1]Applied Research Corporation, Landover, Maryland.
[2]NASA Goddard Space Flight Center, Greenbelt, Maryland.
[3]Department of Environmental Sciences, University of Virginia, Charlottesville.
[4]Now at NASA Goddard Space Flight Center, Greenbelt, Maryland.

Paper number 90JD02284.
0148-0227/91/90JD-02284$05.00

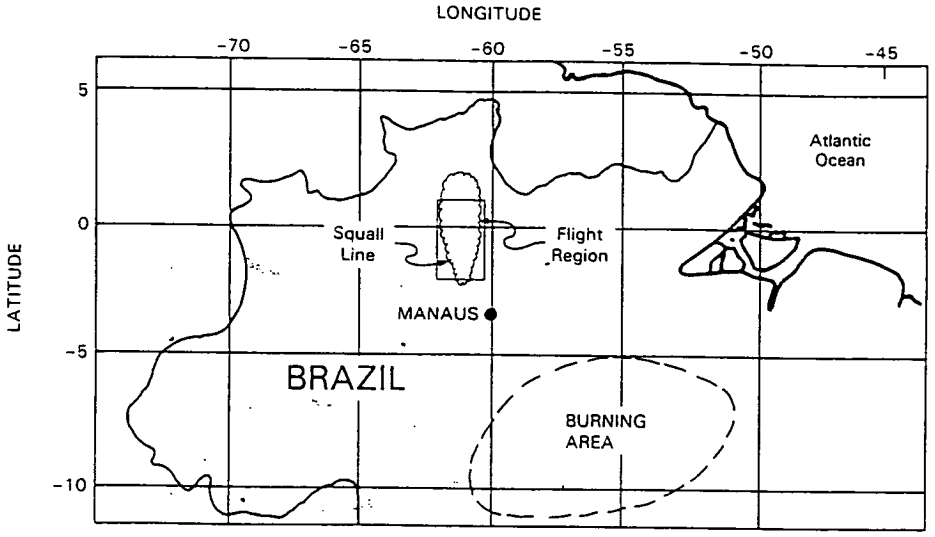

Fig. 1. Map showing the location of the August 3, 1985, squall line while it was sampled and the region containing biomass burning activity. Burning area was delineated by *Kirchhoff et al.* [1988].

data were presented in a series of papers in a special section in *Journal of Geophysical Research* (*93*(D2)). The particular ABLE 2A case (August 3, 1985) which we analyze in this paper was described by *Garstang et al.* [1988], who were responsible for the overall meteorological interpretation of ABLE 2A. This study examines the impact on photochemistry of the August 3 convection. We have extended the analysis of *Garstang et al.* [1988] to include more detailed convective cloud modeling, calculation of air trajectories, transport of trace gases by cloud model-generated wind fields, and photochemical model estimates of ozone production during and following convection.

METEOROLOGICAL CONDITIONS AND CHEMICAL DATA

The ABLE 2A missions in July and August 1985 were conducted primarily in fair weather in an undisturbed troposphere, typical of the dry season. However, the undisturbed conditions deteriorated by August 2, 1985, with the penetration of an upper level disturbance into the central Amazon Basin. On August 3 a well-organized convective system developed rapidly within the southern limb of the equatorial trough. The changes in the large-scale dynamics which permitted deep convective development were likely the result of the Intertropical Convergence Zone (ITCZ) interacting in northern Brazil with the remnants of a higher-latitude frontal boundary [*Garstang et al.*, 1988].

GOES visible imagery for 1501 UT on August 3 depicted a poorly defined area of convection extending north-south approximately 150 km NNW of Manaus, Brazil (see map in Figure 1). Over the next 2 hours the convection organized into a 500-km-long line of vigorous cells. By 1701 UT, individual elements exhibited glaciation and merging of anvils [see *Garstang et al.*, 1988]. Even though this system produced deep convection, the rest of the central basin remained less active, characterized by small cumulus and a few unorganized cumulonimbi. The line exhibited a WSW migration with propagation speeds ranging between 35 and 55 km h^{-1} and a cloud-free wake immediately behind.

Aircraft sampling of the system was designed to enclose the convection in a box by a series of flight tracks flown on either side (that is, in front and behind relative to the system) at altitudes of 150 and 5000 m (Figure 2). Spirals were flown at the corners of the box to determine the vertical structure of the lower troposphere. Vertical profiles of computed equivalent potential temperature (θ_e) at these corners exhibited differences in the gradients of moisture and temperature indicative of the highly convective inflow region to the west (ahead) and the wake outflow area east (behind) of the system [*Garstang et al.*, 1988].

While the aircraft performed the upper transects, the downward looking Differential Absorption Lidar (DIAL) instrument [*Browell et al.*, 1988] revealed considerable horizontal variability in both the convection and mixed layer structure [see *Garstang et al.*, 1988, Plate 2]. The eastern traverses enabled the aircraft to sample the character of the wake outflow near the surface as the system migrated away from this portion of the flight track. Mixed layer heights in this convectively suppressed region averaged 650 m. To the west and in front of the line, vigorous cloud development accompanied mixed layer heights in excess of 1 km.

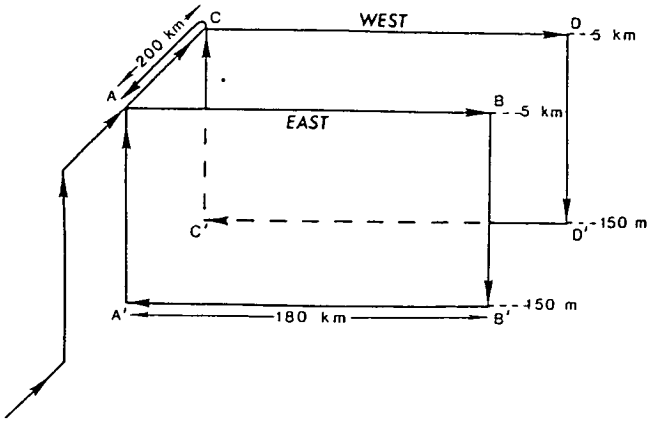

Fig. 2. Flight track for the August 3, 1985, mission. Horizontal flight legs were flown at 150-m and 5-km altitudes on the east (rear) and west (forward) sides of the convective line. Vertical soundings (spirals) were performed at the corners of the box.

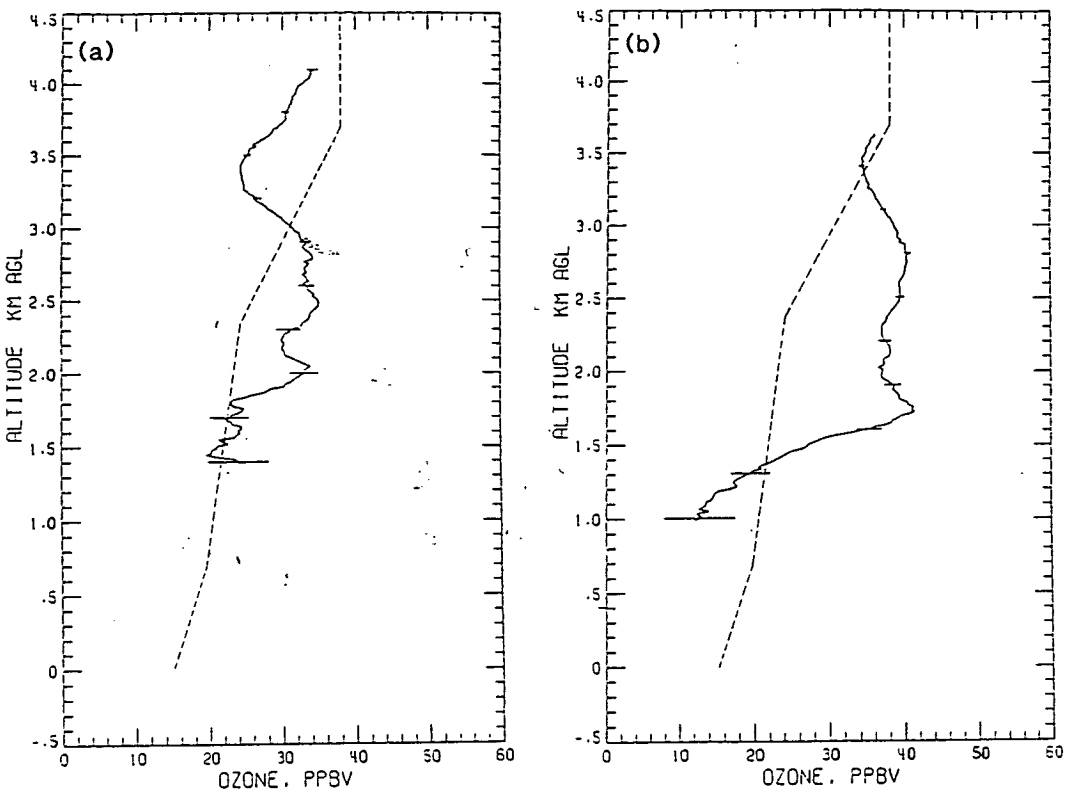

Fig. 3. UV-DIAL profiles of ozone integrated along the sides of the cloud: (*a*) ahead of the storm and (*b*) behind the storm. Dashed line is mean undisturbed O_3 profile for ABLE 2A as shown by *Garstang et al.* [1988].

The cumulative effects of convective mixing are visible in the vertical profiles of ozone obtained by the UV-DIAL [*Browell et al.*, 1988] during the upper level aircraft transects and expressed as horizontally integrated values. The western integration (ahead of the line, Figure 3*a*) required a flying time of 13 min (1657–1710 UT) representing a distance of 78 km. The eastern integration (behind the line, Figure 3*b*) represents a flying time of 15 min (1458–1513 UT) and corresponds to a horizontal distance of 90 km.

Ahead of the squall line the vertical distribution of O_3 in the inflow region of the system shows enhancement relative to the dry season mean in a layer between 1.8 and 3.0 km, likely due to photochemical production in a haze layer that was observed from the aircraft [*Andreae et al.*, 1988] and by the DIAL system. Above 3 km the ozone concentrations are diminished relative to the average undisturbed profile, indicating upward transport of boundary layer air into the system. The ozone enhancement is greater behind the system, reflecting downward transport from the midtroposphere as well as the anthropogenic influence. The enhanced-ozone layer increased in depth in the wake of the storm.

The UV-DIAL O_3 profiles compare well with in situ data [*Gregory et al.*, 1988] taken during aircraft spirals at the corners of the convective box (Figure 4*b*). In situ carbon monoxide data from the aircraft spirals [*Sachse et al.*, 1988] flown ahead (inflow) and behind (outflow) the squall line are shown in Figure 4*a*. The polluted layer is evident from 0.7 to 2.2 km. The squall line appears to have diluted slightly the CO concentrations in the layer and lowered the altitude of the peak concentration. The altitude of the peak O_3 in the UV-DIAL profile (Figure 3*b*) in the wake of the storm (41 ppb at ~1.7 km) closely corresponds to that found on the CO profile taken behind the system. NO profiles observed by *Torres and Buchan* [1988] are shown in Figure 4*c*. Concentrations of NO are relatively low and do not show a significant signal of the polluted layer as in the CO and O_3 profiles (Figures 4*a* and 4*b*). This result indicates that the polluted layer is well aged and any enhanced NO that originally existed in this layer has been converted to other forms of reactive nitrogen (e.g., NO_2, HNO_3, and peroxyacetylnitrate (PAN)) during transport. *Kirchhoff et al.* [1988] showed that mixed layer air masses arriving at Manaus on this day originated to the southeast in a region of biomass burning (forest clearing for agricultural development) in the state of Mato Grosso. The typical transport time to Manaus is between 12 and 24 hours, allowing time for significant conversion of NO to other odd nitrogen species. The amount of lightning which occurred in this squall line is uncertain. Neglect of this source of NO_x does not detract from our analysis of the effects of redistribution of trace gases by convection.

METHODS AND RESULTS

Modeling simulations for the August 3 ABLE 2A convective case were performed in two stages. First, a two-dimensional convective cloud dynamical and microphysical model was run to generate fields of winds, temperature, water vapor, and hydrometeors encompassing the cloud system. The wind fields were used to redistribute the trace gases CO, O_3, and NO_x, which were assumed to act as tracers over the period of mixing by the convective cloud system. In the second step the trace gas profiles generated by the two-dimensional cloud model are used in a series of

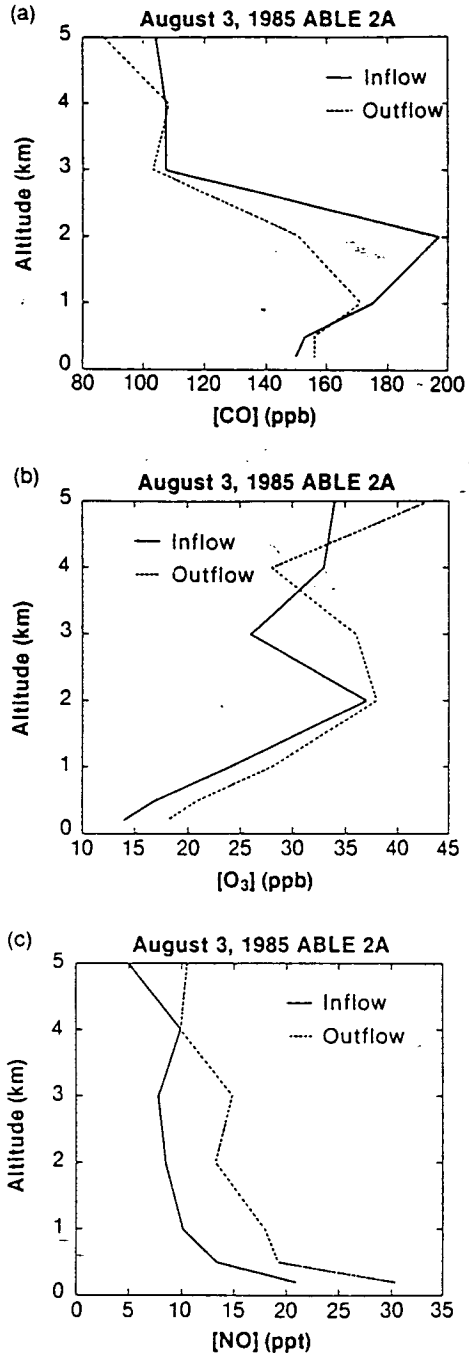

Fig. 4. In situ trace gas profiles taken from the NASA Electra on August 3, 1985, and averaged over 1-km layers. Original observed profiles are shown by *Garstang et al.* [1988]: (*a*) CO (ppb), (*b*) O_3 (ppb), and (*c*) NO (ppt).

one-dimensional photochemical model runs to estimate the rate of ozone production (or destruction) within the cloud while it is active and during the 24-hour period following the convective event. The analysis within the cloud yields a two-dimensional diagnostic presentation of the photochemistry.

Cloud Model and Chemical Tracer Fields

The two-dimensional moist cloud model used in this study is similar to that described by *Soong and Tao* [1980] and *Tao and Simpson* [1989]. Details of how the model was applied to

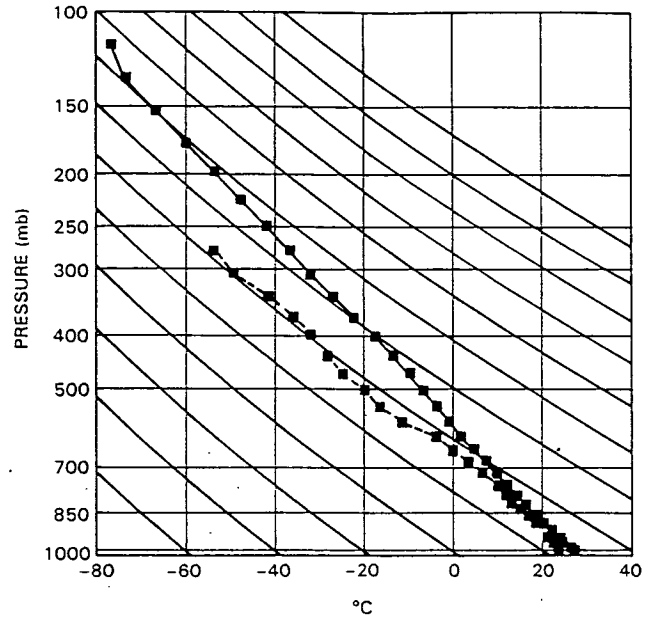

Fig. 5. Smoothed temperature and dew point soundings taken at Reserva Ducke at 1200 UT on August 3, 1985, that were used to initialize the cloud model. Diagonal lines are dry adiabats.

a Brazilian wet season convective simulation are reported by *Scala et al.* [1990]. Further details regarding the two-dimensional cloud model and its modifications are also described.

A stretched vertical coordinate (increment from 200 to 950 m) is used in order to maximize resolution in the lowest levels of the cloud model. Model top is 17.5 km with 31 grid points. The horizontal domain of the model contains 448 grid points with the central 368 points composing a fine grid area with a resolution of 500 m. In the simulations the x coordinate is aligned parallel to the direction of propagation, and the y coordinate is placed parallel to the convective line. Variations along the y axis are assumed to be small relative to those along the x axis. The cloud model time step is 10 s.

The state of the dry season troposphere over Amazonia prior to convective growth is given by the 1200 UT sounding from Ducke (20 km northeast of Manaus) on August 3, 1985. The extensive midtroposphere drying found in this sounding is an environmental condition more commonly associated with mid-latitude squall lines. Initial simulations with the 1200 UT observed thermodynamics failed to produce a sustaining cloud. To simulate deep convection without the use of unrealistic mesoscale forcing, several observed temperature inversions were smoothed to produce the profile shown in Figure 5.

The initial wind profile for the August 3 simulation is based on the Ducke sounding, using the wind component parallel to the direction of squall line propagation. A forward speed of 10.5 m s^{-1} (37.8 km h^{-1}) is subtracted from the observed wind profile to place the simulated cloud in a constant frame of reference. This enables inflow and outflow regions to be observed and investigated relative to the storm. The important components of this profile are a rear low-level inflow at 1.5 km, a prominent easterly wind at midlevels with strong vertical shear above and below, and a third region of relative easterly flow at 11 km.

Typically, about five two-dimensional simulations are

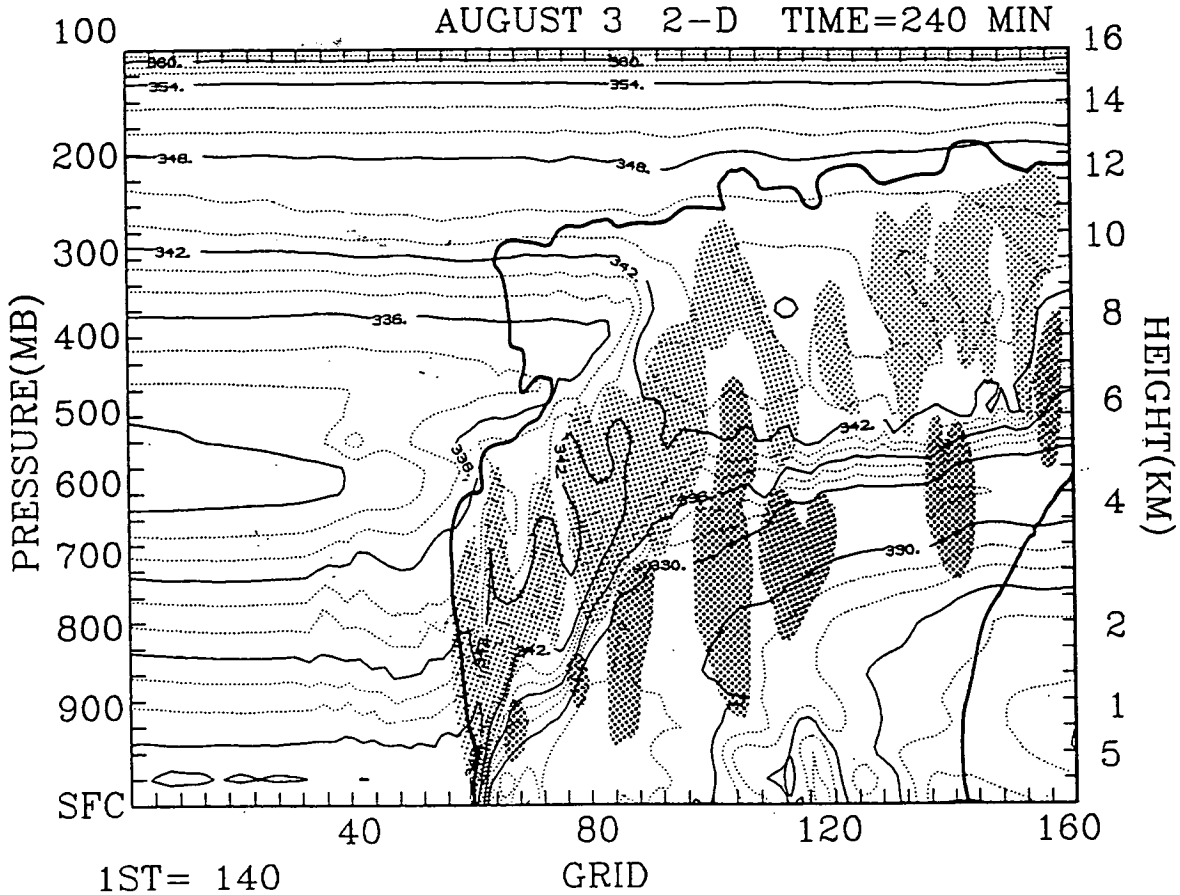

Fig. 6. Cross section of equivalent potential temperature (θ_e) computed by the cloud model at 240 min into the simulation. Light shading indicates the major regions of upward motion and darker shading shows the major regions of downward motion. Horizontal scale shows grid points at 0.5-km intervals. Note that origin is at grid point 140 (70 km on distance scale). For example, 80 on the horizontal scale is cloud model grid point 220. Heavy line is the cloud outline at 240 min based on radar reflectivity computed by the model.

required to reproduce the observed features of a convective system utilizing a semiempirical "tuning" process. Prior to each successive simulation, minor adjustments are made to the input variables (e.g., initial forcing) based on the results of the previous run. The modifications improve specific attributes of the predicted cloud fields (e.g., cloud top height) without altering the general structure and organization, which is accepted as the true behavior of the model cloud. The procedure does not attempt to reproduce a predetermined convective characteristic like an overshooting anvil or an inclined updraft.

Graphical representation of the model-calculated variables (which include horizontal and vertical velocities, temperature, and water vapor mixing ratio) is produced every 30 min during the 8-hour simulations. This time sequence of model-derived cloud fields enables an interpretation of convective updraft and downdraft development, cloud moisture content, surface precipitation structure, and modification of the initial atmosphere by the simulated cloud system.

The convective cloud model produced a cloud with a well-developed anvil by the end of the first 4 hours of the simulation. The satellite-derived cloud top observation of 13 km was reproduced by the model, and the model-generated profiles of equivalent potential temperature (θ_e) compared well with those observed by the aircraft ahead and behind the storm. The two-dimensional model field of θ_e at 240 min is shown in Figure 6, along with the major regions of ascent and descent and the cloud outline as defined by the computed radar reflectivity. Areas of rising air are concentrated in the high θ_e inflow region, whereas the regions of descent are in air with lower θ_e. The multicellular nature of this squall line is indicated by the several centers of upward and downward motion. New cells develop at the leading edge of the system as it propagates westward.

The model-predicted wind fields are stored at 3-min intervals, and trajectories are computed backward and forward in time from these fields to illustrate particular features. Trajectories beginning or ending at blocks of points are used to emphasize the organization and dispersion inherent in the cloud system on a scale larger than that of a single grid cell. The trajectory calculations are performed systematically for groups of points from left to right in the model domain for each of 30 different layers. Each trajectory is computed over an elapsed time of 120 min. Parcel position relative to the convection is obtained by subtracting the modeled system's forward propagation. Trajectories were computed starting at 240 min in the simulation and progressing forward in time to 360 min and backward in time to 120 min. A total of 3900 (130 points in 30 layers) forward trajectories and an equal number of backward trajectories were computed. We have summa-

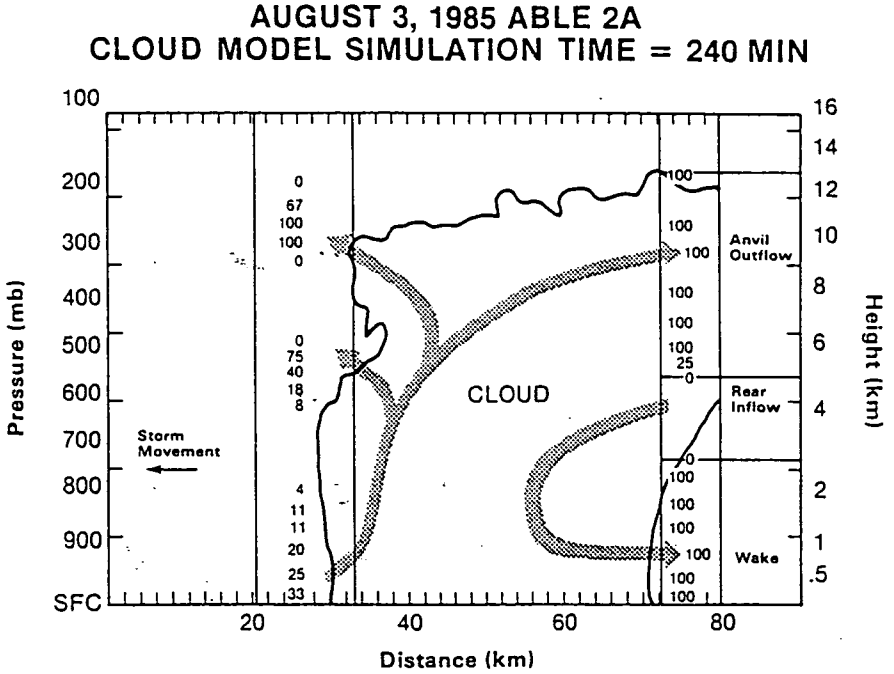

Fig. 7. Summary of back trajectories produced by the cloud model for the August 3, 1985, ABLE 2A case. Numbers in the vertical columns ahead and behind the cloud indicate the percentage of the air at that altitude that is outflow from the cloud. Most of the air pumped out of the boundary layer exits from the anvil (8–12 km), and air in the wake below 5 km has also been "processed." The air in the boundary layer ahead of the storm is unperturbed. Arrows indicate main flow paths.

rized the backward trajectories arriving in the columns of air immediately ahead and behind the cloud (Figure 7). The values given in these columns in the figure represent the percentage of the trajectories, arriving at the indicated altitudes, that have passed through the cloud. Therefore the values can be used to determine the principal regions where air is flowing into and out of the cloud. These results are used to determine which of the aircraft observations should be used to initialize the tracer studies described below. Air is primarily flowing into the cloud in the region below 4 km ahead of the system and in the rear inflow region between 3 and 5 km. Most of the air pumped out of the lower troposphere exits from the anvil, both at the front and rear of the storm. The trajectories showed that some interaction did occur between the main upward and downward motions generalized in Figure 7. Figure 8 is an example of a set of back trajectories arriving at 10.5 km in the anvil outflow behind the storm. Almost all of the air arriving at this location had its origin below 3 km, ahead of the system, and underwent a nearly vertical initial transport in the highly convective region at the leading edge of the storm, indicating the existence of a "hot tower" [*Riehl and Malkus*, 1958; *Riehl and Simpson*, 1979]. Trajectories that arrived near the surface in the wake of the storm showed air parcels entering the cloud in the midlevel rear inflow region and descending through the center of the cloud beneath the ascending core updrafts.

Distributions of CO, O_3, and NO_x are simulated with a layered tracer scheme (similar to that of *Lafore and Moncrieff* [1989]) in which the tracer can be introduced at a specific time (e.g., at 120 min) in the simulation. Tracers are probably more accurate than trajectories for determining the "origin" of air parcels because the effects of subgrid-scale diffusion are included. The inert tracers are introduced as n layers of varying depths based on the characteristics of the undisturbed trace gas profiles. Each layer requires a separate equation to calculate its change in concentration as a result of transport. The tracer T is initialized to unity within the layer and zero elsewhere. The simulation is run for a specific

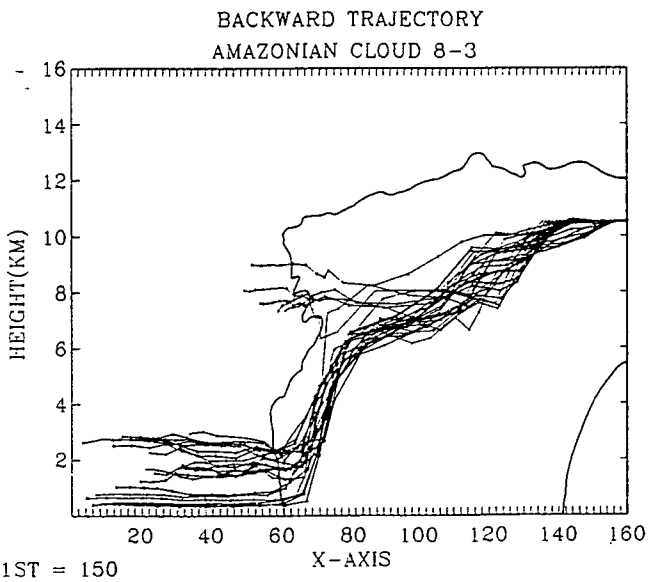

Fig. 8. Set of back trajectories arriving at 10.5 km at the rear of the squall line at 240 min into the simulation. Horizontal scale shows grid points at 0.5-km intervals. Note that origin is at grid point 150 (75 km on distance scale). Heavy line is approximate outline of cloud at 240 min.

forward time period similar to the trajectory analyses but utilizing a 10-s time step. At any time step t the tracer concentration $C(x, z, t)$ at specific points may be computed by summing the contributions from the various layers.

$$C(x, z, t) = \sum c_1 T_1(x, z, t) + c_2 T_2(x, z, t) + \cdots + c_n T_n(x, z, t) \quad (1)$$

where $c_1, c_2, \cdots, c_n$ are the initial concentrations in the layers.

Tracers were introduced into the simulation at 120 min and were allowed to be transported for 4 hours (i.e., until 360 min). Initial tracer concentrations were taken from the aircraft observations in the inflow region ahead of the storm below 5 km (Figure 4). Unfortunately, the NASA Electra did not sample at altitudes greater than 5 km. Therefore above 5 km, O_3 concentrations were taken from an ozonesonde released from Manaus (Reserva Ducke) on the previous day (August 2, 1985), and the CO and NO profiles above 5 km were deduced from other aircraft experiments over or near the region. The CO profile above 5 km was taken from the 1980 dry season experiment over the Brazilian rain forest [*Crutzen et al.*, 1985; *Delany et al.*, 1985]. NO concentrations above 5 km were estimated from the STRATOZ III experiment [*Drummond et al.*, 1988]. Because of the short lifetime of NO the initial NO data were used in a preliminary run of the one-dimensional model to estimate an initial profile of NO_x(NO_x = NO + NO_2) which was transported as a tracer. Because the transport time of an individual air parcel through the cloud model domain was typically 2 hours or less, we can consider NO_x as a quasi-conservative tracer, along with CO and O_3 which have been previously shown to be excellent tracers in convective systems [e.g., *Pickering et al.*, 1988]. The initial tracer concentrations were assumed to be uniform across the horizontal domain of the model (Figures 9*a*, 9*c*, and 9*e*).

Figures 9*b*, 9*d*, and 9*f* show the final two-dimensional fields for CO, O_3, and NO_x, and Figures 10*a*–10*c* show the difference fields for the same three species, obtained by subtracting the initial value from the final value at each grid point. Convective redistribution is demonstrated most dramatically by the CO and O_3 fields, which show the CO peak in the polluted layer and the lower ozone concentrations of the lower troposphere being transported to the upper troposphere. Increases of CO of more than 60 ppb were found in three regions between 2.5 and 6 km, while increases of 20 ppb occurred up to almost 12 km. Ozone concentrations decreased by 30 ppb in the vicinity of 12 km, and decreases of more than 10 ppb occurred in a large region above 5 km. Substantial downward transport of lower CO concentrations and higher O_3 concentrations is evident to the rear of the updraft region. Depletion of CO in the initially polluted layer was by at least 80 ppb in the area of most intense downward motion. Increases of ozone of more than 10 ppb appear in two regions below 4 km.

The tracer results for NO_x are more complex due to the fact that the highest initial concentrations are located both near the surface and in the upper troposphere. NO_x increases reach 30 ppt in the region of upward motion below 1 km, while an area of NO_x enhancement exceeding 10 ppt slopes upward to about 3.5 km. Another region of greater than 10 ppt increase extends from 5 to 8 km in the core of the rising air. A decrease of NO_x is seen in the 9.5- to 13-km layer as air with lower concentrations penetrates into the upper tropospheric region where NO_x is primarily controlled by flux from the stratosphere. Cleaner air is also brought downward to the surface causing NO_x depletion of more than 40 ppt in the storm's wake.

Photochemical Model and Analysis

A time-dependent one-dimensional transport/kinetics model [*Thompson and Cicerone*, 1982, 1986] is used to estimate vertical profiles of net photochemical O_3 production rates. In this study the original chemistry of the model (25 calculated constituents and 73 reactions) has been augmented to give a total of 130 chemical reactions and 33 computed constituents. A modification of the isoprene mechanism of *Lurmann et al.* [1986] has been adopted to simulate the hydrocarbon chemistry. These reactions are listed in Table 1.

Net ozone production $P(O_3)$ is calculated from five rate terms, representing the rate determining steps of the major production and loss mechanisms:

$$P(O_3) = k_1[NO][HO_2] + \Sigma k_{2i}[NO][R_iO_2] - k_3[O(^1D)][H_2O] - k_4[O_3][HO_2] - k_5[O_3][OH] \quad (2)$$

Cloud model values of $[H_2O]$ and values derived from tracer analysis of NO_x, O_3, and CO, along with photochemical model estimates of $[RO_2]$, $[HO_2]$, $[O(^1D)]$, and [OH], are used in calculating $P(O_3)$. The second term in (2) is the sum of six terms, representing oxidation of NO to NO_2 by six RO_2 type radicals: CH_3O_2, $C_2H_5O_2$, CH_3CO_3, RIO_2, VRO_2, and MRO_2 resulting from oxidation of methane, ethane, and isoprene (Table 1). For the 24-hour analysis the ozone production rate is computed at 3-hour intervals over a day from (2), and the eight values are used to compute a diurnally averaged production rate. We refer to this diurnally averaged rate as the "ozone production potential" to emphasize the fact that it is essentially unmeasurable but represents the potential rate of O_3 formation under the given conditions.

Because no photolysis rates were measured directly in ABLE 2A, all photolysis rates are calculated with the model continuously throughout the day. For the in-cloud analysis, model runs were performed using cloudy photolysis rates computed by the method of *Thompson* [1984]. A slab cloud is placed at the altitude of the actual cloud top. Photolysis rates are enhanced above the cloud due to reflection from the cloud and are diminished in and below the cloud. We have placed the slab between 12 and 13 km to simulate a physical cloud top at 13 km, and we have used a cloud top albedo of 0.8.

It has been assumed in modeling studies of nonprecipitating clouds that a portion of certain trace gases and radicals are removed from the interstitial air [e.g., *Lelieveld and Crutzen*, 1990; *Chameides*, 1984]. The major effect on the photochemistry of in-cloud air at cold temperatures is the depletion of HO_2 caused primarily by decreased photolysis of H_2CO due to the dissolution of H_2CO in cloud and rainwater. At warmer temperatures the dissolution of HO_2 itself also becomes important. For a precipitating cloud, trace gas scavenging is followed by removal by precipitation. The latter process represents the rate-determining step for

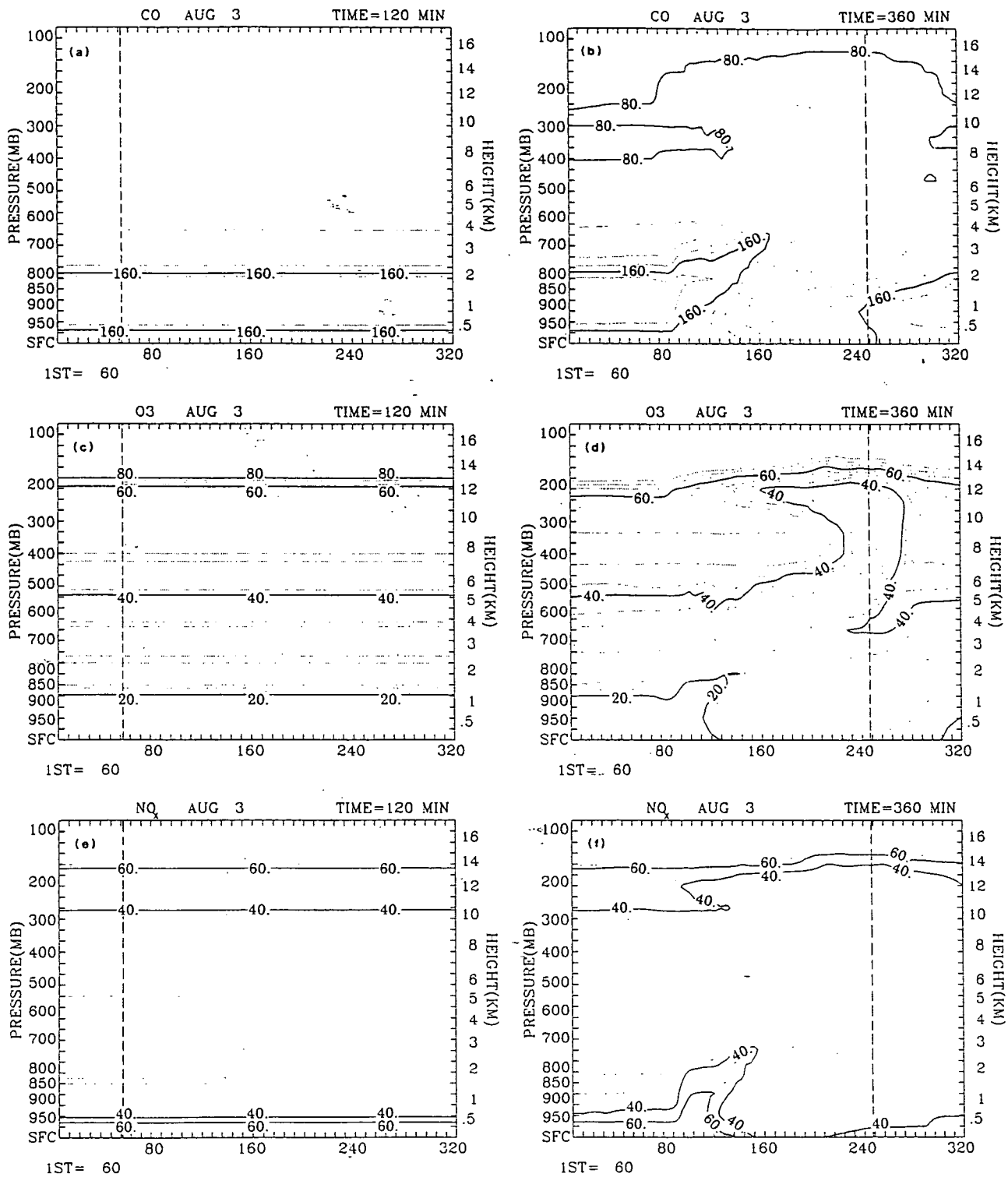

Fig. 9. Tracer distributions (*a*) CO (ppb) at 120 min, (*b*) CO at 360 min, (*c*) O_3 (ppb) at 120 min, (*d*) O_3 at 360 min, (*e*) NO_x (ppt) at 120 min, and (*f*) NO_x at 360 min. Horizontal scale shows grid points at 0.5-km intervals. Note that origin is at grid point 60 (30 km on distance scale). Contour interval is 20 ppb for CO, 5 ppb for O_3, and 5 ppt for NO_x. Vertical dashed lines indicate profiles used in 24-hour photochemical model runs.

overall in-cloud wet removal [*Slinn*, 1974; *Levine and Schwartz*, 1982].

The August 3 squall line was precipitating, so we have simulated heterogeneous losses by use of a first-order wet removal coefficient for a precipitating cloud as described by *Thompson and Cicerone* [1982]. We subject HNO_3, H_2O_2, H_2CO, OH, HO_2, CH_3O_2, and RIO_2 to wet removal. The value of the coefficient for HNO_3 (1.5×10^{-3} s^{-1} at 298 K) was taken from *Levine and Schwartz* [1982] for the conditions of a heavy rainfall rate, which is applicable for this

TABLE 1. Isoprene Oxidation Mechanism

Reaction	Rate Constant, cm molecules s^{-1} units
$ISOP + OH \rightarrow RIO_2$	$1.5 \times 10^{-11} \exp(500/T)$
$RIO_2 + NO \rightarrow 0.9\ NO_2 + 0.45\ MVK + 0.45\ MACR + 0.9\ HO_2 + 0.9\ H_2CO$	$4.2 \times 10^{-12} \exp(180/T)$
$RIO_2 + RIO_2 \rightarrow$ products	2.0×10^{-13}
$RIO_2 + HO_2 \rightarrow IOOH + O_2$	3.0×10^{-12}
$IOOH + h\nu \rightarrow$ products	$0.0005 \times j(NO_2)$
$IOOH + OH \rightarrow RIO_2 + H_2O$	1.0×10^{-11}
$MVK + OH \rightarrow VRO_2$	$3.0 \times 10^{-12} \exp(500/T)$
$VRO_2 + NO \rightarrow 0.9\ NO_2 + 0.6\ CH_3CO_3 + 0.6\ HAC + 0.3\ HO_2 + 0.3\ H_2CO + 0.3\ MGGY$	$4.2 \times 10^{-12} \exp(180/T)$
$VRO_2 + HO_2 \rightarrow IOOH + O_2$	3.0×10^{-12}
$IOOH + OH \rightarrow VRO_2 + H_2O$	1.0×10^{-11}
$MACR + OH \rightarrow MAO_3$	1.02×10^{-11}
$MAO_3 + NO_2 \rightarrow MPAN$	4.7×10^{-12}
$MPAN \rightarrow MAO_3 + NO_2$	$1.95 \times 10^{16} \exp(-13543/T)$
$MAO_3 + 3NO \rightarrow 3NO_2 + HO_2 + MGGY$	$4.2 \times 10^{-12} \exp(180/T)$
$MAO_3 + HO_2 \rightarrow$ products	3.0×10^{-12}
$MACR + OH \rightarrow MRO_2$	$3.86 \times 10^{-12} \exp(500/T)$
$MRO_2 + NO \rightarrow 0.9\ NO_2 + 0.9\ HO_2 + 0.9\ H_2CO + 0.9\ MGGY$	$4.2 \times 10^{-12} \exp(180/T)$
$MRO_2 + HO_2 \rightarrow IOOH + O_2$	3.0×10^{-12}
$IOOH + OH \rightarrow MRO_2 + H_2O$	1.0×10^{-11}
$HAC + OH \rightarrow HACO$	1.5×10^{-11}
$HACO + NO_2 \rightarrow IPAN$	4.7×10^{-12}
$IPAN \rightarrow HACO + NO_2$	$1.95 \times 10^{16} \exp(-13543/T)$
$HACO + NO \rightarrow NO_2 + HO_2 + H_2CO$	$4.2 \times 10^{-12} \exp(180/T)$
$HACO + HO_2 \rightarrow$ products	3.0×10^{-12}
$ISOP + O_3 \rightarrow 0.5\ H_2CO + 0.2\ MVK + 0.3\ MACR + 0.2\ CH_2O_2 + 0.2\ MVKO + 0.3\ MAOO$	$7.0 \times 10^{-15} \exp(-1900/T)$
$MVK + O_3 \rightarrow 0.5\ H_2CO + 0.2\ CH_2O_2 + 0.2\ HO_2 + 0.2\ MCRG + 0.15\ CH_3CHO + 0.5\ MGGY + 0.15\ CH_3CO_3$	$4.0 \times 10^{-15} \exp(-2000/T)$
$MVKO + NO \rightarrow MVK + NO_2$	$4.2 \times 10^{-12} \exp(180/T)$
$MVKO + NO_2 \rightarrow MVK + NO_3$	$4.2 \times 10^{-13} \exp(180/T)$
$MVKO + H_2O \rightarrow$ products	3.4×10^{-18}
$MAOO + NO \rightarrow MACR + NO_2$	$4.2 \times 10^{-12} \exp(180/T)$
$MAOO + NO_2 \rightarrow MACR + NO_3$	$4.2 \times 10^{-13} \exp(180/T)$
$MAOO + H_2O \rightarrow$ products	3.4×10^{-18}
$MCRG + NO \rightarrow MGGY + NO_2$	$4.2 \times 10^{-12} \exp(180/T)$
$MCRG + NO_2 \rightarrow MGGY + NO_3$	$4.2 \times 10^{-13} \exp(180/T)$
$MCRG + H_2O \rightarrow$ products	3.4×10^{-18}
$HAC + h\nu \rightarrow H_2CO + 2HO_2$	$0.0005 \times j(NO_2)$
$MGGY + h\nu \rightarrow CH_3CO_3 + HO_2$	$0.15 \times j(NO_2)$
$MGGY + OH \rightarrow CH_3CO_3$	1.7×10^{-11}
$ISOP + NO_3 \rightarrow INO_2$	3.23×10^{-13}
$INO_2 + NO \rightarrow 2NO_2 + H_2CO + 0.5\ MVK + 0.5\ MACR$	$4.2 \times 10^{-12} \exp(180/T)$
$INO_2 + NO_2 \rightarrow IPN_4$	$4.2 \times 10^{-13} \exp(180/T)$
$INO_2 + HO_2 \rightarrow$ products	3.0×10^{-12}
$MVK + NO_3 \rightarrow MVN_2$	6.0×10^{-14}
$MVN_2 + NO \rightarrow 2NO_2 + H_2CO + 0.5\ CH_3CO_3 + 0.5\ MGGY + 0.5\ HO_2$	$4.2 \times 10^{-12} \exp(180/T)$
$MVN_2 + HO_2 \rightarrow$ products	3.0×10^{-12}
$HAC + NO_3 \rightarrow HNO_3 + HACO$	5.2×10^{-16}
$MAOO + HO_2 \rightarrow$ products	3.0×10^{-12}
$MVKO + HO_2 \rightarrow$ products	3.0×10^{-12}

Reaction mechanism has been taken from *Lurmann et al.* [1986] with modifications described below. All species are defined by *Lurmann et al.* [1986] except IOOH, which is defined here as organic peroxides resulting from isoprene oxidation. MCO_3 is modeled as CH_3CO_3, and all higher aldehydes are modeled as CH_3CHO. The oxidation of isoprene by both OH and O_3 produces two primary products, methyl vinyl ketone (MVK) and methacrolein (MACR), which in turn both react with O_3 and NO_3. We have eliminated the reactions of methacrolein with O_3 and NO_3 because the rates of these reactions are small compared with that for the reaction with OH. The reactions of RIO_2, VRO_2, and MRO_2 with HO_2 have been changed to produce IOOH, as suggested by *Jacob and Wofsy* [1988]. IOOH then photolyzes or reacts with OH. The reactions $RIO_2 + RIO_2$ have been added to the *Lurmann et al.* [1986] mechanism because the results of *Madronich and Calvert* [1990] suggest that this reaction is important in low NO_x environments.

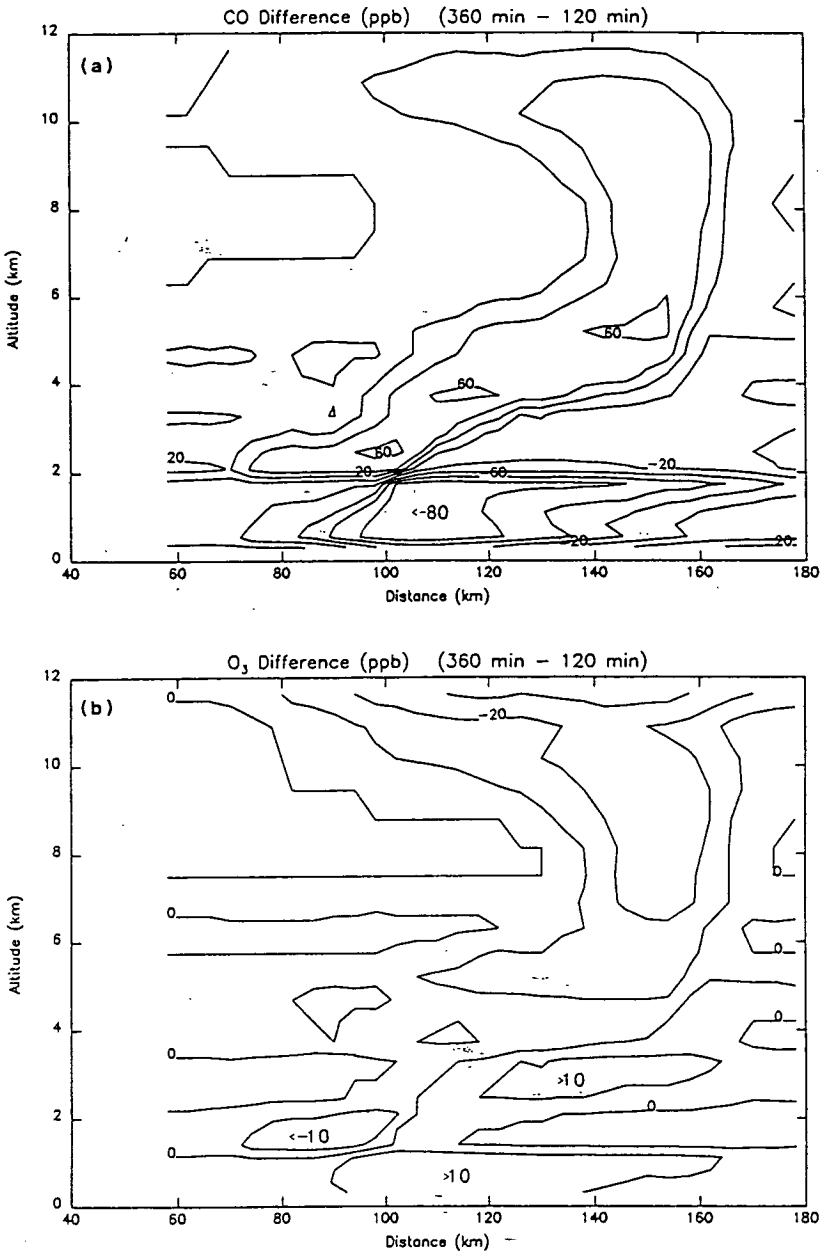

Fig. 10. Difference in tracer concentrations computed by subtracting 120-min fields from 360-min fields: (*a*) CO (ppb), (*b*) O_3 (ppb), and (*c*) NO_x (ppt). Contour interval is 20 ppb for CO, 10 ppb for O_3, and 10 ppt for NO_x.

tropical squall line situation. The values of the coefficients for the other species (with the exception of RIO_2) were scaled against this value based on solubility using values of Henry's law coefficients given by *Lelieveld and Crutzen* [1990]. The wet removal coefficients were adjusted for ambient temperature conditions on the model grid using expressions also given by *Lelieveld and Crutzen* [1990]. The wet removal coefficient for RIO_2 was assumed to be one tenth of that for CH_3O_2. The coefficients were applied only at those vertical grid points at which the cloud model indicated that there was cloud water or rainwater. We have not included scavenging by frozen hydrometeors in the model because there are considerable uncertainties regarding such processes. We have also not included aqueous phase loss of ozone such as described by *Lelieveld and Crutzen* [1990]. The changes in ozone production potential inside the cloud that are reported here are therefore those due only to perturbations in gas phase photochemistry caused by changes in light conditions and scavenging of the gases and radicals listed above.

Nonmethane hydrocarbons (NMHC) were not measured on the aircraft during the August 3 flight, so we constructed isoprene profiles based on other measurements. A daytime flux of 7.7×10^{11} molecules cm^{-2} s^{-1} [*Jacob and Wofsy*, 1988] was used with the photochemical model to generate profiles for the analysis that match the following: (1) a measurement of isoprene (5.11 ppb) within the canopy taken [*Zimmerman et al.*, 1988] in the late morning of August 3 and (2) the median mixed layer concentration (2.7 ppb) during ABLE 2A at noon based on tethered balloon observations of *Zimmerman et al.* [1988]. An air sample taken from the aircraft at 5 km on the previous day (August 2) during

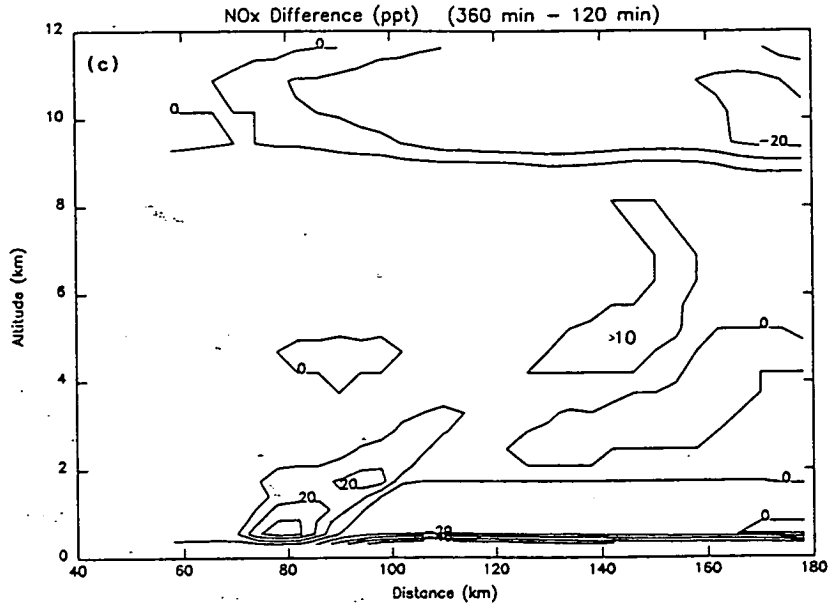

Fig. 10. (continued)

convective conditions contained 0.15 ppb of isoprene [*Rasmussen and Khalil*, 1988]. We have forced the model profile to this value at noon at 5 km in the model runs for cloud-perturbed conditions. The isoprene emission flux is allowed to go to zero at sunset.

Two types of photochemical analyses have been performed. In the first analysis the transient effects on gas-phase photochemistry during the episode itself are examined, and in the second analysis we take the approach of evaluating the aftereffects of convective redistribution. In the first analysis, vertical profiles of CO, O_3, NO_x, temperature, pressure, and water vapor as computed by the cloud model and tracer analyses at the 360-min point of the cloud simulation are used as input to the chemical model, and the instantaneous ozone production rates are estimated for noon for the region containing the squall line and the region a few kilometers ahead of the line. To simulate the photochemical processes within the precipitating cloud system, it is necessary to estimate in-cloud photolysis rates and wet removal of a number of chemical species by cloud water and rainwater.

Second, the diurnally averaged ozone production rate is computed for air that has been processed by the cloud, as well as for undisturbed air ahead of the cloud, over the 24-hour period following the convective event. In this analysis the model is applied assuming that the clouds have dissipated (that is, clear sky photolysis rates were used) and no further convective redistribution occurs.

For the analysis inside the active cloud the model was run from sunrise to noon with the concentrations of CO, O_3, and NO fixed at midday values. Thirty model runs were performed at 4-km intervals across the horizontal grid of the convective cloud model creating a two-dimensional diagnostic presentation of the ozone production rate in the cloud. For the 24-hour model runs, NO is not fixed, and the boundary conditions include daytime upward flux of NO at the surface, a downward flux of NO_y from the stratosphere at the upper model boundary, and dry deposition of NO_2, NO_3, HNO_3, HNO_4, N_2O_5, H_2CO, H_2O_2, and higher peroxides at the surface. The NO flux of 5.2×10^{10} molecules cm^{-2} s^{-1} was taken from *Kaplan and Wofsy* [1988] and represents the average value measured during ABLE 2A. Where resulting NO profiles do not match the NO in the NO_x tracer results above the mixed layer at noon, horizontal and vertical advection was simulated with additional forcing.

A two-dimensional plot of the instantaneous net ozone production rate at noon composed from 30 profiles across the cloud from front to rear is shown in Figure 11. Interpretation of this figure is aided by the shading representing the area containing cloud and/or rainwater and by examination of Figure 10*c* (the NO_x tracer differences). Ahead of the cloud (58–66 km on the distance scale), substantial ozone production occurs near the surface. At the surface, values exceed 300×10^5 molecules cm^{-3} s^{-1}. As NO_x decreases with altitude in the lower troposphere, so do the $P(O_3)$ values, declining to zero at about 3.8 km. Net destruction of ozone occurs from this level to 8 km, where sufficient NO_x again becomes available to catalyze ozone production. Inside the leading edge of the storm (74-km point), ozone production near the surface decreases sharply primarily due to wet removal of trace gases and radicals by the rain. At this point the ozone production at the surface is about 62×10^5 molecules cm^{-3} s^{-1}. Farther to the rear of the cloud (126–154 km on the distance scale), $P(O_3)$ increases near the surface due to the fact that no rain is reaching the surface in this region. A major region of increased ozone production (compared with ahead of the cloud and the forward section of the cloud) exists from 5 to 8 km in the rear portion of the cloud. This region corresponds to the area of increased NO_x concentrations seen from the tracer analysis (Figure 10*c*) and is above the region of liquid water in the cloud and assumed heterogeneous losses of radicals. Examination of the change in instantaneous net ozone production at noon at 3 km at the leading edge of the cloud (70-km point) shows a reduction of 7.0×10^5 molecules cm^{-3} s^{-1} compared with the clear sky conditions ahead of the storm (58-km point). The reduction due to similar processes that was computed

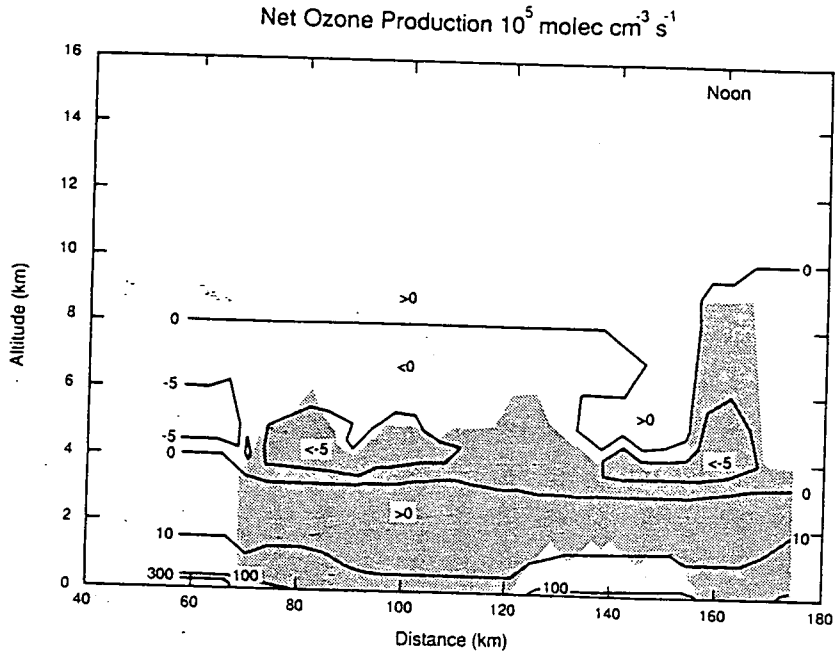

Fig. 11. Two-dimensional diagnostic plot of the instantaneous net ozone production rate at noon across the squall line. Shaded area represents region containing cloud water and rainwater. Contours are labeled in terms of 10^5 molecules cm^{-3} s^{-1}.

by *Lelieveld and Crutzen* [1990] at the same altitude in their cloud located at the equator was comparable at 5.2×10^5 molecules cm^{-3} s^{-1}. Lelieveld and Crutzen indicate that the change is greater if aqueous phase loss of ozone is included.

Figure 12 presents the net ozone production integrated over the tropospheric column from 50 m to 13 km for each of the 30 profiles across the cloud. The large decrease (by 70%) in column production at the forward edge of the cloud is very evident. Farther into the cloud, a decline in column ozone production occurs as NO_x in the lower troposphere decreases because of downward transport of cleaner air. The

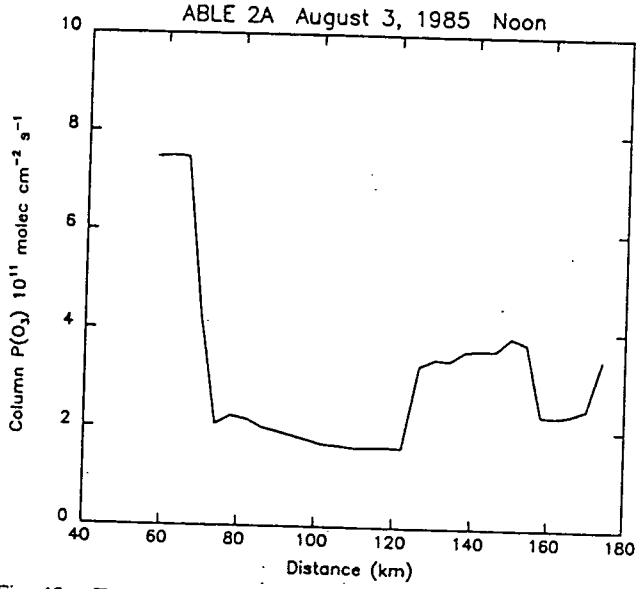

Fig. 12. Tropospheric column net ozone production at noon across the squall line.

126- to 154-km distance range shows an increase in column $P(O_3)$ to 3.90×10^{11} molecules cm^{-2} s^{-1} from the minimum value of 1.62×10^{11} molecules cm^{-2} s^{-1}. This region contains both the local production maximum near the surface that is due to no rainfall reaching the surface and the middle to upper tropospheric local maximum that is due to convectively enhanced NO_x. Integrated over the entire two-dimensional domain, the total net ozone production is 1.07×10^{20} molecules cm^{-1} s^{-1}, compared with 2.60×10^{20} molecules cm^{-1} s^{-1} obtained by assuming that the value from ahead of the storm existed across the entire domain (that is, no convective event). Thus the transient effect of the cloud on net ozone production is a 58% reduction, compared with no cloud.

Results of the model analysis of the aftereffects of the convective event on ozone production in the upper level storm outflow are shown in Figure 13. We have run the one-dimensional photochemical model for the 24-hour period following the time of the transient analysis (noon on August 3, 1985) for two sets of profiles. The first set of profiles, which represent cloud-processed air, is taken from the 154-km point on the model distance scale (indicated with vertical dashed lines on Figures 9*b*, 9*d*, and 9*f*). The model profiles of CO, O_3, NO_x, temperature, and water vapor for this location at 360 min into the cloud model simulation represent boundary layer air that has been carried to the upper troposphere, as well as midtropospheric air that has descended into the storm's wake. The second set of profiles, taken from the 58-km point at 120 min (indicated with dashed lines in Figures 9*a*, 9*c*, and 9*e*, represents undisturbed conditions. Increased NO_x and CO in the 4- to 8-km altitude range is transported downstream following the convective event and enhances ozone production potential. At 8 km, convection has caused a change from diurnally averaged net destruction of ozone to net production. Between 4 and 7 km

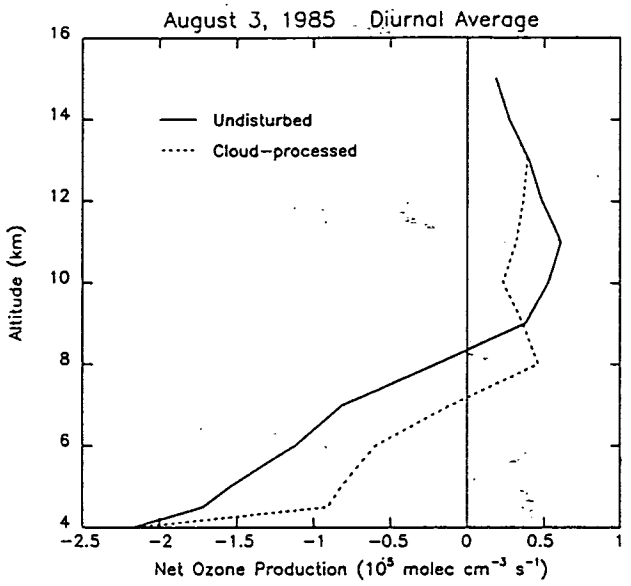

Fig. 13. Diurnally averaged ozone production potential for the 24 hours following the August 3, 1985, convective event.

the net destruction is substantially decreased. The column from 5 to 13 km had a net destruction of ozone of 1.28×10^{10} molecules cm^{-2} s^{-1} in undisturbed air but a net production of 0.60×10^{10} molecule cm^{-2} s^{-1} in air processed by the cloud. Below 4 km (not plotted), only a slight decrease in diurnally averaged $P(O_3)$ occurs. NO_x is initially diminished in the lower troposphere due to the storm downdraft, but NO_x concentrations recover because of flux from the surface.

We have performed sensitivity studies to elucidate the two major processes that cause substantial changes in ozone production in a convective cloud compared with clear sky conditions. Table 2 demonstrates the change in tropospheric column net O_3 production by showing the results of five individual one-dimensional photochemical model runs performed for the same position on the cloud model grid (70 km on the distance scale). This is the first grid point within the leading edge of the cloud. These model runs consisted of (1) assumption of clear sky, (2) assumption of cloud photolysis using the *Thompson* [1984] model, (3) photolysis as in assumption 2 but also including heterogeneous loss of seven species, (4) same as assumption 3 but including convective transport of isoprene to 6 km, and (5) same as assumption 4 but using photolysis rates for in cloud as recommended by *Madronich* [1987]. One of the several cloud photolysis schemes presented by Madronich was selected for testing. This scheme assumes that photolysis is enhanced above an altitude equal to half the full cloud height and diminished below this level. This scheme was selected because the computed reduction in below-cloud UV flux corresponded to that (reduction to about 10% of the clear sky value) measured beneath another Amazon squall line (May 6, 1987, in ABLE 2B).

TABLE 2. Comparison of Column-Integrated Net Ozone Production at Noon for Five Modeling Scenarios at 70 km on Cloud Grid

Scenario	Net $P(O_3)$, molecules cm^{-2} s^{-1}
1. Clear skies	7.347×10^{11}
2. *Thompson* [1984] cloud photolysis	7.317×10^{11}
3. *Thompson* [1984] cloud photolysis Heterogeneous losses	4.139×10^{11}
4. *Thompson* [1984] cloud photolysis Heterogeneous losses Convective transport of isoprene	4.244×10^{11}
5. *Madronich* [1987] cloud photolysis Heterogeneous losses Convective transport of isoprene	4.153×10^{11}

A small decrease in column net O_3 production results from introduction of cloud photolysis (Table 2). Decreased O_3 production because of lesser amounts of HO_2 and RO_2 radicals in the lower light conditions of the cloud is almost balanced by decreased O_3 loss by photolysis. The wet removal process affects net O_3 production to a large degree (about a 40% decrease) because of the reduction in available HO_2 and RO_2 radicals. The *Madronich* [1987] photolysis scheme only changes net O_3 production by 2% compared with the *Thompson* [1984] scheme (comparing model runs 4 and 5), because the bulk of the production occurs below 3 km, a region little affected by the choice of cloud photolysis modeling parameterization.

Figure 14 presents the contributions to $P(O_3)$ of the various production terms of equation (2) for both the region ahead of the cloud (58-km point; clear sky assumed) and in the precipitating region of the cloud (94-km point). In the clear sky region the production term representing oxidation of NO to NO_2 by the RIO_2 radicals that result from isoprene oxidation is about comparable to the term involving HO_2 from the surface to 2 km. However, the contribution of the RIO_2 term diminishes rapidly above 2 km, where the HO_2 and CH_3O_2 terms dominate. Inside the cloud the RIO_2 term is more dominant in the lower troposphere than it is without the cloud. It is the largest production term up to 4 km in the cloud. Convective upward transport of isoprene extends the influence of RIO_2 to higher altitudes in the cloud than ahead of the system. Also, heterogeneous loss of HO_2 and CH_3O_2 radicals has been assumed to be greater than that for RIO_2, allowing the ozone production contribution by the RIO_2 term to exceed that for the other terms. The terms containing VRO_2 and MRO_2 (the other radicals resulting from isoprene oxidation) make smaller contributions to $P(O_3)$ in both the clear and cloudy conditions. Their contribution is approximately an order of magnitude less than the RIO_2 term in the lowest 2 km.

The rate term representing loss of ozone through photolysis and subsequent reaction of $O(^1D)$ with H_2O is the largest loss term from the surface to 7 km under clear conditions. Above this altitude the largest loss of ozone is from the reaction of O_3 with HO_2. Inside the cloud the term involving H_2O decreases in magnitude due to the formation of cloud droplets and rain, but it remains the largest loss term from the surface to 6 km. This loss term is more dominant over those due to reaction of ozone with OH or HO_2 under cloudy, precipitating conditions than in clear conditions due to the heterogeneous loss of OH and HO_2.

DISCUSSION

Both surface-based and aircraft measurements in ABLE 2A have shown that the rain forest constitutes a major sink

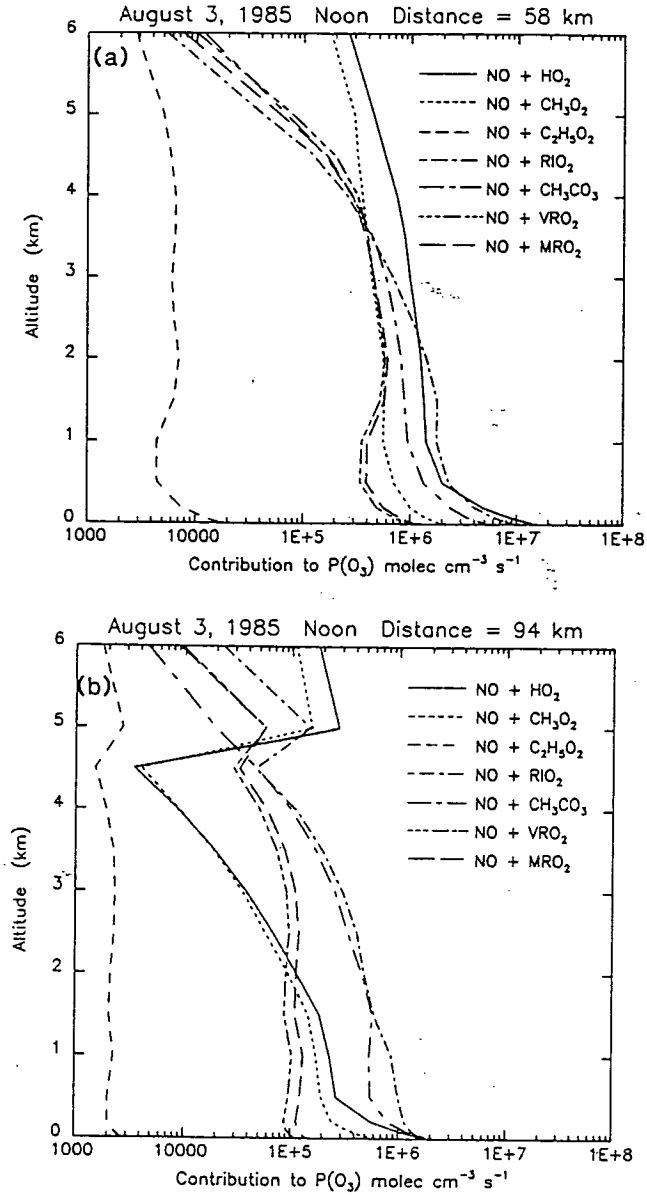

Fig. 14. Contributions to the net photochemical ozone production rate at noon by seven production terms (*a*) ahead of the squall line and (*b*) within the squall line.

for ozone through dry deposition. Daytime losses of O_3 in the morning mixed layer averaged 1.6×10^{12} molecules cm^{-2} s^{-1} and ranged from 7.7×10^{10} to 5.7×10^{12} molecules cm^{-2} s^{-1} [*Gregory et al.*, 1988]. The nighttime flux downward to the forest was estimated to be 5.6×10^{11} molecules cm^{-2} s^{-1} [*Kaplan et al.*, 1988]. We have computed a net photochemical production of ozone in the mixed layer (0–1 km) of 6.93×10^{11} molecules cm^{-2} s^{-1} at noon ahead of the convective storm which is equivalent to 1.1 ppb h^{-1}. This value is somewhat less than the 1.6 ppb h^{-1} computed by *Madronich and Calvert* [1990], primarily due to slightly lower NO measured in the particular case analyzed here. The NO in this case may be lower than the average for the ABLE 2A expedition due to intermittent cloudiness during the hours prior to the squall line passage. Deposition of ozone may also have been below the average rate on this day ahead of the storm, allowing an approximate balance between ozone production and deposition. We have computed a net photochemical production of 1.50×10^{11} molecules cm^{-2} s^{-1} in the mixed layer under the cloud (e.g., at distance 94 km), which probably represents a net loss of ozone in this layer.

Biomass burning in the tropics has been demonstrated to be a major factor in the global tropospheric ozone budget [*Fishman et al.*, 1990]. *Kirchhoff et al.* [1988] noted an increase in ozone throughout the troposphere based on ozonesondes taken from late July to early August 1985 during ABLE 2A at Manaus, Amazonia, as biomass burning activity increased in the state of Mato Grosso and air masses began to arrive at Manaus from this region. *Fishman and Browell* [1988] have shown that both UV-DIAL O_3 profiles and total ozone column measurements from total ozone mapping spectrometer (TOMS) aboard the Nimbus 7 satellite reflect this same increase in tropospheric ozone during the July and August 1985 period. Both *Kirchhoff et al.* [1988] and *Fishman and Browell* [1988] indicated that August 3, 1985, was within this period of increasing tropospheric ozone, but Fishman and Browell also show that the increasing trend continued until late August or early September. The tropospheric portion of the total column ozone may have increased by 10 Dobson units between August 3 and early September, indicating that the August 3 case was in the early part of the annual ozone pollution episode that occurs as a result of tropical biomass burning.

Over the 24-hour period following convection we find that the total ozone production in the tropospheric column was little changed in this case from preconvection conditions. However, a change from net ozone destruction to net production occurred in the middle to upper troposphere as a result of the convection. *Chatfield and Delany* [1990] have demonstrated substantial increases in photochemical ozone production in the middle and upper troposphere during the several days following convective events that transported relatively fresh biomass burning emissions ("mix-then-cook" scenario) and somewhat less production in a scenario in which pollutants accumulate for several days before convection occurs ("cook-then-mix"). The case we have studied corresponds more closely to the cook-then-mix scenario than to the mix-then-cook scenario. Some additional ozone had already been produced in the lower troposphere before the polluted layer encountered the convection after considerable horizontal transport from the burning region. Our results for the first 24 hours following the event appear to show a smaller amount of net ozone production in the middle to upper troposphere than do the Chatfield and Delany calculations for a hypothetical convective event. The Chatfield and Delany cook-then-mix scenario produced ozone at the rate of about 1 ppb d^{-1} at 8 km after convection, whereas our results for this altitude are about one third of that rate, with losses continuing below. The net ozone production rates in the middle to upper troposphere in the cook-then-mix scenario are greater than our results, primarily because Chatfield and Delany's hypothetical convective event took place over the savanna, much closer to the source of biomass burning emissions where substantially more NO_x was available, whereas the ABLE 2A case involved long-range transport of the biomass burning emissions to Amazonia. The August 3, 1985, ABLE 2A case occurred at the beginning of the burning season and pollutant concentrations had not yet accumulated to the levels found later in the

burning season by *Crutzen et al.* [1985] and *Delany et al.* [1985].

CONCLUSIONS

We have developed a technique of using a two-dimensional convective cloud model with detailed microphysics and a one-dimensional photochemical model in tandem to estimate the transient effects and the aftereffects of deep tropical convection on the tropospheric ozone production potential. We have found a substantial reduction of photochemical ozone production within a dry season squall line cloud observed in ABLE 2A (August 3, 1985) but a positive change in ozone production potential in the middle to upper troposphere over the 24 hours following the storm in air redistributed by the convection. Increases of approximately 60 ppb of CO occurred from 2.5 to 6 km as a result of convective transport, and a region containing CO increases of 40 ppb extended to 11 km. NO_x increases are seen up to 8 km at the rear of the storm. There would have been a NO_x increase at even higher altitudes if the emissions from biomass burning were fresher.

The transient effects of the squall line cloud have been investigated using a two-dimensional diagnostic modeling technique. We have found that at noon the cloud causes a reduction of the instantaneous net ozone production rate of 50–60%, compared with clear sky conditions. The majority of the reduction is caused by wet removal of radicals, and a lesser amount is caused by cloud-perturbed photolysis. The greatest reductions therefore occur in the regions of the storm where precipitation is reaching the surface. The reduction may be even larger if aqueous-phase ozone loss is included. The specific choice of cloudy photolysis treatment had little effect on the net O_3 production in the tropospheric column. Net O_3 production is increased in the middle to upper troposphere at the rear of the squall line due to convective transport of NO_x to this region. The existence of the cloud may temporarily prevent the daytime increase of O_3 concentrations in the mixed layer, because deposition to the surface may exceed the net photochemical production rate under the cloud. Ozone production rates in the free tropospheric portion of this cloud system were sufficiently small that ozone can be considered a conserved tracer on the time scale of transport through the cloud.

The aftereffects of the convective storm were investigated with one-dimensional model runs in undisturbed and cloud-processed air for the 24 hours following the passage of the storm. Net column ozone production for the entire troposphere was essentially unchanged. However, the 4- to 8-km layer of cloud-processed air experienced 45% less photochemical loss of O_3, and the column from 5 to 13 km experienced a change from net ozone destruction to net production as a result of the convection.

The convective cloud model results demonstrate strong convective transport of chemical tracers to the middle and upper troposphere by the August 3, 1985, squall line. The majority of the lower tropospheric air that is lifted is transported to the upper troposphere. This dry season storm provides a sharp contrast to the wet season storm described by *Scala et al.* [1990] in which only a small percentage of the air transported from the boundary layer reached the upper troposphere.

This convective case may be typical of conditions early in the biomass burning season. Only small localized burning activity was occurring at the rain forest/savanna transition. Later in the season, NO_x concentrations over the rain forest may be greater due to more frequent and widespread biomass burning plumes being transported to Amazonia. Convective storms occurring under these conditions would have a greater effect on ozone production due to larger NO_x transport to the middle and upper troposphere. We are investigating how representative the transport of this dry season case is by studying deep convection in several different geographic and seasonal regimes.

Acknowledgments. This work was supported under the NASA Tropospheric Chemistry Program. We thank R. C. Harriss for the initial suggestion to examine the chemistry of the ABLE convective case. We acknowledge the following persons who directed the data collection during ABLE 2A and provided it directly to us or through the ABLE 2A data archive: E. V. Browell, G. L. Gregory, M. A. K. Khalil, V. W. J. H. Kirchhoff, R. A. Rasmussen, G. W. Sachse, A. L. Torres, and P. R. Zimmerman. J. W. Drewry and D. Owens were very helpful in providing data from the archive at NASA Langley Research Center. J.R.S. is currently a National Research Council Resident Research Associate. This research was performed under contract at NASA Goddard Space Flight Center, Greenbelt, Maryland. We appreciate the reviewers' helpful comments.

REFERENCES

Andreae, M. O., et al., Biomass-burning emissions and associated haze layers over Amazonia, *J. Geophys. Res.*, *93*, 1509–1527, 1988.

Browell, E. V., G. L. Gregory, R. C. Harriss, and V. W. J. H. Kirchhoff, Tropospheric ozone and aerosol distribution across the Amazon Basin, *J. Geophys. Res.*, *93*, 1431–1451, 1988.

Chameides, W. L., The photochemistry of a remote marine stratiform cloud, *J. Geophys. Res.*, *89*, 4739–4756, 1984.

Chatfield, R. B., and P. J. Crutzen, Sulfur dioxide in remote oceanic air: Cloud transport of reactive precursors, *J. Geophys. Res.*, *89*, 7111–7132, 1984.

Chatfield, R. B., and A. C. Delany, Convection links biomass burning to increased tropical ozone: However, models will tend to overpredict O_3, *J. Geophys. Res.*, *95*, 18,473–18,488, 1990.

Ching, J. K. S., and A. J. Alkezweeny, Tracer study of vertical exchange by cumulus clouds, *J. Clim. Appl. Meteorol.*, *25*, 1702–1711, 1986.

Ching, J. K. S., S. T. Shipley, and E. V. Browell, Evidence for cloud venting of mixed layer ozone and aerosols, *Atmos. Environ.*, *22*, 225–242, 1988.

Crutzen, P. J., A. C. Delany, J. Greenberg, P. Haagenson, L. Heidt, R. Lueb, W. Pollock, W. Seiler, A. Wartburg, and P. Zimmerman, Tropospheric chemical composition measurements in Brazil during the dry season, *J. Atmos. Chem.*, *2*, 233–256, 1985.

Delany, A. C., P. Haagenson, S. Walters, A. F. Wartburg, and P. J. Crutzen, Photochemically produced ozone in the emission from large-scale tropical vegetation fires, *J. Geophys. Res.*, *90*, 2425–2429, 1985.

Dickerson, R. R., et al., Thunderstorms: An important mechanism in the transport of air pollutants, *Science*, *235*, 460–465, 1987.

Drummond, J. W., D. H. Ehhalt, and A. Volz, Measurements of nitric oxide between 0–12 km altitude and 67°N to 60°S latitude obtained during STRATOZ III, *J. Geophys. Res.*, *93*, 15,831–15,849, 1988.

Fishman, J., and E. V. Browell, Comparison of satellite total ozone measurements with the distribution of tropospheric ozone obtained by an airborne UV-DIAL system over the Amazon Basin, *Tellus, Ser. B*, *40*, 393–407, 1988.

Fishman, J., C. E. Watson, J. C. Larsen, and J. A. Logan, Distribution of tropospheric ozone determined from satellite data, *J. Geophys. Res.*, *95*, 3599–3618, 1990.

Garstang, M., et al., Trace gas exchanges and convective transports over the Amazonian rain forest, *J. Geophys. Res.*, *93*, 1528–1550, 1988.

Gidel, L. T., Cumulus cloud transport of transient tracers, *J. Geophys. Res.*, *88*, 6587–6599, 1983.

Gregory, G. L., E. V. Browell, and L. S. Warren, Boundary layer ozone: An airborne survey above the Amazon Basin, *J. Geophys. Res.*, *93*, 1452–1468, 1988.

Harriss, R. C., et al., The Amazon Boundary Layer Experiment (ABLE 2A): Dry season 1985, *J. Geophys. Res.*, *93*, 1351–1360, 1988.

Jacob, D. J., and S. C. Wofsy, Photochemistry of biogenic emissions over the Amazon forest, *J. Geophys. Res.*, *93*, 1477–1486, 1988.

Kaplan, W. A., S. C. Wofsy, M. Keller, and J. M. De Costa, Emission of NO and deposition of O_3 in a tropical forest system, *J. Geophys. Res.*, *93*, 1389–1395, 1988.

Kirchhoff, V. W. J. H., E. V. Browell, and G. L. Gregory, Ozone measurements in the troposphere of an Amazonian rain forest environment, *J. Geophys. Res.*, *93*, 15,850–15,860, 1988.

Lafore, J. P., and M. W. Moncrieff, A numerical investigation of the organization and interaction of convective and stratiform regions of tropical squall lines, *J. Atmos. Sci.*, *46*, 521–544, 1989.

Lelieveld, J., and P. J. Crutzen, Influences of cloud photochemical processes on tropospheric ozone, *Nature*, *343*, 227–233, 1990.

Levine, S. Z., and S. E. Schwartz, In-cloud and below-cloud scavenging of nitric acid vapor, *Atmos. Environ.*, *16*, 1725–1734, 1982.

Lurmann, F. W., A. C. Lloyd, and R. Atkinson, A chemical mechanism for use in long-range transport/acid deposition computer modeling, *J. Geophys. Res.*, *91*, 10,905–10,936, 1986.

Madronich, S., Photodissociation in the atmosphere, 1, Actinic flux and effects of ground reflections and clouds, *J. Geophys. Res.*, *92*, 9740–9752, 1987.

Madronich, S., and J. G. Calvert, Permutation reactions of organic peroxy radicals in the troposphere, *J. Geophys. Res.*, *95*, 5697–5715, 1990.

Pickering, K. E., R. R. Dickerson, G. J. Huffman, J. F. Boatman, and A. Schanot, Trace gas transport in the vicinity of frontal convective clouds, *J. Geophys. Res.*, *93*, 759–773, 1988.

Pickering, K. E., R. R. Dickerson, W. T. Luke, and L. J. Nunnermacker, Clear sky vertical profiles of trace gases as influenced by upstream convective activity, *J. Geophys. Res.*, *94*, 14,879–14,892, 1989.

Pickering, K. E., A. M. Thompson, R. R. Dickerson, W. T. Luke, D. P. McNamara, J. P. Greenberg, and P. R. Zimmerman, Model calculations of tropospheric ozone production potential following observed convective events, *J. Geophys. Res.*, *95*, 14,049–14,062, 1990.

Rasmussen, R. A., and M. A. K. Khalil, Isoprene over the Amazon Basin, *J. Geophys. Res.*, *93*, 1417–1421, 1988.

Riehl, H., and J. S. Malkus, On the heat balance in the equatorial trough zone, *Geophysica*, *6*, 503–538, 1958.

Riehl, H., and J. Simpson, The heat balance of the equatorial trough zone revisited, *Contrib. Atmos. Phys.*, *52*, 287–305, 1979.

Sachse, G. W., R. C. Harriss, J. Fishman, G. F. Hill, and D. R. Cahoon, Carbon monoxide over the Amazon Basin during the 1985 dry season, *J. Geophys. Res.*, *93*, 1422–1430, 1988.

Scala, J. R., et al., Cloud draft structure and trace gas transport, *J. Geophys. Res.*, *95*, 17,015–17,030, 1990.

Slinn, W. G. N., Rate-limiting aspects of in-cloud scavenging, *J. Atmos. Sci.*, *31*, 1172–1173, 1974.

Soong, S.-T., and W.-K. Tao, Response of deep tropical clouds to mesoscale processes, *J. Atmos. Sci.*, *37*, 2035–2050, 1980.

Tao, W.-K., and J. Simpson, Modeling study of a tropical squall-type convective line, *J. Atmos. Sci.*, *46*, 177–202, 1989.

Thompson, A. M., The effect of clouds on photolysis rates and ozone formation in the unpolluted troposphere, *J. Geophys. Res.*, *89*, 1341–1349, 1984.

Thompson, A. M., and R. J. Cicerone, Clouds and wet removal as causes of variability in the trace gas composition of the marine troposphere, *J. Geophys. Res.*, *87*, 8811–8826, 1982.

Thompson, A. M., and R. J. Cicerone, Possible perturbations to atmospheric CO, CH_4, and OH, *J. Geophys. Res.*, *91*, 10,853–10,864, 1986.

Torres, A. L., and H. Buchan, Tropospheric nitric oxide measurements over the Amazon Basin, *J. Geophys. Res.*, *93*, 1396–1406, 1988.

Zimmerman, P. R., J. P. Greenberg, and C. E. Westberg, Measurements of atmospheric hydrocarbons and biogenic emission fluxes in the Amazon boundary layer, *J. Geophys. Res.*, *93*, 1407–1416, 1988.

M. Garstang, Department of Environmental Sciences, University of Virginia, Charlottesville, VA 22903.

K. E. Pickering, Applied Research Corporation, 8201 Corporate Drive, Landover, MD 20785.

J. R. Scala, J. Simpson, and W.-K. Tao, NASA Goddard Space Flight Center, Mail Code 912, Greenbelt, MD 20771.

A. M. Thompson, NASA Goddard Space Flight Center, Mail Code 916, Greenbelt, MD 20771.

(Received June 5, 1990;
revised October 12, 1990;
accepted October 16, 1990.)